Stoichiometry of the interactions between endogenous Orai1 and STIM1 during store-operated Ca^{2+} entry

Yihan Shen

St. John's College

Department of Pharmacology

University of Cambridge

A Thesis submitted for the Degree of

Doctor of Philosophy

September 2021

Contents

Preface

This thesis is the result of my own work and includes nothing which is the outcome of work done in collaboration except as declared here or specified in the text.

It is not substantially the same as any that I have submitted, or, is being concurrently submitted for a degree or diploma or other qualifications. I further state that no substantial part of my dissertation has already been submitted, or, is being concurrently submitted for any such degree, diploma or other qualifications.

It does not exceed the prescribed word limit for the Biology Degree Committee of 60,000 words.

Yihan Shen

September 2021

Acknowledgements

I would like to express my sincere gratitude to my supervisor, *Prof.* Colin W Taylor, for his enthusiastic encouragement, constructive advice, useful critiques and offering me the great opportunity to work in his fantastic lab. I can feel his huge passion in this field, with which he has reached extremely high achievements. He not only guided me through the academic work, but also taught me to develop a critical attitude towards the research and how to present a scientific story adequately. He is a real scientist and an exceptional supervisor. I also would like to thank Dr. Nagendra Babu Thillaiappan, who supervised me on a day-to-day basis and guided me through experiments and analyses. I have always been impressed by his conscientious and meticulous work. He also advised on polishing this thesis. Furthermore, assistance provided by all other members in the lab on my project and daily life was greatly appreciated.

I must express my very profound gratitude to my motherland, China. It is her development and strength that enabled me to study abroad with cultural confidence. I would like to say big thank you to my dear parents, who have provided me with both financial and moral support throughout my study and life since I came to the UK, without which any of my academic work and my pleasant life would not have been possible. They are always there for me. I could not have completed this thesis without the support from my boyfriend, Shengxian Ke. I am profoundly grateful to all my sincere friends, including but not limited to Linshu Feng and Dawei Guo, for their encouragement and company from the very beginning of my academic life till now, particularly Qiushi Gu, who gave me invaluable help with analysing data in a smarter way. In addition, I would like to send my special thanks to my cat, Heimigao, for his lack of interest in my thesis and my keyboard to delete any of my data.

I would like to extend my sincere thanks to video content creators, Cheng Tang and LexBurner, amongst which the former has inspired me of endless possibilities of academic research, and the latter has provided me with great mental support and endowed me with the ability to resist pressure.

Yihan Shen

September 2021

Summary

Ca^{2+} is a ubiquitous intracellular messenger. It regulates a variety of cellular activities, ranging from muscle contraction, neuronal transmission, secretion and cell growth to apoptosis. Store-operated Ca^{2+} entry (SOCE) is a major pathway of Ca^{2+} signalling and exists in almost all metazoans. SOCE is activated by loss Ca^{2+} from the endoplasmic reticulum (ER), which causes stromal interaction molecule 1 (STIM1) to accumulate at junctions between the ER and plasma membrane (PM). Within these membrane contact sites (MCS), STIM1 forms puncta that trap and activate Orai1 Ca^{2+} channels in the PM, allowing Ca^{2+} to flow into the cytoplasm and slowly replenish Ca^{2+} in the ER.

Elucidating the binding stoichiometry of STIM1 and Orai1 is essential for understanding Orai1 gating and mechanisms of SOCE. Most previous studies of SOCE used cells overexpressing STIM1 and/or Orai1, which might perturb their behaviours. This study used a HeLa cell line in which one copy of the endogenous STIM1 gene was tagged with EGFP using CRISPR/Cas9 gene-editing to understand the stoichiometry and dynamics of STIM1 and Orai1 in SOCE.

I confirmed that SOCE was normal in STIM1-EGFP HeLa cells and that the tagged and untagged versions of STIM1 mixed freely and interacted with Orai1. Total internal reflection fluorescence (TIRF) imaging analyses indicated that there was only a modest increase in the average size of STIM1 puncta after store depletion. Stepwise photobleaching analyses revealed that there was an average of 14.5 STIM1 molecules within each punctum in cells with empty Ca^{2+} stores. Orai1 was immunostained and the fluorescence intensity distributions of the Orai1 puncta were minimally affected by store depletion. Furthermore, the fluorescence intensities of Orai1 that colocalized with STIM1 puncta were similar to those remote from them. Only a small proportion (26%) of STIM1 colocalized with Orai1 at MCS identified by MAPPER, a fluorescent marker constitutively present in the ER-PM junctions. I conclude that each SOCE complex comprises a small cluster of STIM1 and is likely to include no more than one active Orai1 channel. The presence of a single Orai1 channel within each SOCE junction is estimated to be enough to account for observed SOCE-mediated Ca^{2+} signals, but it contradicts suggestions that STIM1 promotes clustering of Orai1 within MCS.

Abbreviations

2-APB	2-Aminoethoxydiphenyl borate
aa	Amino acids
Ab	Antibody
AmpR	Ampicillin resistance
ASEM	Atmospheric scanning electron microscope
ATP	Adenosine triphosphate
BAPTA	1,2-Bis(2-Aminophenoxy) ethane-N,N,N,N-tetraacetic acid
bp	Base pair
BSA	Bovine serum albumin
BSC	Backward scatter
$[Ca^{2+}]_c$	Cytosolic Ca^{2+} concentration
$[Ca^{2+}]_{ER}$	ER Ca^{2+} concentration
CAD	CRAC activation domains
CaM	Calmodulin
CaMKII	Ca^{2+}/calmodulin-dependent protein kinase II
CAR	Ca^{2+}-accumulating region
Cas	CRISPR-associated system
CBD	C-terminal binding domain
CC	Coiled-coil
CCE	Capacitative Ca^{2+} entry
CCh	Carbochol
CDI	Ca^{2+}-dependent inactivation
CICR	Ca^{2+}-induced Ca^{2+} release
CMD	CRAC modulatory domain
Co-IP	Co-immunoprecipitation
CPA	Cyclopiazonic acid
CRAC	Calcium release-activated Ca^{2+}
CRACR2A	CRAC regulator 2A
CRISPR	Clustered regularly interspaced short palindromic repeats
DAG	Diacylglycerol
DHPR	Dyhydropyridine receptors

DMEM/F-12	Dulbecco's modified eagle medium/nutrient mixture F-12
DMSO	Dimethyl sulfoxide
DNA	Deoxyribonucleic acid
DRC	Dose-response curve
DSB	Double strand break
dSTORM	Direct stochastic optical reconstruction microscopy
DTT	DL-dithiothreitol
EB	EB1-binding
E-C	Excitation-contraction
ECL	Enhanced chemiluminescence
EDTA	Ethylenediaminetetraacetic acid
EGFP	Enhanced green fluorescent protein
EMRE	Essential MCU regulator
ER	Endoplasmic reticulum
ETON	Extended transmembrane Orai1 N-terminal
FACS	Fluorescence-activated cell sorting
FBS	Fetal bovine serum
FRAP	Fluorescence recovery after photobleaching
FRET	Förster resonance energy transfer
FSC	Forward scatter
GFP	Green fluorescent protein
GOF	Gain-of-function
GPCR	G-protein coupled receptors
gRNA	Guide RNA
HBS	HEPES-buffered saline
HDR	Homology-directed repair
HEK	Human embryonic kidney
HEPES	4-(2-hydroxyethyl)-1-piperazineethanesulfonic acid
$[IP_3]$	IP_3 concentration
IBC	IP_3-binding core
IMM	Inner mitochondrial membrane
IMS	Intermembrane space
Indel	Insertion or Deletion

IP_3	Inositol 1,4,5-trisphosphate
IP_3R	Inositol 1,4,5-trisphosphate receptor
IPAH	Idiopathic pulmonary arterial hypertension
JACoP	Just Another Co-localization Plugin
kb	Kilobases
KRAP	KRAS-induced actin-interacting protein
LB	Lysogeny broth
LDS	Lithium dodecyl sulfate
LED	Light-emitting diode
Letm1	Leucine-zipper-EF-hand-containing transmembrane protein 1
LPEM	Liquid phase electron microscopy
LTC4	Leukotriene C4
MAM	Mitochondria-associated membranes
mCh	mCherry
MCS	Membrane contact sites
MCU	Mitochondrial Ca^{2+} uniporter
MD	Molecular dynamics
MICU	Mitochondrial calcium uptake proteins
NA	Numerical aperture
NAADP	Nicotinic acid adenine dinucleotide phosphate
NBD	N-terminal binding domain
NCLX	$Na^+/Ca^{2+}/Li^+$ exchanger
NCX	Na^+/Ca^{2+} exchanger
NFAT	Nuclear factor of activated T cells
NHEJ	Non-homologous end joining
NMA	Normal mode analysis
NMR	Nuclear magnetic resonance
NS	Non-silencing
OMM	Outer mitochondrial membrane
P/S	Proline/serine-rich domain
PAM	Protospacer adjacent motif
PBD	Polybasic domains
PBS	Phosphate-buffered saline

PBST	Phosphate-buffered saline, with Tween 20
PCR	Polymerase chain reaction
PIP_2	Phosphatidylinositol 4,5-bisphosphate
PLC	Phospholipase C
PM	Plasma membrane
PMCA	Plasma membrane Ca^{2+} ATPases
PTP	Permeability transition pore
PVDF	Polyvinylidene difluoride
RBL	Rat basophilic leukaemia
RNA	Ribonucleic acid
RNAi	RNA interference
ROC	Receptor-operated channels
ROI	Region of interest
rpm	Rotations per minute
RyRs	Ryanodine receptors
SAD	Single wavelength anomalous dispersion
SAM	Sterile alpha motif
SCID	Severe combined immune deficiency
SDCM	Spinning-disc confocal microscopy
SDS-PAGE	Sodium dodecyl sulfate–polyacrylamide gel electrophgpcroresis
SEC	Size-exclusion chromatography
SEM	Standard error of the mean
SERCA	Sarco/endoplasmic reticulum Ca^{2+}-ATPase
SOAP	STIM-Orai association pockets
SOAR	STIM-Orai activation region
SOCE	Store-operated Ca^{2+} entry
SOCs	Store-operated Ca^{2+} channels
SP	Signal peptide
SPCA	Secretory pathway Ca^{2+} ATPase
SR	Sarcoplasmic reticulum
SRM	Super resolution microscopy
STIM	Stromal interaction molecule
STORM	Stochastic optical reconstruction microscopy

TAE	Tris-acetate-EDTA
TALENs	Transcription activator-like effector nucleases
TBS	Tris-buffered saline
TBST	Tris-buffered saline, with Tween 20
TEM	Transmission electron microscopy
TF	Transcription factor
TG	Thapsigargin
TIRFM	Total internal reflection fluorescence microscopy
TM	Transmembrane
TPC	Two-pore channel
TRP	Transient receptor potential
TRPC	Transient receptor potential canonical
TRPML	Transient receptor potential mucolipin
UCP	Uncoupling protein
UTR	Untranslated region
VDAC	Voltage-dependent anion channel
VGCC	Voltage-gated Ca^{2+} channel
WT	Wild type
ZF	Zinc finger
ZFN	Zinc finger nuclease

Chapter 1 Introduction

1.1. Overview of Ca^{2+} signalling

Calcium ions serve as one of the ubiquitous second messengers in cell signalling pathways, particularly in regulating cellular activities including muscle contraction, cellular motility, cell growth and development (Berridge *et al.* 2000; Rash *et al.* 2016). The resting concentration of free Ca^{2+} in the cytoplasm ($[Ca^{2+}]_c$) is around 100 nM, while the extracellular concentration of Ca^{2+} is normally greater than 1 mM (Montero *et al.* 1995; Foskett *et al.* 2007).

Cells maintain the low $[Ca^{2+}]_c$ via many Ca^{2+} signalling mechanisms (***Figure 1.1***). To maintain the massive concentration gradient between extracellular space and cytosol, Ca^{2+} ions must be actively pumped out from cytosol to the extracellular space by plasma membrane Ca^{2+} ATPases (PMCA) utilizing ATP. The Na^+/Ca^{2+} exchanger (NCX) transports Na^+ down its electrochemical gradient of Na^+ across the plasma membrane (PM) in exchange for the countertransport of Ca^{2+}. Thus, each Ca^{2+} is transported out of the PM for every three Na^+ entering the cytosol (Yu and Choi 1997). Ca^{2+} ions are also removed from the cytosol into various intracellular Ca^{2+} stores: by the sarco/endoplasmic reticulum Ca^{2+} ATPases (SERCA) into the ER, the secretory pathway Ca^{2+} ATPases (SPCA) into the Golgi apparatus (Lissandron *et al.* 2010; Vandecaetsbeek *et al.* 2012), and sequentially through voltage-dependent anion channel (VDAC, in outer mitochondrial membrane) and mitochondrial Ca^{2+} uniporter (MCU, in inner mitochondrial membrane) to mitochondria (Kirichok *et al.* 2004). Lysosomes also keep a high resting Ca^{2+} concentration by pumping Ca^{2+} into the organelle via a Ca^{2+} transporter, but Ca^{2+} leaks from lysosomes via transient receptor potential mucolipin (TRPML), two-pore channel 2 (TPC2) and $P2X_4$ receptors (Morgan *et al.* 2011). Ca^{2+} ions are transported into the cytosol by a number of channels. These channels include voltage-gated Ca^{2+} channels (VGCC), ligand-gated Ca^{2+} channels, and store-operated Ca^{2+} channels, like Orai1 (Berridge 1997; Soboloff *et al.* 2006). Ca^{2+} is also released from intracellular Ca^{2+} stores such as ER, via inositol 1,4,5-trisphosphate receptors (IP_3R) mediated by Ca^{2+} and IP_3, and ryanodine receptors (RyRs).

Voltage-gated Ca^{2+} channels are activated upon depolarization of the PM. They are slightly permeable to Na^+ ions but 1000-fold more permeable to Ca^{2+} (Yamakage and Namiki 2002; Catterall 2011). They mediate L-type, P/Q-type, R-type and T-type Ca^{2+} currents. Ligand-gated Ca^{2+} channels are also named receptor-operated channels (ROCs) and, as the name suggests, are activated by ligand binding. For example, on the PM, P2X channels are activated by ATP

binding to the extracellular loop (North 2002), which induces a conformational change and allows cations, including Ca^{2+}, to enter the cytosol. In contrast, intracellularly, IP_3 activates its receptor in a ligand-dependent way which will be discussed in detail later (***Figure 1.2A***), and nicotinic acid adenine dinucleotide phosphate (NAADP) can open the two-pore channel (TPC), which mediates Ca^{2+} transport across endosomal/lysosomal membranes (Galione 2010). Store-operated Ca^{2+} channels, which will be the focus of this thesis, are activated when the ER Ca^{2+} store is empty (Putney 1986). Furthermore, Ca^{2+} ions themselves are able to open ligand-gated

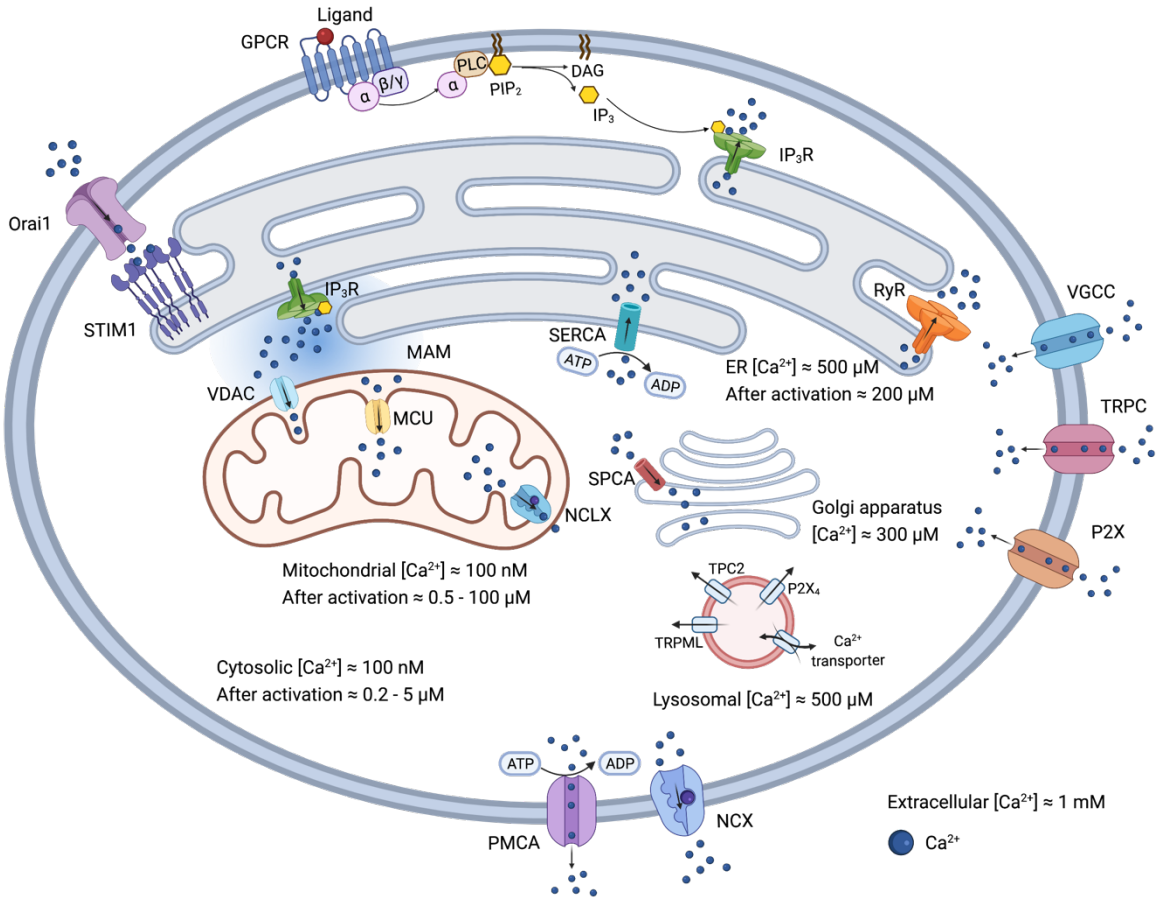

Figure 1.1 A schematic of Ca^{2+} signalling pathways. See ***Abbreviations***. Ca^{2+} is transported from extracellular space into the cytosol through TRPC, VGCC, GPCR, PMCA, NCX and Orai1 (Giorgi *et al.* 2018). Ca^{2+} is transported into ER by SERCA pump and released by IP_3Rs and RyRs. Ca^{2+} is transported into the mitochondria by mitochondrial Ca^{2+} channels, including VDAC, MCU, and out by NCLX (Giorgi *et al.* 2018). Ca^{2+} is pumped into the Golgi apparatus by SPCA (Van Baelen *et al.* 2003). Lysosomes can also be a Ca^{2+} store, where Ca^{2+} leaks from TRPML, TRC2 and $P2X_4$, and enters via Ca^{2+} transporter (Morgan *et al.* 2011).

Ca^{2+} channels as well, known as calcium-induced calcium release (CICR), which is an essential regulatory pathway in IP_3- and RyR-mediated Ca^{2+} release and is vital in excitation-contraction coupling in cardiac muscles (Fabiato 1983).

When Ca^{2+} ions are released into the cytosol from intracellular stores, downstream cellular activities, such as muscle contractions and cell proliferation, are initiated by protein-protein interactions, either through local diffusion of messengers or direct communications between signalling proteins. These interactions influence the spatial organization of Ca^{2+}. As a result, Ca^{2+} signals are selectively delivered to various parts of the cell, inducing different physiological responses (Konieczny *et al.* 2012).

1.2. Intracellular organelles and their Ca^{2+} channels

IP_3 receptors and Ca^{2+} signalling

IP_3Rs mediate one of the most crucial Ca^{2+}-releasing pathways within cells and trigger diverse downstream signalling events, which regulate various cellular activities. IP_3Rs predominantly reside in the ER, but can also be found in small populations in the PM (Dellis *et al.* 2006), nuclear envelope (Rahman *et al.* 2009), and Golgi apparatus (Pinton *et al.* 1998). There are three isoforms in the family of IP_3R, namely IP_3R1 to 3, all of which can assemble with themselves or with each other to form homo-tetrameric or hetero-tetrameric proteins (Supattapone *et al.* 1988; Monkawa *et al.* 1995). The tetramer adopts a square mushroom-like structure (Fan *et al.* 2015) (***Figure 1.2D***). Each subunit contains an IP_3-binding core (IBC) towards the N-terminus, and four subunits collectively create a Ca^{2+}-permeating pore in the centre with large Ca^{2+} conductance, but relatively poor selectivity for Ca^{2+} over K^+ (Bezprozvanny and Ehrlich 1994; Taylor *et al.* 2004). With similar core properties (Lock *et al.* 2018), the IP_3R subtypes differ in IP_3-binding affinities (Iwai *et al.* 2007), regulation by $[Ca^{2+}]_c$ (Cardy *et al.* 1997) and many other properties (Foskett *et al.* 2007).

The initiation of IP_3-mediated Ca^{2+} release starts from a ligand binding to a G_q-coupled receptor on the PM, which activates the GPCR and the Gα subunit subsequently activates phospholipase C β (PLC β). Additionally, the activation of many tyrosine kinases leads to the phosphorylation and activation of PLC γ (Nishibe *et al.* 1990). Activated PLCs then cleave phosphatidylinositol 4,5-bisphosphate (PIP_2) into inositol 1,4,5-trisphosphate (IP_3) and diacylglycerol (DAG). Finally, IP_3 binds to its receptor on the ER membrane and triggers Ca^{2+} release from the intracellular store (***Figure 1.2A***).

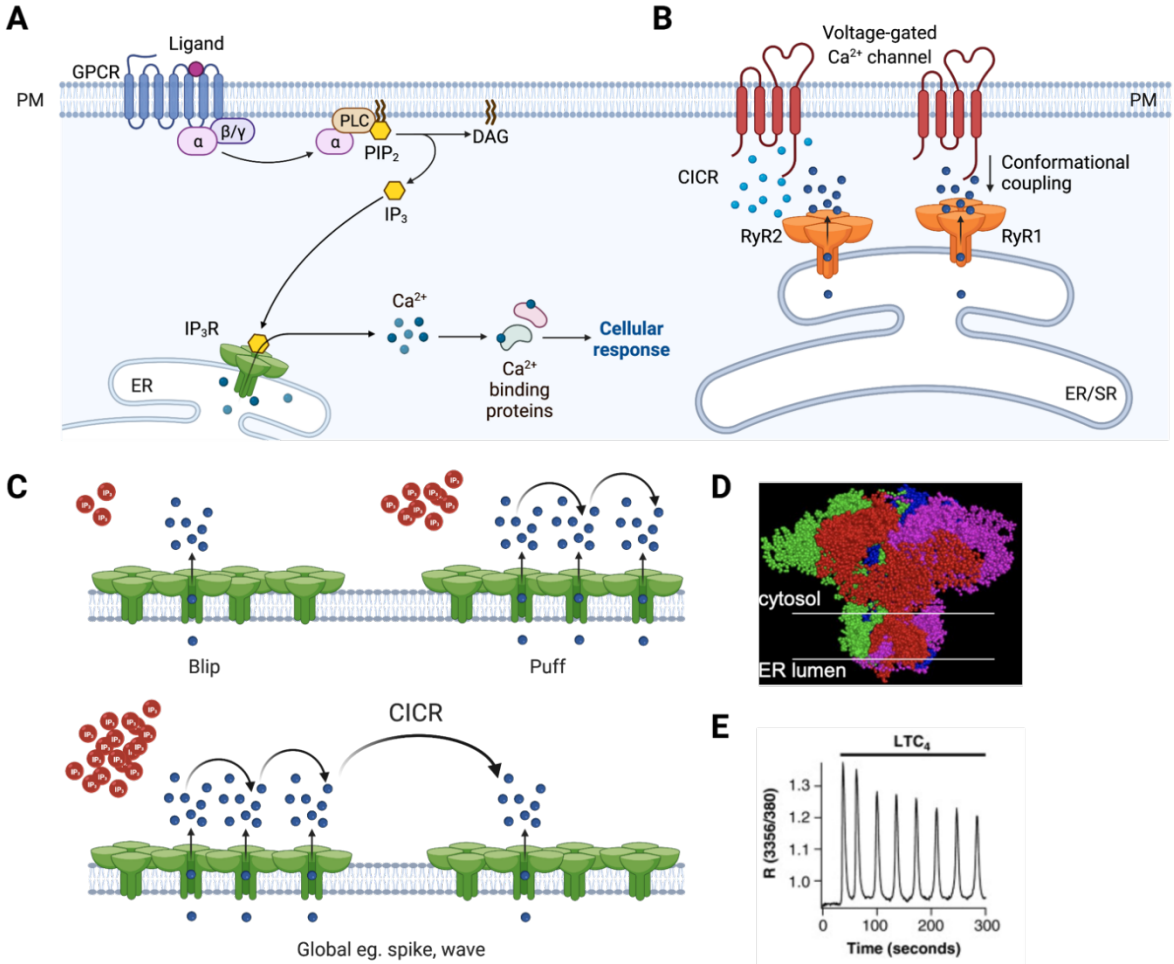

Figure 1.2 Ca^{2+} release by IP_3Rs and RyRs. A. IP_3 mediated Ca^{2+} release. When a ligand binds to a GPCR, the receptor undergoes conformational changes to activate the G_α subunit. G_α subunit activates PLC to cleave PIP_2, which decomposes into IP_3 and DAG. IP_3 diffuses to the cytosol and binds to IP_3Rs on the ER, which primes IP_3Rs to Ca^{2+} binding and subsequently triggers Ca^{2+} release from the ER. **B.** Ca^{2+} release by RyRs. RyRs are close relatives of IP_3Rs, but they are predominantly present in the SR in skeletal and cardiac muscles. RyR1 can be activated by directly interacting with VGCC on the PM while RyR2 are activated by CICR, where the Ca^{2+} comes from VGCC after depolarization. **C.** Schematic of CICR. Ca^{2+} release from IP_3Rs in a hierarchical manner with increasing $[IP_3]$. Low $[IP_3]$ causes a single IP_3R to open and produce blips. The released Ca^{2+} diffuse to neighboring IP_3Rs and activate several clusters of IP_3Rs, which results in Ca^{2+} puffs. With increasing stimulus intensities, Ca^{2+} signals propagate into a global, regenerative wave. **D.** Side view of the structure of IP_3R1, a mushroom-like tetramer (Fan *et al.* 2015). **E.** Ca^{2+} oscillations in response to increased $[IP_3]$, stimulated by 120 nM leukotriene C_4 (LTC_4) in a mast cell line (RBL cells) with presence of 2 mM extracellular Ca^{2+} (Parekh 2010).

The activation of IP_3Rs is initiated by binding IP_3 to the clam-like IBC, and all four IBC on the tetramer have to be occupied for Ca^{2+} release to occur (Alzayady *et al.* 2016). The IBC comprises α and β domains, which undergo conformational changes upon IP_3 binding (Lin *et al.* 2011; Seo *et al.* 2012). The binding of IP_3 promotes Ca^{2+} binding to an IP_3 channel, and both IP_3 and Ca^{2+} bindings are essential for IP_3Rs to open (Marchant and Taylor 1997). Increasing concentrations of IP_3 trigger a hierarchy of Ca^{2+}-releasing events, with the smallest called 'blips', involving a single IP_3R (Parker *et al.* 1996; Berridge 1997). The release of Ca^{2+} from these pioneers evokes Ca^{2+}-induced Ca^{2+} release (CICR) and propagates the signals to neighbouring IP_3Rs. This causes larger elementary events named 'puffs' released by a cluster of IP_3Rs. With even higher [IP_3] and the effect of CICR, more IP_3Rs are activated, and the Ca^{2+} release is further amplified to become a global regenerative wave across the whole cell (***Figure 1.2C***). Recently, it has been revealed that the global Ca^{2+} signals are accompanied by rapid flurries of Ca^{2+} puffs (Lock and Parker 2020). Interestingly, as one of the two essential binding molecules of IP_3Rs, Ca^{2+} activates IP_3Rs at low concentration while inhibiting Ca^{2+} release from IP_3Rs at high concentration (Lino 1990; Bezprozvanny *et al.* 1991).

The phenomenon of IP_3Rs aggregation into clusters induced by IP_3 throughout the ER has been observed (Wilson *et al.* 1998; Tateishi *et al.* 2005; Tojyo *et al.* 2008). Also, IP_3-evoked Ca^{2+} release is usually activated from fixed sites (Thomas *et al.* 2000; Smith *et al.* 2009; Wiltgen *et al.* 2010). However, the visualization and dynamics of fluorescently tagged endogenous IP_3R1 were first reported recently by Thillaiappan *et al*., which suggested that most IP_3Rs assemble into relatively loose clusters (~8 IP_3Rs per cluster). They also found that most IP_3Rs are mobile within the ER but only immobile IP_3R clusters are 'licensed' to respond to IP_3 and mediate Ca^{2+} release (Thillaiappan *et al.* 2017). Furthermore, the same group revealed that these licensed IP_3Rs are immobilized by interacting with KRAS-induced actin-interacting protein (KRAP), which tethers IP_3Rs to actin filaments (Thillaiappan *et al.* 2021). How KRAP licenses IP_3Rs and the role of the larger number of mobile IP_3Rs have not yet been resolved.

Ryanodine receptors (RyRs) and Ca^{2+} signalling

RyRs are another family of intracellular channels that are responsible for Ca^{2+} release from the endoplasmic/sarcoplasmic reticulum (SR), although they are less widely expressed than IP_3Rs (Fill and Copello 2002). There are three subtypes of RyRs, named RyR1 to RyR3 in mammalian cells, and they constitute the major Ca^{2+}-release pathway for excitation-contraction

(E-C) coupling in skeletal and cardiac muscle (Hymel *et al.* 1988; Smith *et al.* 1988; Airey *et al.* 1993). RyRs form giant homo-tetrameric assemblies and constitute large-conductance channels with low selectivity for Ca^{2+}, just like IP_3Rs (Tinker and Williams 1992). All three RyR isoforms are found in different cell types, but RyR1 is the predominant isoform in skeletal muscle (Marks *et al.* 1989), where it is activated by direct interaction with voltage-dependent Ca^{2+} channels (VDCC), namely $Ca_v1.1$, also known as the dihydropyridine receptors (DHPRs) (Protasi 2002). RyR2 and 3 are primarily expressed in the cardiac tissues (RyR2), whereas brain and smooth muscles contain RyR3 (Otsu *et al.* 1990; Hakamata *et al.* 1992). They are mainly opened via a CICR pathway, by Ca^{2+} entry from activated VDCCs after depolarization, particularly in the heart (Sham *et al.* 1995) (***Figure 1.2B***).

Encoding and decoding of intracellular Ca^{2+} signals

When a stimulus is continuously present, Ca^{2+} release often exhibits an oscillatory pattern (Meyer and Stryer 1991; Berridge 1993) (***Figure 1.2E***). Due to the enormous concentration difference between cytosol and intracellular Ca^{2+} stores (~100 nM vs 500 μM in the ER), a brief opening of large-conductance intracellular Ca^{2+} channels produce a sharp increase in the $[Ca^{2+}]_c$. Excessive increases in $[Ca^{2+}]_c$ are generally prevented because Ca^{2+} inhibits RyR and IP_3R. Several pathways, for example SERCA pumps cytosolic Ca^{2+} back to the ER, rapidly restoring $[Ca^{2+}]_c$. Hence, Ca^{2+} signals are often presented to cells as Ca^{2+} spikes. The process can repeat to produce Ca^{2+} oscillations (Wacquier *et al.* 2019), the number, frequency, amplitude, and duration of which encode information that regulate cellular activities.

Cells can decode and interpret the information from different patterns of Ca^{2+} oscillations (Dolmetsch *et al.* 1997; Salazar *et al.* 2008; Parekh 2010). The decoding of Ca^{2+} is performed by several decoder proteins, including calmodulin (CaM) (Linse *et al.* 1991; Tadross *et al.* 2008), calcineurin (Negulescu *et al.* 1994; Colella *et al.* 2008), protein kinase C (Oancea and Meyer 1998), Ca^{2+}/calmodulin-dependent protein kinase II (CaMKII) (Hanson *et al.* 1994; Bradshaw *et al.* 2003), nuclear factor of activated T cells (NFAT) (Tomida *et al.* 2003) and others. For instance, CaMKII is adapted to behave as a frequency decoder. It does not respond to low frequencies of Ca^{2+} stimuli because it needs the binding of Ca^{2+}-calmodulin to be activated, and CaM dissociates within the intervals between Ca^{2+} spikes with low frequency. However, it responds to Ca^{2+} oscillations with higher frequencies (above threshold), where the CaMKII undergoes autophosphorylation and increased enzyme activity (De Koninck and Schulman 1998). When the stimulation is above the threshold frequency of CaMKII and some

sites are autophosphorylated, the kinase becomes more sensitive to low-frequency stimuli, supporting a cooperative activation model (Hanson *et al.* 1994; De Koninck and Schulman 1998; Bradshaw *et al.* 2003; Dupont *et al.* 2003).

Ca^{2+} signalling and mitochondria

Mitochondria are intracellular organelles that produce most cells' supply of adenosine triphosphate (ATP). Ca^{2+} accumulates in energized mitochondria (Vasington and Murphy 1962). Despite the tremendous electrochemical driving force for Ca^{2+}, mitochondria have a low affinity for Ca^{2+} uptake (Gunter and Pfeiffer 1990). Therefore, mitochondrial Ca^{2+} uptake only occurs at specific sites with high intracellular Ca^{2+} concentration, where mitochondria are in close contact with the ER, so-called mitochondria-associated membranes (MAM) (Rizzuto *et al.* 2012) (***Figure 1.1***). The mitochondrial Ca^{2+} uptake requires that it crosses both outer and inner mitochondrial membranes. Cytosolic Ca^{2+} first crosses the outer mitochondrial membrane (OMM) probably via the voltage-dependent anion channel (VDAC) (Gincel *et al.* 2001; Shoshan-Barmatz and Gincel 2003). The passage of Ca^{2+} through the VDAC is tightly regulated instead of free diffusion. VDAC is a large channel permeable to ions and molecules up to 5 kDa (Gincel *et al.* 2001; Hoppe 2010). Interestingly, it was demonstrated that closed VDAC has higher permeability of Ca^{2+}, which would induce cell apoptosis (Rapizzi *et al.* 2002; Tan and Colombini 2007). After crossing the OMM, Ca^{2+} enters the mitochondrial intermembrane space (IMS), and then crosses the inner mitochondrial membrane (IMM) mainly through the mitochondrial Ca^{2+} uniporter (MCU) (Kirichok *et al.* 2004). MCU is a regulated ion channel with high selectivity to Ca^{2+} but low conductance, through which Ca^{2+} moves down its electrochemical gradient when the channel opens (Gunter and Gunter 1994; Marchi and Pinton 2014). It consists of pore-forming units, mitochondrial calcium uptake proteins (MICU 1-3), essential MCU regulator (EMRE) and other regulators (Malli 2017; Pathak 2018). When $[Ca^{2+}]_{IMS}$ is low, MICU 1/2 inhibits the opening of MCU. While $[Ca^{2+}]_{IMS}$ is high, Ca^{2+} binds to the EF hand of MICU 1, which activates MCU and induces Ca^{2+} influx (Mallilankaraman *et al.* 2012; Pathak 2018). There are other proteins involved in Ca^{2+} uptake across the IMM, such as mitochondrial ryanodine receptor (mRyR) (Pacher *et al.* 2002) and permeability transition pore (PTP) (Rasola and Bernardi 2007), but they will not be described in detail here.

Ca^{2+} efflux from the mitochondrial matrix is mediated by the $Na^{+}/Ca^{2+}/Li^{+}$ exchanger (NCLX) (Palty *et al.* 2010). It locates in the IMM of the mitochondria and transports each Ca^{2+}

ion out of the mitochondria in exchange for three Na^+ ions entering it (Pitts 1979). Unlike the NCX localized in the PM, NCLX in the mitochondria also transports Li^+ (Palty *et al.* 2010). Besides the NCLX, a Ca^{2+}/H^+ antiporter, the leucine zipper EF-hand containing transmembrane protein 1 (Letm1), also extrudes Ca^{2+} from the mitochondria independent of Na^+ (Jiang *et al.* 2009; Santo-Domingo and Demaurex 2010).

Apart from its role in Ca^{2+} buffering and homeostasis, mitochondrial Ca^{2+} uptake also affects store-operated Ca^{2+} entry (SOCE) (Glitsch *et al.* 2002). A recent study has demonstrated that upon IP_3-mediated Ca^{2+} release and physiologically activated SOCE, both STIM1 oligomerization and SOCE are impaired when MCU or uncoupling protein 2 (UCP2) is knocked down or deleted (Deak *et al.* 2014). In addition, Ben-Kasus Nissim *et al.* showed that the downregulation of NCLX proteins results in attenuated SOCE (Ben-Kasus Nissim *et al.* 2017).

1.3. Store-operated Ca^{2+} entry

One source of Ca^{2+} signal entering into the cytosol is SOCE (Feske 2010), which is observed in various organisms, from yeasts to mammals (Putney 2004). It was once called capacitative Ca^{2+} entry to represent that Ca^{2+} traversing the ER (the capacitor) as an intermediate step between extracellular Ca^{2+} and the cytosol (Putney 1986). This assumption was proven wrong, and this pathway was renamed store-operated Ca^{2+} entry to describe its mode of activation more precisely and distinguish it from voltage-, ligand- or receptor-gated Ca^{2+} channels (Prakriya and Lewis 2015). SOCE is the principal pathway for Ca^{2+} influx in non-excitable cells, including mast cells and T cells (Berridge 1995; Ma and Beaven 2011; Vaeth *et al.* 2017). It also contributes to the Ca^{2+} homeostasis in excitable cells such as neurons and pancreatic β-cells (Takemura *et al.* 1991; Clementi *et al.* 1992; Miura *et al.* 1997; Klejman *et al.* 2009). SOCE is not voltage-dependent, it can be activated by depletion of intracellular Ca^{2+} stores without a change in membrane potential, thus providing a complementary role for Ca^{2+} influx and replenishing the Ca^{2+} stores. These Ca^{2+} release-activated Ca^{2+} (CRAC) channels have unique structures and modes of regulation compared to other known Ca^{2+} channels. Store-operated channels (SOCs) are physically and functionally closely connected to the ER and are activated by ER Ca^{2+} store depletion, either physiologically via IP_3-mediated Ca^{2+} release or pharmacologically by thapsigargin (TG) or cyclopiazonic acid (CPA) (Thastrup *et al.* 1989), which results in increases in $[Ca^{2+}]_c$ and subsequent refilling of ER (Fanger *et al.* 1995). In addition to homeostatically regulating the ER Ca^{2+} store to maintain a relatively

constant concentration of Ca^{2+} in the ER, the increase in $[Ca^{2+}]_c$ has broader impacts on Ca^{2+} signalling within the cell. As the ER Ca^{2+} store capacity is finite, the release of Ca^{2+} ions could only be transient, generating short Ca^{2+} signals. On the other hand, depletion of the ER Ca^{2+} store could be a sustained process that triggers prolonged SOCE. The time scale of this response ranges from minutes to hours, impacting many other cellular activities, including transcription, modulation of enzymatic activity, and secretion (Prakriya and Lewis 2015).

Although the phenomenon of SOCE triggered by the depletion of intracellular Ca^{2+} stores was proposed in the 1980s (Putney 1986), various proteins were proposed to mediate SOCE, amongst which the transient receptor potential (TRP) family was the most prominent (mainly TRPC1 (Wes *et al.* 1995; Brough *et al.* 2001; Mori *et al.* 2002) and TRPC3 (Wu *et al.* 2000)). However, the biophysical and pharmacological properties of these channels did not match those of CRAC channels (Voets *et al.* 2001). Although TRPCs do not directly form the pore subunits of CRAC channels, they remain important regulators of SOCE (for review see Lopez *et al.* (2020)). The first component critical to SOCE was identified in 2005 by Meyer's group (Liou *et al.* 2005). They used RNA interference (RNAi)-based screening and found suppressed Ca^{2+} influx in cells with reduced expression of stromal interaction molecule (STIM) and proved that STIM1 and STIM2 are important for SOCE. Almost at the same time, another group (Roos *et al.* 2005) transfected HeLa cells with individual siRNAs against 2,304 human signalling proteins and again the absence of STIM1 and STIM2 suppressed SOCE. One year later, three groups identified Orai1 independently and roughly simultaneously (Feske *et al.* 2006; Vig *et al.* 2006; Zhang *et al.* 2006), a novel protein of 33-kDa with four putative transmembrane segments located in the PM. In later investigations, Orai1 has been classified as an essential pore subunit of the CRAC channel (Prakriya *et al.* 2006; Vig *et al.* 2006; Yeromin *et al.* 2006). Further studies (Mercer *et al.* 2006; Peinelt *et al.* 2006; Soboloff *et al.* 2006) illustrated that the overexpression of Orai1 with STIM1 was able to generate much larger store-operated currents than endogenous I_{CRAC}. The later experiments by Zhou *et al.*, in turn, suggested that the interaction between STIM1 and Orai1 alone is sufficient to operate SOCE (Zhou *et al.* 2010).

STIM1, as a Ca^{2+}-sensor, has two primary functions in SOCE - it senses ER Ca^{2+} concentration and activates Orai1. STIM1 is a type I transmembrane protein locating mainly in the ER with a small population in the PM (Liou *et al.* 2005; Luik *et al.* 2008). On the luminal side, there is a canonical EF-hand (cEF), a non-canonical EF-hand (nEF), and a sterile alpha motif (SAM), and they form the EF-SAM domain collectively, which is mainly responsible for sensing Ca^{2+} in the ER (Stathopulos *et al.* 2006). After a short transmembrane domain, the

cytosolic side contains three consecutive coiled-coil (CC) regions, namely CC1 (composed of three helices, α_1, α_2, α_3), CC2, and CC3, where the latter two domains together constitute the CRAC activation domain (CAD) or STIM-Orai-activating region (SOAR) (Park *et al.* 2009; Yuan *et al.* 2009). Additionally, an inactivation domain (ID) is present shortly after CC3, and a proline/serine-rich domain (P/S), an EB1-binding (EB) domain, and the polybasic domain (PBD) near the end of the cytosolic region (***Figure 1.3A***).

The inactive state of STIM1

When the ER is full of Ca^{2+}, STIM1 is in its resting state, it switches to an active state upon ER Ca^{2+} store depletion (***Figure 1.3B***). Several lines of evidence suggest that STIM1 is a dimer in its resting state. Orthogonally labelled wild-type (WT) STIM1 proteins coimmunoprecipitate under resting conditions, revealing that full-length STIM1 self-associates in resting cells (Covington *et al.* 2010). This study also suggested, using orthogonally labelled STIM1 mutants, that the CC1 domain supports the self-association of STIM1 when inactive, while the CAD region further strengthens this interaction. Förster resonance energy transfer (FRET) analyses also suggested that STIM1 already partially pre-associates before ER Ca^{2+} store depletion (Muik *et al.* 2008; He *et al.* 2012). Cross-linking may be the most direct evidence to prove that STIM1 exists as a dimer even without decreasing ER Ca^{2+} content (Srikanth *et al.* 2010; Korzeniowski *et al.* 2017). Stathopulos *et al.* argued that WT EF-SAM is a monomer and only dimerized or oligomerized upon store depletion (Stathopulos *et al.* 2008), but that is not incompatible with a dimeric full-length protein with the EF-SAM regions apart (***Figure 1.3Bi***). However, all these studies used overexpressed proteins, which may promote dimerization or even oligomerization, but the diffusion coefficient of resting STIM1 at a very low expression level (Wu *et al.* 2014) was comparable to that of overexpressed proteins derived from fluorescence recovery after photobleaching (FRAP) experiments (Liou *et al.* 2007; Covington *et al.* 2010). Hence, the oligomeric structure of inactive STIM1 determined from over-expression studies appears not to be artefact of over-expressing STIM1. Additionally, the crystal structure of the SOAR region was revealed by single wavelength anomalous dispersion (SAD) (Yang *et al.* 2012), which showed that the human SOAR (hSOAR) exists primarily as dimers in solution stabilized by hydrogen bonds and hydrophobic interactions (***Figure 1.3B***).

The resting state of STIM1 adopts a different conformation compared to its active form (***Figure 1.3B***). The importance of the C-terminus, especially the coiled-coil region, in stabilizing inactive STIM1 was realized relatively early (Korzeniowski *et al.* 2010; Saitoh *et*

al. 2011; Yu *et al.* 2011). Deletion of the coiled-coil regions shortens the half-life of STIM1, indicating a stabilizing effect in WT STIM1 (Saitoh *et al.* 2011). A STIM1 mutant with the last 200 residues missing (STIM1: 1-485) constitutively interacts with and traps Orai1 intracellularly, thus inhibits SOCE by restricting Orai1's enrichment in the PM (Yu *et al.* 2011). When the deleted region was replaced by GFP or mCherry, the STIM1 chimera restored the normal functions of WT STIM1, suggesting that the C-terminus of STIM1 prevents STIM1 from spontaneous activation via a steric hindrance mechanism. The details of exactly how this region affects the conformation and stability of STIM1 in the resting state were revealed later. The intramolecular interaction between CC1α_1 and CC3 forms a coiled-coil clamp which holds

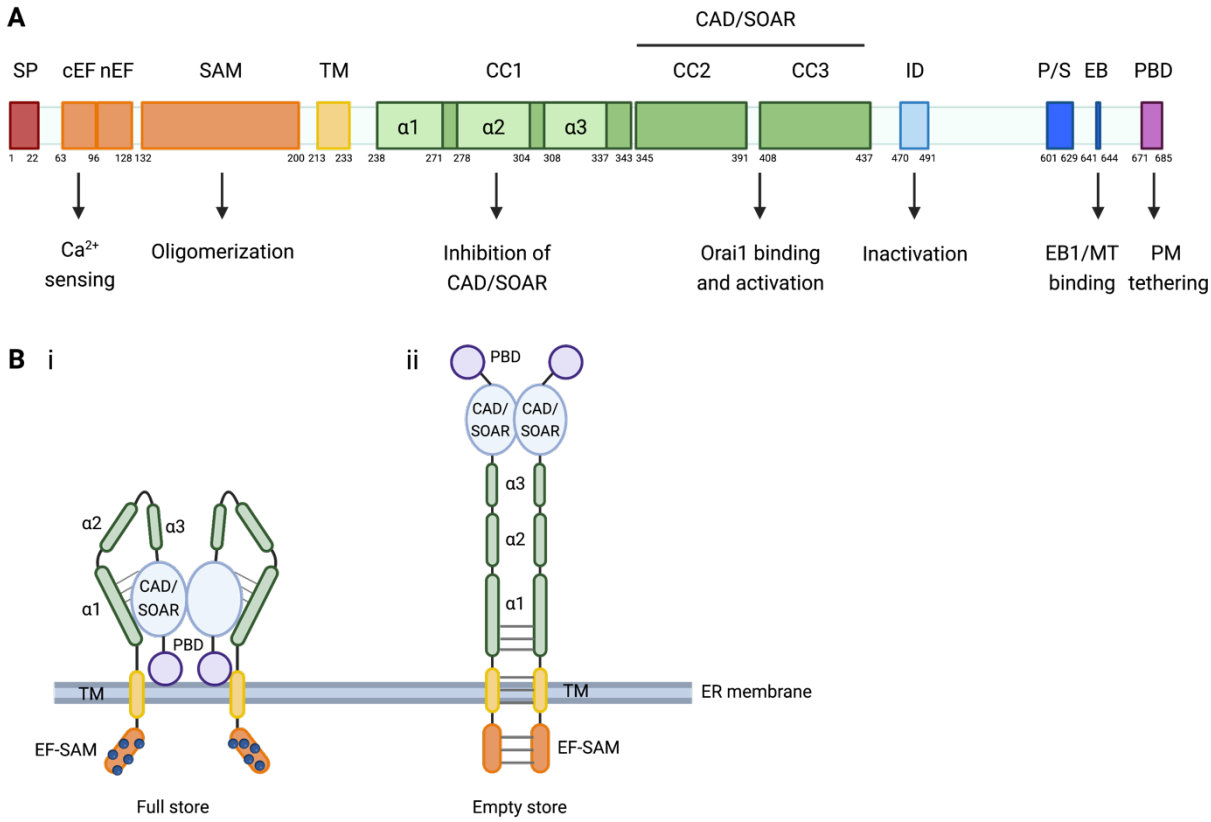

Figure 1.3 The functional domains and an activation model for STIM1. A. Functional domains of STIM1. See ***Abbreviations***. **B(i).** An activation model for STIM1. When the ER Ca^{2+} store is full and EF-SAM domains are bound to Ca^{2+}, STIM1 is in a folded structure at rest, with CC1α_1 binding to the CAD/SOAR domain to inhibit activation of Orai1. **(ii)** When the Ca^{2+} store is depleted, Ca^{2+} ions dissociate from the EF-SAM domain, which brings the EF-SAM and TM regions together. This subsequently triggers a conformational change in the C-terminus of STIM1 to expose CAD/SOAR domains, allowing them to interact with Orai1. Image redrawn from Lewis (2019).

the protein in the quiescent state by shielding the CAD/SOAR domain (Yu *et al.* 2013; Fahrner *et al.* 2014; Korzeniowski *et al.* 2017). The CC1α_3 domain, which was previously termed as inhibitory helix (IH) (Yang *et al.* 2012; Cui *et al.* 2013), was also shown to maintain the resting structure of STIM1 and is critical for the conformational change of STIM1 after store depletion (Cui *et al.* 2013; Korzeniowski *et al.* 2016), which can be attributed to its amphipathic nature (Yu *et al.* 2013). More specifically, a single aromatic residue in the inhibitory helix, tyrosine (aa 316), is critical for keeping STIM1 inactive by hydrogen bonding or hydrophobic bonding with the CAD domain. Mutation of this residue (Y316A) caused spontaneous aggregation and translocation of STIM1 to the PM even in cells with replete Ca^{2+} stores (Yu *et al.* 2013). In addition, the ID region also contributes to the resting state of STIM1 by interacting with the CAD domain via a conserved linker (21-aa long) with the help of CC1 (Lee *et al.* 2020).

The active state of STIM1

As a Ca^{2+} sensor, the primary role of STIM1 is to detect how much Ca^{2+} is left in the ER and call for action by interacting with Orai1 to refill the ER when Ca^{2+} content is low. To describe the entire mechanism of the activation of STIM1, I need to start with its ability to detect Ca^{2+}. The EF-SAM domain of STIM1 is predominantly responsible for sensing Ca^{2+} in the ER (Liou *et al.* 2005; Zhang *et al.* 2005), with an affinity of ~200 μM (Stathopulos *et al.* 2006; Brandman *et al.* 2007; Stathopulos *et al.* 2008). There are two EF-hand motifs contained in the entire domain, namely the canonical EF-hand (cEF), which binds to Ca^{2+} ions, and the non-canonical EF-hand (or hidden EF-hand), which stabilizes the cEF via hydrogen bonding (Stathopulos *et al.* 2008). Mutations in the EF-SAM region lead to the persistent formation of STIM1 puncta and constitutive activation of SOCE, therefore, mutants are widely used for further investigations of STIM1, for example, D76A (Liou *et al.* 2005; Spassova *et al.* 2006; Klejman *et al.* 2009). While it was initially proposed that the cEF can only coordinate a single Ca^{2+} ion (Stathopulos *et al.* 2006), recent evidence has shown that there are 5–6 Ca^{2+}-binding sites on the entire EF-SAM region (Gudlur *et al.* 2018). The binding of the Ca^{2+} to the cEF is essential for subsequent Ca^{2+} binding to other sites, and the occupation of all sites stabilizes the entire molecule in the resting state (Stathopulos and Ikura 2019).

When the ER is full of Ca^{2+}, the EF-SAM domain associates with Ca^{2+} ions, and it adopts an ‘open’ conformation, with the two EF-SAM domains separated from each other (***Figure 1.3Bi***). Loss of Ca^{2+} from the ER allows dissociation of Ca^{2+} from the EF-SAM domain of STIM1, the luminal region of STIM1 then undergoes a conformational change to a ‘closed’

state, in which the two EF-SAM domains come closer (Liou *et al.* 2007; Stathopulos *et al.* 2008; Gudlur *et al.* 2018) (***Figure 1.3Bii***), but without a massive change in the secondary structure of the EF-SAM domain (Gudlur *et al.* 2018). This closer contact has been confirmed by increased FRET between fluorophores attached to the N-terminus of STIM1 (Liou *et al.* 2007; Malli *et al.* 2008; Covington *et al.* 2010). Furthermore, FRET analyses also suggested increased proximity between the TM regions of STIM1 dimers after Ca^{2+} release from the ER (Ma *et al.* 2015) (***Figure 1.3Bii***).

The partial unfolding and dimerization in the luminal part of STIM1 are coupled with further conformational changes associated with the C-terminus, where the CC1α_1 helix dissociates from the CAD/SOAR domain (Lewis 2019). This rearrangement triggers extension of the entire coiled-coil domain and results in exposure of the CAD/SOAR domain (Yu *et al.* 2013; Zhou *et al.* 2013; Fahrner *et al.* 2014; Ma *et al.* 2015) (***Figure 1.3B***), which later allows this domain to interact with the Orai1 channels in the PM after translocation of STIM1 to ER-PM junctions. The extension of STIM1 is followed by one of the iconic features associated with SOCE, the oligomerization of STIM1 to form so-called 'puncta' (Wu *et al.* 2006; Xu *et al.* 2006; Liou *et al.* 2007). Many regions in the STIM1 structure have been shown to contribute to the oligomerization of STIM1. The SOAR/CAD domain is critical in this process, without which STIM1 fails to form puncta (Park *et al.* 2009; Covington *et al.* 2010; Zheng *et al.* 2018). However, although mutations in the CC2 region impair the aggregation of STIM1, CC2 solely cannot demonstrate the full function of CAD in STIM1 oligomerization (Covington *et al.* 2010). The function of the PBD is controversial. Some people reported that STIM1 lacking the PBD (aa 672–685, STIM1-ΔK) cannot form puncta at MCS upon store depletion unless co-overexpressed with Orai1 (Park *et al.* 2009), while others argued that STIM1-ΔK can still form intracellular clusters and translocate to the ER-PM junctions even without the presence of Orai1 (Zheng *et al.* 2018). Maruyama *et al.* took a closer look at the oligomerization of STIM1 using atmospheric scanning electron microscope (ASEM) (Maruyama *et al.* 2012), suggesting that STIM1 aggregates into a belt-like linear structure, up to 2 μm in length and 100 nm in width, instead of the globular structure usually seen under the fluorescent microscope. Oligomerization of STIM1 drives the accumulation of STIM1 to the ER-PM junctions and is sufficient for activating Orai1 channels (Luik *et al.* 2008). Hence, SOCE is closely coupled with this self-organising process of STIM1. A diffusion trap model (Wu *et al.* 2014) (***Figure 1.4***) has been proposed for STIM1 oligomers to translocate to the 10-25 nm gap of ER-PM junctions (Wu *et al.* 2006). STIM1 diffuses within the ER while Orai1 moves in the PM also

by diffusion (Liou *et al.* 2007; Covington *et al.* 2010; Wu *et al.* 2014). When Ca^{2+} dissociates from the EF-SAM domains of STIM1, the protein dimer undergoes conformational changes to exhibit an extended shape (***Figure 1.3B***), followed by accumulation into so-called 'puncta' (Liou *et al.* 2005; Liou *et al.* 2007; Stathopulos *et al.* 2008; Park *et al.* 2009), as described above. The PBD at the extreme C-terminus are also exposed (Muik *et al.* 2011) and interact with phospholipids located in the PM, particularly PIP_2 (Ercan *et al.* 2009; Walsh *et al.* 2009; Bhardwaj *et al.* 2013; Zhou *et al.* 2013). This interaction establishes more of a regulatory role, instead of being essential to SOCE, because the attenuation of SOCE after deletion of phospholipids (PIP_2 and PIP_3) can be rescued by overexpressing Orai1 (Jardin *et al.* 2008; Walsh *et al.* 2009). Many reports emphasized that STIM1 accumulates into puncta and moves

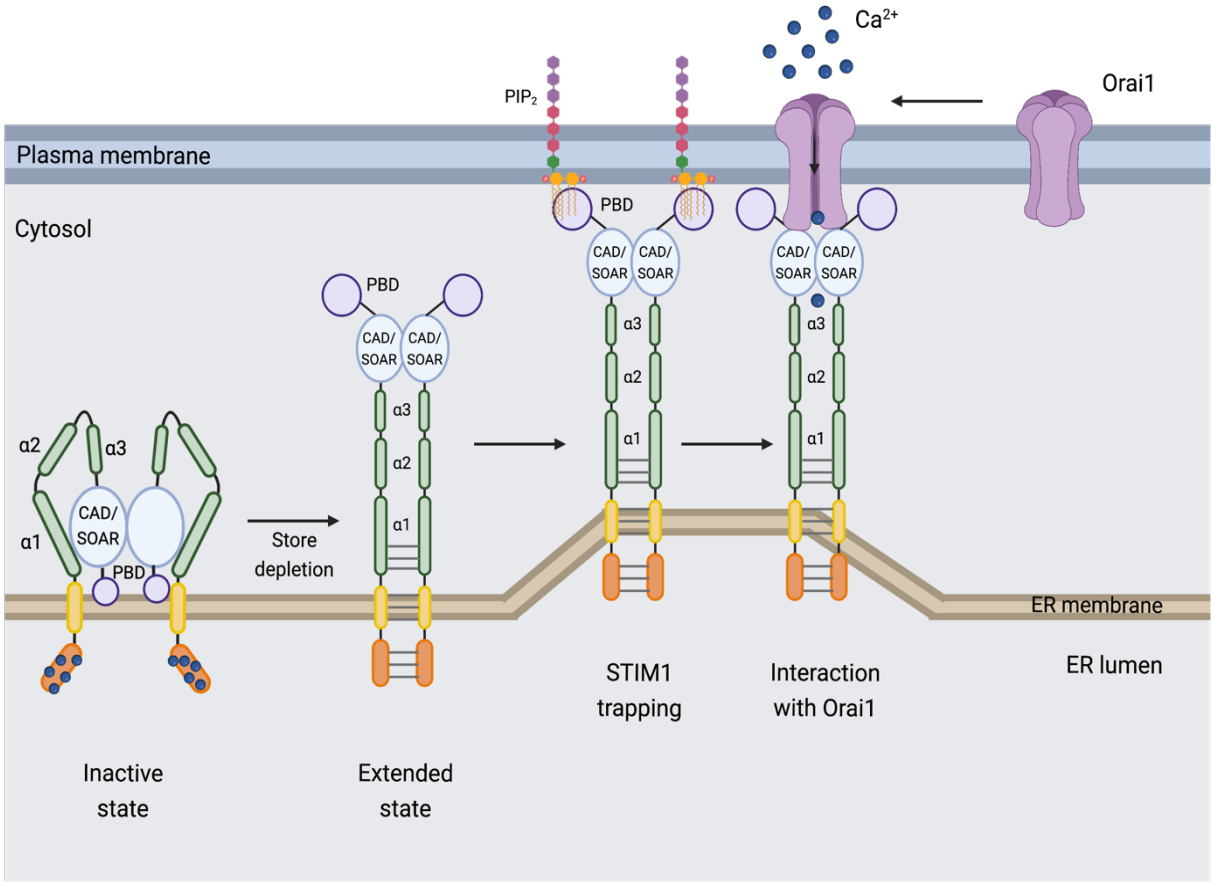

Figure 1.4 A schematic for the diffusion trap model of SOCE. At rest, STIM1 and Orai1 proteins passively diffuse in their membranes. Once ER Ca^{2+} stores are depleted and SOCE is activated, STIM1 undergoes conformational changes, and the exposed polybasic domains (PBD) binds to PIP_2 in the PM. The trapped STIM1 then binds to Orai1 through the CRAC activation domain (CAD), which allows Orai1 to be trapped and activated. Image redrawn from Prakriya and Lewis (2015).

to the vicinity of the PM, but not into the PM (Mercer *et al.* 2006; Wu *et al.* 2006; Xu *et al.* 2006). Therefore, under physiological conditions, where proteins are expressed at endogenous levels, tethering of STIM1 to the PM through binding to PIP_2 is important for clustering of STIM1 and allows STIM1 to move to the proximity of Orai1, which helps their interaction (Wu *et al.* 2014; Zheng *et al.* 2018) due to their sparse distributions. The subsequent interaction between STIM1 and Orai1 will be described later.

When Ca^{2+} is added back, STIM1 oligomerization is reversed. Live-cell imaging has indicated that STIM1 colocalizes with microtubule-like structures during this process, suggesting the involvement of microtubule in regulating SOCE (Liou *et al.* 2007). Microtubule depolymerisation inhibits SOCE supported by endogenous STIM1, but SOCE can be rescued by overexpressing STIM1 (Smyth *et al.* 2007). STIM1 is a target of extracellular-signal-regulated kinases 1 and 2 (ERK1/2) *in vitro*, which phosphorylates STIM1 at several sites (Ser575, Ser608, and Ser621) (Pozo-Guisado et al. 2010) and, in turn, mediates the interaction between STIM1 and end-binding protein 1 (EB1), a protein that regulates microtubule dynamics. Only when these sites are phosphorylated can STIM1 dissociate from EB1, which frees STIM1 to multimerize with other STIM1s before fully accomplishing SOCE (Smyth *et al.* 2012; Casas-Rua *et al.* 2013; Pozo-Guisado *et al.* 2013).

In summary, STIM1 exists as a dimer in ER membranes at rest with a folded structure. When the ER Ca^{2+} stores are depleted, STIM1 undergoes conformational changes to an extended structure, exposing its functional units (CAD/SOAR) and accumulates into puncta. STIM1 puncta then diffuse to ER-PM junctions where the PBD interact with PIP_2, thereby tethering STIM1 to the PM, followed by binding to Orai1 and opening of its channel.

STIM2 – another member of the STIM family

There are two members in the family of STIM, both of which were discovered as free Ca^{2+} sensors (Williams *et al.* 2001; Liou *et al.* 2005). They are likely to have evolved from a common ancestral gene but diverged as early as in bony fish (Cai 2007). They share highly conserved genomic organizations in the luminal domains but exhibit differences in their C-terminal part (Williams *et al.* 2001). Some research groups suggested that STIM2 impairs SOCE moderately (Liou *et al.* 2005; Roos *et al.* 2005; Oh-Hora *et al.* 2008) or even with no effect (Peel *et al.* 2006) when knocked down, while knocking down STIM1 significantly suppresses SOCE, suggesting that STIM2 might be redundant in the regulation of SOCE. However, others revealed that STIM2 inhibits SOCE mediated by STIM1 when expressed

alone (Soboloff *et al.* 2006) but can cause substantial constitutive SOCE when co-expressed with Orai1 (Soboloff *et al.* 2006). Later results may provide a possible explanation for these seemingly contradictory results, where overexpression of an alternatively spliced STIM2 variant, STIM2.1 (or STIM2β), shows an inhibitory effect on SOCE, while STIM2.2 (or STIM2α) promotes SOCE (Miederer *et al.* 2015; Rana *et al.* 2015). From the perspective of the molecular structure, STIM1 has a phenylalanine residue at position 394 while there is a leucine residue in STIM2 at the equivalent position. This substitution is critical for STIM1 being a full agonist of Orai1, but making STIM2 a partial agonist (Wang *et al.* 2014). The consensus is that STIM2 does regulate SOCE, especially in neurons (Berna-Erro *et al.* 2009), dendritic cells (Bandyopadhyay *et al.* 2011), and the brain (Skibinska-Kijek *et al.* 2009), where STIM2 is the predominant isoform of STIM proteins. Furthermore, it can interact with Orai1 to form a complex when $[Ca^{2+}]_{ER}$ slightly drops (Gruszczynska-Biegala and Kuznicki 2013).

The Ca^{2+}-binding affinity (K_d) of STIM2 is ~500 μM, much lower than STIM1 (~200 μM) (Stathopulos *et al.* 2006; Zheng *et al.* 2008). Brandman suggested that STIM2 serves as a feedback regulator of basal cytosolic and ER Ca^{2+} levels (Brandman *et al.* 2007). In their studies, STIM2 was proposed to translocate to the PM upon minor reduction in $[Ca^{2+}]_{ER}$, and then, despite being a poor activator of Orai1, STIM2 causes basal Ca^{2+} influx by regulating Orai1. This was further confirmed in neurons (Gruszczynska-Biegala *et al.* 2011). In contrast, STIM1 can only respond to a much more significant decrease in $[Ca^{2+}]_{ER}$. Therefore, when there is only minimal depletion of ER Ca^{2+} by low stimulus, the activated conformation of STIM2 facilitates its association with STIM1, which promotes the formation of STIM1 puncta and STIM1-Orai1 coupling, thereby makes STIM1-Orai1 complex more sensitive to agonist stimulus (Ong *et al.* 2015; Subedi *et al.* 2018).

Through influencing Ca^{2+} signalling, STIM2 proteins impact many biological processes, including human myoblast differentiation and myotube excitation-contraction coupling (Darbellay *et al.* 2010), development and function of the immune system (Oh-Hora *et al.* 2008; Schuhmann *et al.* 2010), as well as tumorigenesis (Ruano *et al.* 2006; Miao *et al.* 2019) and idiopathic pulmonary arterial hypertension (IPAH) (Song *et al.* 2011). STIM2 could be a therapeutic target for ischemic injury, T cell-mediated disorders (Schuhmann *et al.* 2010), neurodegenerative disorders (Berna-Erro *et al.* 2009) and potentially breast cancer and glioblastoma multiforme (Ruano *et al.* 2006; Miao *et al.* 2019).

The structure of Orai1

Since the discovery of Orai1 (Feske *et al.* 2006; Vig *et al.* 2006; Zhang *et al.* 2006), several independent lines of evidence suggested that the Orai1 channel was a tetramer (Ji *et al.* 2008; Mignen *et al.* 2008; Penna *et al.* 2008; Madl *et al.* 2010). This tetramer structure was further supported by transmission electron microscopy (TEM) (Maruyama *et al.* 2009). Although the techniques used all have their limitations (Chen and Xu 2013; Yen and Lewis 2019), the hexameric structure reported by Hou *et al*. by X-ray crystallography was unexpected (Hou *et al.* 2012) (***Figure 1.5A***). Thompson *et al.* suggested that hexameric concatemers of Orai1 lose the high Ca^{2+}-selectivity, typical of CRAC channels, but this feature is retained in tetrameric concatemers (Thompson and Shuttleworth 2013). Meticulous functional analyses of Orai1 oligomers of unequivocal composition demonstrated that Orai1 hexamers have

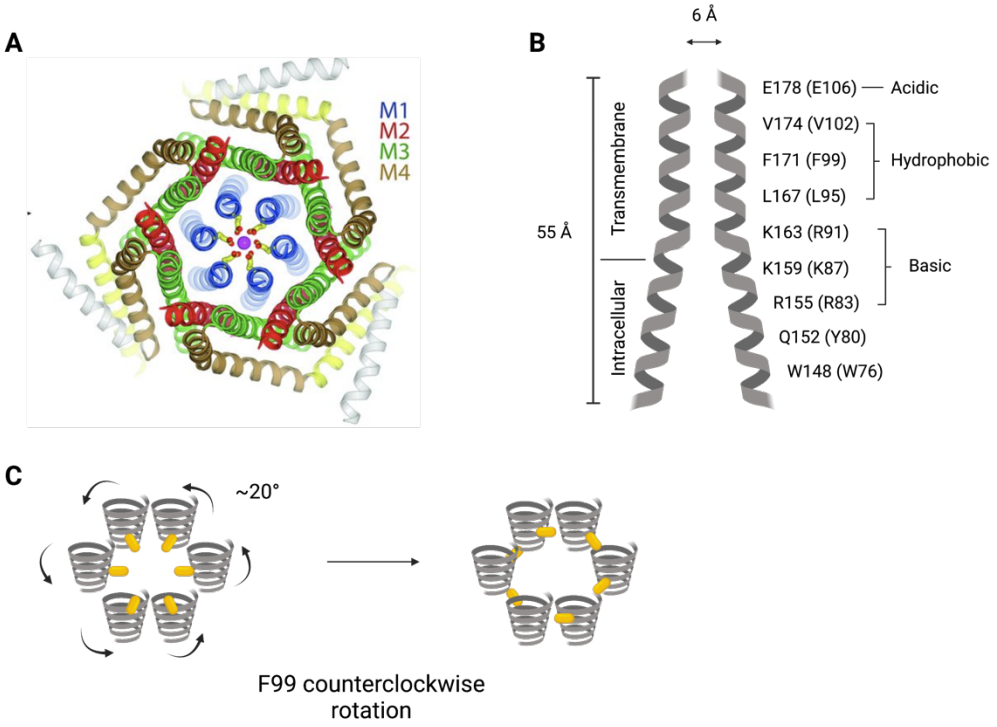

Figure 1.5 The crystal structure and activation model of *Drosophila* Orai. A. Top view of *Drosophila* Orai, showing the arrangement of 6 subunits around a central pore with coiled-coil interactions between the 3 pairs of transmembrane 4 (TM4) extensions (in white). Image reproduced from *Hou et al. (2012)*. **B.** Side view of the pore of dOrai lined by TM1 helices. Pore-lining residues are shown with corresponding amino acids in human Orai1 in brackets. **C.** Pore rotation model for Orai1 activation gating (Yamashita *et al.* 2017). It was proposed that F99 residue undergoes counterclockwise rotation of ~20° to open the gate.

indistinguishable properties from endogenous CRAC channels, including Ca^{2+}-selectivity, unitary conductance, rapid Ca^{2+}-dependent inactivation (CDI), and the response to 2-APB (Yen *et al.* 2016). Also, each subunit in the hexameric concatemer of Orai1 performs equivalently. Cai *et al.* also argued against Thompson's report, showing that the hexameric constructs give rise to similar current properties to tetrameric constructs (Cai *et al.* 2016). The difference in their results can probably be attributed to a much shorter linker used by Thompson *et al*. By substituting subunits of Orai1 hexamer concatemers at different positions with the 'pore-inactive' E106A mutants, results also indicated that Orai1 channels function as hexamers, most likely in a 'trimer of dimers' configuration (Cai *et al.* 2016). Although concatemers have been widely used in investigating the properties of receptors with different numbers of subunits, the length and composition of the linkers need to be carefully designed. Additionally, the resulting receptors may not necessarily contain the expected number of subunits as designed, since subunits can be borrowed from other assemblies or 'looped out' from the assembled receptor (Steinbach and Akk 2011). Therefore, concatemers may not be representative of native proteins.

Orai1 is a PM protein containing four transmembrane α helices (M1 to M4) and M4 has an additional helix extending into the cytosol (M4ext) (Gwack *et al.* 2007; Hou *et al.* 2012) (***Figure 1.5A***). Six M1 helices, one each subunit, are located in the centre forming the narrow ion pore (Zhou *et al.* 2010; Hou *et al.* 2012). The M1 domains are surrounded by the M2 and M3 helices, followed by peripheral M4 helices in an outer ring, responsible for interacting with STIM1 (Muik *et al.* 2008) (***Figure 1.5A***). Each pair of M4ext helices run antiparallel to each other, with one in an extended shape and the other in a bent conformation in the resting state (Hou *et al.* 2012; Tirado-Lee *et al.* 2015; Cai *et al.* 2018). The ion conduction pathway is lined by D110/D112/D114 (in human Orai1), which collectively serve as the 'Ca^{2+}-accumulating region' (CAR) (Frischauf *et al.* 2015), followed by the E106 residue as the main Ca^{2+}-binding site and the selectivity filter (McNally *et al.* 2009; Zhou *et al.* 2010; Hou *et al.* 2018) (***Figure 1.5B***). In addition, there is a hydrophobic region (V102/F99/L95, human Orai1) and a K/R-rich basic region (R91/K87/R83, human Orai1) sitting immediately below the selectivity filter (***Figure 1.5B***), all of which contribute to the gating properties of the Orai1 channel (Zhang *et al.* 2011; Yamashita *et al.* 2017; Yamashita *et al.* 2020).

The interaction between STIM1 and Orai1

A single dimer of STIM1 is sufficient to trap Orai1 in the ER-PM junctions but it cannot induce channel opening (Hoover and Lewis 2011). The mobility of both STIM1 and Orai1 are restricted once they interact (Liou *et al.* 2007; Barr *et al.* 2008; Park *et al.* 2009), as reflected by their reduced diffusion coefficients. It has been well established that STIM1 interacts with the C-terminus binding domain (CBD, aa 267–292) of Orai1, or more specifically, the extension of the M4 helix (M4ext), after Ca^{2+} store depletion. Deletion of the C-terminus or mutation of Leu-273 in this region to serine disrupts coiled-coil formation, prevents the interaction with STIM1 and channel opening, and thus abolishes SOCE (Muik *et al.* 2008; McNally *et al.* 2013; Zheng *et al.* 2013). More specifically, both M4ext helices in the adjacent pair of subunits straighten to an 'unlatched' conformation, allowing binding to the CAD/SOAR region of activated STIM1 (Hou *et al.* 2018; Liu *et al.* 2019; Baraniak *et al.* 2021).

The function of the N-terminus of the Orai1 channel in interacting with STIM1 has been contentious. Some studies suggest that the N-terminus of Orai1 is involved in pore opening and channel gating because truncation of the N-terminus does not prevent STIM1 from interacting with Orai1 but impairs channel opening and SOCE (Li *et al.* 2007; Takahashi *et al.* 2007; Muik *et al.* 2008; Zheng *et al.* 2013). Others reported an essential role of the N-terminus of Orai1 in STIM1 binding, especially amino acid residues 73-90, named extended transmembrane Orai1 N-terminal (ETON) region (Derler *et al.* 2013; McNally *et al.* 2013; Palty and Isacoff 2016). FRET between Orai1 with a truncated N-terminus (Δ1–85 and Δ73–85) or mutation within that region (K85A and K85E) and STIM1 significantly decreased compared to that between WT Orai1 and STIM1. This suggests a role for the N-terminus of Orai1 in the STIM1-Orai1 interaction (McNally *et al.* 2013). When looking closer at this region, the L74, W76 and K85 residues are necessary for the interaction between the CAD/SOAR domain and the N-terminal binding domain (NBD) of Orai1 (Derler *et al.* 2013; Palty and Isacoff 2016). Therefore, a binding model has been proposed that, after Ca^{2+} store depletion, STIM1 is activated, oligomerized into puncta, and the CAD/SOAR domains are exposed to first interact with the C-terminus of Orai1. The interaction induces a modest allosteric rearrangement in the structure of Orai1, resulting in STIM1 binding to the N-terminus of Orai1 (Zheng *et al.* 2013; Tirado-Lee *et al.* 2015; Palty and Isacoff 2016; Maganti *et al.* 2019). This allosteric change further propagates to the M3 and M2, and eventually causes the pore-lining M1 helices to twist outwards, which finally activates the Orai1 channel (Palty *et al.* 2015; Yamashita *et al.* 2017; Cai *et al.* 2018; Liu *et al.* 2019; Hou *et al.* 2020). STIM1 binding to

both termini of Orai1 is required in this model. However, Zhou *et al.* partially disagree with this model by identifying a key 'nexus' region (LVSHK, aa 261-265) near the C-terminus of Orai1 as a necessary and sufficient trigger that remotely controls channel gating via conformational change relay, without the requirement of direct binding of STIM1 to the N-terminus of Orai1 (Zhou *et al.* 2016).

Channel opening and ion selectivity

According to the pore structure of Orai1 (***Figure 1.5B***), directly below the selectivity filter E106 are residues forming the hydrophobic and basic regions. V102 and F99 residues are essential players in the hydrophobic region, mutations of which lose ion selectivity and cause leaky gates that are constitutively open even at rest (McNally *et al.* 2012; Derler *et al.* 2013; Frischauf *et al.* 2017). The pore helices are suggested to rotate counterclockwise by about 20 degrees when activated by STIM1, which twists F99 away from the pore lumen while exposing G98 to face the pore (Yamashita *et al.* 2017; Yeung *et al.* 2018) (***Figure 1.5C***). Dong *et al.* also proposed a 'twist-to-open' gating mechanism by molecular dynamics (MD) simulations combined with normal mode analysis (NMA), where the extracellular part of the channel undergoes counterclockwise rotation to expand the pore formed by TM1 helices. In contrast, the three intracellular N-termini of alternating helices move outwards, and the remaining three helices rotate clockwise (Dong *et al.* 2019). Water molecules may also engage during this process by lowering the energetic barrier to facilitate channel opening and passage of ions (Dong *et al.* 2013; Yamashita *et al.* 2017).

After the ions pass the formerly hydrophobic region, they encounter the basic region. This region comprises mainly R91, K87, and R83 residues which gate the channel either by electrostatic repulsion (Zhang *et al.* 2011) or by an anion plug (Hou *et al.* 2012; Hou *et al.* 2020). The polarity of these residues also contributes to the gating (Yamashita *et al.* 2020). Removal or mutation of these residues perturbs channel activation and SOCE characteristics (Derler *et al.* 2013; Derler *et al.* 2018; Yamashita *et al.* 2020). The basic region of the pore experiences dramatic dilation of ~10Å at K87 upon store depletion and activation by STIM1 and gets rid of the anion plug that stabilizes the resting state, which results in the opening of the channel, as revealed in the crystal and cryo-EM structures of a constitutively open dOrai1 H206A mutant (human H134A) (Hou *et al.* 2018; Hou *et al.* 2020).

Apart from the hydrophobic and basic regions that line the pore, several studies have revealed regulatory roles in both channel gating and ion selectivity of intracellular loop 2

(between TM2 and TM3) (Frischauf *et al.* 2011; Fahrner *et al.* 2018), H134 in TM2 (Frischauf *et al.* 2017), TM1-TM3 interface (Yeung *et al.* 2018) and TM3 itself (Srikanth *et al.* 2011; Tiffner *et al.* 2021).

It is noteworthy that the interaction between STIM1 and Orai1 not only activates the channel but is also necessary for the channel to demonstrate its characteristics, including high ion selectivity, low conductance, appropriate current/voltage (I/V) relationship and Ca^{2+}-dependent inactivation (CDI). In SOCE, the STIM1-mediated channel gating and ion permeation are tightly coupled (McNally *et al.* 2013; Derler *et al.* 2018). The high Ca^{2+}-selectivity of the Orai1 channel is achieved by both the extremely narrow pore diameter (3.8–3.9 Å) at the selectivity filter (Tiffner *et al.* 2021) and the binding of STIM1. Lack of the latter in 'non-binding' Orai1 mutants (e.g., L273S/D) abrogates the STIM1-mediated ion selectivity (McNally *et al.* 2013; Yen and Lewis 2018). Furthermore, the Ca^{2+} selectivity of non-selective mutants of Orai1, such as V102C/A, is restored when they bind fully to STIM1, by altering the pore structure (McNally *et al.* 2012; Derler *et al.* 2013).

Local Ca^{2+}-dependent inactivation of SOCE

The inactivation mechanisms of SOCE were described long before the discovery of STIM1 or Orai1. Like other Ca^{2+} channels, CRAC channels are inactivated via a negative feedback regulation, so-called fast Ca^{2+}-dependent inactivation (CDI) (Hoth and Penner 1993; Zweifach and Lewis 1995; Fierro and Parekh 1999), with time constants of milliseconds. It is considered a local process, where the rise of $[Ca^{2+}]$ in the close vicinity to an individual CRAC channel only inactivates that channel, without affecting its neighbours (Zweifach and Lewis 1995; Fierro and Parekh 1999).

Both STIM1 and Orai1 contain domains that regulate fast CDI. The inactivation domain in STIM1 (ID, aa 470-491) (***Figure 1.3A***) is essential for fast CDI, especially the seven negatively charged residues (aspartate or glutamate) concentrated in this region (aa 474-485, CRAC modulatory domain (CMD)) (Derler *et al.* 2009; Lee *et al.* 2009; Mullins *et al.* 2009). Deletion of this domain or neutralizing mutations of the seven residues reduces or completely abrogates fast CDI. In addition, the N-terminus of Orai1 (aa 68–91) has a calmodulin (CaM)-binding site, which was suggested to be important in fast CDI together with Ca^{2+}-dependent CaM binding since STIM mutations that block CaM binding (such as W76A and Y80E) abolish fast CDI (Mullins *et al.* 2009). However, this direct binding of CaM to the N-terminus of Orai1 was later proven to be impossible due to the steric hindrance caused by the orientations of W76

and Y80, both facing the pore (Hou *et al.* 2012). Also, it was later shown that CaM mutants that fail to bind to Orai1 do not affect CDI (Mullins *et al.* 2016). Therefore, it is now proposed that ID_{STIM1} and W76/Y80 work synergistically for full CDI, probably by inducing conformational changes of the pore (Mullins and Lewis 2016; Mullins *et al.* 2016).

Notably, like ion selectivity, the binding of STIM1 to Orai1 also affects fast CDI (Derler *et al.* 2018). Furthermore, it has been demonstrated that the stoichiometry between STIM1 and Orai1 is vital in regulating CDI, where low ratios of Orai1:STIM1 allow fast CDI, whereas high ratios of Orai1:STIM1 abolishes it (Scrimgeour *et al.* 2009). Additionally, CDI was affected by pore residues E106 and E190 (Yamashita *et al.* 2007), intracellular loop 2 of Orai1 (Srikanth *et al.* 2010; Frischauf *et al.* 2011) and by STIM1 in the PM (Jardin *et al.* 2009; Dionisio *et al.* 2011) despite much lower expression compared to STIM1 in the ER (Koziel *et al.* 2009).

Other isoforms in the Orai family

The other two homologs in the Orai family, Orai2 and Orai3, were both shown to be functional in SOCE (Mercer *et al.* 2006; DeHaven *et al.* 2007; Gwack *et al.* 2007). Orai2 was initially considered to perform roles similar to Orai1 since overexpressing Orai2 with STIM1 in Orai1-knockdown cells restores SOCE (Mercer *et al.* 2006; Gwack *et al.* 2007). However, recent studies (Vaeth *et al.* 2017) revealed that deletion of Orai1 moderately decreases SOCE, while deletion of Orai2 enhances SOCE in naive T cells. Furthermore, it was also indicated that Orai1 and Orai2 form heteromeric channel complexes, in which Orai2 attenuates the function of Orai1 and therefore modulates subsequent biological processes such as immune responses (Vaeth *et al.* 2017).

Although there is limited research on the function of Orai3, they are proteins that differ significantly in sequence and structural features from other Orai proteins and display several unique properties. For example, Orai3 restored SOCE in HEK293 cells where Orai1 proteins were depleted (Mercer *et al.* 2006; DeHaven *et al.* 2007). It may also be involved in store-independent Ca^{2+} entry either by 2-APB or physiologically by agonist-generated levels of intracellular arachidonic acid (Schindl *et al.* 2008; Zhang *et al.* 2008; Mignen *et al.* 2009).

Clinical significance of SOCE

STIM1, Orai1 and the other isoforms in their families are associated with diseases. Apart from the diseases related to STIM2, which was mentioned earlier (***page 16***), STIM1 has long been shown to be important in the regulation of platelet functions. The absence of STIM or mutations of STIM1 can lead to premature platelet activation (Grosse *et al.* 2007), thrombus formation (Varga-Szabo *et al.* 2008) and platelet secretion defects (Nakamura *et al.* 2013). A gain-of-function (GOF) mutation of STIM1 (R304W) causes Stormorken syndrome, an autosomal dominant disorder (Misceo *et al.* 2014; Morin *et al.* 2014). Furthermore, STIM1 overexpression promotes some cancers (Wang *et al.* 2015), while its silencing inhibits the invasion of tumours (Li *et al.* 2013; Wang *et al.* 2017). In the immune system, a STIM1 mutation (R429C) can cause inherited severe combined immune deficiency (SCID) (Fuchs *et al.* 2012). Regarding the therapeutic potential of Orai1, the protein itself was identified in patients with SCID due to a mutant Orai1 (R91W) (Feske *et al.* 2006). Abnormal expression or mutation of Orai1 is associated with myopathy (McCarl *et al.* 2009), glioblastoma (Liu *et al.* 2011), osteoclast differentiation (Hwang and Putney 2012), and so on. Future studies are required for SOCE being targeted to treat diseases including, but not limited to cancer (Yang *et al.* 2009; Zhan *et al.* 2015), neurodegenerative disorders (Popugaeva and Bezprozvanny 2013; Kraft 2015; Lou *et al.* 2020), immunodeficiency (Feske *et al.* 2010), and diabetes (Wang *et al.* 2018).

IP_3Rs and SOCE

As mentioned in previous sections, despite the abundance of IP_3R in the ER, only a small population of those 'licensed' IP_3Rs that are immobile and sitting close to the PM can respond to IP_3 and generate Ca^{2+} release (Thillaiappan *et al.* 2017). These licensed IP_3Rs are juxtaposed to activated STIM1 alongside ER-PM junctions after ER Ca^{2+} store depletion (Thillaiappan *et al.* 2017). The lack of perfect coincidence between SOCE junctions and immobile IP_3Rs can be attributed to the narrow size of ER-PM junctions of around 10-25 nm (Wu *et al.* 2006), where the STIM1-Orai1 complex must be accommodated, which physically prevents the insertion of IP_3Rs. Also, recent findings that IP_3Rs are immobilized by associating with actin through KRAP provides another explanation, that IP_3Rs are excluded from the ER-PM junctions because actin normally terminates at least 100 nm before MCS (Hsieh *et al.* 2017; Thillaiappan *et al.* 2021). This phenomenon inspired researchers to consider the physiological significance of this apposition. The idea of local Ca^{2+} loss regulating SOCE was proposed as

early as 1997 (Sasajima *et al.* 1997). Because of the proximity of IP_3Rs to STIM1 and the high Ca^{2+} conductance of IP_3Rs (Vais *et al.* 2010), it can be speculated that ER Ca^{2+} release from the IP_3Rs causes local ER Ca^{2+} depletion around the ER-PM junctions, reaching the threshold for activation of nearby STIM1, form puncta, move to ER-PM junctions and interact with Orai1 (Taylor and Machaca 2019; Thillaiappan *et al.* 2019). This model also enables the ER to regulate other physiological functions requiring Ca^{2+} that would otherwise be compromised if Ca^{2+} was lost from the entire ER (Berridge 2002).

IP_3Rs also regulate SOCE independent of releasing Ca^{2+}. SOCE appears to be a critical Ca^{2+} entry pathway in *Drosophila*, mediated by dSTIM and dOrai (Venkiteswaran and Hasan 2009). Chakraborty *et al.* demonstrated that deletion or different non-functional mutants of IP_3Rs cause reduced SOCE in *Drosophila* neurons without affecting thapsigargin-evoked Ca^{2+} release (Chakraborty *et al.* 2016), but attenuated SOCE can be rescued by overexpression of dSTIM or dOrai (Agrawal *et al.* 2010; Chakraborty *et al.* 2016). These results indicate that IP_3Rs may exert downstream effects on SOCE by stabilizing the interaction between STIM and Orai. However, it seems that the participation of IP_3Rs in SOCE found in *Drosophila* is not universal to vertebrates since the knockout of IP_3R1 in DT-40 cells does not affect SOCE (Chakraborty *et al.* 2016). One possible explanation is that, while vertebrate STIM1 uses its PBD to interact with PIP_2 and tether to the PM, which helps its interaction with Orai1 (Huang *et al.* 2006; Ercan *et al.* 2009), *Drosophila* STIM has to borrow IP_3R, which also binds PIP_2 (Lupu *et al.* 1998) to compensate for its lack of a PBD. Nonetheless, knockdown of IP_3Rs was shown in human neurons to attenuate thapsigargin-evoked SOCE, but even pore-dead IP_3Rs rescues it as long as they bind IP_3 (Chakraborty *et al*., unpublished results). These results suggest a regulating function of IP_3 in SOCE independent of store depletion in mammalian neurons.

Other proteins regulating SOCE

Although overexpression of both STIM1 and Orai1 causes substantial SOCE, suggesting that STIM1 and Orai1 alone can constitute the elementary unit of SOCE (Luik *et al.* 2006; Takahashi *et al.* 2007), there are various accessory proteins regulating SOCE under physiological conditions. These proteins mainly include septins, CRACR2A, junctate and many more.

Septins are a group of GTP-binding proteins and are considered part of the cytoskeleton (Mostowy and Cossart 2012). By RNAi screening, septin 2, 4 and 5 are important regulators

of SOCE since their depletion reduces SOCE (Sharma *et al.* 2013). They are required to prevent inactive Orai1 from pre-clustering, promote STIM1 translocation to the ER-PM junctions and stabilize the Orai1 clusters and STIM1-Orai1 complexes after store depletion (Sharma *et al.* 2013; Katz *et al.* 2019). On the other hand, knockdown of septin 7 reorganizes the association between STIM and Orai and enhances constitutive Ca^{2+} entry, suggesting septin 7 as a negative regulator of SOCE both in *Drosophila* (Deb *et al.* 2016) and in human neurons (Deb *et al.* 2020) .

CRAC regulator 2A (CRACR2A) contains an EF-hand for sensing Ca^{2+}, and it directly interacts with STIM1 and the N-terminus of Orai1. Upon store depletion, CRACR2A forms a ternary complex with them to stabilize the STIM1-Orai1 assembly, which dissociates with rising cytosolic Ca^{2+} concentration (Srikanth *et al.* 2010). Furthermore, the knockdown of CRACR2A perturbs the clustering of both STIM1 and Orai1, suggesting an important role in mediating protein oligomerization in SOCE (Srikanth *et al.* 2010).

Junctate is also a Ca^{2+}-sensing protein residing in the ER (Treves *et al.* 2004), regulating SOCE by recruiting STIM1 to the ER-PM junctions upon store depletion (Srikanth *et al.* 2012). Depleting junctate attenuates SOCE, while a mutant with reduced Ca^{2+} binding causes STIM1 accumulation and partial activation of SOCE in resting cells (Srikanth *et al.* 2012). These results provide an additional mechanism for STIM1 to cluster at junctions independent of store depletion and indicate that junctate may facilitate STIM1 clustering and interaction with Orai1 at endogenous expression levels.

Potential problems associated with studies of SOCE

Most studies of STIM and Orai interactions utilized overexpressed proteins, often with fluorescent tags to allow visualization of the proteins under the microscope (e.g., Ong *et al.* (2007); Luik *et al.* (2008); Hodeify *et al.* (2015)). Overexpression of Orai1 alone abolishes SOCE, whereas its co-overexpression with STIM1 exaggerates SOCE (Mercer *et al.* 2006; Soboloff *et al.* 2006; Manjarres *et al.* 2010). However, overexpression of both proteins perturbs the structures of the ER and MCS (Scrimgeour *et al.* 2009; Saitoh *et al.* 2011; Gwozdz *et al.* 2012; Perni *et al.* 2015) and the stoichiometry of the interaction between STIM1 and Orai1. Overexpression may also reveal phenomena that may not occur under physiological conditions, for example, Orai1 accumulation and cross-linking after store depletion (Xu *et al.* 2006; Zhou *et al.* 2018).

Another problem that associates with many studies, though not all, is the use of mutants to mimic the activated states of STIM1 and Orai1 (e.g., Hou *et al.* (2018); Yeung *et al.* (2018); Liu *et al.* (2019)). It is undeniable that mutagenesis plays a significant role in molecular biology research, but the constantly active STIM1 or constitutively open Orai1 may not always represent the exact open conformation (native STIM1-bound Orai1) as well as the interaction between them. For example, the cryo-EM structure of the open Orai1 channel derived by Liu *et al.* using dOrai1 P288L (Liu *et al.* 2019) was questioned by Hou *et al.* that the pore is actually closed in this mutant (Hou *et al.* 2020).

Additionally, many studies used fragments of STIM1 and Orai1, focusing on the specific regions they were interested in (e.g., Stathopulos *et al.* (2013); Palty *et al.* (2015)). Although they usually would verify that fragments of proteins produce similar SOCE or interact just like full-length proteins, there is still a risk that the complete STIM1-Orai1 complex could perform differently from their functional fragments.

1.4. Stoichiometry of STIM1 and Orai1

How many Orai1 subunits need to be occupied to activate SOCE?

An important outstanding question in SOCE is the stoichiometry of STIM1:Orai1 (Soboloff *et al.* 2006; Scrimgeour *et al.* 2009). Compared to the common molecule-protein interactions regulating Ca^{2+} signalling pathways, SOCE is an example of direct communications between proteins. In other words, STIM1 act as a 'ligand' which binds to Orai1 and activates SOCE. Furthermore, these protein interactions occur between proteins in different membranes. Therefore, knowing the stoichiometry within the STIM1-STIM1 puncta, STIM1-STIM2 interactions and STIM1-Orai1 complexes becomes essential in understanding the trapping and activation of SOCE.

How many Orai1 subunits need to be occupied by STIM1 to activate SOCE? In the era when Orai1 was believed to be a tetramer, Li and colleagues (Li *et al.* 2010) proposed graded activation of a tetrameric concatemer of Orai1, where two STIM1 molecules could open one Orai1 subunit. They generated a chimeric construct by fusing a pair of STIM1 fragments (aa 336-485, renamed SS domain) to a single Orai1 subunit and showed that this Orai1-SS could evoke maximum SOCE. Then different numbers of the 'non-functioning' L273D mutant were mixed with WT Orai1 subunits, and it was revealed that each pair of SS domains typically binds one Orai1 subunit and the amplitudes of SOCE increase in a graded manner with each extra functional interaction between SS domain and Orai1 subunit. The CRAC channels were

maximally activated when a total of eight STIM1 molecules occupied all four subunits. Hoover and Lewis reached a similar conclusion using a different approach, suggesting that although only one or two STIM1 can trap an Orai1 channel at the ER-PM junctions, it is not sufficient to activate the channels completely. CRAC current increases with increased STIM1:Orai1 until the ratio reaches ~2; and at higher ratios, the current is reduced (Hoover and Lewis 2011). These studies illustrate the highly non-linear relationship of the STIM1-Orai1 protein ratio to CRAC current. However, these interpretations are not aligned with the subsequent discovery of the hexameric structure of Orai1 (Hou *et al.* 2012). With the hexameric structure in mind, the following findings (Yen and Lewis 2018) also used the 'non-functioning' Orai1 L273D mutant. They revealed that even a single substitution of L273D in Orai1 to prevent its binding to STIM1 reduced the open probability by ~90%, suggesting that under physiological conditions, all six subunits of Orai1 need to be occupied by STIM1 for full activation. In recent years, with the development of computer modelling and simulations, a reaction-diffusion model was established. By modelling, the maximum CRAC current was found at STIM1:Orai1 ratios of ~2-2.5 depending on different analysis methods, and the current slightly decreased with higher STIM1:Orai1 ratios (Schmidt *et al.* 2019). This modelling is in good agreement with the experimental results discussed above.

Interactions between STIM1 and STIM2

Upon ER Ca^{2+} store depletion, STIM1 and STIM2 aggregate to form puncta (Darbellay *et al.* 2010; Rana *et al.* 2015). STIM2, probably through its PBD region and SOAR domain, traps STIM1 in the ER-PM junctions. Hence, STIM1 puncta promote the association of STIM1 and Orai1 after Ca^{2+} store depletion (Ong *et al.* 2015; Subedi *et al.* 2018). Therefore, for two proteins closely interacting with one another in regulating one cellular activity, such as STIM1 and STIM2 regulating SOCE, the ratio between them becomes essential to determine the magnitude of SOCE. Varying ratios of STIM1/STIM2 lead to different behaviours of SOCE, which provide mechanistic insights on the control of SOCE.

Overexpression of STIM2 strongly inhibits SOCE in HEK293 cells, which could be due to the distorted ratio between STIM1 and STIM2 (Soboloff *et al.* 2006). At a low STIM2:STIM1 ratio, despite the existence of STIM2 in the STIM1-STIM2 puncta, they are too sparsely distributed to obstruct interaction between the C-terminus of STIM1 and Orai1. In fact, STIM2 forms heterodimers with STIM1 with low stimulus, which confers the better sensitivity of STIM2 to Ca^{2+} with the increased efficacy of STIM1 for activating Orai1 (Ong *et al.* 2015;

Subedi *et al.* 2018). However, at extremely high STIM2:STIM1 ratios, puncta containing more STIM2 effectively compete with STIM1 for binding to Orai1 and thereby reduce channel opening (***Figure 1.6***).

Following identification of the alternative splice variant STIM2.1 (Miederer *et al.* 2015; Rana *et al.* 2015), it has been confirmed that STIM2.1 fails to bind to Orai1 (Zhou *et al.* 2018). While cells only expressing STIM1 showed sustained carbochol (CCh)-evoked Ca^{2+} oscillations, cells co-expressing STIM1 and STIM2.1 at a ratio of 5:1 responded with lower frequency and less sustained Ca^{2+} oscillations, probably due to attenuated SOCE (Zhou *et al.* 2018).

Overall, although it has not been resolved fully, the stoichiometry between STIM1 and STIM2 (and its splice variants) is crucial in regulating SOCE.

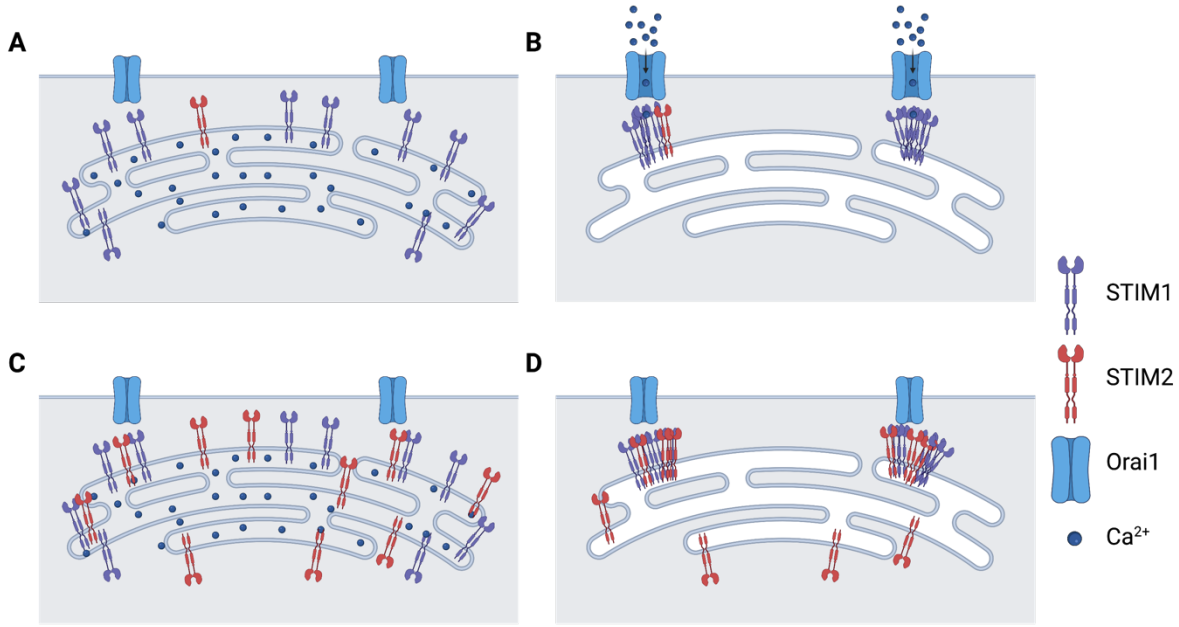

Figure 1.6 Regulation of SOCE with different ratios of STIM1 and STIM2. A. Low ratio of STIM2:STIM1 at resting state. **B.** Upon store depletion, STIM1 and STIM2 are activated, oligomerize and translocate to the ER-PM junctions to interact with Orai1 and evoke SOCE. **C.** High ratio of STIM2:STIM1 at resting state (STIM2 overexpression). **D.** Upon store depletion, STIM1 and STIM2 are also activated and accumulate into puncta. However, excess STIM2 prevents STIM1 puncta from successful interaction with Orai1, thereby inhibiting SOCE. Redrawn from Soboloff *et al.* (2006).

Clustering of STIM1 after store depletion

One signature event in SOCE is the oligomerization of STIM1 when the ER Ca^{2+} store is emptied (Xu *et al.* 2006). Loss of Ca^{2+} from the EF-SAM domain moves the two EF-hands in a STIM1 dimer closer to each other (Covington *et al.* 2010; Gudlur *et al.* 2018), which then causes conformational changes in the cytosolic domains and releases the CAD/SOAR regions. STIM1 subsequently undergoes oligomerization and translocates to the MCS into puncta to be ready to interact with Orai1 (Zheng *et al.* 2011; Fahrner *et al.* 2014). There is overwhelming evidence confirming the clustering of STIM1 upon store depletion. TIRF or confocal fluorescent imaging directly shows the formation of puncta after addition of thapsigargin to deplete Ca^{2+} stores (Xu *et al.* 2006; Calloway *et al.* 2009; Thillaiappan *et al.* 2017). FRET analyses also revealed increased proximity between STIM1 proteins after store depletion and reduced signal when the store is refilled (Liou *et al.* 2007; Malli *et al.* 2008; Shen *et al.* 2011). The clustering of STIM1 into puncta is sufficient for the translocation of STIM1 to the ER-PM junctions where SOCE happens and also helps bind with Orai1 (Luik *et al.* 2008; Malli *et al.* 2008).

Fluorescence imaging or FRET necessitates expression of fluorescently-tagged STIM1, which unavoidably overexpresses the protein. No published studies have yet reported the stoichiometry of endogenous STIM1 puncta.

The stoichiometry of the interactions between STIM1 and Orai1

There are essentially two models proposed for the stoichiometry of the interactions between STIM1 and Orai1 in SOCE. The dimeric binding model suggests that each pair of adjacent Orai1 subunits is bound by one STIM1 dimer (STIM1:Orai1=1:1, ***Figure 1.7A***), while the monomeric binding model proposed that each Orai1 subunit binds its own STIM1 dimer, leaving one STIM1 molecule in each dimer free (STIM1:Orai1=2:1, ***Figure 1.7B***). The latter provides the opportunity for crosslinking of Orai1 by STIM1 (***Figure 1.7C***), making the overall STIM1:Orai1 ratio potentially variable (according to the size of the crosslinked cluster).

The dimeric binding model was first suggested based on nuclear magnetic resonance (NMR) data (***Figure 1.7A***). Stathopulos *et al.* used a dimeric fragment of STIM1 comprising CC1 and CC2 (aa 312–387) and an engineered GST-Orai1 $C_{272–292}$ fusion, and NMR spectra demonstrated each STIM1 dimer forms a pair of STIM-Orai association pockets (SOAP, the CAD/SOAR region) in an antiparallel manner via α_2 helices and binds to two equivalent but

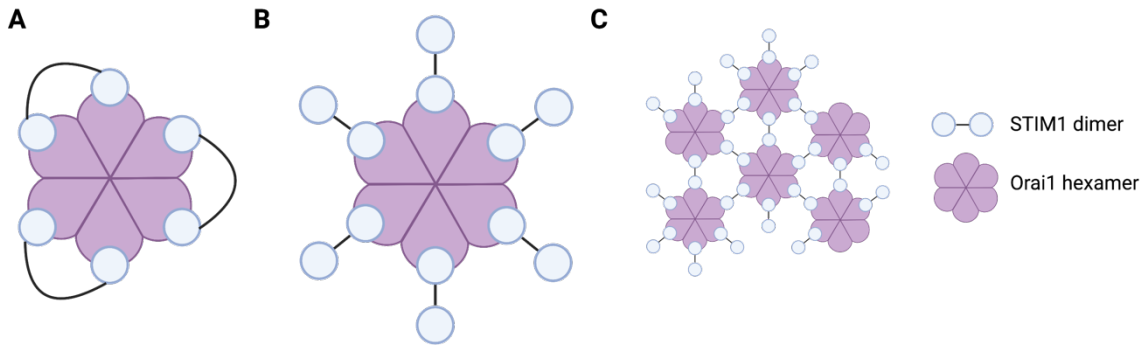

Figure 1.7 Schematic of proposed structures of SOCE complexes. Orai1 is a hexamer, comprising three pairs of dimers (Hou *et al.* 2018). Dimeric STIM1 may activate Orai1 by binding as **A.** three dimers, or **B.** as six dimers, **C.** with the residual STIM1 subunit free to interact with another Orai1 channel (Zhou *et al.* 2018). Image reproduced from Shen *et al.* (2021).

oppositely oriented STIM1-binding sites in Orai1 (M4ext) (Stathopulos *et al.* 2013). Therefore, they proposed that 3 STIM1 dimers can activate an Orai1 hexamer. However, although NMR can resolve protein structure and conformational changes to high resolution *in vitro*, it may not reflect precisely the same interacting relationship *in vivo* under physiological conditions. Moreover, the Orai1 fragment was not activated in their experiments, probably due to the absence of CC3 in the STIM1 fragment they used. Hence, it becomes more difficult to generalise the conclusion to endogenously activated SOCE complexes. This dimeric binding model was further challenged by the crystal structure of a constitutively open Orai1 mutant (H206A), which indicated that M4ext cannot be paired due to steric interference, otherwise it will impair the pore to open (Hou *et al.* 2018). This model may be indirectly supported by the study conducted with a 'non-binding' L273D Orai1 mutant (Yen and Lewis 2018). The WT-L273D heterodimer surprisingly binds to STIM1, which functionally contributes to SOCE, suggesting that STIM1 interacts with pairs of Orai1 C termini, yet the pairs of Orai1 C termini can be in the same Orai1 (dimeric model) or another adjacent channel (monomeric model).

There is also evidence for the monomeric binding model, which was first proposed by Zhou *et al.* (***Figure 1.7B***) (Zhou *et al.* 2015). They utilized a STIM1 mutant (F394H), which resides in the ER and translocates to the ER-PM junctions after store depletion just like native STIM1 but fails to bind to Orai1 or activate SOCE. The WT-F394H SOAR heterodimer strikingly still binds to Orai1 and activates SOCE, indicating that each SOAR in a dimer can interact with one Orai1 binding site independently, leading to a unimolecular interaction between STIM1 dimers

and Orai1 hexamers. It also satisfies the requirement of 2 STIM1 per Orai1 subunit to fully activate SOCE (Li *et al.* 2010; Schmidt *et al.* 2019; Dynes *et al.* 2020). In this model, each STIM1 dimer interacting with one Orai1 channel has one subunit available for interacting with another Orai1 channel, which could end up in crosslinking between multiple STIM1 dimers and Orai1 channels (***Figure 1.7C***), consistent with the clustering of Orai1 after store depletion (Xu *et al.* 2006; Gwozdz *et al.* 2008; Peckys *et al.* 2021). Later the same group found crosslinking between STIM1 SOAR dimers and Orai1 channels with empty Ca^{2+} stores (Zhou *et al.* 2018). However, whether it is Orai1 clustering or crosslinking, they both used overexpressed proteins, which may preferentially accumulate due to high abundance. Therefore, how the native STIM1 and Orai1 interact and whether they cluster upon Ca^{2+} store depletion remains an intriguing question to be investigated.

A third route was proposed recently (Palty *et al.* 2017), suggesting that the SOAR domains in STIM1 first bind to Orai1 channels in a 1:1 stoichiometry to partially activate the channel, which triggers a conformational change to allow binding of more STIM1 molecules to activate SOCE fully.

1.5. Aims of the project

Literature has demonstrated the clustering of STIM1 (Xu *et al.* 2006; Calloway *et al.* 2009; Thillaiappan *et al.* 2017) and Orai1 (Xu *et al.* 2006; Gwozdz *et al.* 2008) upon store depletion, but visualisation of puncta needs overexpression of the proteins. Therefore, endogenous evidence is lacking.

The overall aim of the project is to investigate the molecular mechanism of SOCE using a minimally perturbed system, i.e., without overexpressing STIM1 and Orai1. Specifically, I aim to quantify the aggregation of STIM1 into puncta, and to define the stoichiometry of STIM1-Orai1 complexes. My specific objectives are:

1. To use a minimally perturbed system, I need to characterize an existing cell line where STIM1 has been tagged with EGFP on the C-terminus to confirm the insert location of the EGFP tag and show that the tag does not affect the function of STIM1 proteins. (***Chapter 2***)
2. According to literature, STIM1 aggregates into clusters upon store depletion (Xu *et al.* 2006), and all six subunits of Orai1 need to be occupied by STIM1 for full SOCE activation (Yen and Lewis 2018). My hypothesis is that STIM1 aggregates into small clusters that are just enough to evoke maximum SOCE based on the monomeric model

(Zhou *et al.* 2015), i.e., 12 STIM1 molecules per puncta. I plan to use TIRFM and stepwise photobleaching to reveal the number of STIM1 molecules in each punctum formed after Ca^{2+} store depletion. (***Chapter 3***)

3. After characterizing the number of STIM1 molecules in each puncta, I plan to investigate whether Orai1 aggregates into clusters after Ca^{2+} store depletion. My hypothesis is that Orai1 does not aggregate into clusters upon Ca^{2+} store depletion so that there is no crosslinking according to the monomeric model (Zhou *et al.* 2015). (***Chapter 4***)
4. Design a CRISPR/Cas9-mediated gene-editing strategy to generate a homozygous STIM1-EGFP HeLa cell line. (Attempted in ***Chapter 2***)

Chapter 2 Characterization of HeLa cells with one *STIM1* allele tagged with EGFP

2.1. Introduction – Gene editing

Gene-editing refers to techniques where the bases or fragments are inserted, deleted, modified, or replaced in the native genome. Fundamental to the use of engineered nucleases in gene-editing is the concept of the DNA-double strand break (DSB) repair mechanism. Cells can naturally identify the mistakes that occur in DNA strands and repair them as required. When DNA strands are cleaved by a nuclease at a desired location, the DSB repair mechanism will be activated, in most cases, either through the non-homologous end joining (NHEJ) or homology-directed repair (HDR) (Ceccaldi *et al.* 2016) (***Figure 2.1***).

The NHEJ pathway is a DNA repairing mechanism which directly joins the two ends of the broken DNA strands with the help of many enzymes (Wilson *et al.* 1997; Chen *et al.* 2001; Nick McElhinny and Ramsden 2004). However, since no donor template is provided, the NHEJ pathway is not error-free, and gene rearrangements such as insertions or deletions (indels)

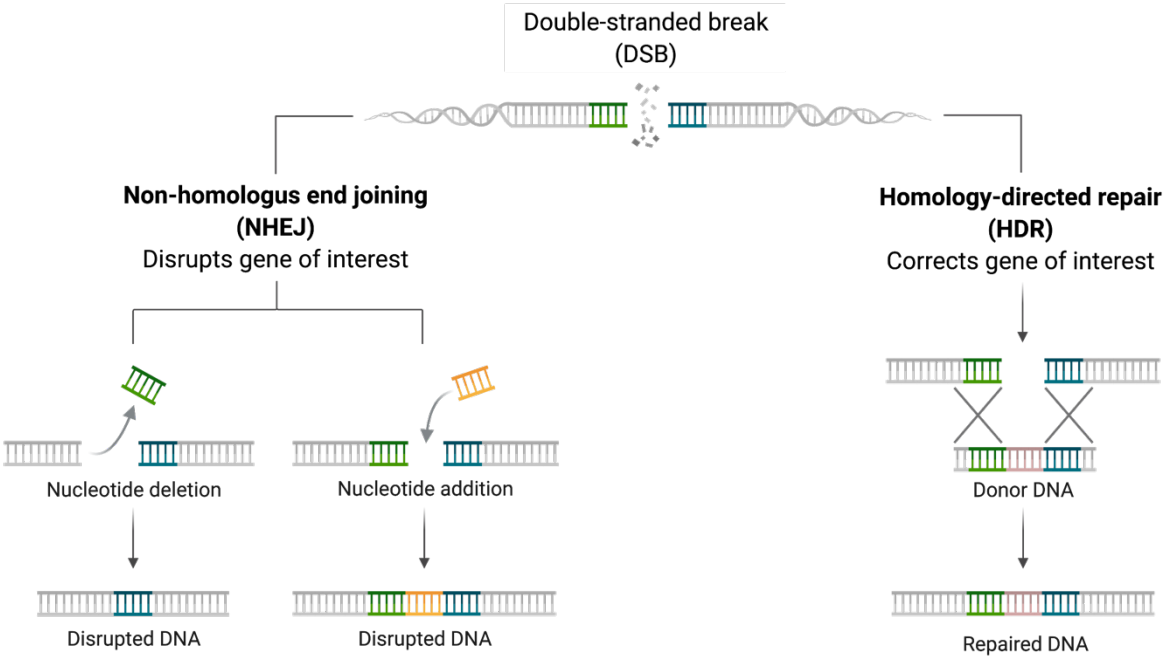

Figure 2.1 A schematic of gene-editing. The DNA double strand is cleaved by the chosen nuclease at a desired location, which triggers the DNA repair mechanism either through the non-homologous end joining (NHEJ) pathway or homology directed repair (HDR) pathway.

sometimes occur. This is not because NHEJ obligatorily induces indels, but is due to the fact that the products of accurate repair can be re-edited easily and repeatedly while indel products cannot (Bétermier *et al.* 2014). Therefore, repeated cycles will lead to accumulation of the mutated genes. Hence, NHEJ is often used for gene disruptions, but not often for gene addition or mutation.

In contrast, in the HDR pathway, a homologous sequence, which acts as a template for the regeneration of continuous DNA at the break point is introduced. The involvement of this template donor sequence would lead to the generation of desired change within the genomic ROI. Therefore, the HDR pathway provides a more efficient and precise way of designed gene-editing, hence HDR is frequently used for gene knock-in or precise modification.

The first engineered nuclease people tried to achieve gene-editing was the zinc finger nuclease (ZFN) (Kim *et al.* 1996). The zinc-finger (ZF) protein is part of the transcription factor IIIA (TFIII A) first discovered in *Xenopus* oocytes, comprising a tandem array with two cysteine and two histidine residues (Cys_2His_2) (Diakun *et al.* 1986). ZF proteins recognize and bind to specific triplets on the DNA (Pavletich and Pabo 1991), and when they are fused with the molecular scissors, *Fok* I endonuclease, the resulting ZFN is able to cleave DNA at the target sites (Desjarlais and Berg 1992; Kim *et al.* 1996). In actual use, a pair of 3-6 individual ZF proteins are connected by linkers with a non-specific *Fok* I endonuclease attached at the end. Since each ZF protein recognizes 3 specific bases, an engineered ZFN can recognize a total of 9-18 bases on each strand of the DNA (Choo *et al.* 1994; Pabo *et al.* 2001). The two *Fok* I endonucleases then dimerize and form a cleavage domain to induce DSB at the desired location (Bitinaite *et al.* 1998; Smith *et al.* 2000) (***Figure 2.2A***). The specificity of ZFN-mediated gene-editing can be reasonably high because a pair of ZFNs is adopted (Smith *et al.* 1999), but it has been difficult to design and assemble desired ZFNs to bind target DNA at high affinity and achieve successful editing (Ramirez *et al.* 2008).

Another widely-used engineered nuclease for gene-editing is the transcription activator-like effector nucleases (TALENs), constituted by a bacterial TALE protein and a *Fok* I endonuclease (Boch *et al.* 2009; Moscou and Bogdanove 2009). The TALE protein is originally used by plant pathogens to infect plants by binding to effector-specific DNA sequences, which alters gene expression transcriptionally (Bogdanove *et al.* 2010). The ability of targeting specific DNA is then exploited in biotechnology. Like ZFNs, TALENs are used in pairs, but each monomer in the DNA-binding domain corresponds to one nucleotide in the target DNA instead of the triplet each ZFN recognizes (Christian *et al.* 2010). Subsequently,

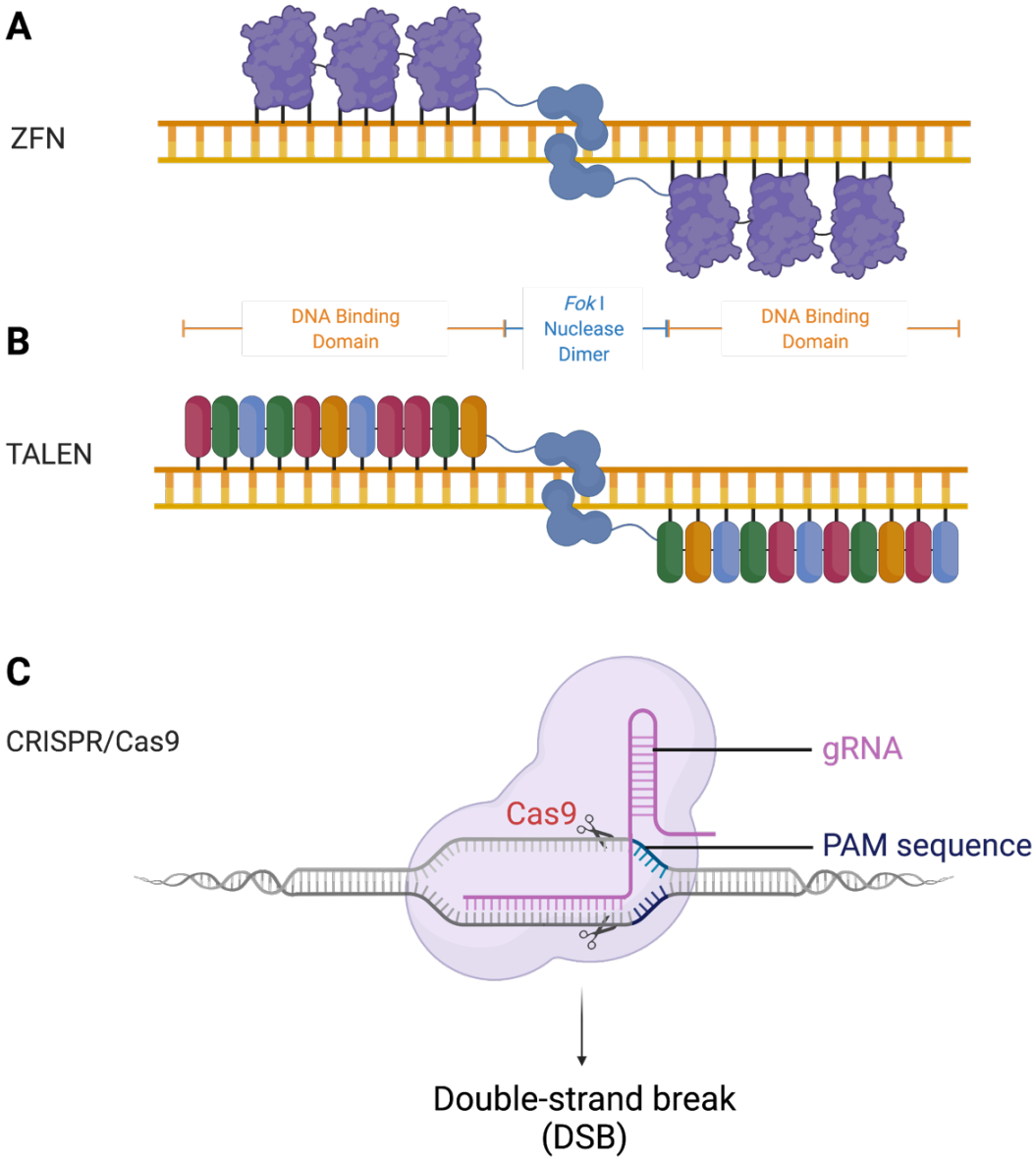

Figure 2.2 A schematic of ZFN, TALENs, and CRISPR/Cas9 systems. A. ZFN-mediated gene-editing. Each ZF protein recognizes a triplet in the target DNA and the *Fok* I endonuclease forms dimer to cleave the DNA. **B.** TALEN-mediated gene-editing. Each monomer in the TALE protein recognizes one nucleotide and the *Fok* I endonuclease also dimerizes to cleave the target DNA. **C.** CRISPR/Cas9-mediated gene-editing. A guide RNA is pre-designed adjacent to a PAM site. The Cas9 enzyme is co-transfected into cells with the gRNA and cut the DNA at a desired location. All three systems result in DSB so that the genome can be modified by the repairing mechanisms.

Fok I endonucleases form dimers to introduce DSB, just like ZFNs (***Figure 2.2B***). Due to the simplicity with designing TALENs and the fact that TALENs can basically target any sites, TALENs quickly become a popular tool for gene-editing.

CRISPR stands for Clustered Regularly Interspaced Short Palindromic Repeats and was originally referred to a family of DNA sequences in bacteria and archaea (Mojica *et al.* 1995; Jansen *et al.* 2002). They act as an adaptive immune system in prokaryotes to protect them from repeated phage infections by allowing prokaryotes to acquire short segments of spacer DNA from foreign attackers, such as viruses or plasmids (Mojica *et al.* 2005; Barrangou *et al.* 2007). Small clusters of *Cas* (CRISPR-associated system) genes are located downstream to CRISPR sequences, which is responsible to introduce DSB and kill the pathogens once they have been recognized (Bolotin *et al.* 2005). There is another important component in this system, namely the protospacer adjacent motif (PAM), a DNA sequence of 3-5 bases long located immediately after the DNA sequence targeted by the Cas9 nuclease. The PAM is only found in the invading pathogens but not in the host bacteria, hence it distinguishes bacterial self from foreign DNA, thereby preventing host DNA from being targeted and destroyed by the nuclease (Mali *et al.* 2013).

In CRISPR/Cas9 mediated gene-editing, a guide RNA (gRNA) is designed to target a sequence flanking the desired location. The gRNA sequence selected needs to be adjacent to a PAM site. Since the PAM site is short enough to be found in various locations in the genome, it allows easy design and precise targeting of gRNA. The Cas9 nuclease is transfected into the cell together with the gRNA. In the cell, gRNA recognizes the sequence and the Cas9 nuclease makes a double strand cut in the genome. The donor DNA is then incorporated to the genome through the HDR mechanism (Cong *et al.* 2013; Mali *et al.* 2013) (***Figure 2.2C***).

Both TALENs and CRISPR/Cas9-mediated gene editing techniques are widely used nowadays. In comparison, the CRISPR/Cas9 system might be even simpler, more efficient and easier to produce and deliver into cells (Cho *et al.* 2013; Cong *et al.* 2013). Furthermore, the easy generation of gRNA library allows rapid functional genomic screening, which can help reveal molecular mechanisms of cellular activities and develop drugs (Nemudryi *et al.* 2014). Nonetheless, while the specificity of TALENs can be controlled by altering the length of customized DNA-binding domain, gRNAs in the CRISPR/Cas9 system are fixed. Therefore, off-target can be a serious problem associated with the CRISPR/Cas9 system (Fu *et al.* 2013; Hsu *et al.* 2013; Mali *et al.* 2013), which requires careful design of gRNAs and other methods such as adopting improved Cas variants, improved delivery methods, or anti CRISPR proteins

(Naeem *et al.* 2020). By all means, both TALENs and CRISPR/Cas9 systems are extremely useful in biotechnology and pharmaceutical industry, particularly in visualizing endogenous proteins and developing potential therapeutic targets and gene therapies.

As suggested in the ***Introduction***, the studies of SOCE mainly utilized overexpression of STIM1 and Orai1, which perturbs both the interaction between the proteins and the structures of the ER and MCS (Scrimgeour *et al.* 2009; Saitoh *et al.* 2011; Gwozdz *et al.* 2012; Hodeify *et al.* 2015; Perni *et al.* 2015; Yen and Lewis 2019). Previous studies have no alternative but overexpressing fluorescently tagged proteins to visualize them in live cells, but with the development of various gene-editing technologies, fortunately, the CRISPR/Cas9 system can be adopted to add a fluorescent tag to the protein of interest with physiological level of expression. A CRISPR-edited HeLa cell line, with STIM1 tagged with EGFP at the C-terminus, has been generated by Dr. Sumita Chakraborty. Most of the functional studies in this thesis will be based on this cell line.

2.2. Materials and Methods

2.2.1. Materials

Table 2.1 Materials

(WB: Western Blot, IC: Immunocytochemistry)

Materials	**Company**	**Catalog number**
Agarose	Bioline	Cat# BIO-41025
Alpha-select gold efficiency chemically competent cells	Bioline	Cat# BIO-85027
Amersham ECL prime western blotting detection reagent	GE Healthcare	Cat# RPN2236
Antibiotic-antimycotic (100X)	Gibco	Cat# A5955
BAPTA	Phion Chemicals	Cat# 81114671
Bovine serum albumin (BSA)	Europa Bioproducts Ltd	Cat# EQBAH68
Calcium chloride solution, ~1 M in H_2O	Sigma-Aldrich	Cat# 21115
Cell dissociation buffer (enzyme-free, PBS)	Gibco	Cat# 13151014
cOmplete™, Mini Protease Inhibitor Cocktail	Sigma-Aldrich	Cat# 11836153001
Custom DNA oligos and primers	Invitrogen	This study
Cyclopiazonic acid (CPA)	Tocris	Cat# 1235
D-Glucose anhydrous	Fisher BioReagents	Cat# AAA1682836
Dimethyl sulfoxide (DMSO)	Sigma-Aldrich	Cat# D2650
DL-Dithiothreitol solution (DTT)	Sigma-Aldrich	Cat# 43816
DNA gel loading dye (6X)	Thermo Scientific	Cat# R0611
Dulbecco's Modified Eagle Medium/Nutrient Mixture F-12 + GlutaMAX™	Gibco	Cat# 31331
EDTA	Sigma-Aldrich	Cat# EDS
EZ-10 spin column DNA gel extraction kit	Bio Basic	Cat# BS354

FastDigest buffer (10X)	Thermo Scientific	Cat# B64
FastDigest *Nhe*I	Thermo Scientific	Cat# FD0973
FastDigest *Pvu*I	Thermo Scientific	Cat# FD0624
FastDigest *Xba*I	Thermo Scientific	Cat# FD0684
Fetal bovine serum	Sigma-Aldrich	Cat# F7524
Fluo-8, AM (21081)	AAT Bioquest	Cat# 21080
GeneRuler 1 kb plus DNA ladder	Thermo Scientific	Cat# SM1331
Goat anti-rat IgG-HRP (WB, 1:5000)	Santa Cruz Biotechnology	Cat# sc-2006 RRID: AB_1125219
Hank's balanced salt solution	Gibco	Cat# 14025
HEPES, Free acid, ULTROL Grade	Merck Millipore Corp.	Cat# 391338
Histamine	Sigma-Aldrich	Cat# H7250
Human plasma fibronectin purified protein	Merck	Cat# FC010
Illustra GFX PCR DNA and gel band purification kit	GE Healthcare	Cat# GE28-9034-66
Ionomycin	Apollo Scientific	Cat# 56092-81-0
KH_2PO_4	Fisher Scientific	Cat# 10757214
LB agar	Formedium	Cat# LMM0202
LB broth	Formedium	Cat# LMM0102
MagicMark™ XP western protein standard	Invitrogen	Cat# LC5602
Magnesium chloride hexahydrate ($MgCl_2 \cdot 6H_2O$)	Fisher BioReagents	Cat# 10386743
mCh-Orai1 in pcDNA3.1+		(Thillaiappan *et al.* 2017)
Midori Green advanced DNA stain	Nippon Genetics Europe	Cat# S6-0022
Mouse IgGκ-binding protein-HRP (WB, 1:5000)	Santa Cruz Biotechnology	Cat# sc-516102 RRID: AB_2687626
Mouse monoclonal anti-mCherry (1C51) (WB: 1:2000)	Abcam	Cat# ab125096 RRID: AB_11133266
Mouse monoclonal anti-rabbit IgG-HRP (WB, 1:5000)	Santa Cruz Biotechnology	Cat# sc-2357 RRID: AB_628497

Mouse monoclonal anti-β-actin (8H10D10) (WB, 1:20,000)	Cell Signaling Technology	Cat# 3700 RRID: AB_2243334
Na_2HPO_4	Fisher Scientific	Cat# S374-500
Novex™ Tris-Glycine SDS running buffer (10X)	Invitrogen	Cat# LC2675
Novex™ WedgeWell™ 4-12% Tris-Glycine mini gels	Invitrogen	Cat# XP04125
Novex™ Tris-Glycine SDS Sample Buffer (2X)	Invitrogen	Cat# LC2676
NuPAGE™ LDS sample buffer (4X)	Invitrogen	Cat# NP0007
NuPAGE™ Tris-Acetate gels (3-8%)	Invitrogen	Cat# EA0375
NuPAGE™ Tris-Acetate SDS running buffer (20X)	Invitrogen	Cat# LA0041
OptiMEM reduced-serum medium	Thermo Scientific	Cat# 31985
Phosphate-buffered saline	Gibco	Cat# 10010
Potassium chloride (KCl)	Fisher BioReagents	Cat# BP366-500
Q5® hot start high-fidelity DNA polymerase	New England Biolabs	Cat# M0493S
QIAGEN plasmid maxi kit	QIAGEN	Cat# 12165
Quick-DNA™ miniprep kit	Zymo Research	Cat# D3024
Rabbit monoclonal anti-STIM1 (D88E10) (WB, 1:1000; IC, 1:500)	Cell Signaling Technology	Cat# 5668 RRID: AB_10828699
Rat monoclonal anti-GFP (WB, 1:1000)	Chromotek	Cat# 3H9-100 RRID: AB_10773374
RFP-Trap magnetic agarose	Chromotek	Cat# rtma-20 RRID: AB_2631363
RunBlue™ Bis-Tris protein gels (4-12%)	Expedeon	Cat# ab270467
RunBlue™ LDS sample buffer (4X)	Expedeon	Cat# ab270226

RunBlue™ MOPS run buffer (20X)	Expedeon	Cat# ab270225
S.O.C. Medium	Invitrogen	Cat# 15544034
siPORT NeoFX transfection agent	Invitrogen	Cat# AM4510
Sodium chloride (NaCl)	Fisher BioReagents	Cat# BP358-1
Sodium hydroxide, 98%, extra pure, pellets (NaOH)	Fisher BioReagents	Cat# 10502731
Spectra™ multicolor broad range protein ladder	Thermo Scientific	Cat# 26634
Thapsigargin	Tocris	Cat# 1138
*Trans*IT-LT1 transfection reagent	Mirus Bio LLC	Cat# MIR 2305
Tris Base	Fisher BioReagents	Cat# 10103203
Tris-acetate-EDTA (TAE) buffer (50X)	National Diagnostics	Cat# EC-872
Triton X-100	Sigma-Aldrich	Cat# T8787-250ML
TrypLE™ Express Enzyme (1X)	Gibco	Cat# 12605
Tween 20	VWR Chemicals	Cat# 0777-1L

Table 2.2 Equipment

Equipment	Company
BioDrop micro-volume measurement platforms	BioDrop
MyCycler™ Thermal Cycler System	Bio-Rad
FlexStation 3 microplate reader	Molecular Devices
iBlot® 7-minute blotting system	Invitrogen
SH800S fluorescence-activated Cell Sorter	Sony
PXi/PXi Touch gel and blot imaging system	Syngene

Table 2.3 Composition of media

Medium	Composition
HEPES-buffered saline (HBS)	135 mM NaCl, 5.9 mM KCl, 1.2 mM $MgCl_2$, 1.5 mM $CaCl_2$, 11.6 mM HEPES, 11.5 mM glucose, pH 7.3
Phosphate-buffered saline (PBS)	137 mM NaCl, 2.7 mM KCl, 10 mM Na_2HPO_4, 2 mM KH_2PO_4, pH 7.4
Tris-buffered saline (TBS)	137 mM NaCl, 20 mM Tris-base, pH 7.6
Tris-buffered saline, with Tween 20 (TBST)	137 mM NaCl, 20 mM Tris-base, pH 7.6, 0.1% Tween 20
Phosphate-buffered saline, with Tween 20 (PBST)	137 mM NaCl, 2.7 mM KCl, 10 mM Na_2HPO_4, 2 mM KH_2PO_4, pH 7.4, 0.1% Tween 20
Lysis buffer	10 mM Tris-base, 150 mM NaCl, 0.5 mM EDTA, 1% Triton X-100, pH 7.5
Blocking buffer	TBST, 5% BSA
Sorting buffer	PBS, 1 mM EDTA, 25 mM HEPES pH 7.0, 1% FBS

Table 2.4 PCR Primers

Primer sequence	Code
AAA TGG TGA CTC GGA GCA G	1F
CTT GTG GCC GTT TAC GTC G	1R
TTG GCG AGG AAA CAG ACT CC	2F
GAG CTG AGG GAA CAG CAA CT	2R

2.2.2. Cell culture and transient transfections

WT and STIM1-EGFP HeLa cells were cultured in Gibco Dulbecco's Modified Eagle Medium/Nutrient Mixture F-12 + GlutaMAX™ supplemented with 10% fetal bovine serum (FBS). The cells were grown at 37°C with 5% CO_2 and passaged using Gibco TrypLE™ Express Enzyme according to standard protocols.

For plasmid DNA transfection in T75 flasks, cells were about 70% confluent prior to transfection. *Trans*IT-LT1 Transfection Reagent was prewarmed to 20°C and gently vortexed before transfection. 19 µg of plasmid DNA was mixed with 57 µl *Trans*IT-LT1 Reagent and 1.9 ml of Gibco Opti-MEM I Reduced Serum Medium. The mixture was incubated at 20°C for 20 min. The mixture was then added dropwise to different areas of the flask to evenly distribute the TransIT-LT1 Reagent: DNA complexes. The cells were used after 24-72h.

For transfection with siRNA in 6-well plates or imaging dishes, siPORT NeoFX transfection agent was used according to the manufacturer's instructions. A reverse transfection method was used where DNA-lipid complex was distributed to culture wells before addition of plating cells. For each well, 5 µL of transfection reagent was diluted in 100 µL Opti-MEM medium, and after 10-minute incubation at 20 °C, mixed with siRNA. 5 nM siRNA (or NS siRNA) for GFP (***Figure 3.11***) or 150 nM siRNA for Orai1 (50 nM of each of the three siRNAs, or 150 nM of NS siRNA, ***Figure 4.3***) were used. The mixture was then incubated (20 °C, 10 min) and dispensed dropwise across the well and mixed with freshly passaged cells (2×10^5 cells per well). Cells were used after 72 hr.

2.2.3. Construction of donor DNA for STIM1

The STIM1-EGFP donor sequence was designed by Dr. Sumita Chakraborty. STIM1-EGFP donor and gRNA sequence were designed by E-CRISPR and the CRISPR target site was deleted from donor sequence to avoid multiple editing. The EGFP sequence was inserted immediately after the stop codon of exon 12 at the C-terminus of STIM1 protein connected by a linker (***Figure 2.3*** *and* ***Figure 2.4***).

gRNA sequence: 5′ -GGGACAGCTTGTCCTTCCCT- 3′

TAGGTTCTGTGTTAGCTTGAGTCCCAGGAAATACAGCCAGCTATGAGAAGGCAGAGATTTTATTGAGGAT
GCCGCCTGTGGAATTTAAGCCTATGGCTGCACCAGTTCAGAGCCAGAGCATTCACCACTGGTGGGGCCCA
GGTATTGGAAAACCATTTGCCAGACAGATGATGGTATGATGACATTTGTTTTTGTTTCTTATCTGTTTCT
TCCCTCCCTATCACTTTTCCCTTTCTTGTCTTTCTCTCTTGGCCCTTCTTTCTACCTGCTTATCCTTTTG
CTTTTCTTCCTCTACAATTCTACTCTCCTTTTCCTGTCTCTTTTCCAATCTATCCTCATTCCCTCCTCCT
GCCTCCTCTCTTATCCTATACTTATGGCTGCTCAACTTCTGTCTATTCCTCTTTCCTCTCTCCTTCCCAC
CTGCCTGTTCATCCTATTTCTCTCTCCTGCCGCTCTATCCCCATTTTCCTACCCTGTCCTTGTCTTCTCG
TGTTGTCCCTCTCTCCTCTTCGCCTTTCCCCTATCACCTCATCCAATATATGTCCCTTTCTTCCTCTCTG
CCCCATGTCTTGCAG**GGATTTGACCCATTCCGATTCGGAGTCCTCCCTCCACATGAGTGACCGCCAGCGT**
GTGGCCCCCAAACCTCCTCAGATGAGCCGTGCTGCAGACGAGGCTCTCAATGCCATGACTTCCAATGGCA
GCCACCGGCTGATCGAGGGGGTCCACCCAGGGTCTCTGGTGGAGAAACTGCCTGACAGCCCTGCCCTGGC
CAAGAAGGCATTACTGGCGCTGAACCATGGGCTGGACAAGGCCCACAGCCTGATGGAGCTGAGCCCCTCA
GCCCCACCTGGTGGCTCTCCACATTTGGATTCTTCCCGTTCTCACAGCCCCAGCTCCCCAGACCCAGACA
CACCATCTCCAGTTGGGGACAGCCGAGCCCTGCAAGCCAGCCGAAACACACGCATTCCCCACCTGGCTGG
CAAGAAGGCTGTGGCTGAGGAGGATAATGGCTCTATTGGCGAGGAAACAGACTCCAGCCCAGGCCGGAAG
AAGTTTCCCCTCAAAATCTTTAAGAAGCCTCTTAAGAAGTAGGCAGGATGGGGTGGCAGTAAAGGGACAG
CTTGTCCTTCCCTGGGTGTTCTGTCTCTCCTTCCCTCCCTTCCTTCAAGATAACTGGCCCCAAGAGTGGG
GCATGGGAAGGGCTGGTCCAGGGGTCTGGGCACTGTACATACCTGCCCCCTCATCCTTGGGTCCTTCATT
ATTATTTATTAACTGACCACCATGGCCTGCCTGCCCTGCCTCCGTCCCAACCATGGGCTGCTGCTGTCAC
TCCCTCTCCACTTCAGTGCATGTCTTAGTTGCTGTTCCCTCAGCTCCCAGCTCCACCTCTGGGGTTCAGC
TTCTGTCTCTGCTGTCCCAGTTTTGAGGTTTGGTTTCTTGTTTCTGTCTCTTGCTTTCGGGCTCCTCCCT
CCCACCACTCCCCAACTTCCCCTAGCAGTTGCAGGGAAGATAGGACGAGTAGCTTCTGACATGTGTGCCT
CAGATCTGTTCCACCCCACTCACAGTGGTTCTGTTTGCTCCAGACTGGGGCTAGGGCCTAATCTTTGAAG
TTTGTTCTTTGGTATTGATGTGGGTCAGAAGGAGCCTCATCCTAATCTCACTCAGGCCTCCAGGGATCCA
TGGGGGAGTGAAACCAATTCTCAGAGAACAACCCACCAGAGACTTTTAAAGAGAGGCCAGGCTTGGGAAT
GGGTTGGGAGAGGCATCTGTTCATTGGAGCATGAGTGGATGCCAGAACTGTAGGTTATAAGGCAGTCACT
TTTTCTCTCTACTCCCACCCACACCTGCCTCCCTCTTACCCCTGCTCCCCCACACTGCAGGAGGATTTGT
CTCTAAGAGGTGCTGCCCCAAAGCTCCCCAAGCATCAATACTCCTAGGGCTCAGGACAAGTGGCTCCCCT
GGCCAGGAGAGCCACAGCCATGATACAGGGCTCTTATGGAGCCCTGGAGTTGTTGGGCAAGGATGCTGTC
ATTTTTTGAACCAAAAGACAAACAGGTTAAAAGGAAAAAAAGTAATCTGAATTTCCCAAGTGCCTACGCT
GCATATTCCCCTTGTTAGATCCCATTTTCATGTTACTTTGTAGCCTTGGCCAGAGGCTCAAAAAGGACAC
AACCAGTTTGGGGAAGGGGTGGCTAAGGAAGATGGTATAGGTGAAGGCGGCTGTGTGACCACTTTCCCCC
ACCCTTCCCACCCTCTAGACAACTCTCTCCCTTACCTGTTTTTGCTATGGCTGTAAAGGTATTTTTCCTC
TGCCCCACTCCCTGCCATACCTTTATCCTGGGATCCTATTTTGGGCCTGGGGTGGGTATACCTGGGGCTG
GTCTTAGGAGGGTGCTAGGCTGCAGACTGCCTTGTACTCCCTGGACACCCTCAAATGGGGTTTTCTGTGT
TATTTCATAAAATTCTTTGAAGTCCAATAAAGCATGTAGGAGATTTTAACCACT

Figure 2.3 DNA sequence of the gene encoding native STIM1 protein near its C-terminus. The intronic region and exon 12 of STIM1 protein in the original sequence are in normal font and in bold, respectively. The stop codon of STIM1 is in red and bold. The CRISPR targeting site (gRNA) is highlighted in teal. The PAM site is underlined. The EGFP sequence will be inserted just before the stop codon of STIM1 protein.

GCTAGCAGAAGGCAGAGATTTTATTGAGGATGCCGCCTGTGGAATTTAAGCCTATGGCTG
CACCAGTTCAGAGCCAGAGCATTCACCACTGGTGGGGCCCAGGTATTGGAAAACCATTTG
CCAGACAGATGATGGTATGATGACATTTGTTTTTGTTTCTTATCTGTTTCTTCCCTCCCT
ATCACTTTTCCCTTTCTTGTCTTTCTCTCTTGGCCCTTCTTTCTACCTGCTTATCCTTTT
GCTTTTCTTCCTCTACAATTCTACTCTCCTTTTCCTGTCTCTTTTCCAATCTATCCTCAT
TCCCTCCTCCTGCCTCCTCTCTTATCCTATACTTATGGCTGCTCAACTTCTGTCTATTCC
TCTTTCCTCTCTCCTTCCCACCTGCCTGTTCATCCTATTTCTCTCTCCTGCCGCTCTATC
CCCATTTTCCTACCCTGTCCTTGTCTTCTCGTGTTGTCCCTCTCTCCTCTTCGCCTTTCC
CCTATCACCTCATCCAATATATGTCCCTTTCTTCCTCTCTGCCCCATGTCTTGCAG**GGAT**
TTGACCCATTCCGATTCGGAGTCCTCCCTCCACATGAGTGACCGCCAGCGTGTGGCCCCC
AAACCTCCTCAGATGAGCCGTGCTGCAGACGAGGCTCTCAATGCCATGACTTCCAATGGC
AGCCACCGGCTGATCGAGGGGGTCCACCCAGGGTCTCTGGTGGAGAAACTGCCTGACAGC
CCTGCCCTGGCCAAGAAGGCATTACTGGCGCTGAACCATGGGCTGGACAAGGCCCACAGC
CTGATGGAGCTGAGCCCCTCAGCCCCACCTGGTGGCTCTCCACATTTGGATTCTTCCCGT
TCTCACAGCCCCAGCTCCCCAGACCCAGACACACCATCTCCAGTTGGGGACAGCCGAGCC
CTGCAAGCCAGCCGAAACACACGCATTCCCCACCTGGCTGGCAAGAAGGCTGTGGCTGAG
GAGGATAATGGCTCTATTGGCGAGGAAACAGACTCCAGCCCAGGCCGGAAGAAGTTTCCC
CTCAAAATCTTTAAGAAGCCTCTTAAGAAGCGAATTCTGCAGTCGACGGTACCGCGGGCC
CGGGATCCACCGGTCGCCACCATGGTGAGCAAGGGCGAGGAGCTGTTCACCGGGGTGGTG
CCCATCCTGGTCGAGCTGGACGGCGACGTAAACGGCCACAAGTTCAGCGTGTCCGGCGAG
GGCGAGGGCGATGCCACCTACGGCAAGCTGACCCTGAAGTTCATCTGCACCACCGGCAAG
CTGCCCGTGCCCTGGCCCACCCTCGTGACCACCCTGACCTACGGCGTGCAGTGCTTCAGC
CGCTACCCCGACCACATGAAGCAGCACGACTTCTTCAAGTCCGCCATGCCCGAAGGCTAC
GTCCAGGAGCGCACCATCTTCTTCAAGGACGACGGCAACTACAAGACCCGCGCCGAGGTG
AAGTTCGAGGGCGACACCCTGGTGAACCGCATCGAGCTGAAGGGCATCGACTTCAAGGAG
GACGGCAACATCCTGGGGCACAAGCTGGAGTACAACTACAACAGCCACAACGTCTATATC
ATGGCCGACAAGCAGAAGAACGGCATCAAGGTGAACTTCAAGATCCGCCACAACATCGAG
GACGGCAGCGTGCAGCTCGCCGACCACTACCAGCAGAACACCCCCATCGGCGACGGCCCC
GTGCTGCTGCCCGACAACCACTACCTGAGCACCCAGTCCAAGCTGAGCAAAGACCCCAAC
GAGAAGCGCGATCACATGGTCCTGCTGGAGTTCGTGACCGCCGCCGGGATCACTCTCGGC
ATGGACGAGCTGTACAAGTAGGCAGGATGGGGTGGCAGTGTTCTGTCTCTCCTTCCCTCC
CTTCCTTCAAGATAACTGGCCCCAAGAGTGGGGCATGGGAAGGGCTGGTCCAGGGGTCTG
GGCACTGTACATACCTGCCCCCTCATCCTTGGGTCCTTCATTATTATTTATTAACTGACC
ACCATGGCCTGCCTGCCCTGCCTCCGTCCCAACCATGGGCTGCTGCTGTCACTCCCTCTC
CACTTCAGTGCATGTCTTAGTTGCTGTTCCCTCAGCTCCCAGCTCCACCTCTGGGGTTCA
GCTTCTGTCTCTGCTGTCCCAGTTTTGAGGTTTGGTTTCTTGTTTCTGTCTCTTGCTTTC
GGGCTCCTCCCTCCCACCACTCCCCAACTTCCCCTAGCAGTTGCAGGGAAGATAGGACGA
GTAGCTTCTGACATGTGTGCCTCAGATCTGTTCCACCCCACTCACAGTGGTTCTGTTTGC
TCCAGACTGGGGCTAGGGCCTAATCTTTGAAGTTTGTTCTTTGGTATTGATGTGGGTCAG
AAGGAGCCTCATCCTAATCTCACTCAGGCCTCCAGGGATCCATGGGGGAGTGAAACCAAT
TCTCAGAGAACAACCCACCAGAGACTTTTAAAGAGAGGCCAGGCTTGGGAATGGGTTGGG
AGAGGCATCTGTTCATTGGAGCATGAGTGGATGCCAGAACTGTAGGTTATAAGGCAGTCA
CTTTTTCTCTCTACTCCCACCCACACCTGCCTCCCTCTTACCCCTGCTCCCCCACACTGC
AGGAGGATTTGTCTCTAAGAGGTGCTGCCCCAAAGCTCCCCAAGCATCAATACTCCTAGG
GCTCAGGACAAGTGGCTCCCCTGGCCAGGAGAGCCACAGCCATGATACAGGGCTCTTATG
GAGCCCTGGAGTTGTTGGGCAAGGATGCTGTCATTTTTTGAACCAAAAGACAAACAGGTT
AAAAGGAAAAAAAGTAATCTGAATTTCCCAAGTGCCTTCTAGA

Figure 2.4 Sequence of EGFP donor vector for *STIM1* in HeLa cells. The NheI restriction site and Xba1 restriction site are highlighted in red and yellow, respectively. The intronic region, linker and *EGFP* sequence are highlighted in grey, pink and green, respectively. The exon region is in bold while the 3'-UTR region is in normal font.

2.2.4. Generation of a cell line with STIM1 endogenously tagged by EGFP

The cell line that is mostly used in this thesis, unless specified otherwise, is the STIM1-EGFP HeLa cell line, which was generated in house by Dr. Sumita Chakraborty. For the generation of STIM1-EGFP HeLa cells, WT HeLa cells grown in a T175 flask were transfected (***Section 2.2.2***) with 10 µg cas9, 10 µg gRNA and 20 µg linearized STIM1-EGFP donor vectors (***Section 2.2.3***). Cells were harvested using TrypLE Express enzyme 72h after transfection and sorted (***Section 2.2.11***) until a monoclonal cell line was generated. All protocols involved in this process will be described in detail in later sections.

For the generation of doubly edited STIM1-EGFP HeLa cell line (referred as de-STIM1-EGFP HeLa cells, ***Section 2.3.5***) did by me, I followed the same protocols (described in detail below) as Dr. Sumita Chakraborty using same cas9, gRNA and donor vectors. In the selection and validation stage after sorting, only monoclonal cell lines with solely STIM1-EGFP proteins were looked for.

2.2.5. Western blotting and in-gel fluorescence

Confluent cells in a T75 flask were washed twice with 10 ml PBS at 20°C. Cells were then incubated with 5 ml cell dissociation buffer (enzyme-free) for 5 min. Cells were dislodged by gentle tapping and 5 ml of PBS was added. Cells were then pelleted by centrifugation at 650 × g for 2 min. The cell pellet was resuspended in 1 ml PBS and transferred into 1.5 ml tube, and pelleted again by centrifugation at 700 × g for 2 min. The pellet was then resuspended in lysis buffer. The lysis mixture was incubated at 4 °C for 1h with gentle rotation followed by sonication (3 × 10 s, Transonic ultrasonic bath). The supernatant from the lysate was recovered after centrifugation at 4 °C at 20, 000 × g for 30 min and used for analysis.

For SDS-PAGE, 700 ml 1X RunBlue MOPS Run Buffer or 1X NuPAGE™ Tris-Acetate SDS Running Buffer was prepared for one gel compartment. 13 µl of protein lysate prepared as described above was mixed with 5 µl LDS and 2 µl of DTT per well. The loading solution was heated at 85 °C for 10 min before loading onto RunBlue™ Bis-Tris Protein Gels (4%-12%) (Expedeon) or NuPAGE™ Tris-Acetate Gels (3%-8%) (Invitrogen). MagicMark protein ladder (3 µl) and Spectra Multicolour Broad Range protein ladder (5 µl) were loaded in the gel. Electrophoresis was performed at 180V for 45 min (Expedeon) or 150V for 1h (Invitrogen).

Protein samples from SDS-PAGE were transferred onto a PVDF membrane using iBlot 7-Minute Blotting System. The membrane was then blocked by blocking buffer (***Table 2.3***) at 20°C for 1h. The membrane was washed briefly with TBST (***Table 2.3***) and incubated with

primary antibody solution (dilutions indicated in ***Table 2.1***) for 16 h at 4 °C. The membrane was then washed 3 times with TBST, each for 5 min. The membrane was incubated in secondary antibody solution (dilutions indicated in ***Table 2.1***) for 1 h at 20 °C. The membrane was washed again with TBST for 3 times, each 5 min. 1 ml of ECL prime Western blotting detection reagents were added on the membrane and the membrane was exposed to a PXi chemiluminescence detector for 4 s to 2 min.

For in-gel fluorescence, protein lysate and loading solution were made as described above, but the loading solution was not heated and directly added to Novex™ WedgeWell™ 4-12% Tris-Glycine Mini Gels. Electrophoresis was performed at 125V in Tris-Glycine SDS running buffer for 90 min.

For analysis, SDS-PAGE gel was placed on the reading chamber of the PXi gel-imaging system and images were captured in manual mode using blue LED (M) module and emission 525nm filter.

2.2.6. Extraction, purification, and analysis of genomic DNA

For DNA extraction from cells, the Quick-DNA mini prep kit was used. The protocol followed the manufacturer's instructions. The principle of the kit is to first lyse cells with guanidinium thiocyanate and N-lauroylsarcosine (sodium salt) (Datasheet 2018) and bind DNA to the solid phase of silica in a spin-column. Ethanol and propan-2-ol (Datasheet 2018) were used to wash DNA twice to remove proteins, salts and other contaminants in the DNA sample. DNA was then eluted by dissolving in small amount of elution buffer or water for subsequent experiments.

Briefly, cells were harvested using TrypLE Express enzyme and the pellet was resuspended in 500 µl of genomic lysis buffer by vortexing 6 s and standing for 10 min at 20 °C. The mixture was transferred to a spin-column in a collection tube and centrifuged (10, 000 × g, 1 min). 200 µl of DNA pre-wash buffer was added to the same spin-column and centrifuged (10,000 × g, 1 min). 500 µl of g-DNA wash buffer was added to the spin-column and centrifuged (10,000 × g, 1 min). The spin-column was then transferred to a clean microcentrifuge tube and 50 µl DNA elution buffer was added. The mixture was incubated at 20 °C for 5 min and centrifuged (17,000 × g, 30 s). The concentration of eluted DNA was measured using the BioDrop micro-volume measurement platform, by measuring the UV absorbance at 260 nm where nucleic acids (DNA and RNA) absorb maximally due to the resonance structure of the purine and

pyrimidine bases (Wilfinger WW 2006). According to the Beer-Lambert law (Beer 1852), the light absorption at 260 nm is proportional to the concentration of nucleic acid in solution.

DNA was purified and analysed by agarose gel electrophoresis. Agarose was dissolved in 200 ml 1× Tris-acetate-EDTA (TAE) buffer to make solutions of 0.8-2.0% and heated until the solution was clear. 10 µl of Midori Green Advanced DNA stain was added to the solution. The solution was cooled to 50-60 °C and poured into the gel tray with combs. When the gel solidified, DNA samples mixed with DNA loading dye (6X) were loaded into wells. Electrophoresis was performed at 115V for 45 min. DNA fragments were visualised under UV light.

For DNA extraction from agarose gel, the illustra GFX PCR DNA and gel band purification kit was used, according to the manufacturer's instructions. The principle of this kit is to dissolve the agarose gel containing DNA where chaotropic salts were present to denature proteins improve the binding of DNA to the silica matrix (Merck). DNA was then adsorbed to the solid phase of silica in a spin-column and purified by washing twice using ethanolic buffers. DNA was then eluted by dissolving in small amount of elution buffer or water for subsequent experiments.

The agarose gel slice containing the DNA was weighed together with a pre-weighed microcentrifuge tube. 10 µl capture buffer was added for each 10 mg of gel slice. The mixture was heated to 60 °C for 15-30 min until the agarose was completely dissolved. The mixture was then transferred to assembled spin-column and collection tube and incubated at 20 °C for 1 min, followed by centrifugation (16, 000 × g, 30 s). 500 µl wash buffer was added to the same column and centrifuged (16, 000 × g, 30 s). 50 µl elution buffer was added to the same column, incubated at 20 °C for one minute and centrifuged at (16, 000 × g, 1 min).

For PCR, Q5 Hot Start High-Fidelity DNA Polymerase was used, according to the manufacturer's instructions. All components were mixed and transferred to a pre-heated (98 °C) PCR machine (***Table 2.5-2.6***) (NEB).

Table 2.5 Composition of PCR reactions

Component	Volume	Final concentration
5X Q5 reaction buffer	10 µl	1X
10 mM dNTPs	1 µl	200 µM
10 µM forward primer	2.5 µl	0.5 µM
10 µM reverse primer	2.5 µl	0.5 µM
Template DNA	variable	up to 1000 ng
Q5 hot start High-Fidelity DNA polymerase	0.5 µl	0.02 U/µl

5X Q5 High GC enhancer (optional)	10 µl	(1X)
Nuclease-free water	up to 50 µl	

Table 2.6 Thermocycling conditions used for PCR reactions

Step	Temperature	Time
Initial denaturation	98°C	30s
25-35 cycles	98°C	10s
	68°C*	30s
	72°C	20-30s per kb
Final extension	72°C	2 min
Hold	4°C	∞

* NEB T_m calculator used to obtain the optimized melting temperature (NEB 2020).

2.2.7. Transformation of bacteria, plasmid amplification and purification

Alpha-select gold efficiency chemically competent cells were thawed on wet ice and 50 µl cells were mixed with DNA solution (250 ng, ≤5 µl). The mixture was incubated on ice for 30 min and placed in 42°C water bath for 30s without shaking. The mixture was re-placed on ice for 2 min and diluted to 1 ml by adding 950 µl LB medium. The mixture was shaken at 200 rpm for 60 min at 37 °C. 100 µl of the cell transformation mixture was plated on LB agar plates containing ampicillin (1:1000) and incubated overnight at 37 °C.

The QIAGEN plasmid maxi kit was used, according to the manufacturer's instructions. The principle of this kit is to lyse the bacterial cells using SDS, followed by adsorption of plasmid DNA on the solid phase of silica in a QIAGEN-tip. The impurities such as RNA, proteins and dyes in the sample were removed by washing twice before elution of plasmid DNA in a high-salt buffer. The plasmid DNA was then concentrated and desalted by isopropanol precipitation. The detailed compositions of buffers included in the kit can be found in the QIAGEN plasmid purification handbook which can be downloaded online (Qiagen).

A single colony was picked from the plate and incubated in a start culture of 2–5 ml LB medium containing ampicillin (1:1000) at 37 °C for 8 h with vigorous shaking (300 rpm). The start culture was diluted 1000 times and incubated for 12-16 h at 37 °C with vigorous shaking (300 rpm). The bacteria were harvested by centrifugation (6,000 × g, 4 °C, 15 min). The bacterial pellet was resuspended in 10 ml of buffer P1. 10 ml buffer P2 was then added and mixed by vigorously inverting 4-6 times. The mixture was then incubated at 20 °C for 5 min before addition of 10 ml buffer P3. The mixture was incubated on ice for 15 min and centrifuged twice (20, 000× g, 4 °C, 30 min and 15 min respectively).

The QIAGEN-tip was equilibrated by 10 ml buffer QBT, before applying the supernatant to it and flowing by gravity. The tip was washed twice by 30 ml buffer QC and DNA was eluted by 15 ml buffer QF. The DNA was precipitated by 10.5 ml isopropanol at 20°C and centrifuged (15,000 × g, 4 °C, 30 min). The DNA pellet was washed with 5 ml 70% ethanol and centrifuged (15,000 × g, 4 °C, 10 min). The pellet was air-dried for 10 min, before redissolving into a suitable volume of appropriate buffer (e.g., TE buffer, pH 8.0, or 10 mM Tris-Cl, pH 8.5).

2.2.8. Linearization of donor sequence

According to ***Figure 2.5***, two restriction sites, NheI and XbaI were inserted at the beginning and the end of the donor sequence, respectively. Since the donor sequence (2819 base pairs) has similar size to the rest of the plasmid (2341 base pairs), they might not separate clearly in gel electrophoresis.

Therefore, according to ***Figure 2.5***, the circular plasmid including the STIM1-EGFP donor sequence was digested using three restriction enzymes, *Nhe*I, *Xba*I and *Pvu*I at their respective restriction sites.

300 µg of plasmid donor DNA was mixed with 15 µl of each restriction enzyme, 60 µl of 10X FastDigest buffer and autoclaved water was added to make 600 µl of reaction solution. The reaction solution was incubated at 37 °C for 6 h to maximise the digesting efficiency and avoid star activity, which typically leads to cleavage at non-canonical restriction sites, or even loss of enzymes' specificity completely (Hsu and Berg 1978; Gardner *et al.* 1982; Robinson and Sligar 1993). The resulting reaction mixture was loaded onto an agarose gel and electrophoresis was performed (***Section 2.2.6***). There were three distinctive bands at 2819 bp, 1436 bp and 905 bp, respectively. The band with size of 2819 bp was extracted from the agarose gel (***Section 2.2.6***), which resulted in linear donor sequence.

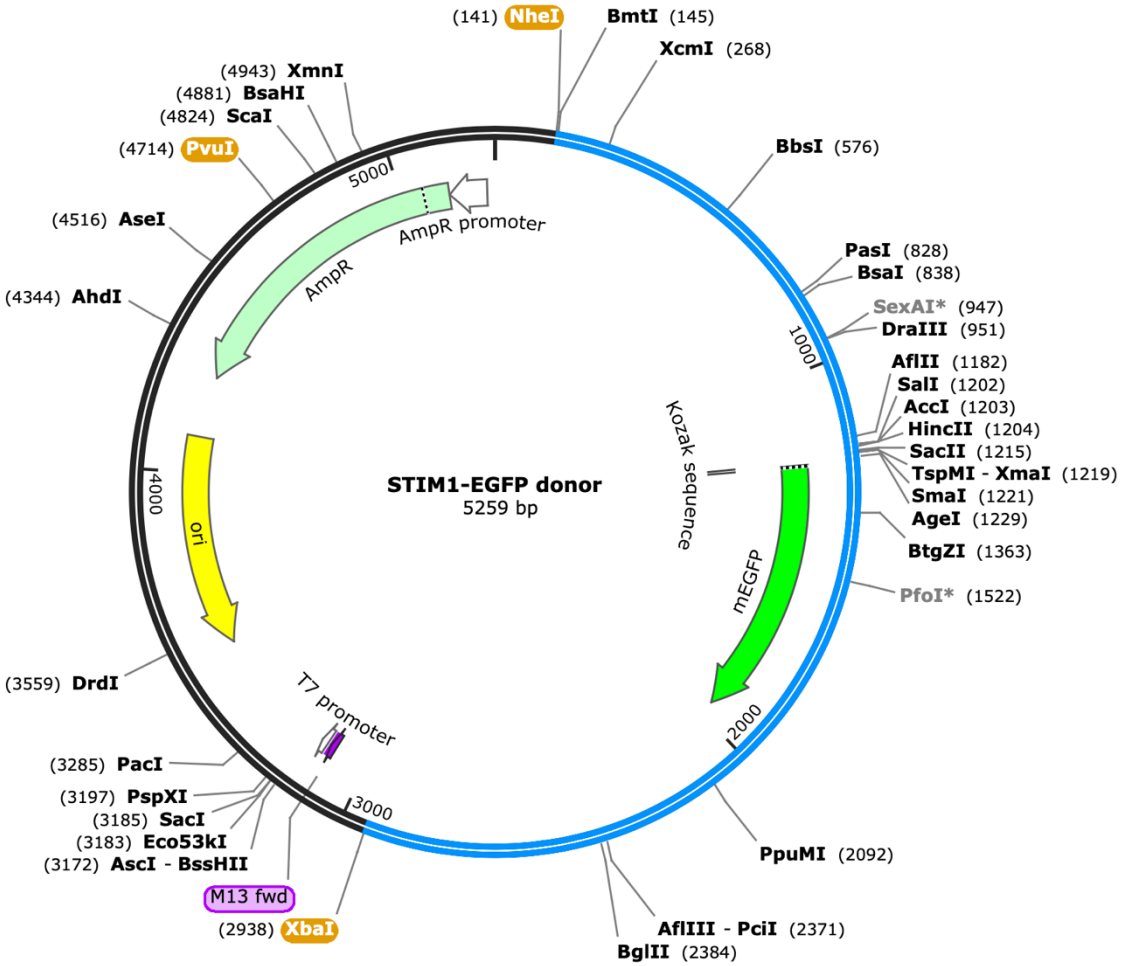

Figure 2.5 The plasmid map for the synthetic donor sequence. The synthetic gene of STIM1-EGFP donor sequence as designed in ***Section 2.2.3*** was inserted into pMA-RQ backbone (ampicillin resistance, AmpR). The sequence in blue indicates the donor sequence encoding STIM1-EGFP. The restriction sites used to linearize the donor sequence are highlighted in brown.

2.2.9. Measurement of $[Ca^{2+}]_c$ in cell populations

WT and STIM1-EGFP HeLa cells were plated in clear-bottomed 96-well plates (Greiner Bio-One) coated with fibronectin (10 μg/ml). Cells were washed with HBS, loaded with Fluo-8 by incubation in HBS with 2 μM of Fluo-8 AM for 60 min at 20°C. The cells were then incubated in HBS for 30 min at 20°C to allow de-esterification of Fluo-8 AM prior to experiments. The Fluo-8 fluorescence was measured using a FlexStation 3 microplate reader. After addition of BAPTA (final concentration = 2.5 mM), drugs (thapsigargin, cyclopiazonic acid or histamine) were added at various concentrations. After incubation for various periods, $CaCl_2$ (final concentration = 10 mM) or ionomycin (final concentration = 5 μM) was added. Fluorescence was collected using SoftMax Pro, Molecular Devices. The results were calibrated to cytosolic free Ca^{2+} concentration using the following equation:

$$\frac{389 \times (F - F_{min})}{(F_{max} - F)}\ nM$$

Where 389 is the dissociation constant (K_d) which defines the affinity of Fluo-8 for Ca^{2+}, F is the measured fluorescence intensity, F_{min} is the fluorescence intensity in the absence of Ca^{2+} and F_{max} is the fluorescence intensity of the Ca^{2+}-saturated dye.

F_{min} is measured by adding BAPTA (final concentration = 2.5 mM) and Triton X-100 (0.1%) while F_{max} is measured by adding $CaCl_2$ (final concentration = 10 mM) and Triton X-100 (0.1%) to cells.

2.2.10. Co-immunoprecipitation

STIM1-EGFP HeLa cells were used for immunoprecipitation (IP) analyses 24 hr after transfection with mCh-Orai1 (19 μg plasmid DNA/T75 flask). RFP-Trap was used to capture the mCherry tag. Cells in a T75 flask were washed twice with PBS, treated with thapsigargin (1 μM, 15 min in Ca^{2+}-free HBS), centrifuged (650 ×g, 2 min), and supernatants from cell lysates (1-2 ml) were then prepared as described for WB samples. Samples (~400 μl, ~1 mg protein) were incubated with washed RFP-Trap agarose beads (150 μl bead slurry) for 1 hr at 4 °C with gentle rotation. The beads were recovered magnetically, washed (3-5 × 500 μl) with TBST containing protease inhibitor cocktail, and the beads were then heated (95 °C, 10 min) in LDS sample buffer (80 μl) before analysis by WB.

2.2.11. Fluorescence-activated cell sorting (FACS)

For the generation of STIM1-EGFP HeLa cells by Dr. Sumita Chakraborty, WT HeLa cells transfected with cas9, gRNA and donor vectors (***Section 2.2.4***) were harvested using TrypLE Express enzyme. After centrifugation (650 × g, 2 min), the cell pellet was resuspended in 1 ml of sorting buffer (***Table 2.3***) and collected with a syringe. A filter cartridge was attached to the syringe and the single cells in the cell suspension were filtered to a falcon tube.

The cells were sorted using a SONY SH800S Cell Sorter (488-nm excitation) (***Figure 2.6A***). When all cells enter the sorting system, they were first selected based on their viability, using forward scatter-area (FSC-A) and backward scatter-area (BSC-A). These two measurements are indicators of cell size and granularity, respectively, and only those living cells enter the next sorting stage (Allman *et al*. 1990) (***Figure 2.6B***). The living cells are further sorted based on whether they are single cells, using parameters of FSC-height (H) and FSC-width (W). Only single living cells can proceed to the next sorting gate (***Figure 2.6C***). These cells are finally sorted by their fluorescence intensities (***Figure 2.6D***). The cells with 10× brighter EGFP fluorescence (~0.1%) than negative control were collected as a polyclonal population in a 15-ml tube (containing 5 ml DMEM-F12 Glutamax™ with 20% FBS, 100 μg/ml penicillin, 100 μg/ml streptomycin, and 0.25 μg/ml amphotericin B).

Polyclonal cells were cultured for two passages before being sorted into single cells into 96-well plates to generate multiple monoclonal cell lines. Each monoclonal cell line was cultured until enough for western blotting (***Section 2.2.5***) which was used to select the desired cell line.

For the generation of doubly edited STIM1-EGFP HeLa cells, same protocols were used as Dr. Sumita Chakraborty, except in the selection stage, where only monoclonal cell lines with solely STIM1-EGFP proteins were looked for.

2.2.12. Quantification and statistical analysis

Analyses were performed without blinding or power calculations to predetermine sample sizes. Sample sizes and statistics are indicated in figure legends. Student's t-test was used for comparisons between 2 sample groups, or ANOVA and *post hoc* tests (details in figure legends) for multiple comparisons; $P < 0.05$ was considered significant.

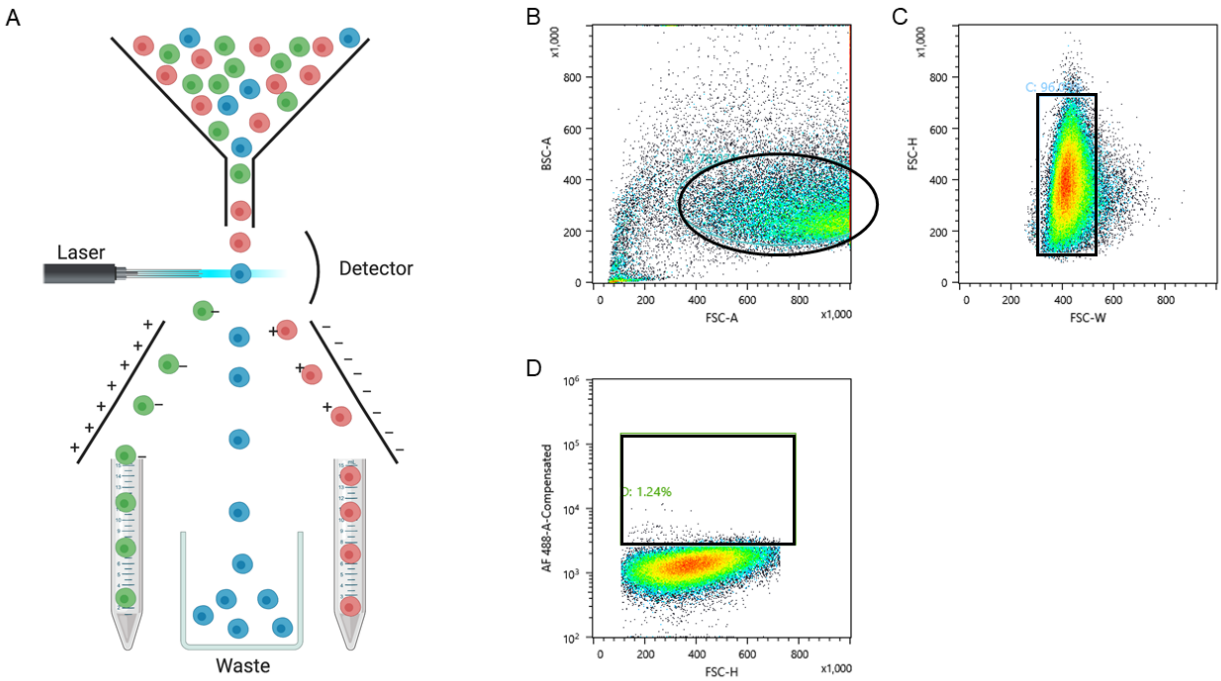

Figure 2.6 FACS sorting. A. The cell suspension flows through a narrow filter chip in a rapidly flowing stream of liquid. The cells are arranged into droplets that only contain a single cell. Each droplet passes a beam of laser which measures their fluorescent intensity. The droplets with chosen fluorescent intensity go through an electrical charging ring and gain charge. The charged droplets then fall through an electrostatic deflection system and diverted into different containers. **B-D.** An example of FACS sorting of STIM1-EGFP HeLa cells. **B.** All cells entered the sorting system and were sorted based on cell viability (FSC-A and BSC-A), where only those in the black circle were selected to enter the next gating. **C.** Cells were further selected based on singlets (FSC-W and FSC-H), where only those in the black square were allowed to proceed to the next stage. **D.** Cells were finally selected based on fluorescence intensity (488 nm), and only those in the black square were collected either as a polyclonal cell population or as single cells to develop monoclonal cell lines later.

2.3. Results

2.3.1. STIM1-EGFP HeLa cells have one allele of *STIM1* tagged with sequence encoding monomeric EGFP

It has been confirmed the STIM1 gene is located on chromosome 11, p15.4 (Rebhan *et al.* 1997), and the karyotyping of WT HeLa cells (Thillaiappan *et al.* 2017) confirmed that HeLa cells have 2 copies of chromosome 11 (***Figure 2.7***). Therefore, there should be two copies of the *STIM1* gene in HeLa cells.

Figure 2.7 The karyogram of chromosome 11 in WT HeLa cells. There are two copies of chromosome 11 in HeLa cells.

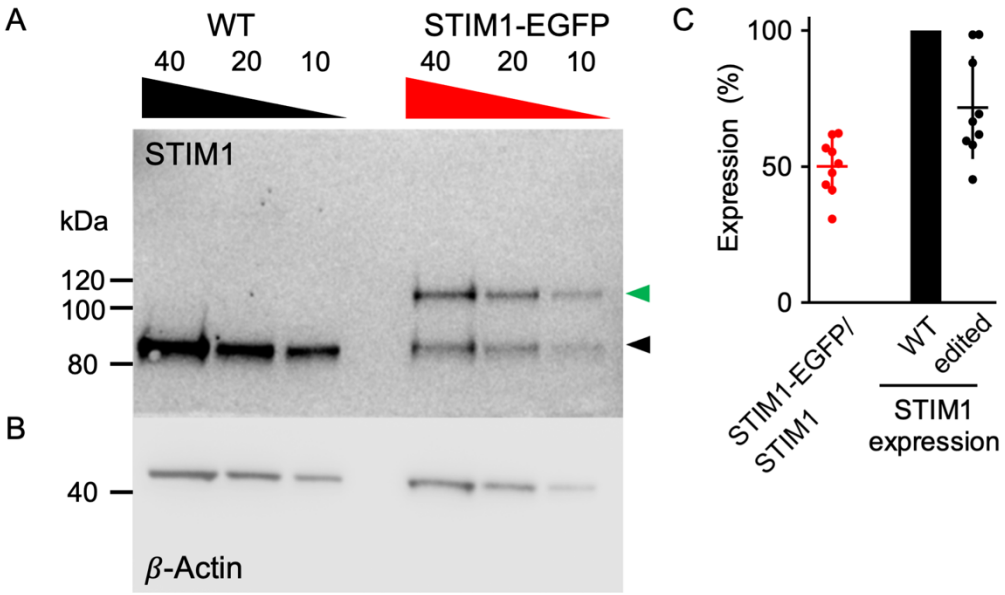

Figure 2.8 Half of STIM1 protein has been tagged with EGFP in STIM1-EGFP HeLa cells. Western blots of WT and STIM1-EGFP HeLa cells using anti-STIM1 and anti-β-actin antibodies. Loadings are shown as μg. **A.** The lower bands (black arrow) indicate the presence of untagged STIM1 protein (expected size = 77 kDa), while the upper bands (green arrow) indicate the presence of EGFP-tagged STIM1 protein (expected size = 110 kDa). **B.** The bands indicate the presence of β-actin, which act as loading controls. Results are representative of 8 independent experiments. **C.** Summary results (mean ± SD, n = 8) show the expression of STIM1-EGFP relative to all STIM1 in the STIM1-EGFP HeLa cells, and the expression of STIM1 in the edited cell line relative to WT cells.

WB analysis using a STIM1 antibody identified a band (~85 kDa) in both WT and STIM1-EGFP HeLa cells (***Figure 2.8A***). The band migrated slightly higher than expected (77 kDa) due to glycosylation (Williams *et al.* 2002). A second band of 110 kDa, corresponding to STIM1-EGFP, was present in the extracts from STIM1-EGFP HeLa cells. As expected, a GFP antibody detected a band at ~110 kDa in WB of STIM1-EGFP HeLa cells, but not in WT cells (***Figure 2.9A***). Quantification of the band intensities in the STIM1 WB established that in STIM1-EGFP HeLa cells, 52 ± 8% of all STIM1 was present as STIM1-EGFP (***Figure 2.8C***). The overall expression of STIM1 proteins in STIM1-EGFP HeLa cells was 73 ± 18% of the amount expressed in WT cells. In-gel fluorescence confirmed that the only fluorescent band present in STIM1-EGFP HeLa cells was at 110 kDa (***Figure 2.9B***). These results establish that the only EGFP-tagged protein expressed in STIM1-EGFP HeLa cells is STIM1-EGFP and they show that 50% of STIM1 is tagged.

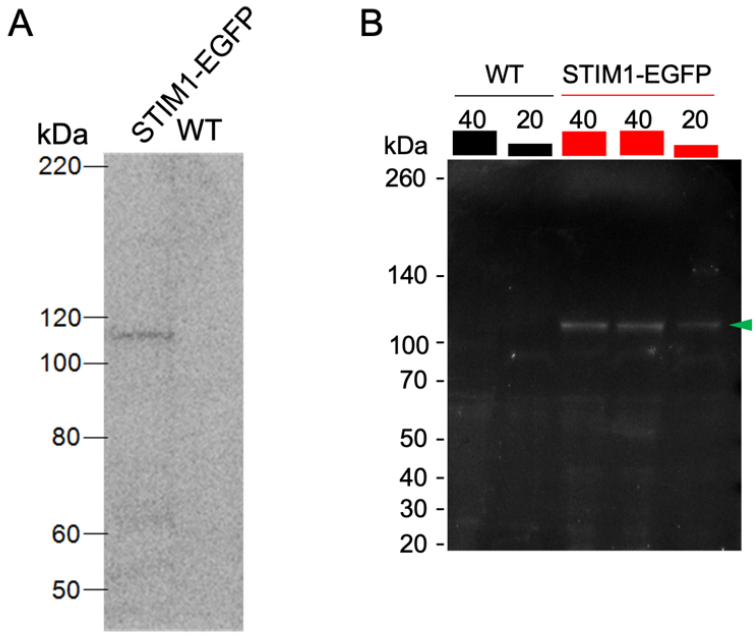

Figure 2.9 STIM1 is the only EGFP-tagged protein expressed in STIM1-EGFP HeLa cells. A. Western blot of WT and STIM1-EGFP HeLa cells using anti-GFP antibody. 40µg of each lysate supernatant was loaded. The band indicates the presence of EGFP-tagged STIM1 proteins (expected size = 110 kDa). Results are representative of 4 independent experiments. **B.** In-gel fluorescence of WT and STIM1-EGFP HeLa cells. Loadings are shown as µg. The bands (green arrow) indicate the presence of EGFP-tagged STIM1 proteins (expected size = 110 kDa).

2.3.2. Successful insertion of EGFP sequence into the *STIM1* gene

PCR and sequencing was used to verify the correct position where EGFP has been tagged to the endogenous STIM1 protein. The region in the genomic DNA in both WT and STIM1-EGFP HeLa cells between primers 1F and 1R (***Table 2.4***), which correspond to sequences within the intronic region outside the donor sequence and within EGFP, were amplified (***Figure 2.10A***). Genomic DNA of STIM1-EGFP HeLa cells showed a clear band at around 1.2 kb (***Figure 2.10C***), which corresponds to the amplified region, while WT HeLa cells did

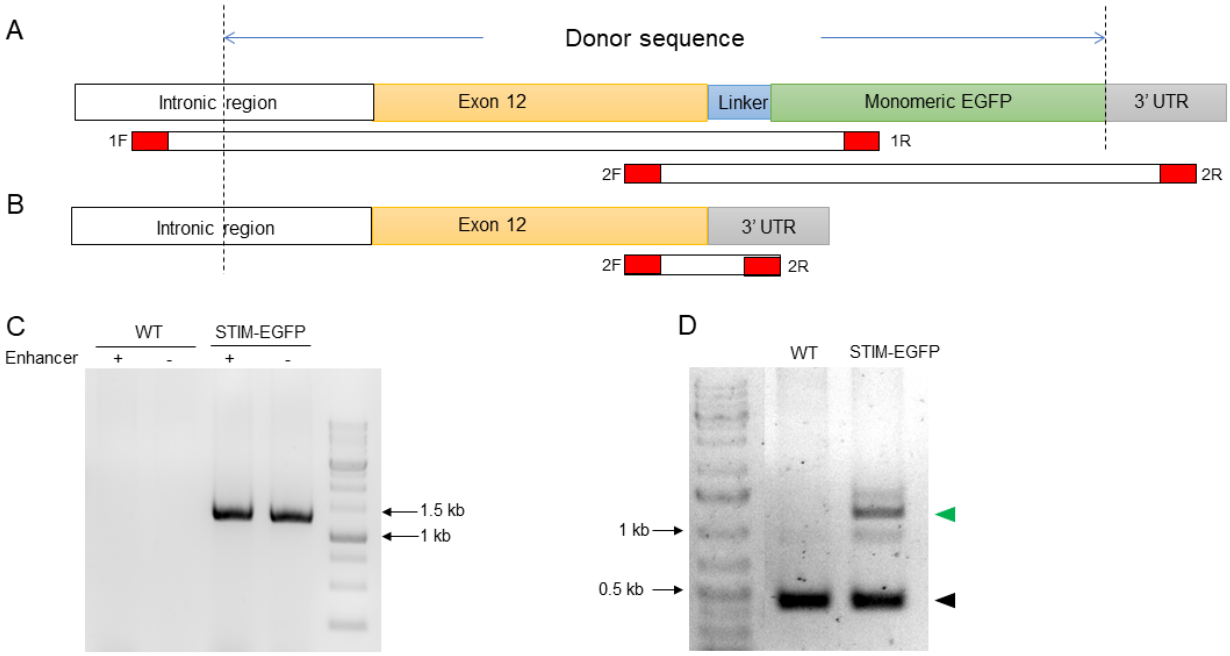

Figure 2.10 PCR analyses of genomic DNA confirms appropriate location of EGFP sequence in STIM1-EGFP HeLa cells. A-B. Schematics of the PCR analyses of genomic DNA of *STIM1* with and without EGFP sequence, respectively. The region between primers 1F and 1R covers intronic region outside the donor sequence until the EGFP. The region between primers 2F and 2R starts from exon 12 and extends to 3'UTR. **C.** Genomic DNA from WT and STIM1-EGFP HeLa cells was extracted and amplified by PCR, using primers 1F and 1R (***Table 2.4***). The expected band size of the amplified region was 1244 bp. The enhancer was used to possibly help the amplification for GC-rich contents. $n = 4$. **D.** Primers 2F and 2R were used to amplify the same genomic DNA extractions. The lower bands (black arrow) indicate the presence of native *STIM1* (expected size = 361 kb), while the upper band (green arrow) indicates the presence of EGFP-tagged *STIM1* sequence (expected size = 1102 kb). $n = 3$.

not show the corresponding band, as expected. The sequencing result confirmed the precise sequence of EGFP, and that the linker is complete.

According to Western blots, only half of STIM1 proteins have been tagged with EGFP (***Figure 2.8***). I would like to further confirm whether *EGFP* was inserted into one of the chromosomes, leaving the other allele native. Similar analyses of genomic DNA using primers 2F and 2R (***Figure 2.10A and B***). A single band (~0.35 kb, black arrow) corresponding to native STIM1 was detected in WT cells. The same band and an additional band (~1 kb, green arrow, corresponding to STIM1 with EGFP attached) were detected in the STIM1-EGFP HeLa cell line (***Figure 2.10D***). Sequencing of the native band from the edited cell line confirmed that it was identical to that from WT cells.

2.3.3. EGFP tagging does not affect the interaction between STIM1/STIM1-EGFP and Orai1

Since the EGFP tag was attached to the C-terminus of STIM1 molecules, there may be questions on whether this affects the interactions between STIM1 and Orai1, as well as whether there are equal possibilities for the native and EGFP-tagged STIM1 to interact with Orai1. In order to validate these, STIM1 was co-immunoprecipitated with Orai1 (using mCherry-Orai1) after store depletion. The use of mCh-Orai1 instead of native Orai1 was because no record was found to successfully pull down native Orai1 due to low endogenous expression level and relatively weak interaction between STIM1 and Orai1, therefore will be easily washed out. These co-immunoprecipitation experiments proved to be challenging, with variability between experiments which is reflected in the SD. The observation is that the ratio of native STIM1 to STIM1-EGFP in cell lysates is preserved in the immunoprecipitate (50:50, ***Figure 2.11A and C***). The similar experiment was also done with WT-HeLa cells, which confirmed that the upper band reports STIM1-EGFP (***Figure 2.11B***). Although the STIM1-EGFP to all-STIM1 ratio (~50%) was indistinguishable in control and cells expressing mCh-Orai1, the efficiency of the pull-down of STIM1 was much greater in cells expressing mCh-Orai1 (***Figure 2.11D***). This indicates an indistinguishable interaction between STIM1/STIM1-EGFP and Orai1.

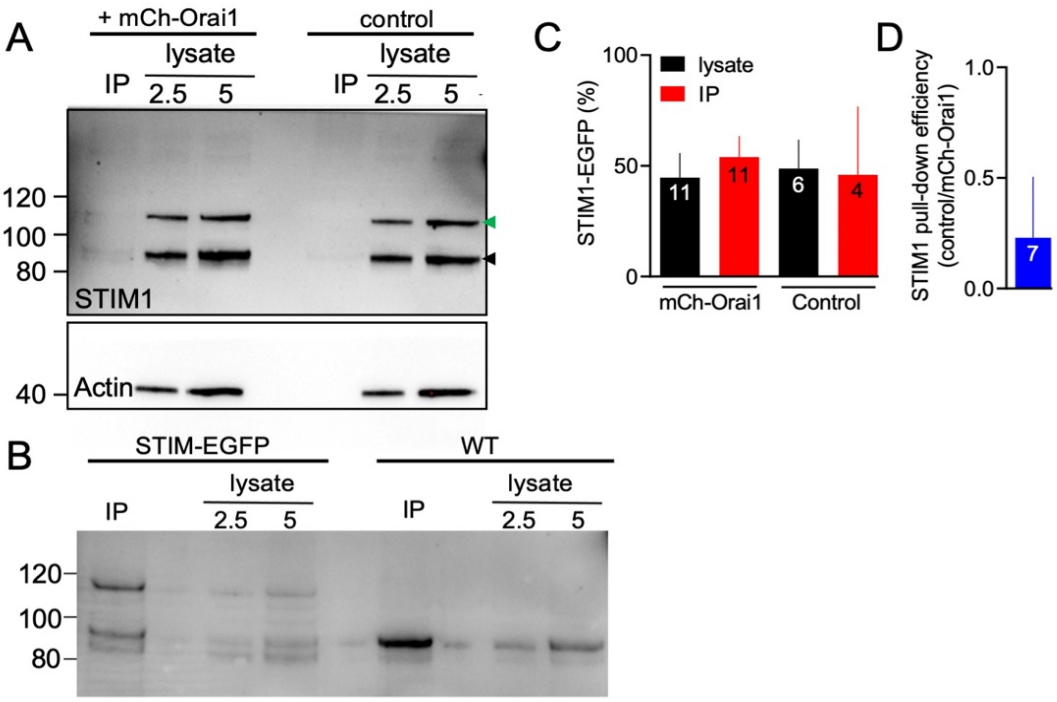

Figure 2.11 Co-immunoprecipitation of STIM1 and mCh-Orai1. A. Typical WB for STIM1 (actin in lower panel) shows immunoreactivity in cell lysates (2.5 and 5 µg protein) and after immunoprecipitation (IP) of mCh-Orai1 with RFP-Trap from STIM1-EGFP HeLa cells with or without (control) expression of mCh-Orai1. Cells were treated with TG (1 µM, 15 min in Ca^{2+}-free HBS) before IP. Molecular markers (kDa) are shown on the left. The green arrow indicates STIM1-EGFP while the black arrow indicates native STIM1. For cells expressing mCh-Orai1, recoveries (IP/lysate) were 27 ± 18 % (mCh-Orai1, mean ± SD, n = 8) and 3.6 ± 5.8 % (STIM1, n = 11). **B.** Similar IP analysis comparing WT and STIM1-EGFP HeLa cells expressing mCh-Orai1. **C.** Summary shows amount of STIM1-EGFP relative to all STIM1 (%) in lysates and IP for cells with and without mCh-Orai1. Mean ± SD for indicated n (values for IP in control cells report only those with detectable STIM1; 4 from 6 blots). **D.** Results show the relative pull-down efficiencies of STIM1 (control/mCh-Orai1 cells) in paired analyses. Mean ± SD, n = 7.

2.3.4. STIM1-EGFP HeLa and WT cells have similar SOCE

The C-terminal tags to STIM1 have been commonly used in studies utilizing overexpressed STIM1 (Calloway *et al.* 2009; Lur *et al.* 2009; Korzeniowski *et al.* 2016), but because of the importance of the C-terminus of STIM1 (Ercan *et al.* 2009; Park *et al.* 2009; Stathopulos *et al.* 2013), it was essential to establish whether Ca^{2+} signalling and STIM1-Orai1 interaction were perturbed in STIM1-EGFP HeLa cells.

Histamine, an agonist for G_q-coupled histamine H_1 receptor, evokes Ca^{2+} signals via the IP_3 pathway in HeLa cells (Hill *et al.* 1997; Jones and Kearns 2011). ***Figure 2.12A*** indicates that histamine-evoked Ca^{2+} release from the ER is similar in STIM1-EGFP and WT HeLa cells.

Cellular responses towards CPA, a reversible inhibitor of the sarco/endoplasmic reticulum Ca^{2+}-ATPase (SERCA), were examined to see if EGFP tagging caused changes in SOCE upon partial store depletion. It is possible that upon maximal store depletion, there will be no difference in responses observed in the two cell lines if a small portion of STIM1 proteins is enough to evoke SOCE. The untagged STIM proteins in gene-edited cells were sufficient to cause effective SOCE. Comparing SOCE upon graded store depletion circumvented the problem and small differences in protein behaviours could be observed.

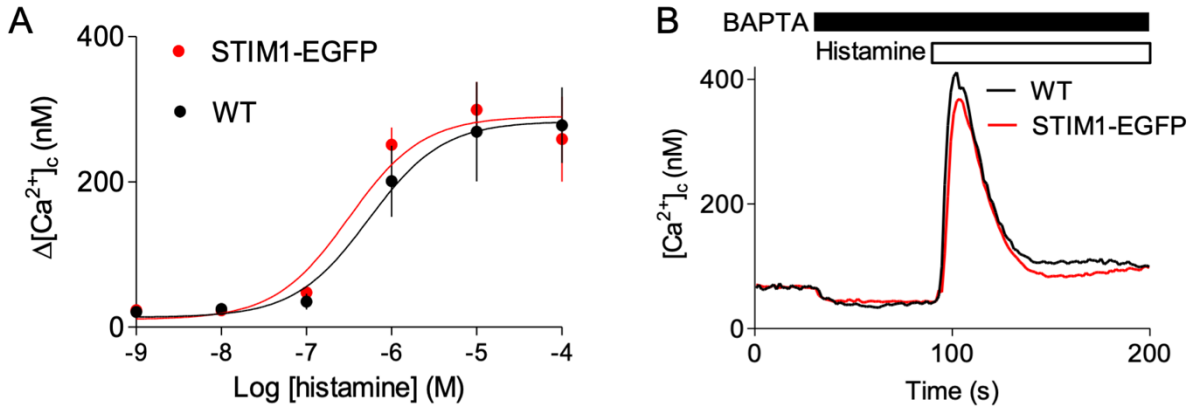

Figure 2.12 Similar effect of histamine on Ca^{2+} release. A. Dose-response curve for histamine in Ca^{2+}-free HBS on the peak increase in $[Ca^{2+}]_c$ ($\Delta[Ca^{2+}]_c$) in populations of WT and STIM1-EGFP HeLa cells. Student's *t*-test shows no statistical significance ($P > 0.05$). Results show mean ± SEM from 4 experiments, each with 6 determinations. **B.** A typical trace of histamine evoked Ca^{2+} release of populations of WT or STIM1-EGFP HeLa cells in HBS. BAPTA (2.5 mM) was added 30s after start to chelate extracellular Ca^{2+} ions and histamine (100 μM) was added at 90s. Results show means of 6 replicates from one experiment.

Ionomycin can release Ca^{2+} from ER into the cytosol. Hence, in my experiments, it was used as an indicator of the amount of Ca^{2+} remaining in the ER after store depletion.

Results from ***Figure 2.13*** suggested that 5 min is sufficient for partially depleting the ER Ca^{2+} store, as dose-dependent CPA response could be observed. There is almost no depletion of the ER Ca^{2+} store at [CPA] = 0.1 μM, hence the dotted traces in ***Figure 2.13A*** representing [CPA] = 0.1 μM could be regarded as a negative control indicating the response to ionomycin without previous partial store depletion. At [CPA] = 10 μM, large store depletion took place, and a much smaller peak was observed after adding ionomycin. Hence when 1 μM of CPA is used, the peak is half the height, indicating partial Ca^{2+} store depletion.

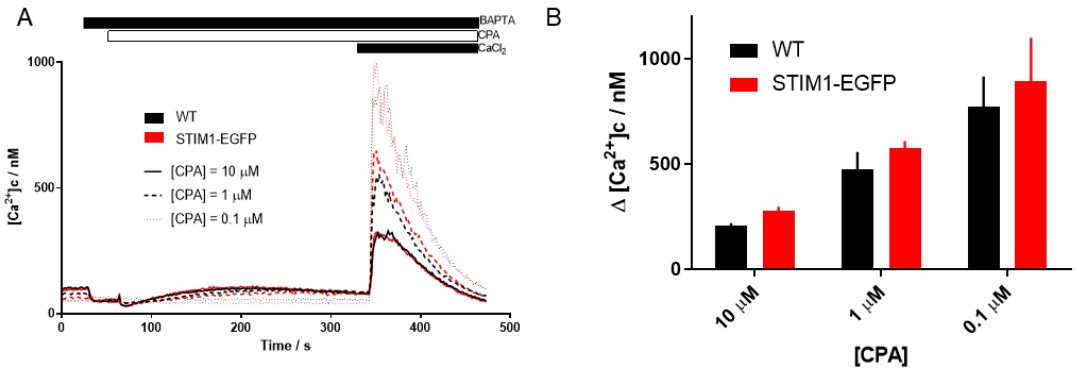

Figure 2.13 5 min is sufficient for partial depletion of the ER Ca^{2+} store. A. A typical trace of ionomycin-induced Ca^{2+} release. BAPTA (2.5 mM) was added 30s after start, followed by CPA at various concentrations at 64 second. The cells were left for recording response for 5 min before the addition of ionomycin (5 μM). Results show means of 6 replicates from one experiment, representative of 3 experiments. **B.** Summary results (mean ± SEM from 3 experiments, each with 6 determinations) of the amplitudes of ionomycin-evoked Ca^{2+} release, which were determined by the difference between the value before and after the addition of ionomycin. Two-way ANOVA test was performed the difference between rows (concentrations) has $^{****}P<0.0001$.

A standard dose-response curve for cyclopiazonic acid (CPA) was first generated for the two cell lines (***Figure 2.14A***). The traces indicate that the responses for CPA-induced store depletion were similar for both cell lines. Hence the same concentration of CPA could be used in both cell lines to induce store depletion to a similar extent.

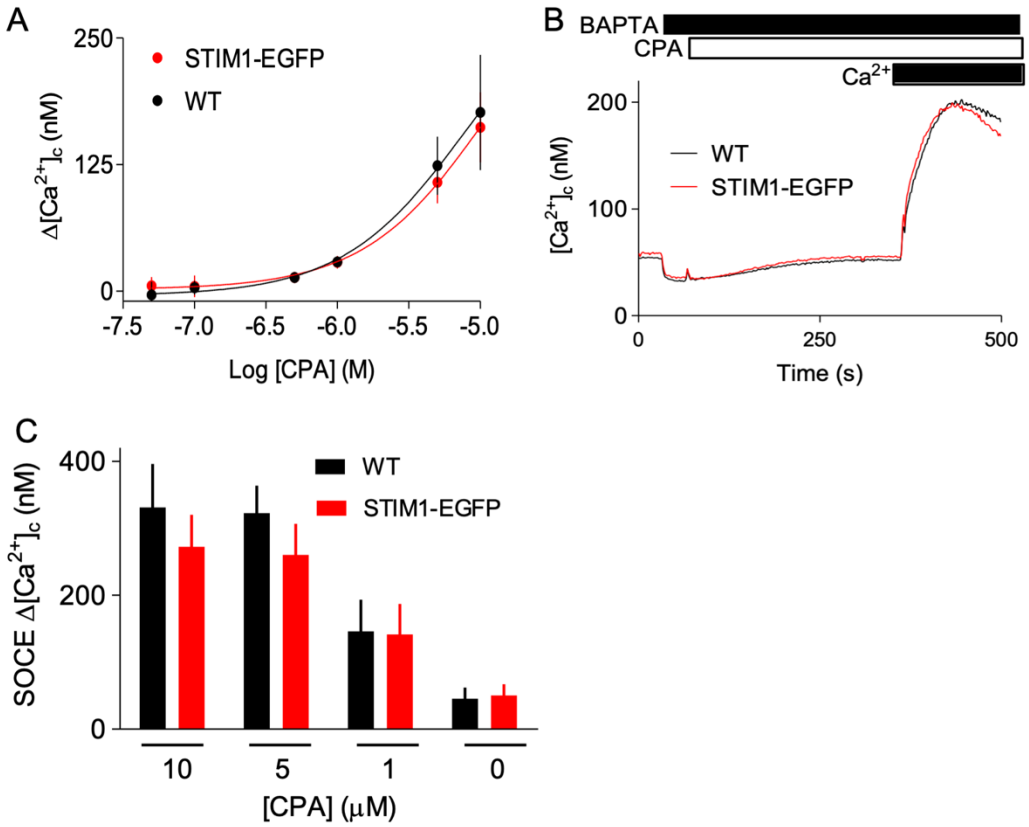

Figure 2.14 CPA-mediated ER Ca^{2+} store depletion followed by SOCE. A. Dose-response curve for CPA in Ca^{2+}-free HBS on the peak increase in $[Ca^{2+}]_c$ ($\Delta[Ca^{2+}]_c$) in populations of WT and STIM1-EGFP HeLa cells. Student's *t*-test shows no statistical significance ($P > 0.05$) at all concentrations. Results show mean ± SEM from 4 experiments, each with 6 determinations. **B.** A typical trace of CPA-mediated ER Ca^{2+} release followed by SOCE of populations of WT or STIM1-EGFP HeLa cells in HBS. BAPTA (2.5 mM) was added 30s after start to chelate extracellular Ca^{2+} ions and CPA (1 μM) was added at 64s. SOCE was stimulated after 5 min by restoration of extracellular Ca^{2+} (final free $[Ca^{2+}]$ ~10 mM). Results show means of 6 replicates from one experiment. **C.** Summary results (mean ± SEM from 4 experiments, each with 6 determinations) of the amplitude of SOCE. Student's *t*-test shows no statistical significance ($P > 0.05$) between WT and STIM1-EGFP HeLa cells at all concentrations.

The amplitudes of SOCE of STIM1-EGFP HeLa cells were also compared with those of WT-HeLa cells. From the traces (***Figure 2.14B***), both the amplitude of CPA-mediated ER Ca^{2+} store release and the levels of SOCE are similar for both WT and STIM1-EGFP HeLa cells. The amplitude of SOCE was determined by the difference between the value before addition of $CaCl_2$ and the peak after it, which is summarized in ***Figure 2.14C***. There is no significant difference between WT and STIM1-EGFP HeLa cells.

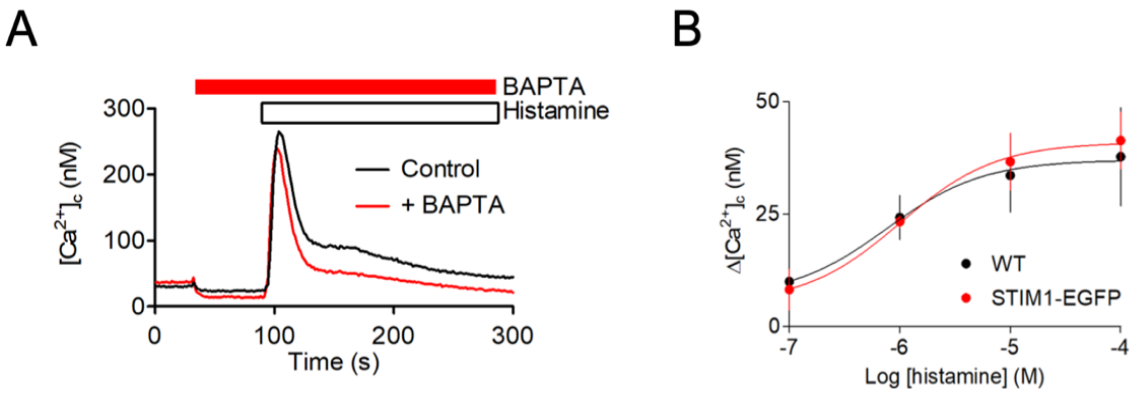

Figure 2.15 Histamine-evoked SOCE in WT and STIM1-EGFP HeLa cells. A. Populations of WT HeLa cells were treated by BAPTA (final concentration = 2.5 mM) or HBS 30s after start, followed by histamine (final concentration = 100 μM) at 64 second. The cells were left for recording until 300s. Results show mean ± SEM from 6 determinations from one experiment. The difference between the sustained Ca^{2+} signals reflects the amplitude of SOCE. **B.** Summary results of amplitude of histamine evoked SOCE. Results show mean ± SEM from 5 experiments, each with 6 determinations. Two-way ANOVA test shows no statistical significance ($P > 0.05$).

Apart from stimulating SOCE pharmacologically using CPA, it is also worth looking at physiologically evoked SOCE by releasing Ca^{2+} via histamine-evoked pathway (***Figure 2.15A***). After the Ca^{2+} release evoked by histamine, the $[Ca^{2+}]_c$ come back to a plateau, with cells in HBS resting at a higher level compared to cells in BAPTA, and this difference probably corresponds to the contribution from SOCE. The DRC of physiologically evoked SOCE shows no significant difference between WT and STIM1-EGFP HeLa cell lines (***Figure 2.15B***), despite a much smaller response compared to CPA-evoked SOCE.

2.3.5. Attempts to generate a homozygous cell line with both alleles of the *STIM1* gene tagged by EGFP

Because of the problems of heterozygous STIM1-EGFP HeLa cells can cause, it is desirable to have both alleles of STIM1 tagged by EGFP. Therefore, I have attempted to generate a cell line with both STIM1 proteins tagged by EGFP (***Section 2.2.4 and 2.2.11***).

In the first round of sorting (***Figure 2.16A-C***), to obtain a threshold for separating edited and non-edited cells, WT-HeLa cells and the currently available heterozygous STIM1-EGFP HeLa cells were recorded. The difference between median fluorescent intensities of cells from the two lines represents the change in emission at λ = 488 nm as a result of single-allele EGFP tagging. Assuming a linear relationship between fluorescence emission and the number of

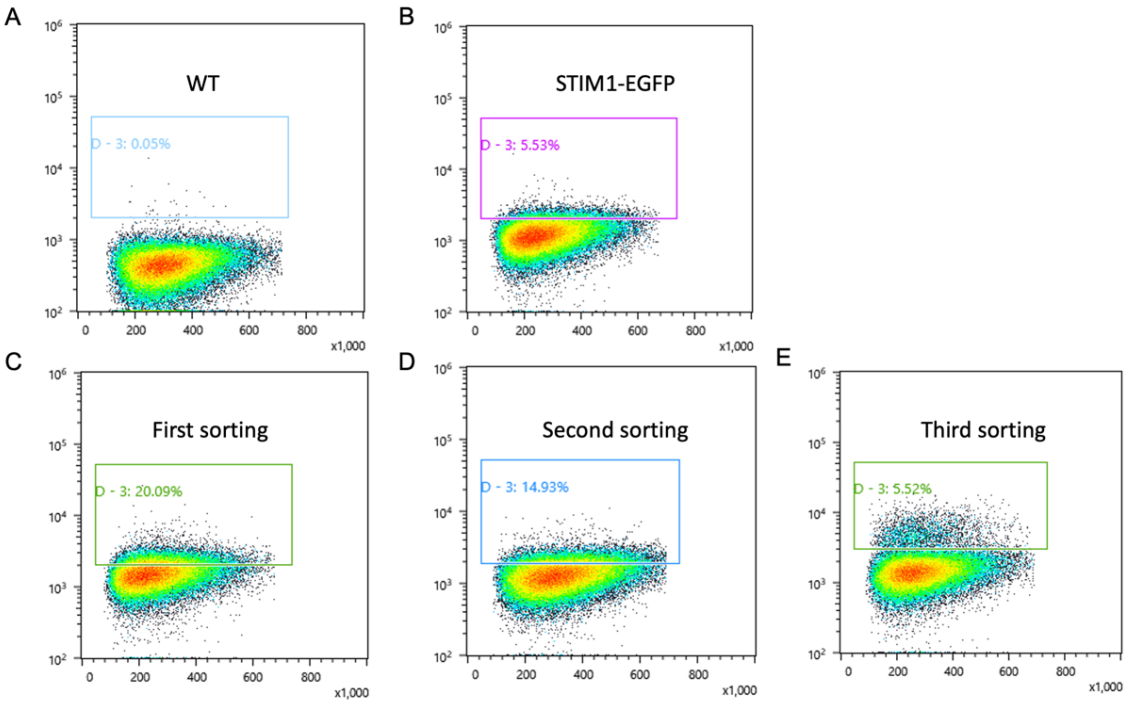

Figure 2.16 FACS sorting of WT HeLa cells transfected with cas9, gRNA and donor vectors. FACS analyses of cell populations at excitation λ = 488 nm, with fluorescence intensity against forward scatter (an estimation of cell's size (Allman *et al.* 1990)) for **A.** WT-HeLa cells. **B.** Current STIM1-EGFP HeLa cells. **C-E.** Transfected WT HeLa cells, three subsequent sorting, respectively. The same gating applies to all sorting, except for ***panel E***, where only the extra population compared to the main population was selected. In the second and third sorting, the fluorescence intensities of WT and STIM1-EGFP HeLa cells were similar to the first-round sorting, hence are not shown here.

alleles of EGFP tagged, tagging of a second allele should see an increase in median intensity from the that of STIM1-EGFP by the median difference. Therefore the lowest bound of the gate was chosen as such.

A second round of sorting was carried out after the polyclonal cell line from the first round has grown to confluency. However, results (***Figure 2.16D***) reveal that the average fluorescence intensity of the transfected cells was not significantly different from the heterozygous STIM1-EGFP HeLa cell line which serves as a negative control. The proportion of cell population in the selected region was even lower than that of the first round of sorting. Despite this unexpected lowering of popupation with high fluorescence intensity, a distinct population of cells appeared after enrichment in the third sorting (***Figure 2.16E***). This population of cells was sorted into monoclonal cells, but not all of them grew enough to perform WB before the national lockdown due to COVID-19.

Several monoclonal cell lines were characterized and two of them were delightfully found doubly-edited (clone 1 and 2), with the lower band which represents native STIM1 disappeared (***Figure 2.17A***). Clone 2 was soon contaminated unfortunately, but I managed to perform further WB on clone 1. Not knowing exactly why, native STIM1 reappeared in this cell line, which shattered the hope of this cell line being doubly edited (***Figure 2.17B***).

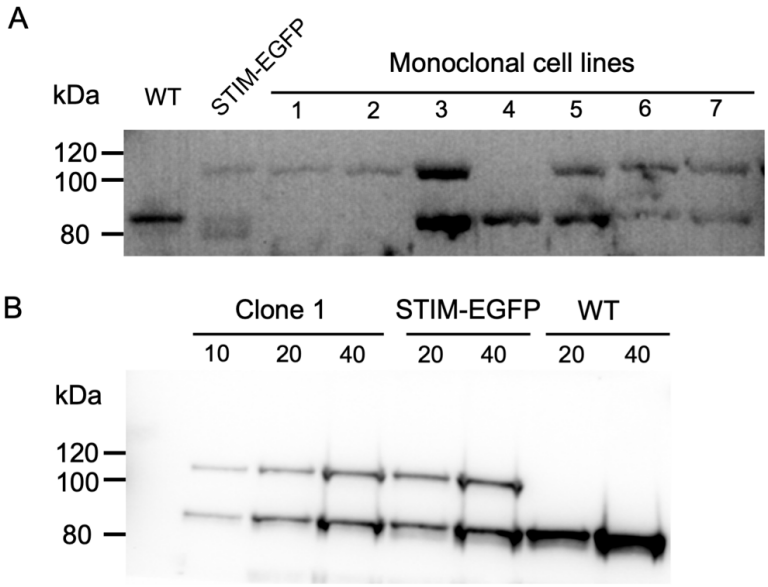

Figure 2.17 Characterization of monoclonal cell lines after FACS. A. A western blot of monoclonal cell lines after FACS, using anti-STIM1 antibody. The concentrations of proteins in each lane were not unified. $n = 1$. **B.** A western blot of WT, STIM1-EGFP HeLa cells and clone 1 from **A**, using anti-STIM1 antibody. Loadings are shown as μg. $n = 3$.

2.4. Discussion

Over-expression of STIM1 was reported to perturb both its interaction with Orai1 (Ji *et al.* 2008; Gwozdz *et al.* 2012; Kilch *et al.* 2013; Hodeify *et al.* 2015; Yen and Lewis 2019), and the structures of the ER and MCS where SOCE occurs (Orci *et al.* 2009; Saitoh *et al.* 2011; Perni *et al.* 2015). The evolution of gene-editing techniques allow direct modifications on genomic DNA, which has huge potential in advancing the studies in biology. Therefore, in this study, a monoclonal HeLa cell line expressing endogenous STIM1 tagged with EGFP, previously generated in the lab using CRISPR/Cas9 was characterized, where the EGFP tag attached to the C-terminus of STIM1 protein to allow visualization of endogenous STIM1 in live cells. Since the C-terminus of STIM1 is crucial to its function, mediating STIM1 aggregation (Li *et al.* 2007; He *et al.* 2012), trapping PIP_2 in the PM (Ercan *et al.* 2009; Park *et al.* 2009) and interacting with Orai1 (Park *et al.* 2009; Yuan *et al.* 2009; Stathopulos *et al.* 2013), the addition of a bulky fluorescent tag to the end of the C-terminus of STIM1 requires extensive characterization to ensure that the STIM1-EGFP HeLa cell line is functional just as WT HeLa cells, before being used to define the number of STIM1 molecules within the puncta that regulate Orai1.

The genomic DNA experiments have revealed that EGFP is successfully inserted into one allele of the genome at the correct position, leaving the other allele not edited (***Figure 2.10***), suggesting successful insertion of EGFP into one of the *STIM1* gene out of two. It has also been confirmed by western blots, that one allele of STIM1 proteins is tagged by EGFP while the other allele is not (***Figure 2.8***). The collective results of in-gel fluorescence and western blot confirmed that EGFP has been tagged to STIM1 proteins explicitly with the lack of off-target tagging (***Figure 2.9***). Off-target effect associated with gene-editing can be serious, causing large deletions, mutations and rearrangements of the gene, and is sometimes lethal at the level of organism (Naeem *et al.* 2020). In this case, if the gene-editing is off target, the green fluorescence may not represent the protein of interest, i.e., STIM1. Also, the functionality of this edited cell line may be affected. All these results suggest that this STIM1-EGFP HeLa cell line has half STIM1 proteins tagged by EGFP and half STIM1 proteins remaining untagged.

Co-immunoprecipitation (Co-IP) experiments were mostly performed on overexpressed STIM1 and Orai1 in previous studies, revealing the direct interactions between STIM1 and Orai1 (Yeromin *et al.* 2006; Balasuriya *et al.* 2014; Liu *et al.* 2019). Co-IP on native STIM1 and Orai1 was proven to be difficult, due to the relatively low expression levels of both proteins

(Gwack *et al.* 2007). Therefore, in this project, co-IP was performed on STIM1-EGFP expressed at endogenous level and overexpressed mCh-Orai1. Results demonstrated that the EGFP tag on STIM1 does not perturb the interaction with Orai1, and that native and tagged STIM1 interact indistinguishably with Orai1, reflected by equal pull-down efficiencies between native and tagged STIM1 and preserved 50:50 ratio of them after immunoprecipitation (***Figure 2.11***).

Regarding the ability to conduct Ca^{2+} signals of the edited cell line, results showed that the IP_3-mediated Ca^{2+} release evoked by histamine was similar compared to WT HeLa cells (***Figure 2.12***). Most importantly, the response to CPA which depletes intracellular Ca^{2+} stores, and subsequent measurement of amplitudes of SOCE, particularly the submaximal stimulation of SOCE, were not affected by the EGFP tagging (***Figure 2.14***). Since only one copy of STIM1 has been tagged with EGFP while the other remains native, it is possible that the expression of native STIM1 is more than enough to evoke maximal SOCE, which masks the function of edited STIM1. Therefore, the comparable submaximal stimulation of SOCE between WT and STIM1-EGFP HeLa cells indicates that the STIM1-EGFP is functionally similar to native STIM1. Furthermore, the amplitudes of physiologically evoked SOCE, despite the small amplitudes, were indistinguishable in the two cell lines as well, suggesting that the EGFP tagging does not affect the IP_3-mediated Ca^{2+} signalling pathway and SOCE (***Figure 2.15***).

Single editing of STIM1 could be problematic later. For example, I cannot confidently say that all STIM1-EGFP mix with native STIM1 uniformly and evenly distribute across the cell either at rest or upon activation. Additionally, whether STIM1-EGFP contributes to SOCE at all is always another problem. It is possible that the remaining native STIM1 proteins are sufficient for carrying out signalling activities. The former will be discussed and solved by experiments in later chapters, while the latter has been confirmed by indistinguishable amplitudes of SOCE evoked by submaximal stimulation of CPA between WT and STIM1-EGFP HeLa cells (***Figure 2.14***). Anyhow, if all STIM1 are uniformly tagged with EGFP (double-edited), many problems and hassles can be avoided. Attempts were made to generate a double-edited STIM1-EGFP HeLa cell line using the same gRNA and donor template Dr. Sumita Chakraborty designed (***Section 2.2.4***), and, despite difficulties, there have been some progress, with a distinct cell population with higher fluorescent intensity showing up (***Figure 2.16***). Unfortunately, not all cells from this cell population had the opportunity to enrich to get enough cells before characterization due to national lockdown caused by COVID-19. Those monoclonal cells lines, which were characterized using WB and appeared to be doubly edited,

lost one EGFP tag shortly (***Figure 2.17***). The difficulties of generating the double-edit cell line mainly arose from the low efficiency of CRISPR-mediated knock-in, particularly knocking in a large construct of EGFP. Unlike knockouts mediated by CRISPR which can easily achieve efficiencies over 70% or even 90% (Incontro *et al.* 2014; Hana *et al.* 2021), an efficiency of ~25% is considered high in knock-in via HDR (Kimura *et al.* 2014; He *et al.* 2016; Shin and Lee 2020), which normally ranges from 1%~10% (Byrne *et al.* 2014; Zhu *et al.* 2015; Zhang *et al.* 2017; Matsuda and Oinuma 2019), especially for primary cell lines and for inserting large constructs like GFP. However, with the evolution of techniques in CRISPR, such as using variants of Cas9, optimizing gRNA designs, improving HDR donors and seeking different delivery methods, the efficiency of large constructs knock-in can be increased up to 70% (Liu *et al.* 2018; Chen *et al.* 2019; Ling *et al.* 2020). On the other hand, while the above problems are technical, the short-lived double-edited cell line may arise concerns biologically, where HeLa cells can live with half native and half edited STIM1 but are intrinsically disabled with all STIM1 tagged, so that one EGFP came off to regenerate native STIM1 after a few days. This is untenable to some extent, because the monoclonal cell line (clone 1) has grown for a few weeks to get enough cells for the first WB. There was no reason why EGFP did not come off earlier. Anyway, given the unavailability of double-edited STIM1-EGFP cell line, this heterozygous STIM1-EGFP cell line was extensively characterized to ensure that it is functional as WT cell line and that the functions of EGFP-tagged STIM1 are not masked by the native STIM1.

Overall, even though only half of the STIM1 proteins were tagged endogenously by EGFP, these results demonstrated that STIM1-EGFP HeLa cells have similar ability of Ca^{2+} signalling and SOCE, so that the EGFP tagging does not have significant impact on amplitude of SOCE as well as the interaction between STIM1 and Orai1. This justifies the use of these cells for subsequent optical analyses of STIM1 redistribution and its interaction with Orai1 upon store depletion to addresses the final research question.

Chapter 3 STIM1 accumulate into small clusters after store depletion

3.1. Introduction

As discussed in the ***Introduction***, in animal cells, SOCE is one of the most important Ca^{2+} signalling pathways that refills intracellular Ca^{2+} store. When Ca^{2+} is lost from the ER Ca^{2+} store, STIM1 senses this reduction in ER Ca^{2+} concentration by dissociation of Ca^{2+} from the luminal Ca^{2+}-binding sites (Liou *et al.* 2005; Zhang *et al.* 2005), followed by oligomerization of STIM1 proteins and relocation to the ER-PM junctions (Wu *et al.* 2006; Liou *et al.* 2007; Luik *et al.* 2008). This subsequently causes STIM1 to interact with the PM Ca^{2+} channel, Orai1, which opens its pore to allow extracellular Ca^{2+} to flow into the cell through the SOCE pathway (Lewis 2019; Gudlur *et al.* 2020).

The process of oligomerization of STIM1 plays an essential role in activation and regulation of SOCE, which couples ER Ca^{2+} depletion with CRAC channel activation (Luik *et al.* 2008). STIM1 exists as a dimer at resting state (Luik *et al.* 2008; Huang *et al.* 2009; Covington *et al.* 2010; He *et al.* 2012). When Ca^{2+} store is depleted, STIM1 activates by rearranging its EF-SAM region to apposition, which subsequently triggers large conformational changes in the C-terminus of STIM1, releasing the CAD/SOAR region that is otherwise hidden (Zheng *et al.* 2011; Yu *et al.* 2013; Zhou *et al.* 2013; Fahrner *et al.* 2014; Gudlur *et al.* 2018) (***Figure 1.3B***). Besides its necessity in interacting and activating Orai1, the C-terminus of STIM1 undeniably is crucial to aggregation of STIM1 (Li *et al.* 2007; Yu *et al.* 2011; Zheng *et al.* 2018). STIM1 lacking the full or large part of C-terminus fails to form stable oligomers after store depletion, which can be rescued by addition of CAD/SOAR, suggesting the importance of CAD/SOAR in this process (Covington *et al.* 2010; Korzeniowski *et al.* 2017). Notably, the entire CAD/SOAR region is required for STIM1 oligomerization, where STIM1 containing only CC2 does not oligomerize in response to store depletion (Covington *et al.* 2010).

The STIM1 oligomers then translocate to the proximity to the PM while still residing in the ER, namely the ER-PM junctions, and form puncta (Luik *et al.* 2006; Wu *et al.* 2006; Xu *et al.* 2006). This process is also very critical for subsequent interaction with Orai1, due to the apposition of STIM1 and Orai1 which allows direct binding between these two in the junctions where SOCE can only occur (Baba *et al.* 2006). The PBD of STIM1 assists the targeting of

STIM1 to the PM, by binding PIP_2 in the PM (Ercan *et al.* 2009; Walsh *et al.* 2009; Wu *et al.* 2014). Furthermore, STIM1 diffuses slower upon store depletion, leading to the proposal of the diffusion trap model of STIM1 activation (Liou *et al.* 2007; Wu *et al.* 2014; Qin *et al.* 2020) (***Figure 1.4***). With all these preparations in place, the CAD/SOAR domain of STIM1 is ready to interact with Orai1 (Kawasaki *et al.* 2009; Park *et al.* 2009; Yuan *et al.* 2009).

The stoichiometry of STIM1 cluster regulates the interaction model with Orai1 (***Figure 1.7***), hence is a pivotal determinant in understanding the mechanism of SOCE. The phenomenon of STIM1 clustering and puncta formation at the ER-PM junction has been clearly visualized under the microscope and characterized using FRET (Luik *et al.* 2006; Wu *et al.* 2006; Liou *et al.* 2007; Malli *et al.* 2008). There was also indirect evidence showing engineered STIM1 (ehSTIM1) accumulates into bundles of 1-6 dimers (Srinivasan 2019). However, the precise number of native STIM1 molecules within one punctum has not been revealed yet. Therefore, to figure out the exact stoichiometry of STIM1 clusters and unmask the unusual behaviour of SOCE, where channel opening and Ca^{2+} influx is controlled by direct interactions between two proteins located in different membranes, a CRISPR-mediated gene-edited cell line was utilized. A fluorescent tag was attached to the C-terminus of STIM1 protein to allow fluorescence imaging analyses to help understand the amounts of endogenous STIM1 and Orai1 within the MCS and define the stimulus-response relationship within the SOCE pathway.

After characterization of the STIM1-EGFP HeLa cell line and confirmation of one allele being tagged by EGFP as described in ***0***, the experimental focus switched to look closer at the distribution and composition of STIM1 puncta using microscopy. Since conventional wide-field fluorescence microscopes evenly illuminate the entire sample axially, the background fluorescence noise from outside the focal plane, such as deeper in the cell, is usually large (***Figure 3.1A***). This can be very problematic especially if only the fluorescence signals near the cell surface are of interest. This signal disturbance can be eliminated by various mechanisms to ensure the excitation and detection of fluorophores are restricted to a thin region of the specimen, which consequently improves the spatial resolution of the features or events of interest. Confocal microscopy is one of the solutions. A point light source, such as laser, illuminates the sample and the emitted fluorescence travels through a pinhole before the detector to eliminate the out-of-focus signal (King and Delaney 1994). As a result, only the fluorescence produced very close to the focal plane can be detected, which hugely increases the resolution in the axial direction. However, since most light is blocked by the pinhole filter, greater laser intensity and longer exposure time is usually required.

Another option is the total internal reflection fluorescence microscopy (TIRFM), which has been used in most experiments throughout this study. It works by emitting a parallel beam of laser towards the glass coverslip through an aqueous specimen medium, traversing an immersion medium (usually oil) (Mattheyses *et al.* 2010). This normally causes refraction due to lower refractive index of water than glass and oil, but when the incident laser is directed at

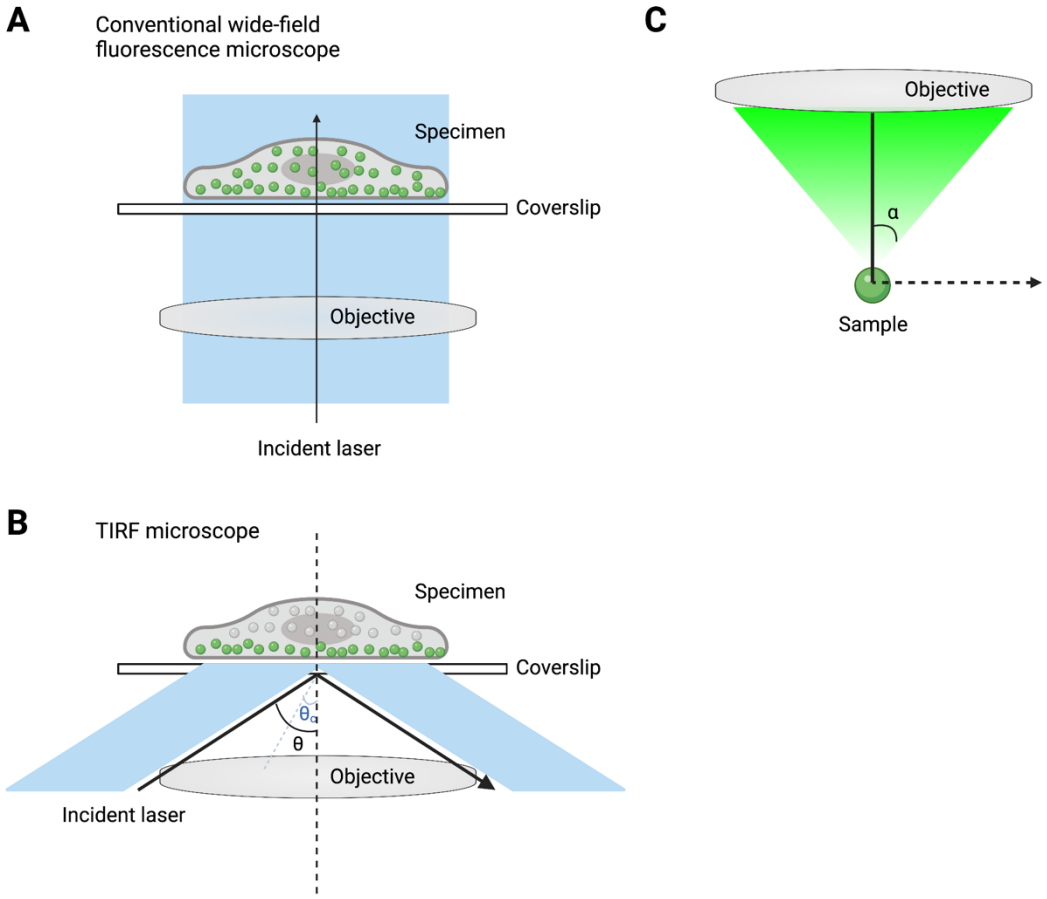

Figure 3.1 TIRF microscopy. A. In conventional wide-field fluorescence microscope, the incident light shines directly through the whole specimen, illuminating all fluorophores at the same time across all focal planes. **B.** In TIRFM, the incident laser passes from an angle (θ) greater than the critical angle (θ_c), which causes total internal reflection. This only illuminates a very thin section of specimen of approximately 100 nm, depending on the wavelength of incident laser. Therefore, only fluorophores near the PM of adherent cells are excited and result in selective visualization of living cells with high axial resolution. **C.** Numerical aperture is proportional to the refractive index of the medium between the objective and the coverslip (n) and sin α, where α is the maximum angle of the light cone that the objective can accept from the sample.

an angle (θ) larger than the critical angle (θ_c) of the oil/glass-water interface, leading to total internal reflection, only a very thin layer of the specimen of around 100 nm is illuminated (***Figure 3.1B***). Therefore, TIRFM allows researchers to see cellular structures and activities happening at or immediately beneath the plasma membrane in adherent cells, without the signal disturbance from regions farther away from the cell surface (Ambrose 1956; Axelrod 1981). Besides the incident angle, another factor that is important in a successful TIRM is the numerical aperture (NA) of the objective (Mattheyses *et al.* 2010; Martin-Fernandez *et al.* 2013). It is critical in determining both the resolution and the brightness of TIRF images and has the formula of $NA = n \sin \alpha$, where n is the refractive index of immersion medium between the lens and the specimen (usually immersion oil, with n = 1.51 (Cargille 1985)) and α is the maximum angle of acceptance of the objective (***Figure 3.1C***). A higher NA, usually greater than 1.45 for TIRFM, allows larger incident angles of laser, and results in brighter images with higher resolution.

TIRFM has been widely used in Ca^{2+} signalling, combining with Ca^{2+} indicators or fluorescent proteins (Shuai and Parker 2005; Luik *et al.* 2006; Nystoriak *et al.* 2013; Thillaiappan *et al.* 2017). The advantages of TIRFM include its focus on an extremely thin section of specimen and ability to visualize and monitor dynamic processes there. However, the resolution of TIRF is limited by both the wavelength of emitted light and the NA, which is defined by the Rayleigh criterion with an equation of

$$r = \frac{0.61\lambda}{NA} \qquad \textbf{\textit{Equation 1}}$$

where r is the smallest distance between two resolvable points (resolution), λ is the wavelength of the incident laser, while NA is the numerical aperture. As the equation suggests, resolution is higher (two spots separated by smaller distance can be resolved) with lower wavelength and higher NA. For the TIRFM I used in this project, each pixel in an image represents 160 nm.

A lot of techniques have been developed to increase the resolution of microscopy, collectively referred to as super resolution microscopy (SRM). They can be based on wide-field, TIRFM or confocal microscopy and can achieve resolutions of a few tens of nanometres (Schermelleh *et al.* 2019). Stochastic optical reconstruction microscopy (STORM) is one of SRMs based on TIRFM, using photoswitchable dyes to decorate the target protein (Rust *et al.* 2006). The principle of STORM is to take thousands of frames where each frame has a random subset of optically resolvable fluorophores switched on, so that the precise position of each fluorophore can be determined by fitting a two-dimensional Gaussian to find the centroid with

a resolution of ~20 nm and the overall image can be reconstructed (Rust *et al.* 2006). Soon after the invention of STORM, a 'direct' variant was discovered (dSTORM), utilizing conventional fluorescent dyes that can blink between 'on' and 'off' states without the presence of an activator fluorophore reported previously (Bates *et al.* 2005; Rust *et al.* 2006; Huang *et al.* 2008), simplifying the protocols of STORM and producing super resolution images beyond the diffraction limit (van de Linde *et al.* 2008). However, the high resolving power of (d)STORM is in exchange for long acquisition time and complicated subsequent analyses. Furthermore, (d)STORM was initially designed for imaging fixed cells (Betzig *et al.* 2006), and the special 'switching' buffers dSTORM need can be harmful to live cells (van de Linde *et al.* 2008; Endesfelder *et al.* 2011), leading to difficulties in imaging live cells, although not impossible (Fernandez-Suarez and Ting 2008; Klein *et al.* 2010; Jones *et al.* 2011). Regarding experimental difficulties, localizations of particles in (d)STORM are restricted by the label density, as well as the requirement of extremely stable environment and platform to avoid any vibration of samples.

In order to investigate the stoichiometry of STIM1 puncta based on microscopy, a technique named single-molecule stepwise photobleaching has been utilized. This technique has widely been used to count the number of fluorophores within the region of interest (ROI) and is usually used for studying oligomers of, particularly, membrane proteins (Ulbrich and Isacoff 2007). Photobleaching refers to the loss of fluorescence from fluorophores due to continuous illumination. In single-molecule stepwise photobleaching, the target proteins are labelled with fluorescent tags, such as GFP, which are slowly and irreversibly photobleached using appropriate intensity of laser. The fluorescence-time traces are recorded and when one fluorophore is photobleached, there should be a sudden drop in the trace (Ulbrich and Isacoff 2007; Yu *et al.* 2009; Zhang *et al.* 2009). Then the fluorescence intensity of the first frame is divided by the amplitude of the last bleaching step, which is likely to represent a single fluorophore, to determine the number of individual fluorophores within the ROI. If one can ensure that each protein is attached to one fluorophore, this calculation is equivalent to the number of proteins in a multimer (Fricke *et al.* 2015).

Since SOCE is a pathway that involves protein interactions within the MCS, the specific aim of this chapter is to use TIRF microscopy to visualize the oligomerization of STIM1 beneath the plasma membrane and examine the number of STIM1 proteins associated within one punctum by stepwise photobleaching.

3.2. Materials and Methods

Many materials and methods used in this chapter have already been described in ***Section 2.2***.

3.2.1. Materials

Table 3.1 Materials

(IC: Immunocytochemistry)

Materials	**Company**	**Catalog number**
Donkey anti-rabbit IgG-AlexaFluor 594 (AbRa594, IC, 1:500)	Thermo Scientific	Cat# A21207 RRID: AB_141637
EGFP siRNA	Thermo Scientific	Cat # AM4626
mCherry-ER-3 plasmid	Addgene	Cat# 55041 RRID: Addgene_55041
Paraformaldehyde	Alfa Aesar	Cat# 43368
pcDNA $3.1^{(+)}$ mammalian expression vector	Invitrogen	Cat# V79020
pSUPER-retro-puro-shSTIM1	Addgene	Cat# 89816 RRID: Addgene_89816

3.2.2. Total internal reflection fluorescence microscopy (TIRFM)

Total internal reflection fluorescence microscopy (TIRFM) allows observation of a thin layer of the specimen, usually approximately 100 nm (***Figure 3.1***). Coverglass-bottomed imaging dishes (35 × 10 mm) were coated with fibronectin, by applying 10 μg/ml of fibronectin, incubating for 45 min and washing with HBS. Cells were seeded on fibronectin-coated coverglass-bottomed imaging dishes to ~70% confluency and washed with HBS. The cells were either directly imaged or transfected with plasmids using *Trans*IT-LT1 (***Section 2.2.2***). The cells were usually imaged 24h after seeding or transfection, unless specified otherwise.

WT and STIM1-EGFP HeLa cells were imaged using an iXon Ultra 897 EMCCD camera (Andor, 512 x 512 pixels) and Olympus IX83 microscope equipped with a 100x oil-immersion TIRF objective (numerical aperture, NA = 1.49) and an iLas2 targeted laser illumination system (Cairn, Faversham, Kent, UK). TIRF were captured using MetaMorph software. All images were background corrected by subtracting the mean fluorescence intensity of a region outside the cell using ImageJ or, for photobleaching analyses, Metamorph (version 7.8.4).

Cells containing more than one colour of fluorophores were imaged for red fluorescence (561 nm excitation) and green fluorescence (488 nm excitation), respectively. The images were merged using Fiji ImageJ software.

3.2.3. Immunocytochemistry

Cells were seeded on fibronectin-coated coverglass-bottomed imaging dishes (***Section 3.2.2***) to ~70% confluency and washed with PBS twice. Cells were then fixed by paraformaldehyde (4% in PBS, 15 min, 20 °C), washed 3 times, permeabilized in PBS containing Triton X-100 (0.1%, 15 min, 20 °C), and washed 3 times. Cells were blocked by skimmed milk (5% in PBS, 30 min, 20 °C), followed by BSA (5% in PBS, 30 min, 20°C), incubated with primary antibody in PBS (16 hr, 4°C, dilutions in ***Table 2.1***), washed (4 × 5 min), incubated with secondary antibody with fluorophores in PBS (1 hr, 20°C, dilutions in ***Table 3.1***), washed (4 × 5 min) and used for TIRFM. All washing buffers were PBS.

3.2.4. Automated detection of fluorescent puncta

Two Fiji plugins were used to identify fluorescent puncta. All TIRF images were first background corrected using Fiji, by subtracting the mean fluorescence intensity of a region outside the cell boundary. Most analyses used TrackMate (Tinevez *et al.* 2017) to identify fluorescent puncta in background-corrected TIRF images automatically. TrackMate uses a 'difference of Gaussians' filter after applying a consistent threshold (***Figure 3.2***). For definition of colocalization between puncta which uses measurements of distances between puncta, DiAna was used (Gilles *et al.* 2017). The details of DiAna will be described in ***Section 4.2.3***.

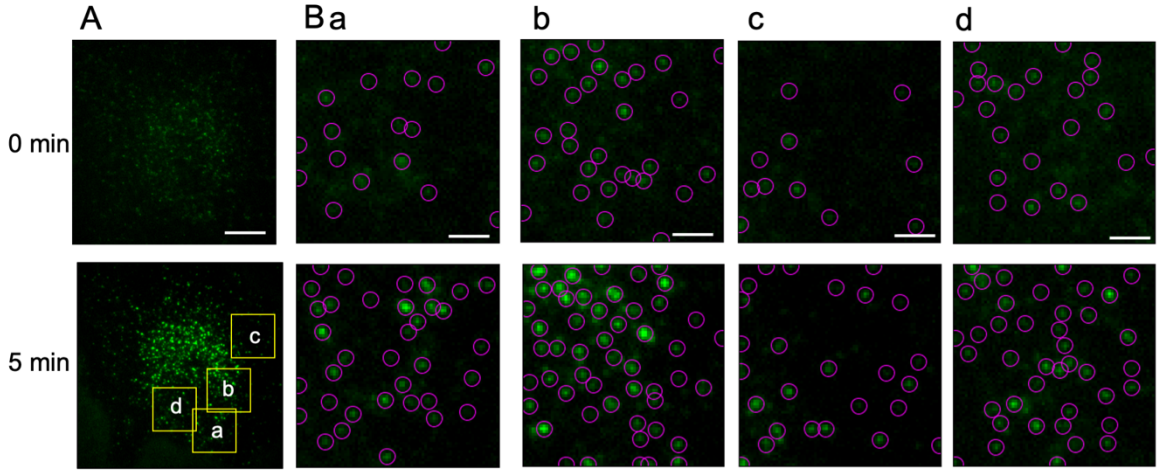

Figure 3.2 STIM1-EGFP puncta were identified automatically by TrackMate. **A.** TIRF images of STIM1-EGFP HeLa cells before and 5 min after thapsigargin (1 μM, Ca^{2+}-free HBS). Scale bar = 10 μm. **B (a-d).** Enlargements of boxed areas in **A**, where the magenta circles indicate the ROI identified by TrackMate. Scale bars = 2 μm.

3.2.5. Colocalization studies

For colocalization studies of STIM1-EGFP with ER and STIM1-EGFP with immunostained STIM1, TIRF images were taken according to ***Section 3.2.2***, and processed by JACoP (Just Another Co-localization Plugin) in ImageJ (Bolte and Cordelieres 2006). Each background-corrected image was thresholded, which was determined individually, to produce a binary image. The location of each white pixel on one binary image was assessed on another binary image to ask whether there was a white pixel on the same location. Randomization was performed within the plugin by randomly shuffling one image 100 times to determine the statistical significance of any colocalization. $P < 0.05$ was considered significant.

3.2.6. Stepwise photobleaching

STIM1-EGFP HeLa cells were seeded on fibronectin-coated coverglass-bottomed imaging dishes to ~70% confluency. They were washed by PBS twice before treatment with thapsigargin (1 μM) for 15 min, fixed in paraformaldehyde (4%, 15 min) and washed 3 times with PBS. They were then imaged according to ***Section 3.2.2***. Low laser intensity (~6%) and a short time (< 3 s) were used to identify a cell for subsequent photobleaching, in order to minimize pre-bleaching (***Figure 3.8***). The images were then captured (laser power = 60%, capture time = 200 ms) in series. The laser power was adjusted to bleach the cells slowly enough to see the last step, and quick enough for timesaving. After background correction in MetaMorph, all puncta were identified by manually circling ROIs on the first image in ImageJ. The trace of fluorescent intensity against time of each punctum was generated using Fiji Time Series Analyzer. The number of total steps is calculated by dividing the fluorescent intensity of the first frame by the size of the amplitude of the final bleaching step (***Figure 3.9***).

3.3. Results

3.3.1. STIM1-EGFP are the only fluorescent puncta detected by TIRFM

Most of subsequent experiments are based on TIRF imaging of STIM1-EGFP puncta. Therefore, it is important to ensure that STIM1-EGFP are the only fluorescent puncta detected by TIRFM.

Before turning to TIRF imaging, the specificity and efficiency of shSTIM1 knock-down must be verified. STIM1-EGFP HeLa cells were transfected with plasmids encoding either shSTIM1 (***Table 3.1***) or non-silencing shRNA (NS) and performed WB. Results (***Figure 3.3A and B***) show 80.8% knock-down efficiency of shSTIM1.

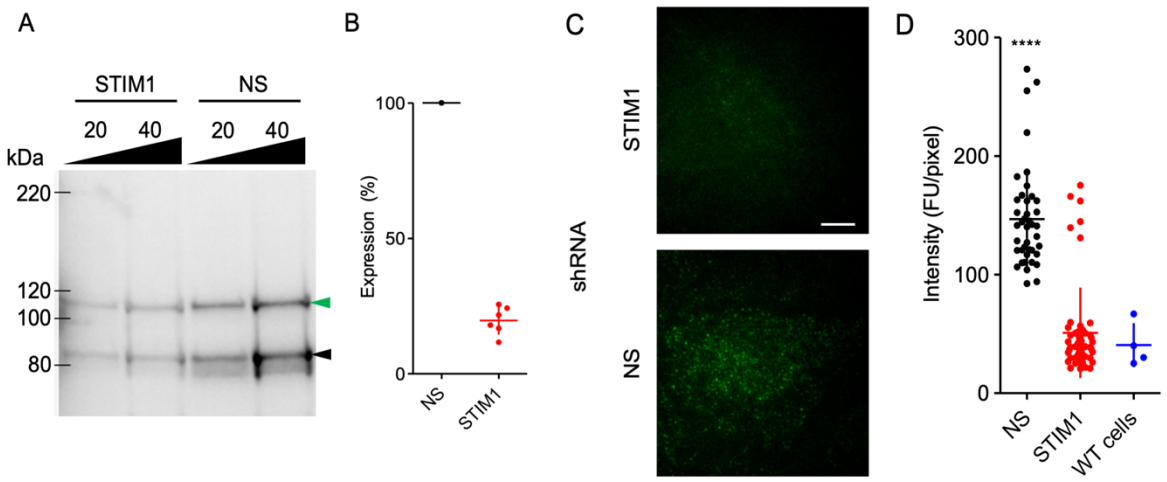

Figure 3.3 STIM1-EGFP are the only fluorescent puncta detected by TIRFM. **A.** Western blots using STIM1 antibody of STIM1-EGFP cells transfected with plasmids encoding either shSTIM1 or non-silencing (NS) shRNA. Loadings are shown in µg. The upper band (green arrow) indicates STIM1-EGFP, while the lower band (black arrow) indicates native STIM1. **B.** Summary results (mean ± SD, $n = 3$) show the expression of STIM1 proteins after transfection of shSTIM1 relative to non-silencing shRNA. **C.** TIRF images of STIM1-EGFP HeLa cells transfected with the indicating shRNAs before store depletion. Scale bar = 10 µm. **D.** Summary results (individual values, mean ± SD, $n = 3$ independent experiments, each with ~30 cells analysed) show mean fluorescent intensity (whole cell fluorescent intensity divided by cell area, FU/pixel) of each cell. WT HeLa cells ($n = 4$) were also imaged and quantified. FU, fluorescence units. $^{****}P < 0.0001$, ANOVA with Bonferroni test, relative to WT cells.

STIM1-EGFP HeLa cells were then transfected with the same shRNAs and imaged by TIRFM. The TIRF images (***Figure 3.3C***) show clearly that STIM1-EGFP puncta are much diminished when transfected with shSTIM1 compared to transfection with non-silencing shRNA. Statistics (***Figure 3.3D***) confirm that the mean fluorescent intensity of whole cell area has significantly reduced by 65.3% with shSTIM1, around the same level as WT cells. A few cells, however, remain the similar fluorescence level as NS STIM1. Since the cells were all randomly selected, this probably indicate the transfection efficiency (80.8%).

3.3.2. STIM1 puncta accumulate beneath the PM after store depletion

STIM1-EGFP HeLa cells were transfected with plasmids encoding mCherry-ER (***Section 2.2.2***) and imaged by TIRFM (***Section 3.2.2***). Results show that STIM1-EGFP are distributed within the ER membrane before store depletion (***Figure 3.4***).

It has been shown in various reports that STIM1 accumulate into puncta in the ER-PM junctions upon store depletion using over-expressed STIM1 (Liou *et al.* 2005; Liou *et al.* 2007;

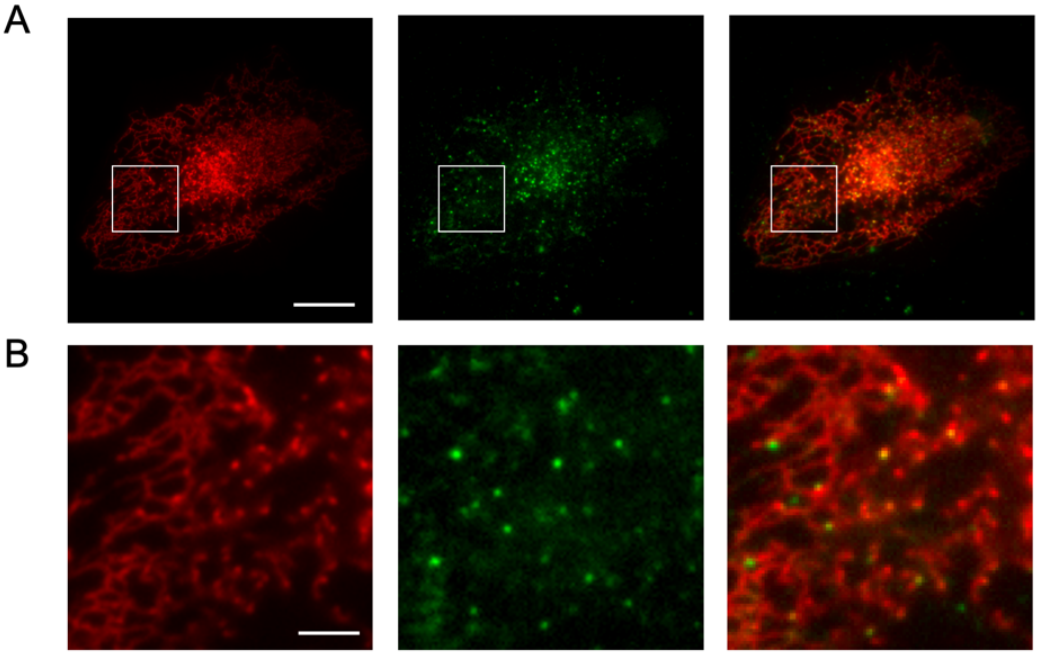

Figure 3.4 STIM1-EGFP are distributed within the ER before store depletion. **A.** TIRF images of unstimulated STIM1-EGFP HeLa cells transfected with mCherry-ER showing ER (red) and STIM1-EGFP (green) and their overlay. Scale bar = 10 μm. **B.** Enlargements of the boxed area in **A**. Scale bar = 2 μm. Manders split coefficient for colocalization of STIM1-EGFP with mCh-ER in peripheral regions is 0.87 ± 0.08, mean ± SD, n = 9 cells.

Stathopulos *et al.* 2008; Park *et al.* 2009). Therefore, I would like to confirm that STIM1-EGFP are functional as such.

STIM1-EGFP HeLa cells were imaged under TIRF before store depletion. Then they were treated with TG (1 μM in Ca^{2+}-free HBS) to deplete the Ca^{2+} stores and imaged after the addition of TG at different time points (5, 10, 15 min). The puncta were automatically identified using TrackMate (***Figure 3.2***). As shown in ***Figure 3.5*** and ***Figure 3.6A-B***, there were few puncta before the addition of TG, while after store depletion, the number of puncta doubled, and the puncta became brighter and clearer. This also indicates that the aggregation of STIM1-EGFP into puncta was half complete by ~2 min, reached maximum accumulation within ~4 min and was stable thereafter for at least 15 min. Therefore, the treatment of TG of cells was limited to 5 min for subsequent experiments. These results are comparable to investigations using over-expressed STIM1 (Liou *et al.* 2005; Wu *et al.* 2006).

The fluorescence intensity distributions of STIM1-EGFP puncta before and 5 min after store depletion by CPA (10 μM in Ca^{2+}-free HBS) and summary results (***Figure 3.6C***) show that the mean fluorescence intensities of STIM1-EGFP puncta modestly increase upon store

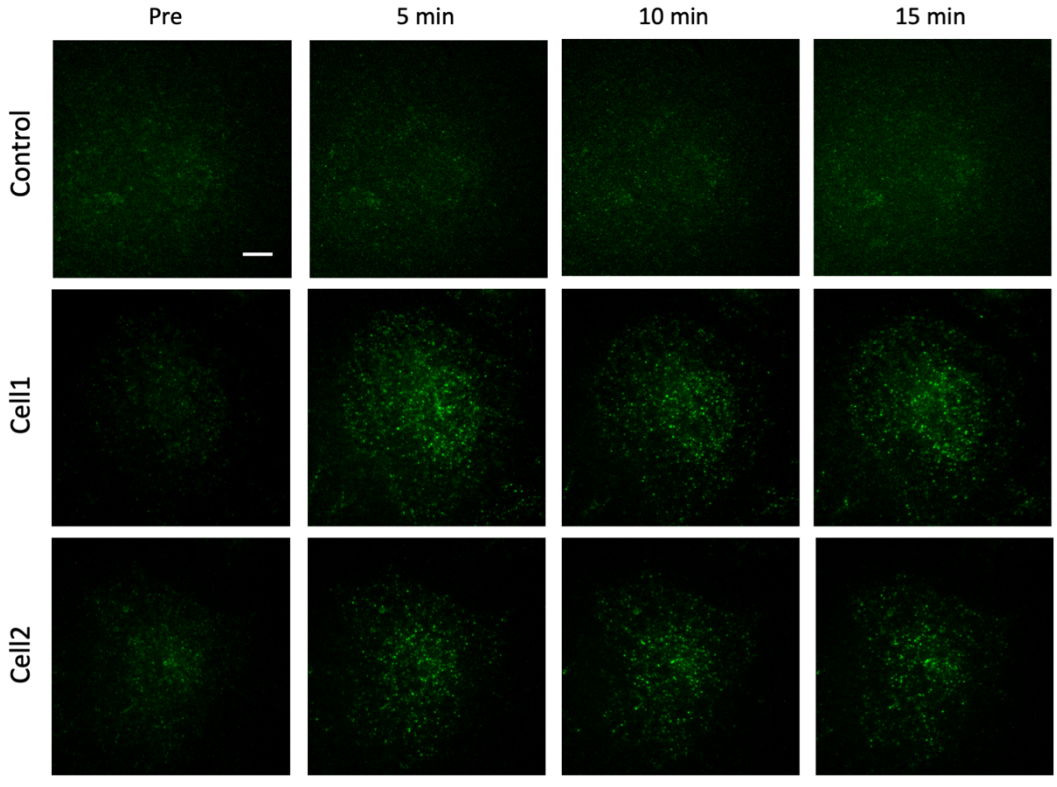

Figure 3.5 STIM1 puncta accumulate beneath the PM after store depletion. TIRF images of STIM1-EGFP cells before and after addtion of BAPTA (2.5 mM) and TG (1 μM, cell1 and 2) or HBS (control) at 5, 10, 15 min. Scale bar = 10 μm.

depletion (from 20794 FU to 28702 FU, 38% increase), and the distribution becomes flatter. The bottom panel of ***Figure 3.6C*** and ***Figure 3.6D*** show the 'difference' panels, where the numbers of puncta in each fluorescence intensity category before and after store depletion were compared. In each fluorescence intensity category, the numbers of STIM1 puncta before store depletion were subtracted from that after store depletion, and this difference was divided by all

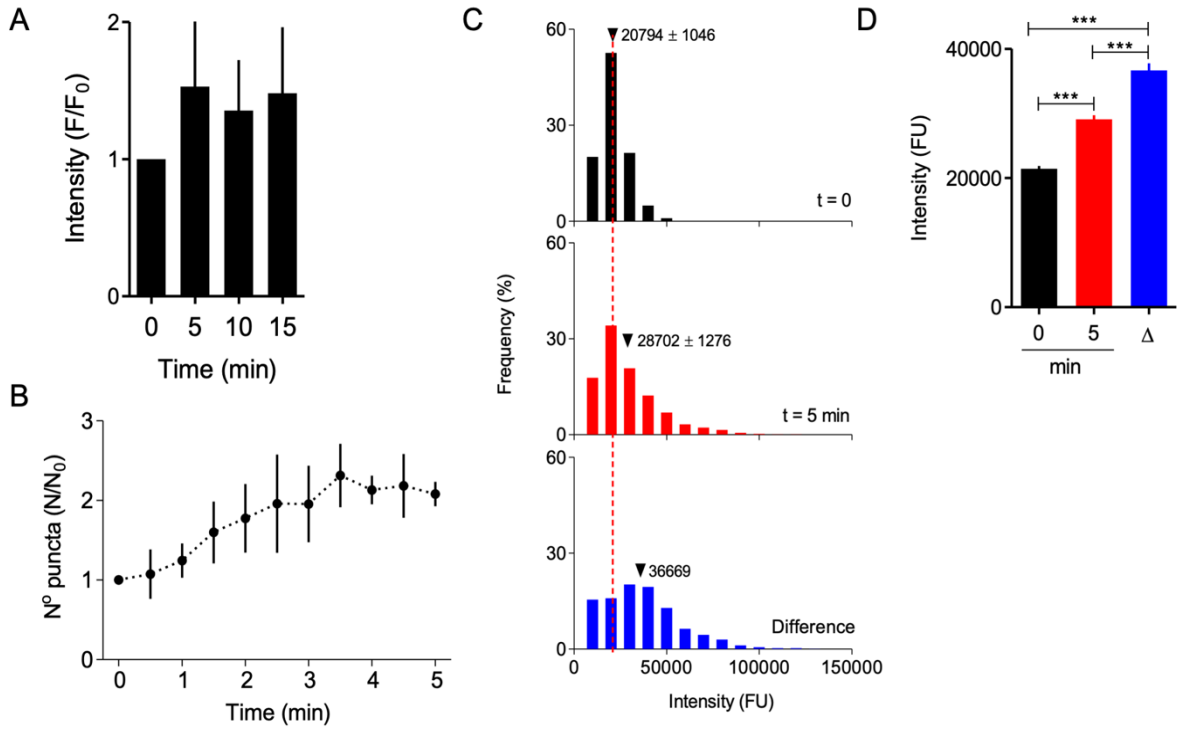

Figure 3.6 Quantification of STIM1 accumulation. A. Summary results (mean ± SD, n = 7) show fluorescence intensity (F) of whole cell area 5, 10 and 15 min after addition of TG relative to fluorescence before its addition (F_0) **B.** Number of puncta detected by TrackMate (N) relative to the number before addition of CPA (N_0) of cells treated with TG (10 µM in Ca^{2+}-free HBS), mean ± SD, n = 5 cells. **C.** Fluorescence intensity distributions (mean ± SD shown, n = 6) of STIM1-EGFP puncta detected by TrackMate before and 5 min after store depletion by CPA (10 µM in Ca^{2+}-free HBS). The red dashed line indicates the mean value for cells before store depletion. Bottom panel (mean only) shows the 'difference' distribution, which is calculated from the difference in the number of puncta within each fluorescence intensity category before and after store depletion. **D.** Summary results (mean ± 95% CI) show fluorescence intensities of STIM1-EGFP puncta before and 5 min after store depletion by CPA and for puncta that appeared as a consequence of store depletion (Δ). $^{***}P < 0.001$, Student's t-test.

'extra' puncta (1362 puncta before and 2737 puncta after, so 1375 'extra' puncta) to get the percentage (***Figure 3.6C****, bottom panel*). The mean fluorescence intensity of STIM1 puncta in stimulated cells within each bin and the number of 'extra' puncta in that bin were used to calculate the weighted average of 'extra' puncta (***Figure 3.6D****, blue bar*). The 'extra' STIM1 puncta fall in each category can be classified as those only appear after store depletion, with the mean fluorescence intensity only 28% greater than that of all puncta in cells with empty stores (36669 FU and 28702 FU, respectively).

Subsequent experiments and analyses of single-step photobleaching (***Figure 3.10C***) suggest that the amplitudes of a single bleaching event, which corresponds to the fluorescence intensity of a single fluorophore (i.e., STIM1-EGFP), is indistinguishable between cells with empty or full stores. This indicates that all the STIM1-EGFP puncta analysed were similarly located just beneath the PM. Therefore, the brighter the punctum is, the more STIM1-EGFP were contained in that punctum. All above results demonstrate that endogenously EGFP tagged STIM1 proteins were able to aggregate at the ER-PM junction and form puncta that are both larger and more abundant after depletion of Ca^{2+} store.

3.3.3. STIM1-EGFP mix interchangeably with native STIM1

According to the genetic results (***Figure 2.10***), one allele of *STIM1* out of two has been tagged by EGFP. Western blots (***Figure 2.8***) also suggest that the EGFP tag is only fused to half of the STIM1 proteins. Hence, it becomes important to determine whether these EGFP-tagged STIM1 mix thoroughly with native STIM1. We can only trust the results from TIRF imaging for subsequent photobleaching analyses if STIM1-EGFP form puncta together with native STIM1, instead of playing with tagged ones each other.

To confirm this, STIM1-EGFP HeLa cells were treated with TG (1 μM, 15 min), immunostained with STIM1 antibody, followed by a secondary antibody which is covalently linked to a red fluorophore (AbRa594) and imaged under TIRF using both green and red fluorescence.

Since the STIM1 antibody is able to recognize both tagged and untagged STIM1, if STIM1-EGFP mix with native STIM1 and assemble into puncta together, the more STIM1-EGFP there are, the more immunostained STIM1 there should be. In other words, the fluorescent intensities of immunostained STIM1 should be in linear relationship with STIM1-EGFP. The overlay TIRF images of STIM1-EGFP and immunostained STIM1 (***Figure 3.7A***) show 72 ± 3%

overlap between the two fluorophores, and summary results (***Figure 3.7B***) indeed suggest a linear relationship between them.

Furthermore, after store depletion by TG (1 µM, 15 min), STIM1 puncta in both WT and STIM1-EGFP cell lines were immunostained with AlexaFluor 594 and the fluorescence intensity distributions were indistinguishable in both cells (***Figure 3.7C***). This further confirms that the EGFP tag does not affect the ability of STIM1 to form puncta and that native STIM1 and STIM1-EGFP mix interchangeably within the puncta upon store depletion.

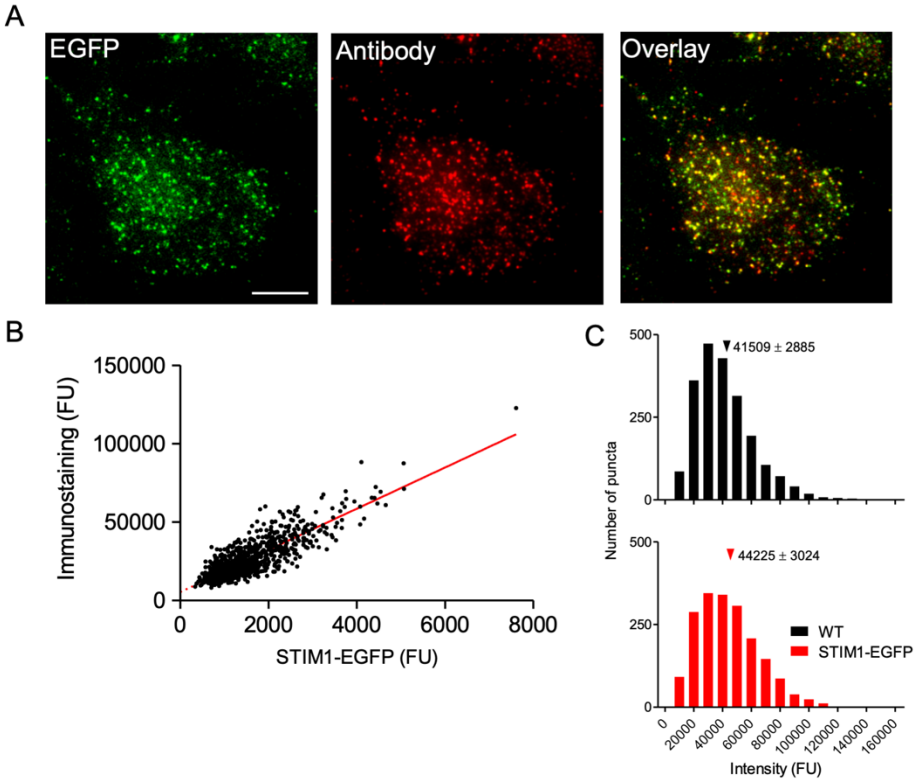

Figure 3.7 STIM1-EGFP mix thoroughly with native STIM1. A. TIRF images of STIM1-EGFP HeLa cells with Ca^{2+} stores depleted and immunostained for STIM1 using AlexaFluor 594. Scale bar = 10 µm. Manders coefficient for overlap of immunostained STIM1 with STIM1-EGFP = 0.72 ± 0.03 (mean ± SD, n = 6 cells from 3 independent experiments). **B.** A plot of the fluorescence intensity (FU, fluorescence unit) of immunostained STIM1 against STIM1-EGFP. It shows a linear relationship (least-squares linear correlation coefficient, r = 0.834, P < 0.0001). **C.** Frequency distribution of the fluorescence intensities of immunostained STIM1 in WT (2116 puncta, 5 cells) and STIM1-EGFP HeLa cells (1891 puncta, 5 cells) after store depletion by TG (1µM, 15 min in Ca^{2+}-free HBS) Each from 3 independent experiments. Mean intensities (± SEM) are shown. P > 0.05, Student's t-test.

3.3.4. STIM1 and STIM1-EGFP form small clusters after store depletion

In order to address the important question of how many STIM1 there are within a single punctum, stepwise photobleaching was performed on STIM1-EGFP HeLa cells after store depletion (***Section 3.2.6***). Low laser (6%) and short time (< 3 s) were used to identify cells

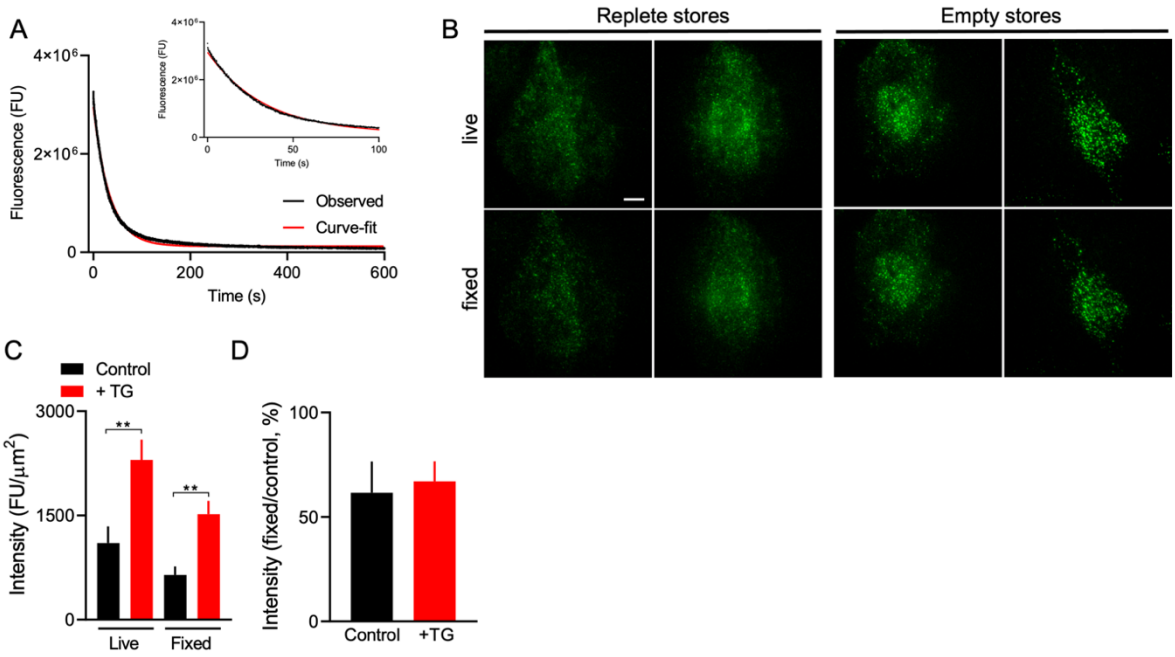

Figure 3.8 Negligible effect of pre-bleaching on finding cells and fixation on puncta aggregation. A. Fluorescence of STIM1-EGFP HeLa cells was recorded during continuous illumination with low laser power (6%) and the sum of fluorescence intensities of all puncta within one cell was plotted against time. The black line indicates the observed trace, and the red line is an exponentially fitted curve, where the half-life ($t_{1/2}$) is determined. Inset shows enlarged trace of the first 100 s. Results show the time-course of the decay in fluorescence from a single cell (typical of 3 cells from one experiment). $t_{½}$ = 30 ± 6 s. **B.** TIRF images of STIM1-EGFP HeLa cells before and after fixation (4% PFS in PBS, 15 min, followed by washing) with replete stores (HBS) or empty stores (TG, 1 µM, 15 min in Ca^{2+}-free HBS). Scale bar = 10 µm. **C.** Summary results show the sum of the fluorescence intensities of all STIM1 puncta in each cell, FU/µm^2. n = 10 cells for each condition. Mean ± SEM. $^{**}P < 0.01$, Student's unpaired t-test. **D.** Summary results show the fluorescence intensity of STIM1 puncta for each individual cell before and after fixation for control cells or cells treated with TG. No significant difference, Student's unpaired t-test.

before photobleaching and it caused negligible pre-bleaching, which was quantified by bleaching the target cell using low laser and the sum of fluorescence intensities of all puncta versus time was plotted. Ideally the curve should follow an exponential decay, from which a half-life ($t_{1/2}$) can be calculated and hence how much fluorescence was lost in 3 s. Results show that during the 3 s pre-bleach with low laser power, no more than 7% of the initial fluorescence of puncta was lost (***Figure 3.8A***).

It has also been reported that the fixation step before photobleaching can cause store depletion and activate SOCE (Demuro *et al.* 2011; Perni *et al.* 2015). Therefore, it is important to ensure that fixation does not affect the final results. STIM1-EGFP HeLa cells, either with replete or empty stores, were fixed on-stage carefully and images before and after fixation of the same cell were taken (***Figure 3.8B***). The results demonstrate that fixation of cells for immunofluorescence and photobleaching causes some loss of fluorescence (***Figure 3.8D***), but it does not promote accumulation of STIM1 or activate SOCE (***Figure 3.8C***).

After confirming that the effect of pre-bleaching is negligible, the actual stepwise photobleaching and associated analysis can be safely conducted (***Section 3.2.6***). Results show that STIM1-EGFP HeLa cells with empty store (TG, 1 μM, 15 min in Ca^{2+}-free HBS) contains an average of 5.82 ± 0.31 fluorophores per punctum (***Figure 3.9A and B***). Due to the nature of photobleaching, not all puncta are amenable to stepwise photobleaching analysis, but those that resolve a clear final bleaching step (365/1477, ~25%) have similar fluorescence intensity distributions and mean intensities compared to all puncta (***Figure 3.10A and B***). These results demonstrate that the puncta amenable to analysis are an unbiased sample of all STIM1-EGFP puncta. It has been suggested that only ~80% EGFP tags can be detected as fluorophores (Ulbrich and Isacoff 2007), from which the average number of STIM1-EGFP fluorophores in each punctum can be calculated to be 7.28 ± 0.39.

Since only half of STIM1 are tagged with EGFP (***Figure 2.8***), hence visible under microscope, and that STIM1-EGFP mix indistinguishably with native STIM1 in puncta (***Figure 2.11, Figure 3.7***), this number further increases to give an average of 14.55 ± 0.79 STIM1 molecules in each punctum (***Figure 3.9C***). Similar experiments and analyses were done on STIM1-EGFP cells with replete stores (***Figure 3.9D***), and results suggest an average of 3.51 ± 0.21 fluorophores within each STIM1-EGFP punctum before Ca^{2+} store depletion. After a similar calculation, it becomes an average of 8.8 ± 0.5 STIM1-EGFP proteins per punctum in unstimulated cells (***Figure 3.9E***).

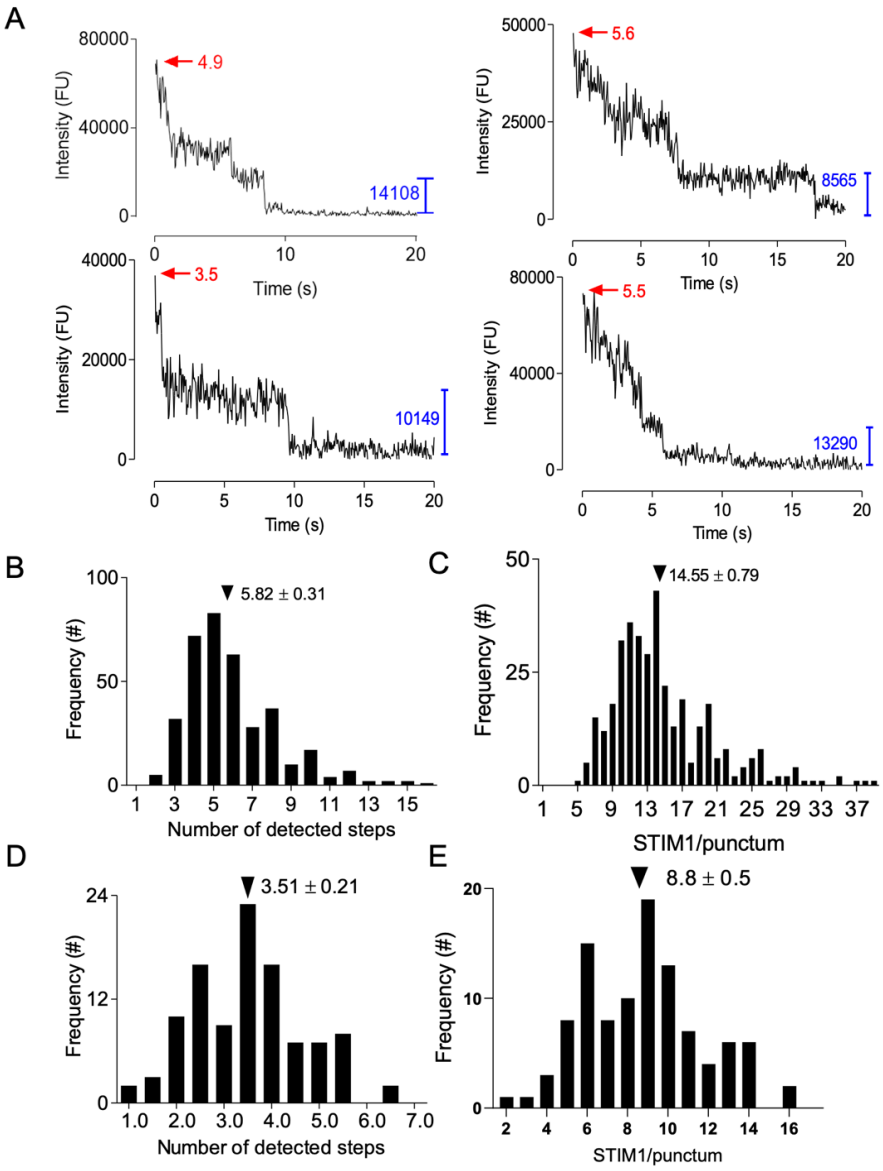

Figure 3.9 Stepwise photobleaching analysis of STIM1 puncta. A. Example time-course photobleaching traces of 4 STIM1-EGFP puncta in a cell with empty Ca^{2+} store with a clear final bleaching step. The amplitudes of the final step (blue) and calculated number of steps (red) are shown. **B.** Frequency distribution of the calculated number of bleaching steps from STIM1-EGFP puncta in cells with empty Ca^{2+} stores. Results are from 365 puncta across 5 cells from 3 independent experiments. Mean (± SEM) number of steps/punctum is shown. **C.** Frequency distribution of the calculated (from ***panel B***) number of STIM1 proteins per punctum in STIM1-EGFP HeLa cells with empty stores. Mean (± SEM) number of STIM1 proteins/punctum is shown. **D.** Frequency distribution of the calculated number of bleaching steps from STIM1-EGFP puncta (steps/punctum) in cells with replete Ca^{2+} stores. Results (mean ± SEM) are from 107 puncta across 3 cells from one experiment. **E.** Frequency distribution of the calculated (from ***panel D***) number of STIM1 proteins per punctum in STIM1-EGFP HeLa cells with full stores. Mean (± SEM) number of STIM1 proteins/punctum is shown.

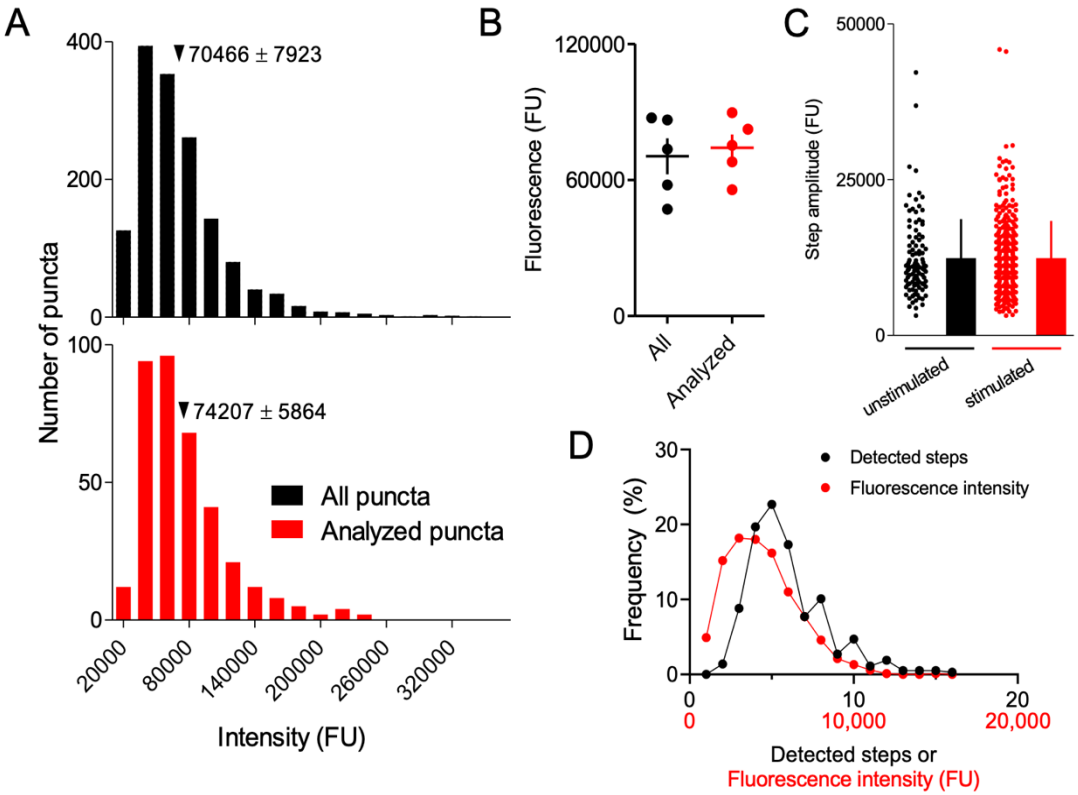

Figure 3.10 Characterization of stepwise photobleaching. A. Fluorescence intensity distributions of all puncta (1477 puncta) and those amenable to photobleaching analysis (with a clear final bleaching step, 365 puncta). Results are from 5 STIM1-EGFP HeLa cells treated with TG (1 µM, 15min in Ca^{2+}-free HBS). Mean ± SEM is shown. **B.** Summary results (mean ± SEM, n = 5 cells) show mean fluorescence intensities of all STIM1 puncta and those amenable for photobleaching analysis, P > 0.05, Student's t-test. **C.** Summary results (individual values and mean ± SD) show the amplitude of the final bleaching step of STIM1-EGFP puncta in cells with replete Ca^{2+} stores (107 puncta from 3 cells) and in cells with empty Ca^{2+} stores (365 puncta from 5 cells). P > 0.05, Student's t-test. **D.** Frequency distributions of the numbers of calculated bleaching steps/punctum for STIM1-EGFP puncta in cells with empty Ca^{2+} stores (from **B**, 365 puncta from 5 cells) and of the fluorescence intensities of the individual puncta (from ***Figure 3.6C***, 1891 puncta from 5 cells). For each distribution, observations are reported as percentages of the entire population, which were categorized into 16 bins.

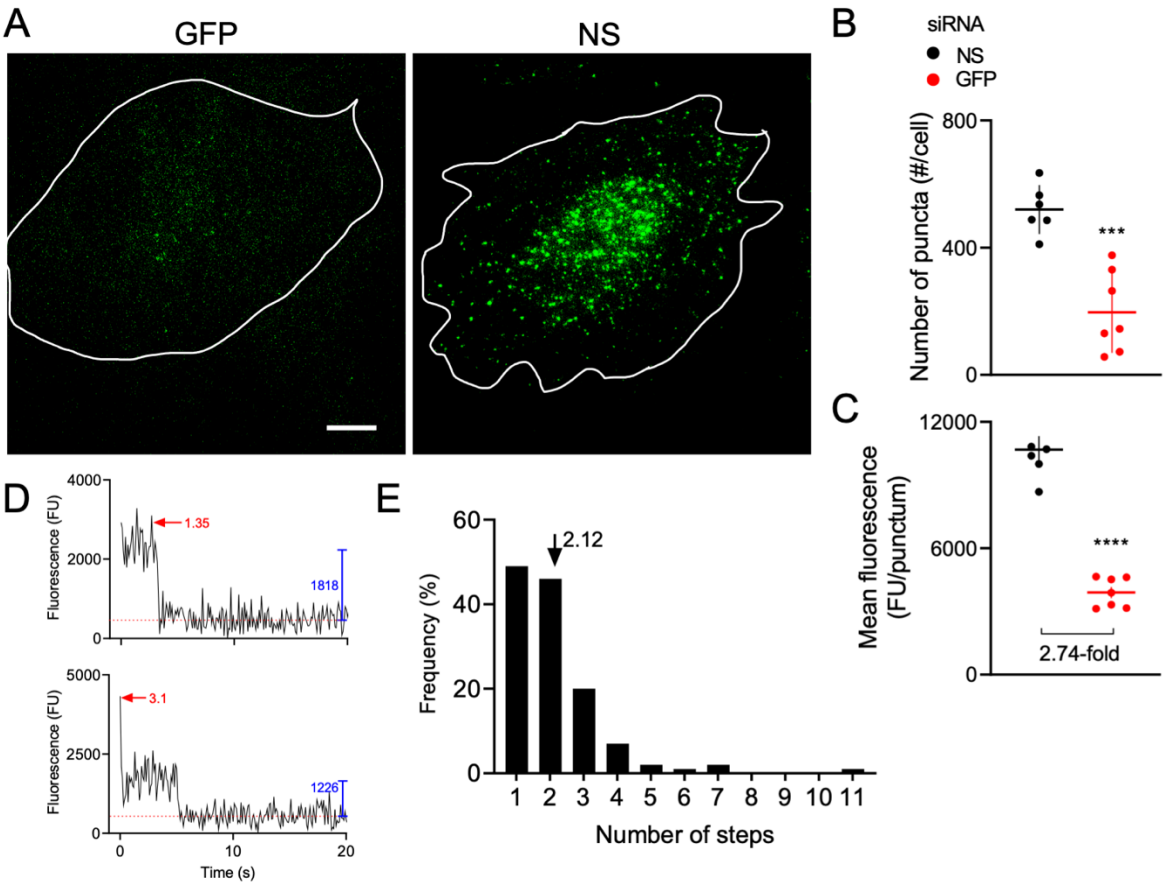

Figure 3.11 Similar results can be achieved by calibrating against cells treated with GFP-siRNA. A. TIRF images of STIM1-EGFP HeLa cells treated with either GFP-siRNA or NS (non-silencing) siRNA for 72 h and then treated with TG (1 µM, 15 min in Ca^{2+}-free HBS) to deplete stores. Scale bar = 10 µm. **B.** Summary results (mean ± SD, *n* = 6-7 cells from 2 independent experiments) of number of STIM1-EGFP puncta in cells treated with either GFP-siRNA or NS siRNA. **C.** Summary results (mean ± SEM, *n* = 6-7 cells) of mean fluorescence intensities of the puncta. $^{****}P < 0.0001$, $^{***}P < 0.001$, Student's unpaired t-test. The code in B applies also to panel C. The difference in mean intensities for cells treated with NS and GFP siRNA is shown. **D.** Example time-course photobleaching traces of STIM1 puncta in cells treated with GFP-siRNA. The amplitudes of the final step (blue) and calculated number of steps (red) are shown. **E.** Summary results (128 puncta from 3 cells from 2 independent experiments) show the number of fluorescence steps calculated in cells treated with GFP-siRNA with empty Ca^{2+} stores. The mean value is shown.

The frequency distributions of calculated bleaching steps were compared with that of fluorescence intensities of STIM1 puncta summarized in ***Figure 3.6C***, where both distributions share a similar general shape (***Figure 3.10D***), suggesting that the variability in the size of puncta (***Figure 3.7C, Figure 3.9C, Figure 3.10A***) is an intrinsic feature of the puncta instead of the limitation from photobleaching analyses.

A complementary approach was also carried out, where STIM1-EGFP cells were treated with siRNA against EGFP, attempting to reduce the number of fluorophores of each visible STIM1 to close to one, so that the fluorescence intensities of resulting STIM1 puncta can be used as a calibration signal (***Figure 3.11***). The fluorescence intensity distributions of 'native' STIM1-EGFP puncta with the 'calibration' signal can then be compared to estimate the number of fluorophores in each STIM1 punctum. Results showed that treatment of siRNA against EGFP diminished the fluorophore content of each residual punctum to an average of 2.12 fluorophores, demonstrated by stepwise photobleaching (***Figure 3.11D and E***). Furthermore, the mean fluorescence of native STIM1 puncta is 2.74-fold compared to siRNA treated ones (***Figure 3.11C***). These two numbers were combined to provide a similar estimate of the number of fluorophores per punctum (2.74 × 2.12 = 5.81) in cells treated with non-silencing siRNA and with empty Ca^{2+} stores. Due to the same limitation of EGFP detection efficiency and single edit of STIM1, this suggests a mean value of 14.52 STIM1 proteins/punctum in cells with empty Ca^{2+} stores. This is very similar to the result directly obtained from stepwise photobleaching (***Figure 3.9C***).

The enrichment of STIM1 puncta in the ER-PM junctions after Ca^{2+} store depletion was also examined in WT HeLa cells, with immunostained STIM1 puncta (***Figure 3.12***). Results indicated that the increase in the average fluorescence intensity of the entire TIRF footprint is 56% (from 4867 to 7608 FU/μm^2, respectively, ***Figure 3.12A and B***) and that of individual STIM1 punctua is 55% (from 7138 to 11056 FU/punctum, respectively, ***Figure 3.12C***) upon store depletion.

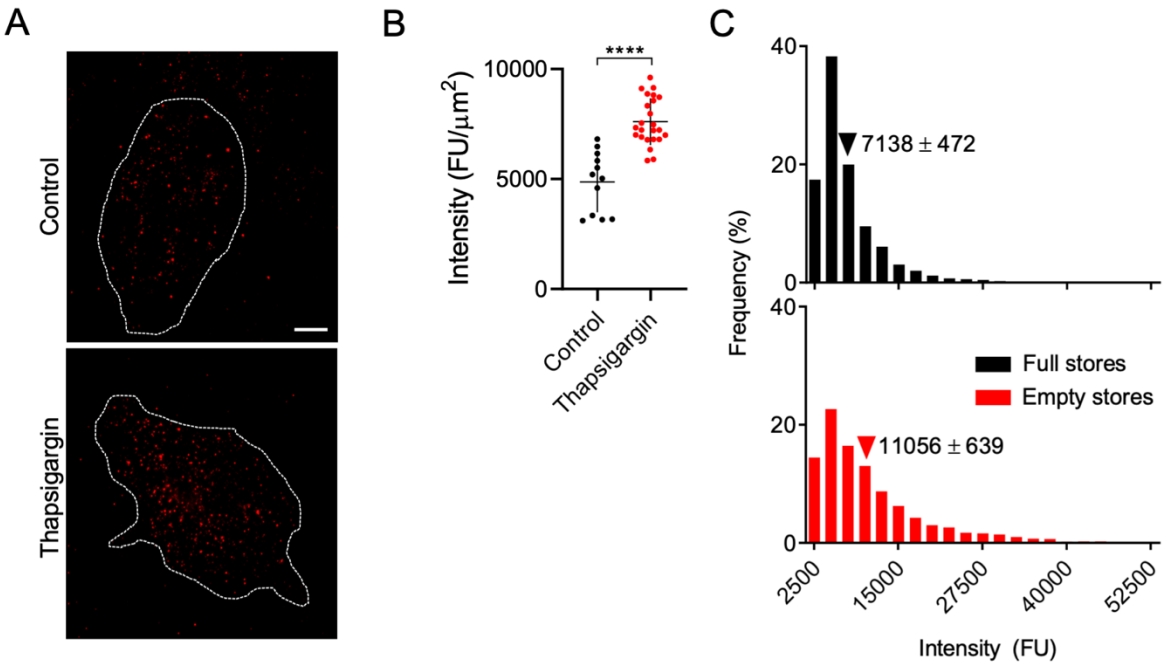

Figure 3.12 Fluorescence intensity of STIM1 puncta in WT HeLa cells. A. WT HeLa cells treated with either HBS or TG (1 µM, 15 min in Ca^{2+}-free HBS) were immunostained using STIM1 antibody followed by AlexaFluor 594. Scale bar = 10 µm. **B.** Summary results (individual values from 12 control cells and 24 TG-treated cells from 3 independent experiments, mean ± SD) show background-corrected whole-cell TIRF fluorescence from each cell. $^{****}P < 0.0001$, Student's t-test. **C.** Fluorescence intensity distributions of immunostained STIM1 puncta in WT HeLa cells with full and empty Ca^{2+} stores. Results (6 cells for each condition, 3419 puncta from cells with full stores, and 3804 puncta from cells with empty stores) show mean ± SEM, $^{***}P < 0.001$, Student's t-test.

3.4. Discussion

Overexpressed C-terminal tagged STIM1 has been widely used before the development of CRISPR-mediated gene-editing and it was proven that the C-terminal tag does not affect the functionality of STIM1 (Calloway *et al.* 2009; Lur *et al.* 2009; Korzeniowski *et al.* 2016). However, given the functional importance of the C-terminus of STIM1 (Ercan *et al.* 2009; Park *et al.* 2009; Stathopulos *et al.* 2013), it is essential to perform comprehensive characterization on the heterozygous STIM1-EGFP HeLa cell line, confirming not only the correct position of the EGFP tag, but also that the functions of STIM1-EGFP are not masked by native STIM1. It has been confirmed by in-gel fluorescence (***Figure 2.9B***) and TIRF imaging combined with siRNA against STIM1 (***Figure 3.3***), that STIM1-EGFP is the only fluorescent protein in the STIM1-EGFP HeLa cell line. Due to the fact that only half of the STIM1 proteins have been endogenously tagged by EGFP (***Figure 2.8***), it was also essential to make sure that EGFP-tagged STIM1 mix interchangeably with untagged native STIM1, which is shown in ***Figure 3.7*** and ***Figure 2.11***.

From the result of stepwise photobleaching, each punctum in cells with full Ca^{2+} stores contain an average of 8.8 STIM1 proteins (***Figure 3.9D***), and this number increases to about 14.5 after store depletion induced by TG (***Figure 3.9C***), confirmed also by the complementary approach using EGFP siRNA (***Figure 3.11***). In comparison with the stimulated cells, there is only a modest increase (~50%) in the average number of STIM1 proteins within each punctum (from ~10 to ~15). This result is similar to the estimate from mean fluorescence intensity of puncta (138% increase, ***Figure 3.6C***). This conclusion is further confirmed by analyses of immunostained STIM1 puncta in WT HeLa cells, where the increase in both whole-cell fluorescence intensity (to 156%, ***Figure 3.12A and B***) and mean fluorescence intensity of individual STIM1 puncta (to 155%, ***Figure 3.12C***) are comparable to the increase in EGFP fluorescence in STIM1-EGFP HeLa cells (to 148%, ***Figure 3.6A***, and to 138%, ***Figure 3.6C***, respectively).

Since about half of STIM1 puncta in store-depleted cells are already present near the plasma membrane before store depletion (***Figure 3.4-3.6***), it has been considered whether this might cause the substantial underestimation of the size of puncta formed after ER Ca^{2+} depletion induced by thapsigargin. Therefore, using the 'difference' plots (***Figure 3.6C and D***), if only those 'additional' puncta are included in the analyses, the estimate of the average number of STIM1 molecules in each punctum in store-depleted cells will increase from 14.5 to 18.5

STIM1. Even if assuming that the brightest 50% of puncta were formed exclusively after store depletion, the estimate of the average number of STIM1 molecules per punctum would become only 19.0 (***Figure 3.10A***). Consequently, it can be concluded that in cells with empty Ca^{2+} stores, native puncta contain rather few STIM1 molecules. There is variability between puncta (***Figure 3.9B and C, Figure 3.10A***), but the variability arises from puncta containing different numbers of STIM1 molecules, hence is the nature of the puncta rather than coming from photobleaching analyses (***Figure 3.10D***). This can be confirmed by fluorescence intensity distributions of puncta without photobleaching analyses (***Figure 3.6C and Figure 3.7C***), where similar variability can be observed with STIM1-EGFP puncta and immunostained WT and STIM1-EGFP puncta. In cells with empty stores, the vast majority of puncta (99.5%) contain at least 6 STIM1 proteins, but only 15.6% contain more than 20 STIM1 and only 2.2% have more than 30 (***Figure 3.10A***). Given these relatively small numbers, it can be concluded that most STIM1 clusters formed after store depletion are comprised of a small number of STIM1 molecules. It can therefore be deduced that there is little chance for most STIM1 clusters to activate more than one Orai1 channel. This will be investigated in more detail later in ***Chapter 4***.

Results suggest that in cells treated with TG to deplete their Ca^{2+} stores, STIM1 and STIM1-EGFP only form small clusters (***Figure 3.5-3.6, 3.9-3.12***). There are on average seven STIM1 dimers and a single Orai1 channel present in each SOCE complex. Regarding the binding models between STIM1 and Orai1, a monomeric and a dimeric model were proposed where

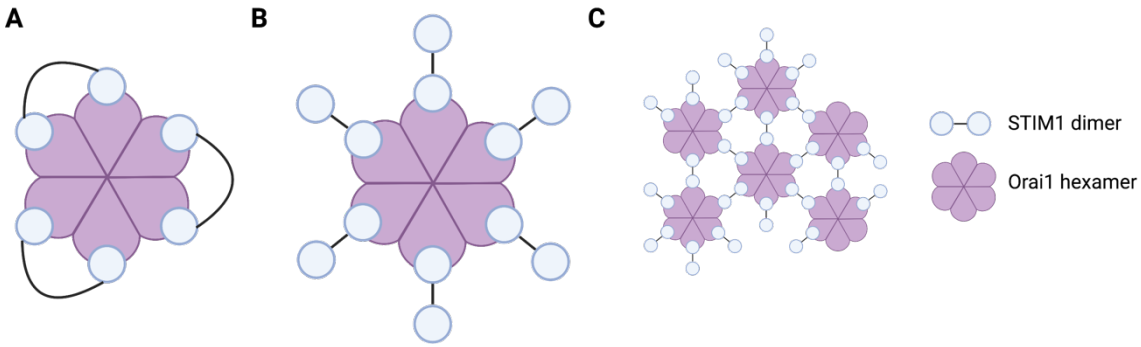

Figure 3.13 Schematic of proposed structures of SOCE complexes. Orai1 is a hexamer, comprising three pairs of dimers (Hou *et al.* 2018). Dimeric STIM1 may activate Orai1 by binding as **A.** three dimers, or **B.** as six dimers, **C.** with the residual STIM1 subunit free to interact with another Orai1 channel (Zhou *et al.* 2018). Image reproduced from *Shen et al. (2021)*.

each STIM1 dimer binds to one or two subunits of a hexameric Orai1 channel, respectively, but both of the models have some evidence yet neither very convincing, discussed in ***Section 1.4*** (***Figure 3.13***). However, since each SOCE junction typically comprises an average of only seven STIM1 dimers, in which only ~2% of them containing more than 15 dimers (***Figure 3.9C***), there would hardly be any chance for the crosslinking of active Orai1 channels by STIM1 as reported in cells over-expressing STIM1 (Ji *et al.* 2008; Perni *et al.* 2015; Zhou *et al.* 2018). Cross-linking is only possible if Orai1 can be activated by binding fewer STIM1, but other evidence has suggested that all six subunits of Orai1 must be occupied by STIM1 to be fully activated (Yen and Lewis 2018). Hence, it can be concluded that most native puncta in store-depleted cells contain only enough STIM1 to activate no more than two Orai1 channels assuming each STIM1 dimer binds two subunits of an Orai1 channel (***Figure 3.13A***), and only one Orai1 channel if each subunit binds its own STIM1 dimer, leaving one of STIM1 molecules in the dimer free (***Figure 3.13B***).

These estimates did not consider any contribution from STIM2. STIM2 has a similar luminal region with STIM1, but a rather different C-terminus, both genetically and functionally (Williams *et al.* 2001; Wang *et al.* 2014). It also responds to decrease in $[Ca^{2+}]_{ER}$ and aggregate into puncta in the ER-PM junctions (Brandman *et al.* 2007; Bandyopadhyay *et al.* 2011; Ong *et al.* 2015). There is evidence of STIM2 aggregating with STIM1 that promotes the assembly of STIM1 and Orai1 (Ong *et al.* 2015; Subedi *et al.* 2018), while overexpression of STIM2 inhibits the association of STIM1 and Orai1 (Soboloff *et al.* 2006). The STIM1/STIM2 association could also contribute to the stoichiometry of the puncta, but the expression of STIM2 is only 7.7% that of STIM1 in HeLa cells (Hein *et al.* 2015), the effect of which should be minimal.

There might be concerns arising regarding the reliability of stepwise photobleaching method used to characterize the number of STIM1 molecules in each punctum, since one of the evidence in revealing the wrong structure of Orai1 tetramer was also stepwise photobleaching (Ji *et al.* 2008). Although single molecule stepwise photobleaching has been utilized for several years and has successfully resolved the stoichiometry of many protein multimers (Ulbrich and Isacoff 2007; Yu *et al.* 2009; Zhang *et al.* 2009), one of the major weaknesses of stepwise photobleaching lies in about 80% of traces not resolvable (Ji *et al.* 2008). This is also true in my own experience, albeit it was confirmed that those resolvable puncta have similar fluorescence distributions compared with all puncta (***Figure 3.10A and B***). Additionally, the distinct bleaching steps become more difficult to be distinguished with

increasing number of subunits due to large noise resulted from blinking of GFP fluorescence (Dickson *et al.* 1997). Therefore, a complementary method was applied to reduce the number of fluorophores within each punctum as far as possible using an EGFP siRNA, which indeed diminished the average number of bleaching steps to ~2 that should be resolvable more easily (***Figure 3.11***). Combined with the mean fluorescence intensity reduced by 2.74-fold, the calculation results in similar average bleaching steps in 'native' STIM1-EGFP puncta compared with the number obtained directly from stepwise photobleaching (***Figure 3.9B***). in summary, the average bleaching steps of ~5.8 and subsequent ~14.5 STIM1 dimers/punctum are reliable.

Additional problems can be associated with the use of TIRFM, because of its relatively low resolving power. The theoretical lateral resolution calculated from ***Equation 1*** gives ~200nm (for GFP), and each pixel in all images in this project represents 160 nm, which is not enough to distinguish two puncta close to each other within about 200 nm. Indeed, super resolution microscopy such as STORM can resolve multiple puncta present in one large punctum observed in TIRF (Huang *et al.* 2008; Jones *et al.* 2011; Thillaiappan *et al.* 2017). Therefore, those puncta containing more than ~20 STIM1 molecules may be constructed by more than one punctum, which potentially skews the average number of STIM1 molecules towards a greater number. Although STORM itself cannot provide direct stepwise photobleaching, TIRF and STORM can probably be combined, so that all STIM1 puncta can first be photobleached using TIRF and then the finer distribution of puncta can be resolved in STORM, using a different fluorophore, to get a more accurate average number of bleaching steps, hence number of STIM1 molecules per punctum.

Chapter 4 SOCE junctions include only a single Orai1 channel associated with a small cluster of STIM1

4.1. Introduction

Once the intracellular Ca^{2+} store has been emptied either physiologically or pharmacologically, the loss of Ca^{2+} is detected by the STIM1 proteins sitting in the ER (Liou *et al.* 2005; Zhang *et al.* 2005). STIM1 aggregates into clusters via interactions between the luminal regions, especially the EF-SAM domains (Stathopulos *et al.* 2006). This is followed by relocation of STIM1 clusters to the ER-PM junctions (Liou *et al.* 2007; Luik *et al.* 2008) to interact with the other main player in the SOCE, Orai1, by directly binding (Park *et al.* 2009). Based on the molecular structure of the Orai1 hexamer (Hou *et al.* 2012), the cytosolic extension of its M4 helices (M4ext) on the carboxyl terminus project into the cytosol and bind the CAD/SOAR domain of STIM1, which is both sufficient and necessary for Orai1 activation (Zhou *et al.* 2010). The essential role of the M4ext in STIM1:Orai1 interaction has been confirmed by mutagenesis (Navarro-Borelly *et al.* 2008) or deletion (Li *et al.* 2007; McNally *et al.* 2013) of this region which completely or partially impair Orai1 activation.

The involvement of the N-terminus of Orai1 in directly binding to STIM is contentious. Some studies provided evidence that the N-terminus of Orai1 affects pore opening without directly interacting with STIM1 (Li *et al.* 2007; Muik *et al.* 2008). However, others argued that STIM1 has to interact with both the N- and C-terminus of Orai1 for channel activation (Derler *et al.* 2013; McNally *et al.* 2013; Palty and Isacoff 2016). Deletion of the 73-90 residues of Orai1 region (named ETON), abolishes SOCE by interrupting the STIM1-Orai1 association and subsequent channel activation (Derler *et al.* 2013; McNally *et al.* 2013; Derler *et al.* 2018). A third model was proposed that five residues in the C-terminus of Orai1 form the 'nexus', which binds to STIM1 and remotely control the pore helix without the need to directly interact with the N-terminus of Orai1, through transducing conformational changes (Zhou *et al.* 2017).

Apart from the obvious functions of STIM1 binding to Orai1, namely activation of SOCE, STIM1 also affects Orai1 in multiple ways. One example is the ion selectivity of CRAC channels. The high Ca^{2+} selectivity, which is one of the signatures of SOC channels, is only bestowed by STIM1 binding (McNally *et al.* 2012), probably in a stoichiometric way (Scrimgeour *et al.* 2009). It was also shown more directly that the occupancy of all six subunits

of Orai1 channel not only effectively opens the pore, but also generates extremely low conductance and high Ca^{2+} selectivity of Orai1 channels (Yen and Lewis 2018). These observations indicate that the stoichiometry of STIM1 binding to Orai1 has a significant impact on the mechanism of SOCE, from trapping Orai1 channels and regulating their activation and inactivation gating to modification of their pore structure to achieve their specific ion selectivity and conductance.

All these interactions between STIM1 and Orai1 occur at the close appositions between the ER and the plasma membrane, known as the ER-PM junctions (Liou *et al.* 2005; Wu *et al.* 2006). They were first discovered in muscle cells more than 60 years ago (Porter and Palade 1957), but it was not until the discovery of STIM1 and its activity during SOCE when the functions and significance of ER-PM junctions became resurgent. It was shown in early research on the SOCE complex that Orai1 can form a complex with STIM1 in space between 9 nm and 14 nm (Varnai *et al.* 2007), which corroborates evidence from electron microscopic analysis of the size of gaps (10-25 nm, with an average of 17 nm) between ER and PM contact sites (Wu *et al.* 2006). Both the number and size of ER-PM junctions increase by thapsigargin-induced STIM1 translocation in STIM1-overexpressed cells (Orci *et al.* 2009), which becomes another reason to avoid overexpression to study the behaviour of STIM1 under endogenous environment.

Since the discovery of Orai1 as the essential pore subunit of the Ca^{2+}-release-activated Ca^{2+} (CRAC) channel by a number of research groups independently (Feske *et al.* 2006; Vig *et al.* 2006; Zhang *et al.* 2006), there are various investigations on the behaviour of Orai1 channels both at rest and upon store depletion. Transfection of Orai1-EGFP (Xu *et al.* 2006; Gwozdz *et al.* 2008) into cells was widely used for optical analyses, which generally showed obvious clustering of Orai1 channels upon store depletion. Other microscopy techniques such as liquid phase electron microscopy (LPEM) also suggested that Orai1 predominantly relocates within the plasma membrane into puncta and appears to form elongated clusters (Peckys *et al.* 2021). Western blots and biotinylation reported enhanced surface expression of Orai1 after treatment with thapsigargin (Woodard *et al.* 2008), which agrees with the 'trafficking trap' model proposed by Hodeify *et al* (Hodeify *et al.* 2015), where clustered STIM1 recruits Orai1 from vesicles in close proximity to the PM to relocate to the plasma membrane upon store depletion at intermediate STIM1 expression level. In contrast, despite the wrong tetramer structure of Orai1 they defined, Ji *et al.* demonstrated that active Orai1 channels do not aggregate into larger clusters but form single puncta or small clusters instead (Ji *et al.* 2008). Evidence from

electron microscopy (EM) indicated a lack of Ca^{2+}-mediated interactions between native Orai1 channels (Perni *et al.* 2015) as well. However, these investigations all have their own limitations. The phenomena of Orai1 channel clustering were much observed in cells with overexpressed proteins, which may have the tendency to aggregate into puncta, or even cross-link, while controversial methods were adapted in the other researches, like small sample sizes (91 events from 2 cells) and stepwise photobleaching on Orai1 tandem constructs which leads to the wrong tetramer structure (Ji *et al.* 2008).

The stoichiometry of STIM1-EGFP puncta has been revealed in ***Chapter 3***, and I have discussed the proposed models about monomeric or dimeric binding of STIM1 to Orai1 hexamers. Next, I would like to further confirm this conclusion from the other perspective. That is, since endogenous STIM1 can only form clusters enough to activate no more than two Orai1 channels, do Orai1 channels cluster upon store depletion? Therefore, since *Orai1* has not been gene-edited to contain an endogenous fluorescent label, the native Orai1 proteins are immunostained with verified primary antibody followed by fluorescently conjugated secondary antibody to assess the clustering activity after Ca^{2+} store depletion. The colocalization of Orai1 and STIM1-EGFP as well as the relationship between SOCE complexes and MCS will also be examined.

4.2. Materials and Methods

Many materials and methods used in this chapter have already been described ***Sections 2.2 and 3.2***.

4.2.1. Materials

Table 4.1 Materials

Materials	**Company**	**Catalog Number**
AllStars Negative Control siRNA	QIAGEN	Cat# 1027281
Goat anti-rabbit IgG-AlexaFluor 647 antibody (AbRa647, IC: 1:500)	ThermoFisher	Cat# A21244 RRID: AB_2525812
Orai1 siRNA1	ThermoFisher	Cat# AM16708 siRNA ID 216908
Orai1 siRNA2	ThermoFisher	Cat# 4392420 siRNA ID s228396
Orai1 siRNA3	ThermoFisher	Cat# 1299001 siRNA ID HSS131373
Rabbit anti-Orai1 (anti-peptide antibody to N-terminal) (WB, 1:1000; IC, 1: 200)	ProSci Inc, Poway, CA	Cat# 4041 RRID: AB_735415
GFP-MAPPER in pcDNA3.1+		(Chang *et al.* 2013)
mCh-MAPPER in pcDNA3.1+		(Thillaiappan *et al.* 2017)

4.2.2. Double immunostaining

Double immunostaining for both Orai1 and STIM1 (***Figure 4.9-4.10***) required primary antibodies that were both raised in rabbits. Cells grown to ~70% confluency were washed with PBS twice, then fixed by paraformaldehyde (4% in PBS, 15 min, 20 °C). Cells were then washed 3 times, permeabilized in PBS containing Triton X-100 (0.1%, 15 min, 20 °C), and washed 3 times. After blocking by skimmed milk (5% in PBS, 30 min, 20 °C) and BSA (5% in PBS, 30 min, 20°C), cells were first stained for STIM1 with the primary and secondary Ab (AbRa647) (***Section 3.2.3***), washed with PBS (5 × 15 min with gentle agitation), and then stained for Orai1 using a different secondary Ab (AbRa594). It has been confirmed that the washing steps were good enough to allow selective immunostaining of STIM1 and Orai1 by absence of the primary Orai1 Ab (***Figure 4.1***).

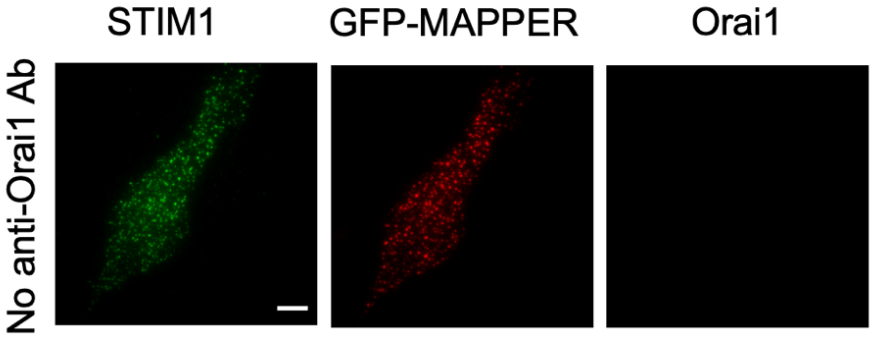

Figure 4.1 The specificity of dual immunostaining. TIRF images of WT HeLa cells with empty Ca^{2+} stores expressing GFP-MAPPER and immunostained for STIM1 (AbRa647 for 2nd Ab) and Orai1 (AbRa594 for 2nd Ab) without Orai1 primary antibody. Scale bars = 10 µm.

4.2.3. Object-based colocalization analysis using DiAna

For analyses involving the distances between puncta to define colocalization, the Fiji plugin DiAna was used (Gilles *et al.* 2017). This algorithm identifies all local intensity maxima and then uses a threshold to select the local maximum for each punctum. Similar numbers of puncta can be identified in cells with full or empty stores by automated detection of puncta using either TrackMate or DiAna (***Figure 4.2A***), but different fluorescence intensities attributed to puncta are recognized by TrackMate or DiAna (***Figure 4.2B***). Most analyses of the fluorescence intensities of puncta used TrackMate. Only for those analyses prior to colocalization studies between STIM1 and Orai1, DiAna was used (***Figure 4.6***).

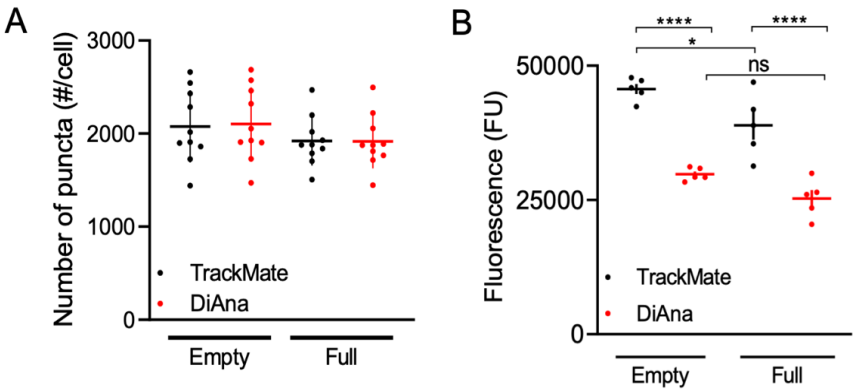

Figure 4.2 Automated identification of puncta by TrackMate or DiAna. A. Comparison of TrackMate and DiAna for automated identification of puncta. STIM1-EGFP HeLa cells with full or empty Ca^{2+} stores were immunostained for Orai1 (primary Ab 1:200), and puncta were identified in the same cells using either TrackMate or DiAna. Results show individual values from 10 cells from one experiment, mean ± SD. No significant difference, one-way ANOVA. **B.** Similar analysis of the mean fluorescence intensity of the puncta. Results show individual values from 5 cells, mean ± SEM. $^{****}P < 0.0001$, $^{*}P < 0.05$, ns $P > 0.05$, one-way ANOVA with Bonferroni test.

4.2.4. Quantification and statistical analysis

Analyses were performed without blinding or power calculations to predetermine sample sizes, except when analysing cells expressing MAPPERs (GFP- or mCh-) (***Figure 4.7-4.11***). MAPPER is a fluorescent marker which is constitutively present in the ER-PM junctions. In these analyses, the expression of MAPPER was first assessed and only those cells with 'acceptable' expression of MAPPER (***Figure 4.7A***) were identified before observing the STIM1-EGFP puncta. All sample sizes are described in figure legends. The statistical tests and significance levels are the same as ***Section 2.2.12***.

Colocalization studies used JACoP (for ER and STIM colocalization) (Bolte and Cordelieres 2006) or DiAna (for STIM1 and Orai1 colocalization) (Gilles *et al.* 2017) as described in ***Sections 3.2.5*** and ***4.2.3***, respectively. For the analyses with DiAna, since STIM1 and Orai1 puncta are not evenly distributed across the cell, 3-5 ROIs (together including ~55% of the TIRF footprint) were selected in each cell to exclude areas sparsely populated by Orai1 and STIM1 (***Figure 4.5A***). This selection criterion is required to allow valid determination of the statistical significance of any colocalization, where the distribution of STIM1 puncta was randomly shuffled for 100 times within each ROI and then distances between each Orai1 punctum and its nearest STIM1 punctum were re-assessed (Costes *et al.* 2004).

4.3. Results

4.3.1. siRNA-mediated protein knockdown confirms the specificity of Orai1 antibody

Since cell line with endogenously tagged Orai1 was not available yet, immunostaining against Orai1 was used to visualise Orai1 under TIRF microscope, even though the precise stoichiometry of Orai1 cannot be determined. Consequently, the specificity of Orai1 antibody need to be confirmed.

The combination of 3 siRNAs against Orai1 (or non-silencing siRNA) was used to knock down Orai1 (***Section 2.2.2***) and cells were imaged after 72h of treatment (***Figure 4.3A***). Although due to the efficiency of the siRNAs, not all cells experience successful knock-down, the fluorescence intensities of 46.7% (42 out of 90) of cells were lower than the lowest fluorescence intensity of cells treated with NS siRNA (***Figure 4.3B***). Hence, these results demonstrate the selectivity of the antibody for immunostaining of Orai1.

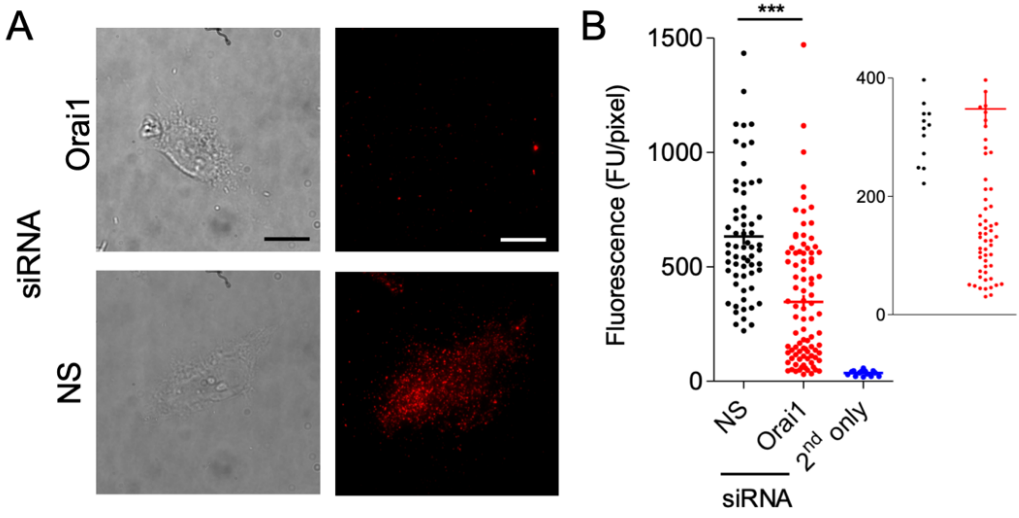

Figure 4.3 Orai1 antibody only binds to Orai1. A. Brightfield and TIRF images of unstimulated WT HeLa cells immunostained for Orai1 after treatment with NS or Orai1 siRNA. Scale bar = 10 µm. **B.** Summary results show whole-cell immunofluorescence for cells treated with non-silencing (NS) or siRNA against Orai1 or treated with only secondary Ab (AbRa594) (individual values, mean ± SD, n = 3 independent treatments). FU, fluorescence unit. $^{***}P < 0.0001$, Student's t-test. Inset shows enlarged lower part of the graph.

4.3.2. Orai1 antibody can recognize Orai1 clustering if exists

An essential property of the antibody that needs to be confirmed for comparison of the sizes of Orai1 clusters before and after store depletion is whether the Orai1 antibody binds to Orai1 channels 'densely' or 'sparsely'. In other words, whether the Orai1 antibody could detect clustering of channels. If the antibody can only bind to Orai1 sparsely (for example with only 1 in 10 Orai1 channels recognized by the antibody, ***Figure 4.4A***), then even if Orai1 forms clusters, it would not be reflected by an increase in the fluorescence intensity, but only increase in the chance for a cluster to be recognized. To address this, cells with replete stores were immunostained with different dilutions of primary antibody (1:200 and 1:800, ***Figure 4.4B***). The argument is, if the dilution of primary Ab (1:200) which is normally used for immunostaining Orai1, can achieve 'dense' labelling, reducing the concentration of primary Ab to 1:800 should reduce the mean fluorescence intensity of immunostained Orai1 puncta.

Results show that the mean intensity of each punctum and the number of puncta detected from immunostaining with more diluted primary antibody (1:800) are significantly lower relative to the usual dilution of primary Ab (1:200) (***Figure 4.4C***). A mathematical model was also generated (***Figure 4.4D***), assuming each unstimulated cell has N Orai1 puncta, each with n binding sites for Orai1 Ab; Ab binds independently to each binding site; and $n = 6$ in an unstimulated cell because Orai1 channels are hexamers (Hou *et al.* 2012). A 4-fold dilution of the primary Ab (from 1:200 to 1:800) causes the TIRF immunofluorescence of each cell to decrease to 20.9 ± 3.9% (mean ± SD, $n = 6$ cells, ***Figure 4.4C***), which is not significantly different from the 25% expected with a linear relationship between Ab concentration and immunostaining. Therefore, it can be assumed that the probability of Ab binding to a single epitope is P1 for the 1:800 dilution and 4P1 for the 1:200 dilution. From the binomial distribution, the probability ($P_{discovery}$) of the Ab identifying any of the 6 sites within a punctum is: $P_{discovery} = 1 - (1 - P1)^6$ for 1:800 and $P_{discovery} = 1 - (1 - 4P1)^6$ for 1:200. With the 1:800 dilution, the number of puncta detected is 54.5% of the number detected with the 1:200 Ab dilution (***Figure 4.4C***). Hence,

$$0.545 = \frac{P_{1:800\ discovery}}{P_{1:200\ discovery}} = \frac{1 - (1 - P1)^6}{1 - (1 - 4P1)^6}$$

from which, solving by iteration, P1 = 0.119.

With P1 = 0.119, $P_{discovery}$ for the conditions used for subsequent analyses of fluorescence intensity distributions (primary Ab = 1:200; ***Figure 4.5 and 4.10***) = $1 - (1 - 4P1)^6 = 0.98$.

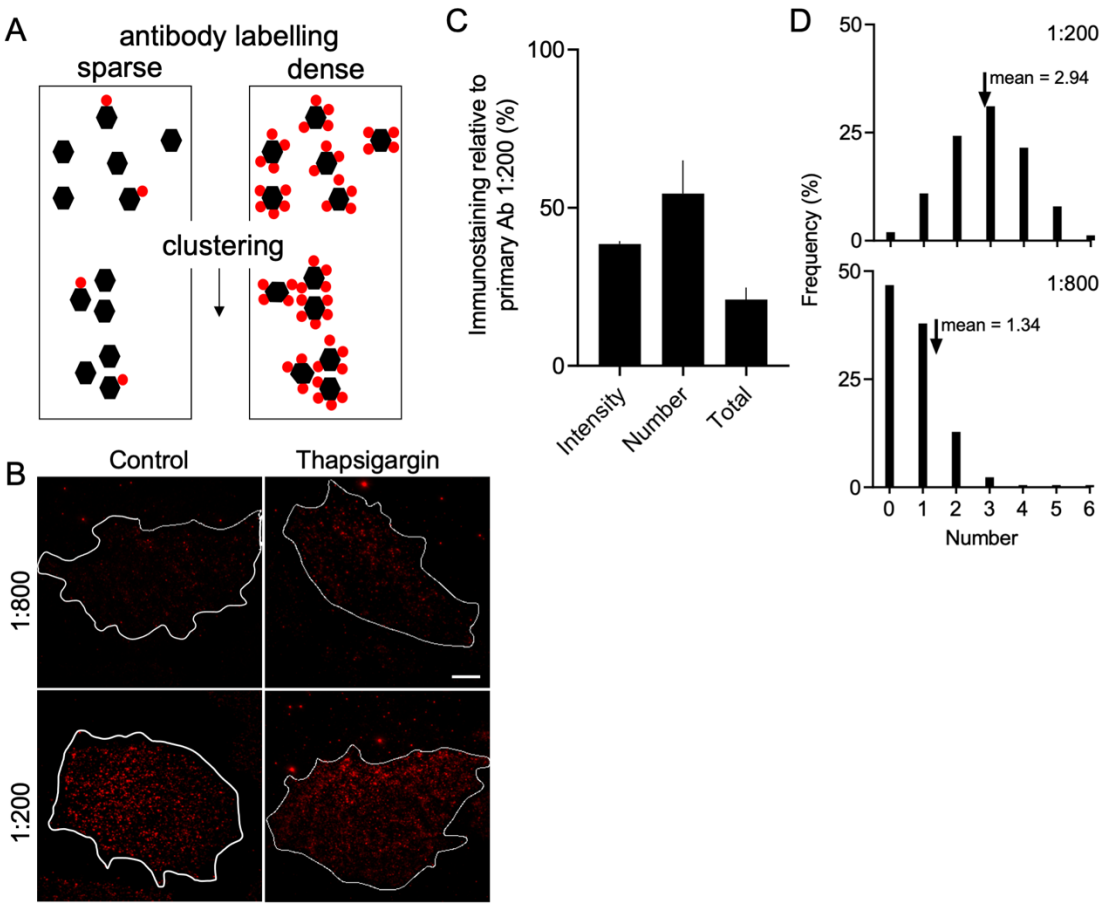

Figure 4.4 Orai1 antibody binds to Orai1 channels densely. A. Schematic of sparse labelling or dense labelling. The black hexamers represent Orai1 channels, and they are decorated by antibody (red). **B.** TIRF images of unstimulated STIM1-EGFP HeLa cells with replete (Control) or empty Ca^{2+} stores (Thapsigargin), each immunostained for Orai1 with two dilutions of primary Ab. Scale bar = 10 µm. **C.** Summary results (n = 6 cells from 3 independent experiments) for unstimulated cells show mean intensity (FU/punctum), number (#/cell) of puncta and total fluorescence for the entire TIRF footprint of cells immunostained with the Orai1 primary Ab diluted 1:800 relative to 1:200. Results show values obtained with the 1:800 dilution relative to those with the 1:200 dilution (%), mean ± SEM (intensity) or mean ± SD (number of puncta and total fluorescence). Puncta were identified using TrackMate. **D.** Predicted frequency of detection of 0-6 subunits of an Orai1 channel with Ab dilutions of 1:200 and 1:800. Predicted mean fluorescence intensity of the detected puncta is shown for each dilution. The predicted values (1:800/1:200 = 46%) aligns with observed values (39%, C).

Therefore, most Orai1 puncta are expected to be detected, i.e., dense labelling, with very few 'missed events', and any clustering of Orai1 channels should be readily resolved as an increase in the fluorescence intensity of puncta.

4.3.3. Store depletion does not cause Orai1 channels to cluster

After confirmation of both the specificity of the antibody and its ability to resolve clustering of Orai1 by increased fluorescence intensity of immunostained Orai1, the number of Orai1 Ca^{2+} channels associated with a STIM1 punctum can be estimated using TIRFM after immunostaining for Orai1 before and after store depletion. It is expected that before store depletion, the distribution of fluorescence intensities for each immunostained spot likely indicates a single hexameric Orai1 channel recognized by antibody, while after store depletion, that determined for Orai1 colocalized with STIM1 reports the number of Orai1 channels associated with a SOCE complex.

STIM1-EGFP HeLa cells were immunostained for Orai1 with a fluorescent secondary Ab (AbRa594) and treated with either HBS (control) or TG (1 μM in Ca^{2+}-free HBS, 15 min), and imaged under TIRFM. The Orai1 puncta were identified automatically using TrackMate (***Section 3.2.4***). The fluorescence intensity distributions and number of puncta for immunostained Orai1 puncta were indistinguishable for WT and STIM1-EGFP HeLa cells, and minimally affected by depletion of the Ca^{2+} stores (***Figure 4.5B and C***). In unstimulated WT cells, the mean fluorescence intensity was 90 ± 12% (n = 5 cells) of that in STIM1-EGFP HeLa cells (n = 5 cells).

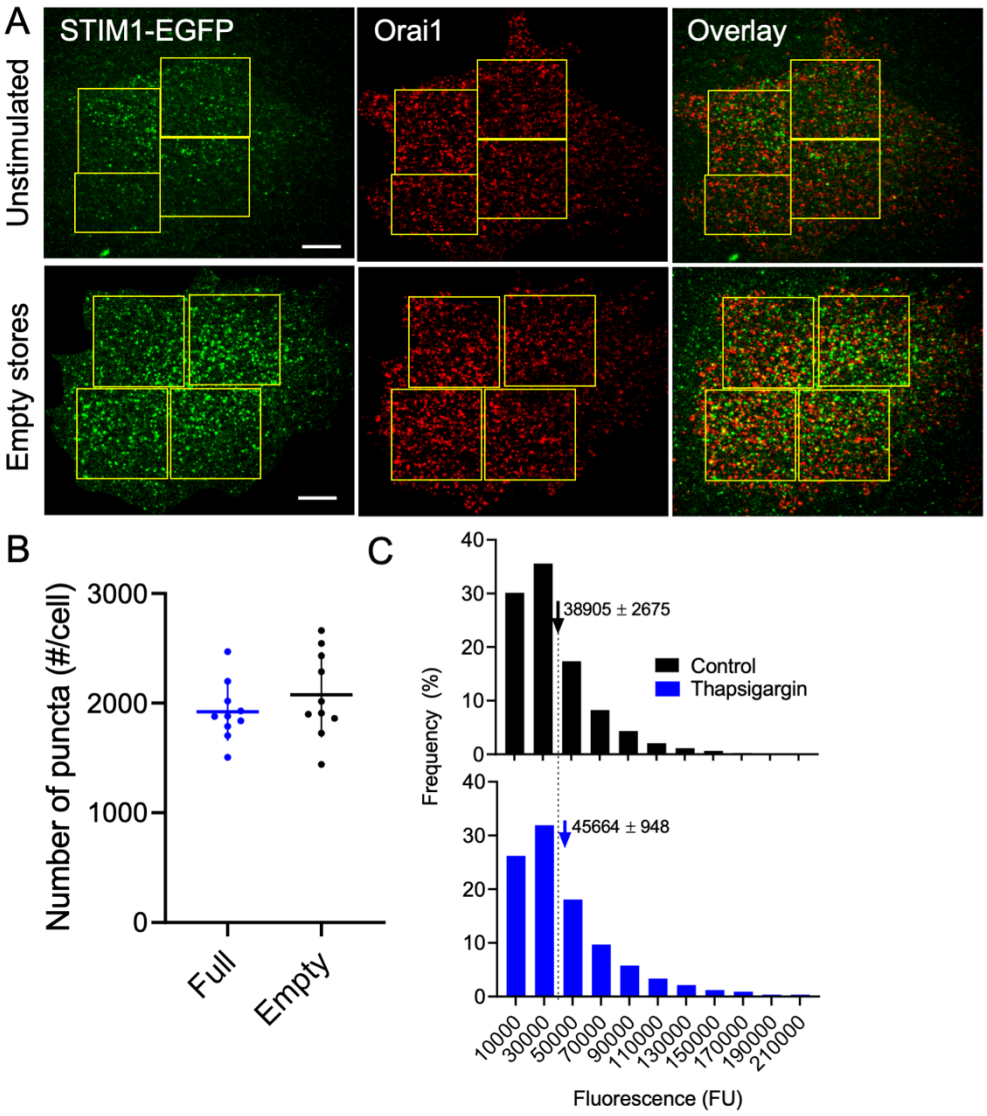

Figure 4.5 Orai1 do not cluster after store depletion. A. TIRF images show Orai1 puncta immunostained with Orai1 Ab (AbRa594 as secondary) in STIM1-EGFP HeLa cells, before and after depleting intracellular Ca^{2+} stores (1 μM TG in Ca^{2+}-free HBS, 15 min). The yellow boxes represent the areas where colocalization studies were performed, as described in ***Section 4.2.4***. Scale bar = 10 μm. **B.** Number of Orai1 puncta detected by TrackMate in the TIRF field of STIM1-EGFP HeLa cells before and after store depletion (individual values, mean ± SD, n = 10 cells from 3 independent experiments). **C.** Summary results show distributions of fluorescence intensities of immunostained Orai1 puncta in STIM1-EGFP HeLa cells before (10160 puncta from 5 cells) or after store depletion (10579 puncta from 5 cells), each from 3 independent experiments. The x-axes are truncated for greater clarity; 0.3% of values (included in means) lie beyond the truncation. Mean ± SEM, $^{*}P < 0.05$, Student's t-test.

4.3.4. Only a small population of STIM1 puncta colocalise with Orai1 channels

According to ***Section 4.2.4***, in order to achieve valid statistical significance of colocalization by random shuffling, several areas within one cell were chosen as ROIs to avoid analysing unequal distributions of puncta. These selected regions together occupied 50.7 ± 10.0% (mean ± SD, n = 5 cells) of the TIRF footprint for unstimulated cells and 58.4 ± 7.4% (mean ± SD, n = 5 cells) for cells with empty stores (***Figure 4.5A***). An object-based colocalization method (Gilles *et al.* 2017) was used (***Section 4.2.3***) to measure distances between the centres of each Orai1 punctum and the nearest STIM1 punctum in cells with replete and empty stores.

Results revealed that 4.8 ± 0.9% of Orai1 puncta in cells with full stores have a STIM1 puncta within 320 nm, which is regarded as colocalization, while 14.5 ± 0.4% of Orai1 puncta colocalized with STIM1 in cells treated with TG (***Figure 4.6A***). Randomization showed that the colocalization in unstimulated cells was not significant, but a significant proportion of Orai1 puncta colocalized with STIM1 in stimulated cells (***Figure 4.6B***). In cells with empty stores, for the Orai1 puncta colocalized with STIM1 puncta (centroid separations < 320 nm) or away from them (centroid separations > 960 nm), the fluorescence intensities only minimally differ between them (***Figure 4.6C***). These results confirm that depletion of ER Ca^{2+} stores cause clustering of STIM1 and its association with Orai1, but there is no discernible aggregation of Orai1 channels.

Regarding the relationship between MCS, Orai1 and STIM1, it is best to use STIM1-EGFP HeLa cells to be transfected with MAPPER, an indicator of MCS, and subsequently immunostained for Orai1 (with a colour other than green). This is not only because other experiments above were mainly done on this cell line and the entire story was built on it, but also because both antibodies for Orai1 and STIM1 were raised in rabbit, which requires double immunostaining and is not straightforward.

MAPPER is composed of an N-terminal signal sequence that directs it to the ER, the transmembrane helix from STIM1, and the polybasic motif of the small G protein Rit which makes MAPPER constitutively present in the ER-PM junctions by trapping phosphoinositides in the PM (Chang *et al.* 2013). Although GFP-MAPPER has been suggested not to perturb MCS in SOCE, at least the maximally activated SOCE is not affected (Chang *et al.* 2013), mCh-MAPPER was reported by our lab to perturb MCS (Thillaiappan *et al.* 2017). Since STIM1 puncta are green, the use of mCh-MAPPER might be inescapable. Therefore, the expressions of the two MAPPERs are compared in cells transfected with both plasmids.

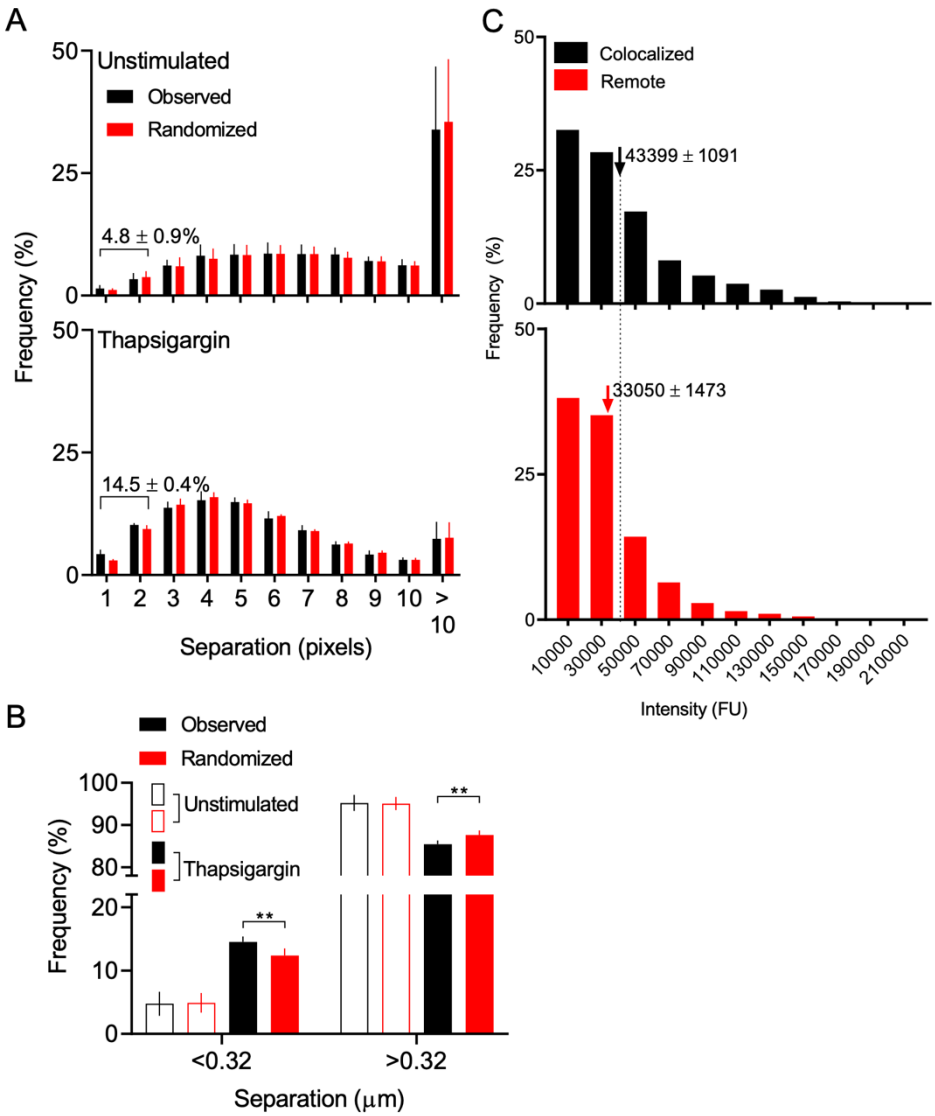

Figure 4.6 Only a small population of STIM1 puncta colocalise with Orai1 channels. **A.** Distribution of distances between centres of each Orai1 punctum and its nearest STIM1 punctum in cells with full (4711 Orai1 puncta, 5 cells) or empty Ca^{2+} stores (6795 Orai1 puncta, 5 cells), each from 3 independent experiments. Separations ≤ 320 nm (two pixels) were regarded as colocalization. STIM1 puncta were randomly shuffled 100 times within each ROI and distances were compared with observed separations (Costes *et al.* 2004). **B.** Frequency distributions segregated into Orai1 colocalized with STIM1 (separation < 0.32 µm, 2 pixels) or not (> 0.32 µm). Mean ± SEM. $^{**}P < 0.01$, $^{*}P < 0.05$, Student's t-test, relative to randomized STIM1. **C.** Fluorescence intensities distribution of immunostained Orai1 puncta in STIM1-EGFP HeLa cells with empty Ca^{2+} stores, categorized by whether Orai1 puncta colocalized with STIM1 (separation < 0.32 µm; 1032 puncta, 5 cells) or were remote from it (> 0.96 µm; 2334 puncta, 5 cells), each from 3 independent experiments. Mean ± SEM, $^{*}P < 0.05$, Student's t-test. The x- axes are truncated for greater clarity; <0.3% of values (included in means) lie beyond the truncation.

Since mCh-MAPPER was previously reported to perturb the MCS, shorter transfection time was allowed to examine whether better results can be achieved. WT HeLa cells transfected with either GFP- or mCh-MAPPER were imaged 8 hrs after transfection (***Figure 4.7A***). It was obvious that some cells show 'acceptable' expression of MAPPER which contain clear punctate structures amenable to analysis, while others show perturbed MCS. 30 from 50 cells for expression of GFP-MAPPER were 'acceptable' and 29 from 80 cells for mCh-MAPPER. The high Manders split coefficients of both ways indicate the near-perfect colocalization between GFP- and mCh-MAPPER (***Figure 4.7B***), which suggests that both MAPPERs were directed to the same positions. Even in those 'rejected' cells where expression of MAPPER caused perturbation of MCS, there was also substantial colocalization of the two MAPPERs. The mean fluorescence intensities of GFP- and mCh-MAPPER puncta and numbers of puncta were not affected by co-expression of both MAPPERs (***Figure 4.7C and D***). Overall, despite the fact that MCS in some cells were perturbed by either GFP- or mCh-MAPPER, both MAPPERs identify MCS. Only those cells with 'acceptable' expression of either GFP- or mCh-MAPPER were used for further analyses.

In order to examine the relationship between STIM1 and MCS, and subsequent colocalization of STIM1, Orai1 and MCS, STIM1-EGFP HeLa cells were transfected with mCh-MAPPER and imaged after 8 hrs. For those cells that were successfully transfected and expressing 'acceptable' mCh-MAPPER, both STIM1 and MAPPER puncta were identified (***Figure 4.8A***). Results show that when mCh-MAPPER was expressed in STIM1-EGFP cells, the mean intensities of STIM1 puncta dropped to 82.0% compared to control cells, while the mean number of puncta per cell reduced to 57.7% (***Figure 4.8B and C***). The average number of mCh-MAPPER puncta was also reduced to 79.9% by accumulation of STIM1 puncta beneath the PM upon Ca^{2+} store depletion (***Figure 4.8D and E***). All these results indicate that MAPPER may perturb the accumulation of STIM1 at MCS, perhaps because they occupy the same location and so compete with each other.

Nonetheless, a significant colocalization of STIM1 puncta (~50%, ***Figure 4.8F***) with mCh-MAPPER can be observed in both control and TG-treated STIM1-EGFP HeLa cells. There are, of course, more STIM1 puncta accumulate in the ER-PM junctions of cells with depleted Ca^{2+} stores (***Figure 3.6C***) and therefore should be more within identified MCS, but this colocalization might be underestimated if STIM1 and mCh-MAPPER compete for occupancy of MCS (***Figure 4.8B - E***).

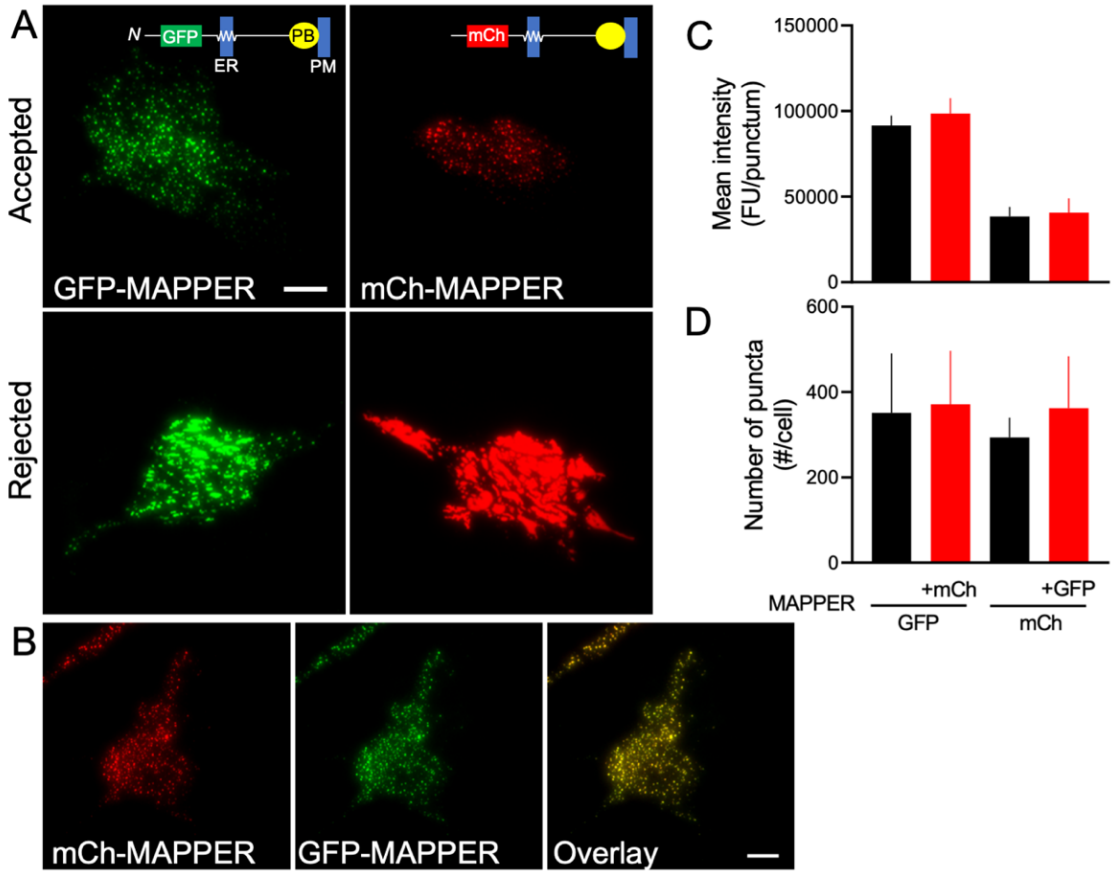

Figure 4.7 Comparison of expression of GFP- and mCh- MAPPER. A. TIRF images of WT HeLa cells transfected with GFP- or mCh-MAPPER and observed 8 hr after transfection. Both are shown after depletion of ER Ca^{2+} stores with thapsigargin (1 µM, 15 min in Ca^{2+}-free HBS). Typical images show cells 'acceptable' for analysis (30 from 50 cells for GFP; 29 from 80 cells for mCh, each from 3 independent experiments) or 'rejected'. Scale bar = 10 µm. **B.** TIRF images of WT HeLa cells transfected with both GFP-MAPPER and mCh-MAPPER (15 from 44 cells were considered acceptable for analysis). Manders split coefficients for mCh colocalized with GFP, and for GFP colocalized with mCh were 0.90 ± 0.04 and 0.87 ± 0.04, respectively (mean ± SD, n = 5 cells). Scale bar = 10 µm. **C.** Mean fluorescence intensity in each cell of GFP-MAPPER or mCh-MAPPER puncta (FU/punctum) for HeLa cells expressing one MAPPER or both, recorded 8 hr after transfection. Results are from 5-6 'acceptable' cells from 3 independent experiments (~60% of cells had acceptable expression of MAPPER). Mean ± SEM. No significant differences, Student's unpaired t-test. **D.** Similar analyses of the numbers of GFP-MAPPER or mCh-MAPPER puncta detected in the TIRF field (#/cell). Mean ± SD, n = 5-6 cells. No significant differences, one-way ANOVA.

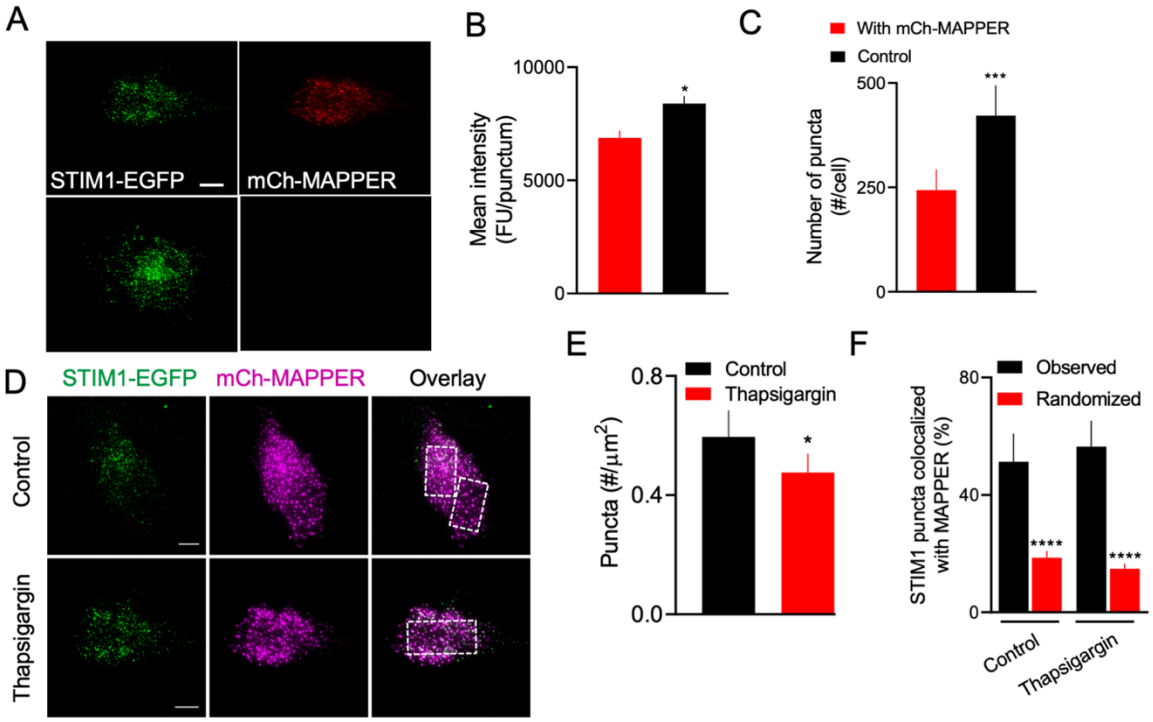

Figure 4.8 STIM1-EGFP colocalizes with mCh-MAPPER. A. TIRF images of STIM1-EGFP HeLa cells imaged 8 hrs after being transfected with mCh-MAPPER and then treated with TG (1 μM, 15 min in Ca^{2+}-free HBS) to deplete intracellular stores of Ca^{2+}. Cells were first selected based on 'acceptable' expression of mCh-MAPPER before observing STIM1-EGFP. Representative images show STIM1-EGFP in cells expressing 'acceptable' mCh-MAPPER and those that appear not to have been successfully transfected. **B.** Summary results show the mean fluorescence intensity of STIM1 puncta, mean ± SEM, $n = 5$ (mCh-MAPPER) or 7 (control) cells from 2 independent experiments. **C.** Numbers of STIM1 puncta detected in the TIRF field (#/cell), mean ± SD, $n = 5$-7 cells for STIM1-EGFP HeLa cells with or without mCh-MAPPER. **D.** TIRF images of STIM1-EGFP HeLa cells expressing mCh-MAPPER under control conditions or after treatment with TG (1 μM, 15 min in Ca^{2+}-free HBS) to deplete intracellular Ca^{2+} stores. The white boxes represent the areas where colocalization studies were performed. **E.** Summary results showing numbers of mCh-MAPPER puncta (#/μm²). Mean ± SD, $n = 6$ cells from 2 independent experiments. **F.** Colocalization of STIM1-EGFP with mCh-MAPPER puncta (centroid separations < 320 nm) in control and TG-treated cells. Mean ± SD, $n = 6$ cells from 2 independent experiments.

Scale bars = 10 μm. $^{*}P < 0.05$, $^{***}P < 0.001$, $^{****}P < 0.0001$, Student's unpaired t-test.

Regarding the relationship between STIM1, Orai1 and MCS, it is ideal to use STIM1-EGFP HeLa cells, transfected with mCh-MAPPER and immunostained for Orai1 (with a different colour, e.g., far-red), due to the reasons discussed above. However, it was impracticable to make the 3-way comparison because the immunostaining for Orai1 using fluorescence secondary antibody (AlexaFluor 647) was not as good as with AlexaFluor 594 as the 2nd Ab (***Figure 4.9***). Also, it was difficult to find a cell with all 3 puncta appearing appropriate (***Figure 4.9***, top panels). Therefore, I had to compromise to use WT HeLa cells, transfected with GFP-MAPPER and dual immunostained for STIM1 and Orai1 (***Section 4.2.2***). Similar to STIM1-EGFP HeLa cells, the fractions of STIM1 puncta associated with GFP-MAPPER were comparable in WT HeLa cells with full (39 ± 6%) or empty intracellular Ca^{2+} stores (47 ± 3%) (***Figure 4.10B, Figure 4.11A and B***). After store depletion, the percentage of STIM1 puncta colocalized with both MAPPER and Orai1 significantly increased (from 17.9 ± 6.0% to 26.1 ± 4.2%, *n* = 6), while the STIM1 puncta that only colocalized with Orai1, but not MAPPER, did not change significantly (***Figure 4.11C***).

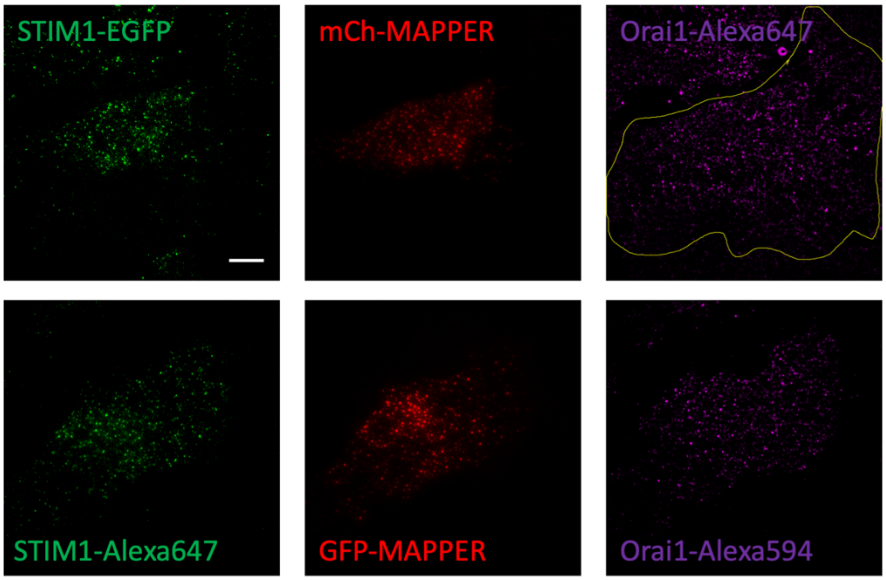

Figure 4.9 Bad immunostaining of AlexaFluor 647 for Orai1. STIM1-EGFP (top) and WT (bottom) cells transfected with mCh- or GFP-MAPPER and treated with TG (1 µM, 15 min in Ca^{2+}-free HBS). They were either immunostained for Orai1 with fluorescent 2nd Ab (AbRa647) or dual-immunostained for STIM1 with AbRa647 as the 2nd Ab, and for Orai1 with AbRa594 as the 2nd Ab and then imaged under TIRF. Scale bar = 10 µm.

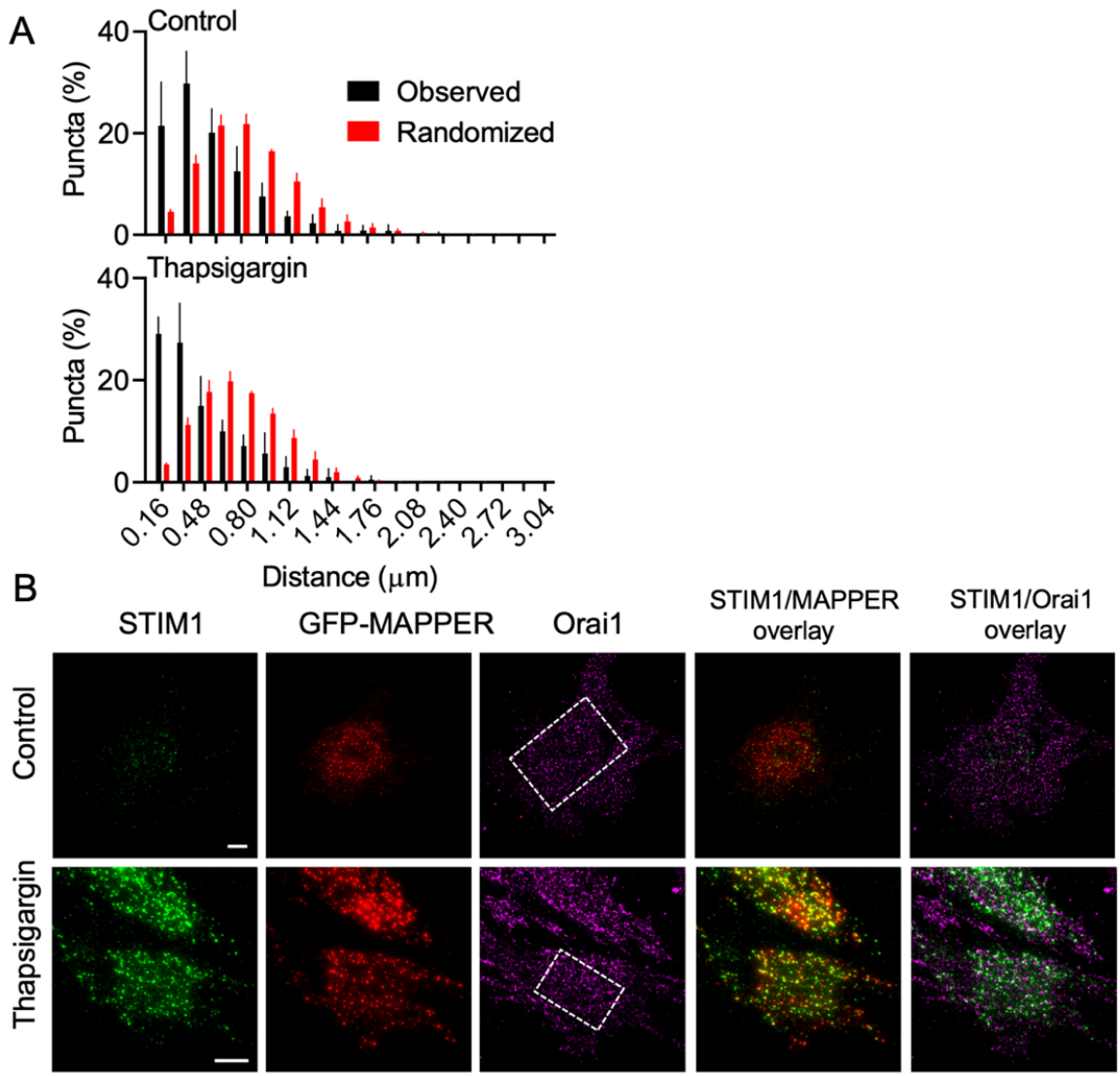

Figure 4.10 Relationships between MAPPER, STIM1 and Orai1. A. The distribution of centroid distances between each STIM1 punctum and its nearest mCh-MAPPER in STIM1-EGFP HeLa cells with replete or empty Ca^{2+} store. Analyses used TIRF images similar to those shown in ***Figure 4.8 A and D***. Results (mean ± SD, n = 6 cells from 2 independent experiments) show observed separations and separations after 100 random shuffles of mCh-MAPPER puncta. Summary results shown in ***Figure 4.8F***. **B.** TIRF images of WT HeLa cells expressing GFP-MAPPER and double immunostained for Orai1 and STIM1. Scale bars = 10 μm.

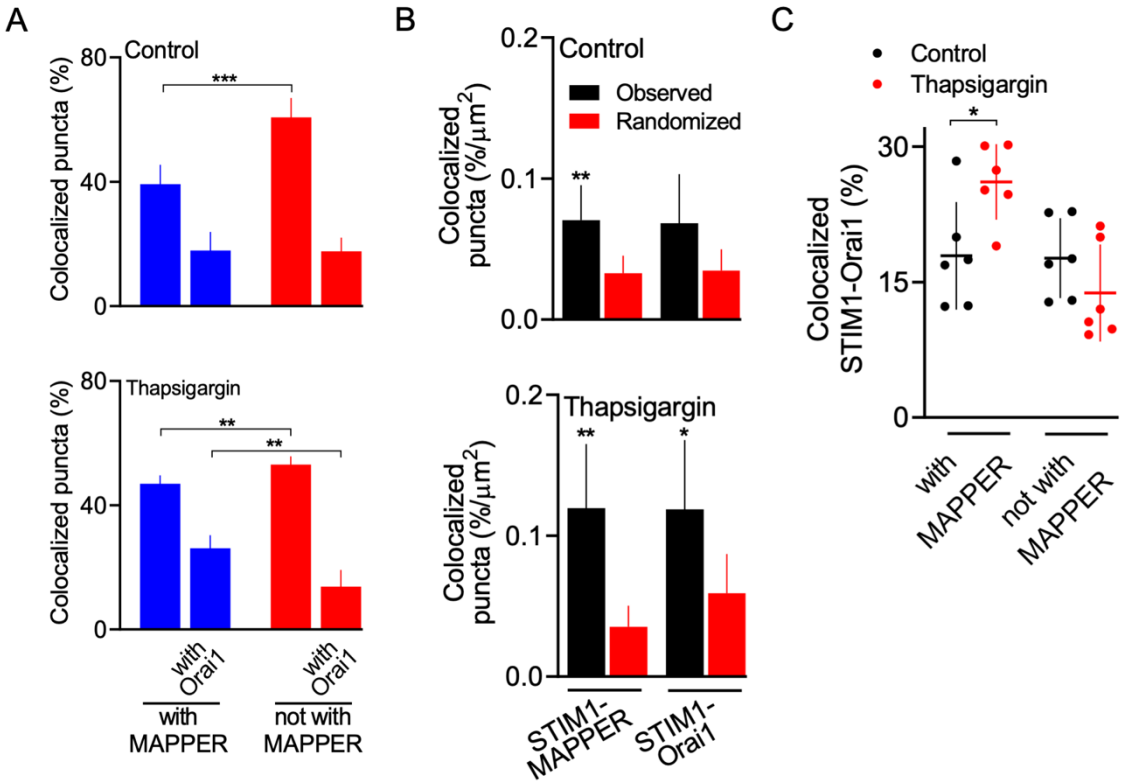

Figure 4.11 Quantification of colocalization between Orai1, MAPPER and STIM1. A. ROI similar to boxed areas in ***Figure 4.10B*** were used to determine numbers of STIM1 puncta colocalized (%, centroid separations < 320 nm) with MAPPER and Orai1 in control cells and after treatment with TG (1 µM, 15 min in Ca^{2+}-HBS) to deplete intracellular Ca^{2+} stores. In each case, colocalization was determined by measuring the centre-to-centre distance from each STIM1 punctum to the nearest MAPPER or Orai1 punctum. Results show all STIM1 puncta colocalized or not with MAPPER, and within these categories the STIM1 puncta that colocalized with Orai1. Mean ± SD from 6 cells from 2 independent experiments. $^{**}P < 0.01$, Student's t-test comparing only matched observations that were colocalized or not colocalized with MAPPER. **B.** Comparison of observed colocalizations with those determined after randomization of the distribution of MAPPER or Orai1 puncta. Mean ± SD, n = 6 cells from 2 independent experiments. $^{*}P < 0.05$, $^{**}P < 0.01$, Student's t-test, relative to randomized. **C.** Summary results (mean ± SD) show the percentages of colocalized STIM1 and Orai1 that also colocalize with MAPPER for cells with full (control) or empty Ca^{2+} stores.

4.4. Discussion

Most studies have reported clustering of Orai1 channels upon store depletion (e.g., Xu *et al.* (2006); Gwozdz *et al.* (2008); Peckys *et al.* (2021)), or enrichment of Orai1 at the plasma membrane (Woodard *et al.* 2008; Hodeify *et al.* 2015), by overexpressing fluorescently tagged Orai1 and/or STIM1. However, as discussed earlier, overexpression of the two proteins may lead to problems including perturbation both between them and to the ER and MCS. For example, with Orai1 overexpressed, SERCA, which plays an important role in SOCE, may be pushed too far away from the high Ca^{2+} microdomains formed in SOCE and therefore uncouples Ca^{2+} ER uptake from PM entry, hence reduces the amplitude of SOCE (Manjarres *et al.* 2010). Here, native Orai1 were immunostained and visualized under TIRF microscope, together with endogenously tagged STIM1-EGFP proteins. Subsequent analyses on dual-immunostained STIM1 and Orai1, and expression of GFP-MAPPER identifying MCS, allow the relationship between the three participants to be revealed.

After confirmation of the specificity and dense labelling of the antibody against Orai1 (***Figure 4.3-4.4***), results from optical imaging indicate that Orai1 do not cluster upon store depletion, and the mean fluorescence intensities of Orai1 in unstimulated STIM1-EGFP cells were minimally affected compared to store depleted cells (38905 and 45664 FU, respectively, ***Figure 4.5C***). Subsequent colocalization studies (***Section 4.2.3***) based on the TIRF images demonstrated that only a small portion of Orai1 puncta (14.5 ± 0.4%) colocalized with STIM1 in store-depleted cells (***Figure 4.6A***), but the colocalization is statistically significant compared to either unstimulated cells or randomization analysis (***Figure 4.6A and B***).

In this study, STIM1 puncta were identified both by immunostaining (***Figure 3.7C, Figure 3.12C***) and as STIM1-EGFP (***Figure 3.7B, Figure 3.9B, Figure 3.11B, Figure 4.8C***) in HeLa cells. Nonetheless, the number of STIM1 puncta in cells with empty store (~400/cell) is comparable to the number of MCS identified by MAPPER in the TIRF field (~340/cell, ***Figure 4.7D***). There are substantially more Orai1 channels (~2000/cell, ***Figure 4.2A***) and since each STIM1 cluster is only big enough to activate no more than a single Orai1 channel (***Figure 4.5-4.6***), I suggest that the native complex within which STIM1 activates SOCE typically includes only one Orai1 hexamer and that most sites where both proteins occur coincide with MCS identified by MAPPER (***Figure 4.12***).

As discussed in ***Sections 1.4 and 3.4***, there have been essentially two models proposed for the binding stoichiometry between STIM1 and Orai1, namely monomeric (Zhou *et al.* 2015)

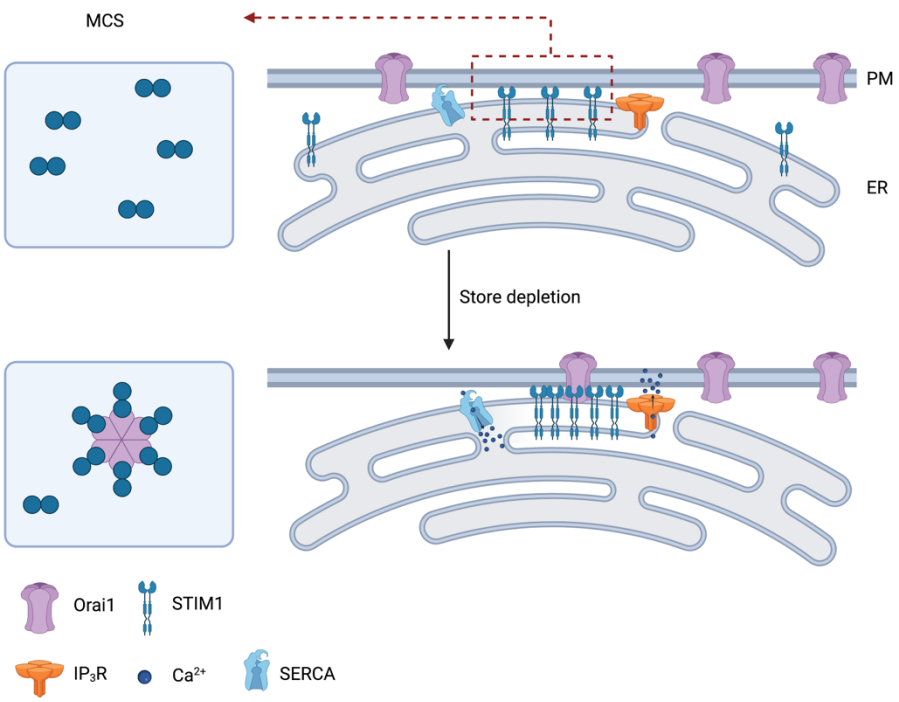

Figure 4.12 Schematic of the interaction of STIM1 and Orai1 in the MCS. Within each MCS, store depletion modestly increases the number of STIM1 dimers (typically from 5 to 7) as they assemble around a single Orai1 channel (left). Local redistribution of STIM1 within each tiny MCS (~300 nm across) (Hogan 2015) may allow each to behave as a digital switch, activated by local depletion of ER Ca^{2+} (right). Image reproduced from *Shen et al. (2021)*.

or dimeric (Stathopulos *et al.* 2013; Fahrner *et al.* 2014) binding. Results from this study have demonstrated that STIM1 only clusters into small puncta after store depletion and can only activate a single Orai1 hexamer channel. There is only modest increase, from about 5 to about 7 dimers, in size of STIM1 puncta after store depletion (***Figure 3.6C, Figure 3.9B and D***). This change just straddles the minimum stoichiometry requirement (six) for STIM1 binding to fully activate Orai1 in the monomeric binding model (***Figure 3.13B***). This model also provides the possibility of cross-linking between Orai1 channels (Zhou *et al.* 2018) (***Figure 3.13C***), but the requirement of full occupation for an Orai1 hexamer to be sufficiently activated declines the chance of cross-linking of Orai1 with such a small number of STIM1 per punctum (Yen and Lewis 2018). This conclusion is consistent with the findings of Perni *et al.*, which indicated that a complete small STIM1 cluster can associate with a single Orai1 particle, but it is not sufficiently large to cover two clusters, thus demonstrating an approximate 1:1 relationship between Orai1 channels and small STIM1 clusters (Perni *et al.* 2015). There was also evidence on engineered human STIM1 (ehSTIM) with EGFP tags showing that bundles of activated

ehSTIM1 dimers possibly range from 1-6 and they presented a question on whether there is an underlying molecular mechanism restricting on the oligomerization states of ehSTIM1 dimers beyond six (Srinivasan 2019). This question can be answered now, by the interaction between a small STIM1 cluster, with an average size of 7 dimers, and one active Orai1 channel.

Compared to HeLa cells, however, Jurkat cells may present another story. They rely more heavily on SOCE and their CRAC currents are unusually large. Taken the whole-cell SOCE current, number of active CRAC channels and the number of ER-PM junctions into account, the best estimate suggests about 5 open Orai1 channels per MCS (Hogan 2015). Hence in most mammalian cells, even with maximally depleted stores, there are probably very few Orai1 channels open in each SOCE junction (Hogan 2015). The assembly of native STIM1 puncta around Orai1 channels after store depletion can therefore be speculated to be driven primarily by recruitment of STIM1 dimers already resident within the MCS. The local depletion of the ER Ca^{2+} by licensed IP_3Rs activates SOCE, which then allows each MCS to function as an autonomous digital regulator of SOCE (Thillaiappan *et al.* 2017; Thillaiappan *et al.* 2019) (***Figure 4.12***).

The stoichiometry within STIM1 clusters and between STIM1 and Orai1 channels is important in understanding the molecular mechanism of SOCE, and the findings of this study is stimulating and awaiting confirmation on other cell lines. However, several limitations to this study need to be acknowledged. For example, although the specificity of Orai1 Ab was confirmed by siRNA-mediated knockdown (***Figure 4.3***), significant background noise of TIRF images with Orai1 immunostained can still be observed (***Figure 4.5A, Figure 4.10B***). This method is not as quantitative and can only indirectly reflect the assembly of Orai1, which requires other approaches, such as CRISPR/cas9-mediated gene-editing of Orai1, to visualize and quantify the number of Orai1 channels in one punctum before and after store depletion more directly, just as the investigations done on STIM1. Additionally, the attempt to visualize STIM1, Orai1 and MCS identified by MAPPER simultaneously appeared to be difficult. Even though expression of mCh-MAPPER does not perturb the identification of MCS by GFP-MAPPER (***Figure 4.7***), mCh-MAPPER reduces the number STIM1 puncta near the PM in cells with empty Ca^{2+} stores and *vice versa*. These results are consistent with competition between mCh-MAPPER and STIM1 for occupancy of MCS. The effects of GFP-MAPPER on formation of endogenously tagged STIM1-EGFP puncta cannot be determined due to their same optical appearance, but it seems likely that GFP-MAPPER would also perturb assembly of STIM1 puncta (***Figure 4.8***).

Chapter 5 Summary

The STIM1-EGFP HeLa cell line which was previously generated by Dr. Sumita Chakraborty via CRISPR/Cas9 has been characterized. It has been confirmed that one out of two *STIM1* alleles has been tagged with EGFP (***Figure 2.10***) and that half of expressed proteins have EGFP tags while the other half remain native (***Figure 2.8 and Figure 2.11***). STIM1 is the only fluorescent protein both in the in-gel fluorescence (***Figure 2.9***) and under the TIRF microscope (***Figure 3.3***), and the EGFP tag does not impair the IP_3-mediated Ca^{2+} release and SOCE in the edited cell line (***Figure 2.12, Figure 2.14-2.15***). Attempts have been made to generate a homozygous STIM1-EGFP HeLa cell line to avoid many problems that can be associated with the single-edit cell line, but unfortunately have not been successful (***Figure 2.16-2.17***).

STIM1-EGFP mixes interchangeably with native STIM1, and they interact with Orai1 undistinguishably (***Figure 2.11 and Figure 3.7***). Therefore, STIM1-EGFP in subsequent analyses can be representative of all STIM1. Results demonstrated that STIM1-EGFP resides in the ER at rest, and translocates to the ER-PM junctions to form puncta after Ca^{2+} store depletion (***Figure 3.4-3.6***). There is only a modest increase in the fluorescence intensities (~50%) and sizes of STIM1-EGFP puncta in stimulated cells, from ~5 to ~7 dimers (***Figure 3.9-3.11***). These results are also comparable to analyses using overexpressed STIM1, although the latter shows large variations (ranging from 120-400%, with a mean 286 ± 86% and a median of 280%), depending on cell types and different agonists for stimulation (***Table 5.1***). Combined with the result that Orai1 does not form clusters after Ca^{2+} store depletion (***Figure 4.5***) and that only a small number of STIM1 colocalizes with Orai1 within the MCS (***Figure 4.6, Figure 4.10-4.11***), I can conclude that each SOCE complex only comprises a small cluster of STIM1 proteins and one active Orai1 channel.

In the TIRF field of cells with empty Ca^{2+} stores, 26.1 ± 4.2% of STIM1 puncta colocalize with Orai1 at MCS identified by MAPPER (***Figure 4.11A***), although as discussed, the number of MCS in store-depleted cells (***Figure 4.8D and E***) might be underestimated due to competition between STIM1 and MAPPER. From ***Figure 2.14C***, the amplitude of SOCE of maximally activated cells by treatment of 10 μM CPA is 272 ± 48 nM, determined ~60 s after Ca^{2+} restoration. Assuming the cytosolic volume of a Hela cell is 1.6 pico litre (Milo *et al.* 2010) and the ratio of bound to free Ca^{2+} is around 40 (Zhou and Neher 1993), the influx can be estimated to be about $9x10^{-18}$ mol/cell during the first 15 s (half-life is ~15 s, ***Figure 2.14B***).

Cells	Near—PM STIM1 (%)	Reference
HEK 293	225	Figure 3A (Kilch *et al.* 2013)
HEK 293	400	Figure 1A, B (Smyth *et al.* 2008)
HEK 293	350	Figure 3b (Ong *et al.* 2015)
HEK 293	350	Figure 8D (Smyth *et al.* 2007)
HeLa	240	Figure 4C (Liou *et al.* 2005)
HeLa	350	Figure 4b (Sharma *et al.* 2013)
Jurkat	400	Figure 3g (Zhang *et al.* 2005)
Jurkat	160	Figure 4C (Wu *et al.* 2006)
Jurkat	215	Figure 3A (Srikanth *et al.* 2012)
Jurkat	120-250	Figure 2a, b, S3a, b (Luik *et al.* 2008)
DT40	280	Figure 4D (Baba *et al.* 2006)

Table 5.1 STIM1 accumulation when overexpressed. Summary results from published work showing the increase in the fluorescence intensities of near-PM STIM1 after Ca^{2+} store depletion as a percentage of that before store depletion in cells overexpressing STIM1 with a fluorescent tag.

This is equivalent to the maximal rate of Ca^{2+} influx into each cell of about 350,000 Ca^{2+}/s. The optical observations above suggest that there are around 400 STIM1-EGFP puncta in TIRF field, and 26% of them (~100) were colocalized with a single active Orai1 in the ER-PM junction in store-depleted cells. Due to the nature of TIRF field, only one side of a cell is visualized, I therefore assume that the observed puncta account for about 50% of all puncta. This estimates about 200 active Orai1 channels per cell. Each single active Orai1 is estimated to conduct 6300 Ca^{2+} per second (Hogan 2015), so 200 active channels can deliver ~10^6 Ca^{2+} per second into a cell. This is more than sufficient to account for the observed increase in cytosolic [Ca^{2+}].

Further questions may be worth investigating based on the results of this study. Why does only a small fraction of STIM1 puncta interact with Orai1? What does the remaining STIM1 puncta that also translocated to the plasma membrane upon store depletion do? Is the distribution of STIM1 pre-localizing within the ER active or random? If they are active, how are they mediated functionally? It has been demonstrated that STIM1 accumulates at junctions adjacent to immobile IP_3Rs, the only IP_3Rs that are licensed to respond to IP_3 and release Ca^{2+} from the ER (Thillaiappan *et al.* 2017), due to its interaction between KRAP and actin

(Thillaiappan *et al.* 2021). Recent evidence also suggested that SOCE is abolished in in human neural progenitor cells (hNPCs) and SH-SY5Y cells lacking IP_3Rs (Chakraborty *et al*., unpublished results). Hence the relationship between STIM1, IP_3R, KRAP and cytoskeleton remain to be determined.

References

Agrawal, N., G. Venkiteswaran, S. Sadaf, N. Padmanabhan, S. Banerjee and G. Hasan (2010). Inositol 1,4,5-trisphosphate receptor and dSTIM function in Drosophila insulin-producing neurons regulates systemic intracellular calcium homeostasis and flight. *J. Neurosci.* **30**(4): 1301-1313.

Airey, J. A., M. M. Grinsell, L. R. Jones, J. L. Sutko and D. Witcher (1993). Three ryanodine receptor isoforms exist in avian striated muscles. *Biochemistry* **32**(22): 5739-5745.

Allman, R., A. C. Hann, A. P. Phillips, K. L. Martin and D. Lloyd (1990). Growth of Azotobacter vinelandii with correlation of coulter cell size, flow cytometric parameters, and ultrastructure. *Cytometry* **11**(7): 822-831.

Alzayady, K. J., L. Wang, R. Chandrasekhar, L. E. Wagner, 2nd, F. Van Petegem and D. I. Yule (2016). Defining the stoichiometry of inositol 1,4,5-trisphosphate binding required to initiate Ca^{2+} release. *Sci. Signal.* **9**(422): ra35.

Ambrose, E. J. (1956). A surface contact microscope for the study of cell movements. *Nature* **178**(4543): 1194-1194.

Axelrod, D. (1981). Cell-substrate contacts illuminated by total internal reflection fluorescence. *J. Cell Biol.* **89**(1): 141-145.

Baba, Y., K. Hayashi, Y. Fujii, A. Mizushima, H. Watarai, M. Wakamori, T. Numaga, Y. Mori, M. Iino, M. Hikida and T. Kurosaki (2006). Coupling of STIM1 to store-operated Ca^{2+} entry through its constitutive and inducible movement in the endoplasmic reticulum. *PNAS* **103**(45): 16704-16709.

Balasuriya, D., S. Srivats, R. D. Murrell-Lagnado and J. M. Edwardson (2014). Atomic force microscopy (AFM) imaging suggests that stromal interaction molecule 1 (STIM1) binds to Orai1 with sixfold symmetry. *FEBS J.* **588**(17): 2874-2880.

Bandyopadhyay, B. C., S. C. Pingle and G. P. Ahern (2011). Store-operated Ca^{2+} signaling in dendritic cells occurs independently of STIM1. *J. Leukoc. Biol.* **89**(1): 57-62.

Baraniak, J. H., Jr., Y. Zhou, R. M. Nwokonko, M. R. Jennette, S. A. Kazzaz, J. M. Stenson, A. L. Whitsell, Y. Wang, M. Trebak and D. L. Gill (2021). Orai channel C-terminal peptides are key modulators of STIM-Orai coupling and calcium signal generation. *Cell Rep.* **35**(13): 109322.

Barr, V. A., K. M. Bernot, S. Srikanth, Y. Gwack, L. Balagopalan, C. K. Regan, D. J. Helman, C. L. Sommers, M. Oh-Hora, A. Rao and L. E. Samelson (2008). Dynamic movement of the calcium sensor STIM1 and the calcium channel Orai1 in activated T-cells: puncta and distal caps. *Mol. Biol. Cell* **19**(7): 2802-2817.

Barrangou, R., C. Fremaux, H. Deveau, M. Richards, P. Boyaval, S. Moineau, D. A. Romero and P. Horvath (2007). CRISPR provides acquired resistance against viruses in prokaryotes. *Science* **315**(5819): 1709-1712.

Bates, M., T. R. Blosser and X. Zhuang (2005). Short-range spectroscopic ruler based on a single-molecule optical switch. *Phys. Rev. Lett.* **94**(10): 108101.

Beer (1852). Bestimmung der absorption des rothen lichts in farbigen flüssigkeiten. *Annalen der Physik* **162**(5): 78-88.

Ben-Kasus Nissim, T., X. Zhang, A. Elazar, S. Roy, J. A. Stolwijk, Y. Zhou, R. K. Motiani, M. Gueguinou, N. Hempel, M. Hershfinkel, D. L. Gill, M. Trebak and I. Sekler (2017). Mitochondria control store-operated Ca^{2+} entry through Na^{+} and redox signals. *EMBO J.* **36**(6): 797-815.

Berna-Erro, A., A. Braun, R. Kraft, C. Kleinschnitz, M. K. Schuhmann, D. Stegner, T. Wultsch, J. Eilers, S. G. Meuth, G. Stoll and B. Nieswandt (2009). STIM2 regulates capacitive Ca^{2+} entry in neurons and plays a key role in hypoxic neuronal cell death. *Sci. Signal.* **2**(93): ra67.

Berridge, M. J. (1993). Inositol trisphosphate and calcium signalling. *Nature* **361**(6410): 315-325.

Berridge, M. J. (1995). Capacitative calcium entry. *Biochem. J.* **312**(Pt 1): 1-11.

Berridge, M. J. (1997). Elementary and global aspects of calcium signalling. *J. Physiol.* **499**(Pt 2): 291-306.

Berridge, M. J. (2002). The endoplasmic reticulum: a multifunctional signaling organelle. *Cell Calcium* **32**(5-6): 235-249.

Berridge, M. J., P. Lipp and M. D. Bootman (2000). The versatility and universality of calcium signalling. *Nat. Rev. Mol. Cell. Biol.* **1**(1): 11-21.

Bétermier, M., P. Bertrand and B. S. Lopez (2014). Is non-homologous end-joining really an inherently error-prone process? *PLoS Genet.* **10**(1): e1004086-e1004086.

Betzig, E., G. H. Patterson, R. Sougrat, O. W. Lindwasser, S. Olenych, J. S. Bonifacino, M. W. Davidson, J. Lippincott-Schwartz and H. F. Hess (2006). Imaging intracellular fluorescent proteins at nanometer resolution. *Science* **313**(5793): 1642-1645.

Bezprozvanny, I. and B. E. Ehrlich (1994). Inositol (1,4,5)-trisphosphate ($InsP_3$)-gated Ca channels from cerebellum: conduction properties for divalent cations and regulation by intraluminal calcium. *J. Gen. Physiol.* **104**(5): 821-856.

Bezprozvanny, I., J. Watras and B. E. Ehrlich (1991). Bell-shaped calcium-response curves for $Ins(1,4,5)P_3$- and calcium-gated channels from endoplasmic reticulum of cerebellum. *Nature* **351**(6329): 751-754.

Bhardwaj, R., H. M. Muller, W. Nickel and M. Seedorf (2013). Oligomerization and Ca^{2+}/calmodulin control binding of the ER Ca^{2+}-sensors STIM1 and STIM2 to plasma membrane lipids. *Biosci. Rep.* **33**(5): 833-845.

Bitinaite, J., D. A. Wah, A. K. Aggarwal and I. Schildkraut (1998). *Fok* I dimerization is required for DNA cleavage. *PNAS* **95**(18): 10570-10575.

Boch, J., H. Scholze, S. Schornack, A. Landgraf, S. Hahn, S. Kay, T. Lahaye, A. Nickstadt and U. Bonas (2009). Breaking the code of DNA binding specificity of TAL-Type III effectors. *Science* **326**(5959): 1509-1512.

Bogdanove, A. J., S. Schornack and T. Lahaye (2010). TAL effectors: finding plant genes for disease and defense. *Curr. Opin. Plant Biol.* **13**(4): 394-401.

Bolotin, A., B. Quinquis, A. Sorokin and S. D. Ehrlich (2005). Clustered regularly interspaced short palindrome repeats (CRISPRs) have spacers of extrachromosomal origin. *Microbiology* **151**(Pt 8): 2551-2561.

Bolte, S. and F. P. Cordelieres (2006). A guided tour into subcellular colocalization analysis in light microscopy. *J. Microsc.* **224**(3): 213-232.

Bradshaw, J. M., Y. Kubota, T. Meyer and H. Schulman (2003). An ultrasensitive Ca^{2+}/calmodulin-dependent protein kinase II-protein phosphatase 1 switch facilitates specificity in postsynaptic calcium signaling. *PNAS* **100**(18): 10512-10517.

Brandman, O., J. Liou, W. S. Park and T. Meyer (2007). STIM2 is a feedback regulator that stabilizes basal cytosolic and endoplasmic reticulum Ca^{2+} levels. *Cell* **131**(7): 1327-1339.

Brough, G. H., S. Wu, D. Cioffi, T. M. Moore, M. Li, N. Dean and T. Stevens (2001). Contribution of endogenously expressed Trp1 to a Ca^{2+}-selective, store-operated Ca^{2+} entry pathway. *FASEB J.* **15**(10): 1704-1710.

Byrne, S. M., L. Ortiz, P. Mali, J. Aach and G. M. Church (2014). Multi-kilobase homozygous targeted gene replacement in human induced pluripotent stem cells. *Nucleic Acids Res.* **43**(3): e21-e21.

Cai, X. (2007). Molecular evolution and functional divergence of the Ca^{2+} sensor protein in store-operated Ca^{2+} entry: stromal interaction molecule. *PLoS One* **2**: e609.

Cai, X., R. M. Nwokonko, N. A. Loktionova, R. Abdulqadir, J. H. Baraniak, Jr., Y. Wang, M. Trebak, Y. Zhou and D. L. Gill (2018). Pore properties of Orai1 calcium channel dimers and their activation by the STIM1 ER calcium sensor. *J. Biol. Chem.* **293**(33): 12962-12974.

Cai, X., Y. Zhou, R. M. Nwokonko, N. A. Loktionova, X. Wang, P. Xin, M. Trebak, Y. Wang and D. L. Gill (2016). The Orai1 store-operated calcium channel functions as a hexamer. *J. Biol. Chem.* **291**(50): 25764-25775.

Calloway, N., M. Vig, J. P. Kinet, D. Holowka and B. Baird (2009). Molecular clustering of STIM1 with Orai1/CRACM1 at the plasma membrane depends dynamically on depletion of Ca^{2+} stores and on electrostatic interactions. *Mol. Biol. Cell* **20**(1): 389-399.

Cardy, T. J. A., D. Traynor and C. W. Taylor (1997). Differential regulation of types 1 and 3 inositol trisphosphate receptors by cytosolic Ca^{2+}. *Biochem. J.* **328**(Pt 3): 785-793.

Cargille, J. J. (1985). Immersion oil and the microscope.

Casas-Rua, V., I. S. Alvarez, E. Pozo-Guisado and F. J. Martin-Romero (2013). Inhibition of STIM1 phosphorylation underlies resveratrol-induced inhibition of store-operated calcium entry. *Biochem. Pharmacol.* **86**(11): 1555-1563.

Catterall, W. A. (2011). Voltage-gated calcium channels. *Cold Spring Harb. Perspect. Biol.* **3**(8): a003947.

Ceccaldi, R., B. Rondinelli and A. D. D'Andrea (2016). Repair pathway choices and consequences at the double-strand break. *Trends Cell Biol.* **26**(1): 52-64.

Chakraborty, S., B. K. Deb, T. Chorna, V. Konieczny, C. W. Taylor and G. Hasan (2016). Mutant IP_3 receptors attenuate store-operated Ca^{2+} entry by destabilizing STIM-Orai interactions in *Drosophila* neurons. *J. Cell Sci.* **129**(20): 3903-3910.

Chang, C. L., T. S. Hsieh, T. T. Yang, K. G. Rothberg, D. B. Azizoglu, E. Volk, J. C. Liao and J. Liou (2013). Feedback regulation of receptor-induced Ca^{2+} signaling mediated by E-Syt1 and Nir2 at endoplasmic reticulum-plasma membrane junctions. *Cell Rep.* **5**(3): 813-825.

Chen, L., K. Trujillo, W. Ramos, P. Sung and A. E. Tomkinson (2001). Promotion of Dnl4-catalyzed DNA end-joining by the Rad50/Mre11/Xrs2 and Hdf1/Hdf2 complexes. *Mol. Cell.* **8**(5): 1105-1115.

Chen, L. and T. Xu (2013). On the stoichiometry of resting and activated CRAC channels. *Curr. Top Membr.* **71**: 95-108.

Chen, S., S. Sun, D. Moonen, C. Lee, A. Y.-F. Lee, D. V. Schaffer and L. He (2019). CRISPR-READI: Efficient generation of knockin mice by CRISPR RNP electroporation and AAV donor infection. *Cell Rep.* **27**(13): 3780-3789.e3784.

Cho, S. W., S. Kim, J. M. Kim and J.-S. Kim (2013). Targeted genome engineering in human cells with the Cas9 RNA-guided endonuclease. *Nat. Biotechnol.* **31**(3): 230-232.

Choo, Y., I. Sánchez-García and A. Klug (1994). In vivo repression by a site-specific DNA-binding protein designed against an oncogenic sequence. *Nature* **372**(6507): 642-645.

Christian, M., T. Cermak, E. L. Doyle, C. Schmidt, F. Zhang, A. Hummel, A. J. Bogdanove and D. F. Voytas (2010). Targeting DNA double-strand breaks with TAL effector nucleases. *Genetics* **186**(2): 757-761.

Clementi, E., H. Scheer, D. Zacchetti, C. Fasolato, T. Pozzan and J. Meldolesi (1992). Receptor-activated Ca^{2+} influx: Two independently regulated mechanisms of influx stimulation coexist in neurosecretory PC12 cells. *J. Biol. Chem.* **267**(4): 2164-2172.

Colella, M., F. Grisan, V. Robert, J. D. Turner, A. P. Thomas and T. Pozzan (2008). Ca^{2+} oscillation frequency decoding in cardiac cell hypertrophy: role of calcineurin/NFAT as Ca^{2+} signal integrators. *PNAS* **105**(8): 2859-2864.

Cong, L., F. A. Ran, D. Cox, S. Lin, R. Barretto, N. Habib, P. D. Hsu, X. Wu, W. Jiang, L. A. Marraffini and F. Zhang (2013). Multiplex genome engineering using CRISPR/Cas systems. *Science* **339**(6121): 819-823.

Costes, S. V., D. Daelemans, E. H. Cho, Z. Dobbin, G. Pavlakis and S. Lockett (2004). Automatic and quantitative measurement of protein-protein colocalization in live cells. *Biophys. J.* **86**(6): 3993-4003.

Covington, E. D., M. M. Wu and R. S. Lewis (2010). Essential role for the CRAC activation domain in store-dependent oligomerization of STIM1. *Mol. Biol. Cell* **21**(11): 1897-1907.

Cui, B., X. Yang, S. Li, Z. Lin, Z. Wang, C. Dong and Y. Shen (2013). The inhibitory helix controls the intramolecular conformational switching of the C-terminus of STIM1. *PLoS One* **8**(9): e74735.

Darbellay, B., S. Arnaudeau, D. Ceroni, C. R. Bader, S. Konig and L. Bernheim (2010). Human muscle economy myoblast differentiation and excitation-contraction coupling use the same molecular partners, STIM1 and STIM2. *J. Biol. Chem.* **285**(29): 22437-22447.

Datasheet, S. (2018). Safety Data sheet for DNA wash buffer, *Zymo Research*.

Datasheet, S. (2018). Safety Data Sheet of DNA lysis buffer, *Zymo Research*.

De Koninck, P. and H. Schulman (1998). Sensitivity of CaM Kinase II to the Frequency of Ca^{2+} Oscillations. *Science* **279**(5348): 227-230.

Deak, A. T., S. Blass, M. J. Khan, L. N. Groschner, M. Waldeck-Weiermair, S. Hallstrom, W. F. Graier and R. Malli (2014). IP3-mediated STIM1 oligomerization requires intact mitochondrial Ca2+ uptake. *J Cell Sci* **127**(Pt 13): 2944-2955.

Deb, B. K., P. Chakraborty, R. Gopurappilly and G. Hasan (2020). SEPT7 regulates Ca^{2+} entry through Orai channels in human neural progenitor cells and neurons. *Cell Calcium* **90**: 102252.

Deb, B. K., T. Pathak and G. Hasan (2016). Store-independent modulation of Ca^{2+} entry through Orai by Septin 7. *Nat. Commun.* **7**: 11751.

DeHaven, W. I., J. T. Smyth, R. R. Boyles and J. W. Putney, Jr. (2007). Calcium inhibition and calcium potentiation of Orai1, Orai2, and Orai3 calcium release-activated calcium channels. *J. Biol. Chem.* **282**(24): 17548-17556.

Dellis, O., S. Dedos, S. C. Tovey, T.-U.-. Rahman, S. J. Dubel and C. W. Taylor (2006). Ca^{2+} entry through plasma membrane IP_3 receptors. *Science* **313**(5784): 229-233.

Demuro, A., A. Penna, O. Safrina, A. V. Yeromin, A. Amcheslavsky, M. D. Cahalan and I. Parker (2011). Subunit stoichiometry of human Orai1 and Orai3 channels in closed and open states. *PNAS* **108**(43): 17832–17837.

Derler, I., C. Butorac, A. Krizova, M. Stadlbauer, M. Muik, M. Fahrner, I. Frischauf and C. Romanin (2018). Authentic CRAC channel activity requires STIM1 and the conserved portion of the Orai N terminus. *J. Biol. Chem.* **293**(4): 1259-1270.

Derler, I., M. Fahrner, M. Muik, B. Lackner, R. Schindl, K. Groschner and C. Romanin (2009). A Ca^{2+} release-activated Ca^{2+} (CRAC) modulatory domain (CMD) within STIM1 mediates fast Ca^{2+}-dependent inactivation of ORAI1 channels. *J. Biol. Chem.* **284**(37): 24933-24938.

Derler, I., P. Plenk, M. Fahrner, M. Muik, I. Jardin, R. Schindl, H. J. Gruber, K. Groschner and C. Romanin (2013). The extended transmembrane Orai1 N-terminal (ETON) region combines binding interface and gate for Orai1 activation by STIM1. *J. Biol. Chem.* **288**(40): 29025-29034.

Desjarlais, J. R. and J. M. Berg (1992). Toward rules relating zinc finger protein sequences and DNA binding site preferences. *PNAS* **89**(16): 7345-7349.

Diakun, G. P., L. Fairall and A. Klug (1986). EXAFS study of the zinc-binding sites in the protein transcription factor IIIA. *Nature* **324**(6098): 698-699.

Dickson, R. M., A. B. Cubitt, R. Y. Tsien and W. E. Moerner (1997). On/off blinking and switching behaviour of single molecules of green fluorescent protein. *Nature* **388**(6640): 355-358.

Dionisio, N., C. Galan, I. Jardin, G. M. Salido and J. A. Rosado (2011). Lipid rafts are essential for the regulation of SOCE by plasma membrane resident STIM1 in human platelets. *Biochim. Biophys. Acta.* **1813**(3): 431-437.

Dolmetsch, R. E., R. S. Lewis, C. C. Goodnow and J. I. Healy (1997). Differential activation of transcription factors induced by Ca^{2+} response amplitude and duration. *Nature* **386**(6627): 855-858.

Dong, H., G. Fiorin, V. Carnevale, W. Treptow and M. L. Klein (2013). Pore waters regulate ion permeation in a calcium release-activated calcium channel. *PNAS* **110**(43): 17332-17337.

Dong, H., Y. Zhang, R. Song, J. Xu, Y. Yuan, J. Liu, J. Li, S. Zheng, T. Liu, B. Lu, Y. Wang and M. L. Klein (2019). Toward a model for activation of Orai channel. *iScience* **16**: 356-367.

Dupont, G., G. Houart and P. De Koninck (2003). Sensitivity of CaM kinase II to the frequency of Ca^{2+} oscillations: a simple model. *Cell Calcium* **34**(6): 485-497.

Dynes, J. L., A. V. Yeromin and M. D. Cahalan (2020). Cell-wide mapping of Orai1 channel activity reveals functional heterogeneity in STIM1-Orai1 puncta. *J. Gen. Physiol.* **152**(9): e201812239.

Endesfelder, U., S. Malkusch, B. Flottmann, J. Mondry, P. Liguzinski, P. J. Verveer and M. Heilemann (2011). Chemically induced photoswitching of fluorescent probes—A general concept for super-resolution microscopy. *Molecules* **16**(4): 3106-3118.

Ercan, E., F. Momburg, U. Engel, K. Temmerman, W. Nickel and M. Seedorf (2009). A conserved, lipid-mediated sorting mechanism of yeast Ist2 and mammalian STIM proteins to the peripheral ER. *Traffic* **10**(12): 1802-1818.

Fabiato, A. (1983). Calcium-induced release of calcium from cardiac sarcoplasmic reticulum. *Am. J. Physiol.* **245**(1): C1-C14.

Fahrner, M., M. Muik, R. Schindl, C. Butorac, P. Stathopulos, L. Zheng, I. Jardin, M. Ikura and C. Romanin (2014). A coiled-coil clamp controls both conformation and clustering of stromal interaction molecule 1 (STIM1). *J. Biol. Chem.* **289**(48): 33231-33244.

Fahrner, M., S. K. Pandey, M. Muik, L. Traxler, C. Butorac, M. Stadlbauer, V. Zayats, A. Krizova, P. Plenk, I. Frischauf, R. Schindl, H. J. Gruber, P. Hinterdorfer, R. Ettrich, C. Romanin and I. Derler (2018). Communication between N terminus and loop2 tunes Orai activation. *J. Biol. Chem.* **293**(4): 1271-1285.

Fan, G., M. L. Baker, Z. Wang, M. R. Baker, P. A. Sinyagovskiy, W. Chiu, S. J. Ludtke and I. I. Serysheva (2015). Gating machinery of $InsP_3R$ channels revealed by electron cryomicroscopy. *Nature* **527**(7578): 336-341.

Fanger, C. M., M. Hoth, G. R. Crabtree and R. S. Lewis (1995). Characterization of T cell mutants with defects in capacitative calcium entry: genetic evidence for the physiological roles of CRAC channels. *J. Cell Biol.* **131**(3): 655-667.

Fernandez-Suarez, M. and A. Y. Ting (2008). Fluorescent probes for super-resolution imaging in living cells. *Nat. Rev. Mol. Cell Biol.* **9**(12): 929-943.

Feske, S. (2010). CRAC channelopathies. *Pflugers Arch.* **460**(2): 417-435.

Feske, S., Y. Gwack, M. Prakriya, S. Srikanth, S. H. Puppel, B. Tanasa, P. G. Hogan, R. S. Lewis, M. Daly and A. Rao (2006). A mutation in Orai1 causes immune deficiency by abrogating CRAC channel function. *Nature* **441**(7090): 179-185.

Feske, S., C. Picard and A. Fischer (2010). Immunodeficiency due to mutations in ORAI1 and STIM1. *Clin. Immunol.* **135**(2): 169-182.

Fierro, L. and A. B. Parekh (1999). Fast calcium-dependent inactivation of calcium release-activated calcium current (CRAC) in RBL-1 cells. *J. Membr. Biol.* **168**(1): 9-17.

Fill, M. and J. A. Copello (2002). Ryanodine receptor calcium release channels. *Physiol. Rev.* **82**(4): 893-922.

Foskett, J. K., C. White, K. H. Cheung and D. O. Mak (2007). Inositol trisphosphate receptor Ca^{2+} release channels. *Physiol. Rev.* **87**(2): 593-658.

Fricke, F., M. S. Dietz and M. Heilemann (2015). Single-molecule methods to study membrane receptor oligomerization. *ChemPhysChem* **16**(4): 713-721.

Frischauf, I., M. Litvinukova, R. Schober, V. Zayats, B. Svobodova, D. Bonhenry, V. Lunz, S. Cappello, L. Tociu, D. Reha, A. Stallinger, A. Hochreiter, T. Pammer, C. Butorac, M. Muik, K. Groschner, I. Bogeski, R. H. Ettrich, C. Romanin and R. Schindl (2017). Transmembrane helix connectivity in Orai1 controls two gates for calcium-dependent transcription. *Sci. Signal.* **10**(507): eaao0358.

Frischauf, I., R. Schindl, J. Bergsmann, I. Derler, M. Fahrner, M. Muik, R. Fritsch, B. Lackner, K. Groschner and C. Romanin (2011). Cooperativeness of Orai cytosolic domains tunes subtype-specific gating. *J. Biol. Chem.* **286**(10): 8577-8584.

Frischauf, I., V. Zayats, M. Deix, A. Hochreiter, I. Jardin, M. Muik, B. Lackner, B. Svobodova, T. Pammer, M. Litvinukova, A. A. Sridhar, I. Derler, I. Bogeski, C. Romanin, R. H. Ettrich and R. Schindl (2015). A calcium-accumulating region, CAR, in the channel Orai1 enhances Ca^{2+} permeation and SOCE-induced gene transcription. *Sci. Signal.* **8**(408): ra131.

Fu, Y., J. A. Foden, C. Khayter, M. L. Maeder, D. Reyon, J. K. Joung and J. D. Sander (2013). High-frequency off-target mutagenesis induced by CRISPR-Cas nucleases in human cells. *Nat. Biotechnol.* **31**(9): 822-826.

Fuchs, S., A. Rensing-Ehl, C. Speckmann, B. Bengsch, A. Schmitt-Graeff, I. Bondzio, A. Maul-Pavicic, T. Bass, T. Vraetz, B. Strahm, T. Ankermann, M. Benson, A. Caliebe, R. Fölster-Holst, P. Kaiser, R. Thimme, W. W. Schamel, K. Schwarz, S. Feske and S. Ehl (2012). Antiviral and regulatory T cell immunity in a patient with stromal interaction molecule 1 deficiency. *J. Immunol.* **188**(3): 1523-1533.

Galione, A. (2010). NAADP receptors. *Cold Spring Harb. Perspect Biol.* **3**(1): a004036.

Gardner, R. C., A. J. Howarth, J. Messing and R. J. Shepherd (1982). Cloning and sequencing of restriction fragments generated by Eco RI*. *DNA* **1**(2): 109-115.

Gilles, J. F., M. Dos Santos, T. Boudier, S. Bolte and N. Heck (2017). DiAna, an ImageJ tool for object-based 3D co-localization and distance analysis. *Methods* **115**: 55-64.

Gincel, D., H. Zaid and V. Shoshan-Barmatz (2001). Calcium binding and translocation by the voltage-dependent anion channel: a possible regulatory mechanism in mitochondrial function. *Biochem. J.* **358**(Pt 1): 147-155.

Giorgi, C., A. Danese, S. Missiroli, S. Patergnani and P. Pinton (2018). Calcium dynamics as a machine for decoding signals. *Trends Cell Biol.* **28**: 258-273.

Giorgi, C., S. Marchi and P. Pinton (2018). The machineries, regulation and cellular functions of mitochondrial calcium. *Nature Reviews Molecular Cell Biology* **19**(11): 713-730.

Glitsch, M. D., D. Bakowski and A. B. Parekh (2002). Store-operated Ca^{2+} entry depends on mitochondrial Ca^{2+} uptake. *EMBO J.* **21**(24): 6744-6754.

Grosse, J., A. Braun, D. Varga-Szabo, N. Beyersdorf, B. Schneider, L. Zeitlmann, P. Hanke, P. Schropp, S. Muhlstedt, C. Zorn, M. Huber, C. Schmittwolf, W. Jagla, P. Yu, T. Kerkau, H. Schulze, M. Nehls and B. Nieswandt (2007). An EF hand mutation in Stim1 causes premature platelet activation and bleeding in mice. *J. Clin. Invest.* **117**(11): 3540-3550.

Gruszczynska-Biegala, J. and J. Kuznicki (2013). Native STIM2 and ORAI1 proteins form a calcium-sensitive and thapsigargin-insensitive complex in cortical neurons. *J. Neurochem.* **126**(6): 727-738.

Gruszczynska-Biegala, J., P. Pomorski, M. B. Wisniewska and J. Kuznicki (2011). Differential roles for STIM1 and STIM2 in store-operated calcium entry in rat neurons. *PLoS One* **6**(4): e19285.

Gudlur, A., A. E. Zeraik, N. Hirve and P. G. Hogan (2020). STIM calcium sensing and conformational change. *J. Physiol.* **598**(9): 1695-1705.

Gudlur, A., A. E. Zeraik, N. Hirve, V. Rajanikanth, A. A. Bobkov, G. Ma, S. Zheng, Y. Wang, Y. Zhou, E. A. Komives and P. G. Hogan (2018). Calcium sensing by the STIM1 ER-luminal domain. *Nat. Commun.* **9**(1): 4536.

Gunter, K. K. and T. E. Gunter (1994). Transport of calcium by mitochondria. *J. Bioenerg. Biomembr.* **26**(5): 471-485.

Gunter, T. E. and D. R. Pfeiffer (1990). Mechanisms by which mitochondria transport calcium. *Am. J. Physiol.* **258**(5 Pt 1): C755-786.

Gwack, Y., S. Srikanth, S. Feske, F. Cruz-Guilloty, M. Oh-Hora, D. S. Neems, P. G. Hogan and A. Rao (2007). Biochemical and functional characterization of Orai family proteins. *J. Biol. Chem.* **282**(22): 16232-16243.

Gwozdz, T., J. Dutko-Gwozdz, C. Schafer and V. M. Bolotina (2012). Overexpression of Orai1 and STIM1 proteins alters regulation of store-operated Ca^{2+} entry by endogenous mediators. *J. Biol. Chem.* **287**(27): 22865-22872.

Gwozdz, T., J. Dutko-Gwozdz, V. Zarayskiy, K. Peter and V. M. Bolotina (2008). How strict is the correlation between STIM1 and Orai1 expression, puncta formation, and I_{CRAC} activation? *Am. J. Physiol. Cell Physiol.* **295**(5): C1133-1140.

Hakamata, Y., J. Nakai, H. Takeshima and K. Imoto (1992). Primary structure and distribution of a novel ryanodine receptor/calcium release channel from rabbit brain. *FEBS Lett.* **312**(2-3): 229-235.

Hana, S., M. Peterson, H. McLaughlin, E. Marshall, A. J. Fabian, O. McKissick, K. Koszka, G. Marsh, M. Craft, S. Xu, A. Sorets, T. Torregrosa, C. Sun, C. E. Henderson and S.-C. Lo (2021). Highly efficient neuronal gene knockout in vivo by CRISPR-Cas9 via neonatal intracerebroventricular injection of AAV in mice. *Gene Ther.*

Hanson, P. I., T. Meyer, L. Stryer and H. Schulman (1994). Dual role of calmodulin in autophosphorylation of multifunctional CaM kinase may underlie decoding of calcium signals. *Neuron* **12**(5): 943-956.

He, J., T. Yu, J. Pan and H. Li (2012). Visualisation and identification of the interaction between STIM1s in resting cells. *PLoS One* **7**(3): e33377.

He, X., C. Tan, F. Wang, Y. Wang, R. Zhou, D. Cui, W. You, H. Zhao, J. Ren and B. Feng (2016). Knock-in of large reporter genes in human cells via CRISPR/Cas9-induced homology-dependent and independent DNA repair. *Nucleic Acids Res.* **44**(9): e85-e85.

Hein, M. Y., N. C. Hubner, I. Poser, J. Cox, N. Nagaraj, Y. Toyoda, I. A. Gak, I. Weisswange, J. Mansfeld, F. Buchholz, A. A. Hyman and M. Mann (2015). A human interactome in three quantitative dimensions organized by stoichiometries and abundances. *Cell* **163**(3): 712-723.

Hill, S. J., C. R. Ganellin, H. Timmerman, J. C. Schwartz, N. P. Shankley, J. M. Young, W. Schunack, R. Levi and H. L. Haas (1997). International Union of Pharmacology. XIII. Classification of histamine receptors. *Pharmacol. Rev.* **49**(3): 253-278.

Hodeify, R., S. Selvaraj, J. Wen, A. Arredouani, S. Hubrack, M. Dib, S. N. Al-Thani, T. McGraw and K. Machaca (2015). A STIM1-dependent 'trafficking trap' mechanism regulates Orai1 plasma membrane residence and Ca^{2+} influx levels. *J. Cell Sci.* **128**(16): 3143-3154.

Hogan, P. G. (2015). The STIM1-ORAI1 microdomain. *Cell Calcium* **58**(4): 357-367.

Hoover, P. J. and R. S. Lewis (2011). Stoichiometric requirements for trapping and gating of Ca^{2+} release-activated Ca^{2+} (CRAC) channels by stromal interaction molecule 1 (STIM1). *PNAS* **108**(32): 13299-13304.

Hoppe, U. C. (2010). Mitochondrial calcium channels. *FEBS Lett.* **584**(10): 1975-1981.

Hoth, M. and R. Penner (1993). Calcium release-activated calcium current in rat mast cells. *J. Physiol.* **465**(1): 359-386.

Hou, X., S. R. Burstein and S. B. Long (2018). Structures reveal opening of the store-operated calcium channel Orai. *Elife* **7**: e36758.

Hou, X., I. R. Outhwaite, L. Pedi and S. B. Long (2020). Cryo-EM structure of the calcium release-activated calcium channel Orai in an open conformation. *Elife* **9**: e62772.

Hou, X., L. Pedi, M. M. Diver and S. B. Long (2012). Crystal structure of the calcium release-activated calcium channel Orai. *Science* **338**(6112): 1308-1313.

Hsieh, T. S., Y. J. Chen, C. L. Chang, W. R. Lee and J. Liou (2017). Cortical actin contributes to spatial organization of ER-PM junctions. *Mol. Biol. Cell* **28**: 3171-3180.

Hsu, M. and P. Berg (1978). Altering the specificity of restriction endonuclease: effect of replacing Mg^{2+} with Mn^{2+}. *Biochemistry* **17**(1): 131-138.

Hsu, P. D., D. A. Scott, J. A. Weinstein, F. A. Ran, S. Konermann, V. Agarwala, Y. Li, E. J. Fine, X. Wu, O. Shalem, T. J. Cradick, L. A. Marraffini, G. Bao and F. Zhang (2013). DNA targeting specificity of RNA-guided Cas9 nucleases. *Nat. Biotechnol.* **31**(9): 827-832.

Huang, B., W. Wang, M. Bates and X. Zhuang (2008). Three-dimensional super-resolution imaging by stochastic optical reconstruction microscopy. *Science* **319**(5864): 810-813.

Huang, G. N., W. Zeng, J. Y. Kim, J. P. Yuan, L. Han, S. Muallem and P. F. Worley (2006). STIM1 carboxyl-terminus activates native SOC, I_{CRAC} and TRPC1 channels. *Nat. Cell Biol.* **8**(9): 1003-1010.

Huang, Y., Y. Zhou, H. C. Wong, Y. Chen, Y. Chen, S. Wang, A. Castiblanco, A. Liu and J. J. Yang (2009). A single EF-hand isolated from STIM1 forms dimer in the absence and presence of Ca^{2+}. *FEBS J* **276**(19): 5589-5597.

Hwang, S. Y. and J. W. Putney (2012). Orai1-mediated calcium entry plays a critical role in osteoclast differentiation and function by regulating activation of the transcription factor NFATc1. *FASEB J* **26**(4): 1484-1492.

Hymel, L., M. Inui, S. Fleischer and H. Schinder (1988). Purified ryanodine receptor of skeletal muscle sarcoplasmic reticulum forms Ca^{2+}-activated oligomeric Ca^{2+} channels in planar bilayers. *PNAS* **85**(2): 441-445.

Incontro, S., Cedric S. Asensio, Robert H. Edwards and Roger A. Nicoll (2014). Efficient, complete deletion of synaptic proteins using CRISPR. *Neuron* **83**(5): 1051-1057.

Iwai, M., T. Michikawa, I. Bosanac, M. Ikura and K. Mikoshiba (2007). Molecular basis of the isoform-specific ligand-binding affinity of inositol 1,4,5-trisphosphate receptors. *J. Biol. Chem.* **282**(17): 12755-12764.

Jansen, R., J. D. Embden, W. Gaastra and L. M. Schouls (2002). Identification of genes that are associated with DNA repeats in prokaryotes. *Mol. Microbiol.* **43**(6): 1565-1575.

Jardin, I., J. J. Lopez, P. C. Redondo, G. M. Salido and J. A. Rosado (2009). Store-operated Ca^{2+} entry is sensitive to the extracellular Ca^{2+} concentration through plasma membrane STIM1. *Biochim. Biophys. Acta.* **1793**(10): 1614-1622.

Jardin, I., P. C. Redondo, G. M. Salido and J. A. Rosado (2008). Phosphatidylinositol 4,5-bisphosphate enhances store-operated calcium entry through hTRPC6 channel in human platelets. *Biochim. Biophys. Acta.* **1783**(1): 84-97.

Ji, W., P. Xu, Z. Li, J. Lu, L. Liu, Y. Zhan, Y. Chen, B. Hille, T. Xu and L. Chen (2008). Functional stoichiometry of the unitary calcium-release-activated calcium channel. *PNAS* **105**(36): 13668-13673.

Jiang, D., L. Zhao and D. E. Clapham (2009). Genome-wide RNAi screen identifies Letm1 as a mitochondrial Ca^{2+}/H^{+} antiporter. *Science* **326**(5949): 144-147.

Jones, B. L. and G. L. Kearns (2011). Histamine: new thoughts about a familiar mediator. *Clin. Pharmacol. Ther.* **89**(2): 189-197.

Jones, S. A., S. H. Shim, J. He and X. Zhuang (2011). Fast, three-dimensional super-resolution imaging of live cells. *Nat. Methods* **8**(6): 499-508.

Katz, Z. B., C. Zhang, A. Quintana, B. F. Lillemeier and P. G. Hogan (2019). Septins organize endoplasmic reticulum-plasma membrane junctions for STIM1-ORAI1 calcium signalling. *Sci. Rep.* **9**: 10839.

Kawasaki, T., I. Lange and S. Feske (2009). A minimal regulatory domain in the C terminus of STIM1 binds to and activates ORAI1 CRAC channels. *Biochem. Biophys. Res. Commun.* **385**(1): 49-54.

Kilch, T., D. Alansary, M. Peglow, K. Dorr, G. Rychkov, H. Rieger, C. Peinelt and B. A. Niemeyer (2013). Mutations of the Ca^{2+}-sensing stromal interaction molecule STIM1 regulate Ca^{2+} influx by altered oligomerization of STIM1 and by destabilization of the Ca^{2+} channel Orai1. *J. Biol. Chem.* **288**(3): 1653-1664.

Kim, Y. G., J. Cha and S. Chandrasegaran (1996). Hybrid restriction enzymes: zinc finger fusions to Fok I cleavage domain. *PNAS* **93**(3): 1156-1160.

Kimura, Y., Y. Hisano, A. Kawahara and S.-i. Higashijima (2014). Efficient generation of knock-in transgenic zebrafish carrying reporter/driver genes by CRISPR/Cas9-mediated genome engineering. *Sci. Rep.* **4**(1): 6545.

King, R. G. and P. M. Delaney (1994). Confocal microscopy in pharmacological research. *Trends in Pharmacological Sciences* **151**(8): 275-279.

Kirichok, Y., G. Krapavinsky and D. E. Clapham (2004). The mitochondrial calcium uniporter is a highly selective ion channel. *Nature* **427**(6972): 360-364.

Klein, T., A. Loschberger, S. Proppert, S. Wolter, S. van de Linde and M. Sauer (2010). Live-cell dSTORM with SNAP-tag fusion proteins. *Nat. Methods* **8**(1): 7-9.

Klejman, M. E., J. Gruszczynska-Biegala, A. Skibinska-Kijek, M. B. Wisniewska, K. Misztal, M. Blazejczyk, L. Bojarski and J. Kuznicki (2009). Expression of STIM1 in brain and puncta-like co-localization of STIM1 and ORAI1 upon depletion of Ca^{2+} store in neurons. *Neurochem. Int.* **54**(1): 49-55.

Konieczny, V., M. V. Keebler and C. W. Taylor (2012). Spatial organization of intracellular Ca^{2+} signals. *Semin. Cell Dev. Biol.* **23**(2): 172-180.

Korzeniowski, M. K., B. Baird and D. Holowka (2016). STIM1 activation is regulated by a 14 amino acid sequence adjacent to the CRAC activation domain. *AIMS Biophys.* **3**(1): 99-118.

Korzeniowski, M. K., I. M. Manjarres, P. Varnai and T. Balla (2010). Activation of STIM1-Orai1 involves an intramolecular switching mechanism. *Sci. Signal.* **3**(148): ra82.

Korzeniowski, M. K., E. Wisniewski, B. Baird, D. A. Holowka and T. Balla (2017). Molecular anatomy of the early events in STIM1 activation - oligomerization or conformational change? *J. Cell Sci.* **130**(17): 2821-2832.

Koziel, K., M. Lebiedzinska, G. Szabadkai, M. Onopiuk, W. Brutkowski, K. Wierzbicka, G. Wilczynski, P. Pinton, J. Duszynski, K. Zablocki and M. R. Wieckowski

(2009). Plasma membrane associated membranes (PAM) from Jurkat cells contain STIM1 protein is PAM involved in the capacitative calcium entry? *Int. J. Biochem. Cell Biol.* **41**(12): 2440-2449.

Kraft, R. (2015). STIM and ORAI proteins in the nervous system. *Channels (Austin)* **9**(5): 245-252.

Lee, K. P., J. P. Yuan, W. Zeng, I. So, P. F. Worley and S. Muallem (2009). Molecular determinants of fast Ca^{2+}-dependent inactivation and gating of the Orai channels. *PNAS* **106**(34): 14687-14692.

Lee, S. K., M. H. Lee, S. J. Jeong, X. Qin, A. R. Lee, H. Park and C. Y. Park (2020). The inactivation domain of STIM1 acts through intramolecular binding to the coiled-coil domain in the resting state. *J. Cell Sci.* **133**(1): jcs237354.

Lewis, R. S. (2019). Store-operated calcium channels: from function to structure and back again. *Cold Spring Harb. Perspect. Biol.* **12**(5): a035055.

Li, G., Z. Zhang, R. Wang, W. Ma, Y. Yang, J. Wei and Y. Wei (2013). Suppression of STIM1 inhibits human glioblastoma cell proliferation and induces G0/G1 phase arrest. *J. Exp. Clin. Cancer Res.* **32**(1): 20.

Li, Z., L. Liu, Y. Deng, W. Ji, W. Du, P. Xu, L. Chen and T. Xu (2010). Graded activation of CRAC channel by binding of different numbers of STIM1 to Orai1 subunits. *Cell Res.* **21**(2): 305-315.

Li, Z., J. Lu, P. Xu, X. Xie, L. Chen and T. Xu (2007). Mapping the interacting domains of STIM1 and Orai1 in Ca^{2+} release-activated Ca^{2+} channel activation. *J. Biol. Chem.* **282**(40): 29448-29456.

Lin, C. C., K. Baek and Z. Lu (2011). Apo and $InsP_3$-bound crystal structures of the ligand-binding domain of an $InsP_3$ receptor. *Nat. Struct. Mol. Biol.* **18**(10): 1172-1174.

Ling, X., B. Xie, X. Gao, L. Chang, W. Zheng, H. Chen, Y. Huang, L. Tan, M. Li and T. Liu (2020). Improving the efficiency of precise genome editing with site-specific Cas9-oligonucleotide conjugates. *Sci. Adv.* **6**(15): eaaz0051.

Lino, M. (1990). Biphasic Ca^{2+} dependence of inositol 1,4,5-trisphosphate-induced Ca^{2+} release in smooth muscle cells of the guinea pig taenia caeci. *J. Gen. Physiol.* **95**(6): 1103-1122.

Linse, S., A. Helmersson and S. Forsén (1991). Calcium binding to calmodulin and its globular domains. *J. Biol. Chem.* **266**(13): 8050-8054.

Liou, J., M. Fivaz, T. Inoue and T. Meyer (2007). Live-cell imaging reveals sequential oligomerization and local plasma membrane targeting of stromal interaction molecule 1 after Ca^{2+} store depletion. *PNAS* **104**(22): 9301-9306.

Liou, J., M. L. Kim, W. D. Heo, J. T. Jones, J. W. Myers, J. E. Ferrell, Jr. and T. Meyer (2005). STIM is a Ca^{2+} sensor essential for Ca^{2+}-store-depletion-triggered Ca^{2+} influx. *Curr. Biol.* **15**(13): 1235-1241.

Lissandron, V., P. Podini, P. Pizzo and T. Pozzan (2010). Unique characteristics of Ca^{2+} homeostasis of the trans-Golgi compartment. *PNAS* **107**(20): 9198-9203.

Liu, H., J. D. Hughes, S. Rollins, B. Chen and E. Perkins (2011). Calcium entry via ORAI1 regulates glioblastoma cell proliferation and apoptosis. *Exp. Mol. Pathol.* **91**(3): 753-760.

Liu, H., C. Liu, Y.-h. Zhao, X.-j. Han, Z.-w. Zhou, C. Wang, R.-f. Li and X.-l. Li (2018). Comparing successful gene knock-in efficiencies of CRISPR/Cas9 with ZFNs and TALENs gene editing systems in bovine and dairy goat fetal fibroblasts. *J. Integr. Agric.* **17**(2): 406-414.

Liu, X., G. Wu, Y. Yu, X. Chen, R. Ji, J. Lu, X. Li, X. Zhang, X. Yang and Y. Shen (2019). Molecular understanding of calcium permeation through the open Orai channel. *PLoS Biol.* **17**(4): e3000096.

Lock, J. T., K. J. Alzayady, D. I. Yule and I. Parker (2018). All three IP_3 receptor isoforms generate Ca^{2+} puffs that display similar characteristics. *Sci. Signal.* **11**(561): eaau0344.

Lock, J. T. and I. Parker (2020). IP_3 mediated global Ca^{2+} signals arise through two temporally and spatially distinct modes of Ca^{2+} release. *eLife* **9**: e55008.

Lopez, J. J., I. Jardin, J. Sanchez-Collado, G. M. Salido, T. Smani and J. A. Rosado (2020). TRPC channels in the SOCE scenario. *Cells* **9**(1): 126.

Lou, D., J. Wang and X. Wang (2020). Single nucleotide polymorphisms in the non-coding region of STIM1 gene are associated with Parkinson disease risk in Chinese Han population. *Medicine (Baltimore)* **99**(9): e19234.

Luik, R. M., B. Wang, M. Prakriya, M. M. Wu and R. S. Lewis (2008). Oligomerization of STIM1 couples ER calcium depletion to CRAC channel activation. *Nature* **454**(7203): 538-542.

Luik, R. M., M. M. Wu, J. Buchanan and R. S. Lewis (2006). The elementary unit of store-operated Ca^{2+} entry: local activation of CRAC channels by STIM1 at ER-plasma membrane junctions. *J. Cell Biol.* **174**(6): 815-825.

Lupu, V. D., E. Kaznacheyeva, U. M. Krishna, J. R. Falck and I. Bezprozvanny (1998). Functional coupling of phosphatidylinositol 4,5-bisphosphate to inositol 1,4,5-trisphosphate receptors. *J. Biol. Chem.* **273**(23): 14067-14070.

Lur, G., L. P. Haynes, I. A. Prior, O. V. Gerasimenko, S. Feske, O. H. Petersen, R. D. Burgoyne and A. V. Tepikin (2009). Ribosome-free terminals of rough ER allow formation of STIM1 puncta and segregation of STIM1 from IP_3 receptors. *Curr. Biol.* **19**(19): 1648-1653.

Ma, G., M. Wei, L. He, C. Liu, B. Wu, S. L. Zhang, J. Jing, X. Liang, A. Senes, P. Tan, S. Li, A. Sun, Y. Bi, L. Zhong, H. Si, Y. Shen, M. Li, M. S. Lee, W. Zhou, J. Wang, Y.

Wang and Y. Zhou (2015). Inside-out Ca^{2+} signalling prompted by STIM1 conformational switch. *Nat. Commun.* **6**: 7826.

Ma, H. T. and M. A. Beaven (2011). Regulators of Ca^{2+} signaling in mast cells: potential targets for treatment of mast cell-related diseases? *Adv. Exp. Med. Biol.* **716**: 62-90.

Madl, J., J. Weghuber, R. Fritsch, I. Derler, M. Fahrner, I. Frischauf, B. Lackner, C. Romanin and G. J. Schutz (2010). Resting state Orai1 diffuses as homotetramer in the plasma membrane of live mammalian cells. *J. Biol. Chem.* **285**(52): 41135-41142.

Maganti, L., S. Dutta, M. Ghosh and J. Chakrabarti (2019). Allostery in Orai1 binding to calmodulin revealed from conformational thermodynamics. *J. Biomol. Struct. Dyn.* **37**(2): 493-502.

Mali, P., J. Aach, P. B. Stranges, K. M. Esvelt, M. Moosburner, S. Kosuri, L. Yang and G. M. Church (2013). CAS9 transcriptional activators for target specificity screening and paired nickases for cooperative genome engineering. *Nat. Biotechnol.* **31**(9): 833-838.

Mali, P., K. M. Esvelt and G. M. Church (2013). Cas9 as a versatile tool for engineering biology. *Nat. Methods* **10**(10): 957-963.

Mali, P., L. Yang, K. M. Esvelt, J. Aach, M. Guell, J. E. DiCarlo, J. E. Norville and G. M. Church (2013). RNA-guided human genome engineering via Cas9. *Science* **339**(6121): 823-826.

Malli, R., S. Naghdi, C. Romanin and W. F. Graier (2008). Cytosolic Ca^{2+} prevents the subplasmalemmal clustering of STIM1: an intrinsic mechanism to avoid Ca^{2+} overload. *J. Cell Sci.* **121**(Pt 19): 3133-3139.

Malli, R. a. G. W. F. (2017). The Role of Mitochondria in the Activation/Maintenance of SOCE: The Contribution of Mitochondrial Ca2+ Uptake, Mitochondrial Motility, and Location to Store-Operated Ca2+ Entry. 297--319.

Mallilankaraman, K., P. Doonan, C. Cardenas, H. C. Chandramoorthy, M. Muller, R. Miller, N. E. Hoffman, R. K. Gandhirajan, J. Molgo, M. J. Birnbaum, B. S. Rothberg, D. O. Mak, J. K. Foskett and M. Madesh (2012). MICU1 Is an essential gatekeeper for MCU-mediated mitochondrial Ca^{2+}uptake that regulates cell survival. *Cell* **151**: 630-644.

Manjarres, I. M., A. Rodriguez-Garcia, M. T. Alonso and J. Garcia-Sancho (2010). The sarco/endoplasmic reticulum Ca^{2+} ATPase (SERCA) is the third element in capacitative calcium entry. *Cell Calcium* **47**(5): 412-418.

Marchant, J. S. and C. W. Taylor (1997). Cooperative activation of IP_3 receptors by sequential binding of IP_3 and Ca^{2+} safeguards against spontaneous activity. *Curr. Biol.* **7**(7): 510-518.

Marchi, S. and P. Pinton (2014). The mitochondrial calcium uniporter complex: molecular components, structure and physiopathological implications. *J. Physiol.* **592**(5): 829-839.

Marks, A. R., P. Tempst, K. S. Hwang, M. B. Taubman, M. Inui, C. Chadwick, S. Fleischer and B. Nadal-Ginard (1989). Molecular cloning and characterization of the ryanodine/junctional channel complex cDNA from skeletal muscle sarcoplasmic reticulum. *PNAS* **86**(22): 8683-8687.

Martin-Fernandez, M. L., C. J. Tynan and S. E. Webb (2013). A 'pocket guide' to total internal reflection fluorescence. *J. Microsc.* **252**(1): 16-22.

Maruyama, Y., T. Ebihara, H. Nishiyama, M. Suga and C. Sato (2012). Immuno EM-OM correlative microscopy in solution by atmospheric scanning electron microscopy (ASEM). *J. Struct. Biol.* **180**(2): 259-270.

Maruyama, Y., T. Ogura, K. Mio, K. Kato, T. Kaneko, S. Kiyonaka, Y. Mori and C. Sato (2009). Tetrameric Orai1 is a teardrop-shaped molecule with a long, tapered cytoplasmic domain. *J. Biol. Chem.* **284**(20): 13676-13685.

Matsuda, T. and I. Oinuma (2019). Optimized CRISPR/Cas9-mediated in vivo genome engineering applicable to monitoring dynamics of endogenous proteins in the mouse neural tissues. *Sci. Rep.* **9**(1): 11309.

Mattheyses, A. L., S. M. Simon and J. Z. Rappoport (2010). Imaging with total internal reflection fluorescence microscopy for the cell biologist. *J. Cell Sci.* **123**(21): 3621-3628.

McCarl, C. A., C. Picard, S. Khalil, T. Kawasaki, J. Rother, A. Papolos, J. Kutok, C. Hivroz, F. Ledeist, K. Plogmann, S. Ehl, G. Notheis, M. H. Albert, B. H. Belohradsky, J. Kirschner, A. Rao, A. Fischer and S. Feske (2009). ORAI1 deficiency and lack of store-operated Ca^{2+} entry cause immunodeficiency, myopathy, and ectodermal dysplasia. *J. Allergy Clin. Immunol.* **124**(6): 1311-1318 e1317.

McNally, B. A., A. Somasundaram, A. Jairaman, M. Yamashita and M. Prakriya (2013). The C- and N-terminal STIM1 binding sites on Orai1 are required for both trapping and gating CRAC channels. *J. Physiol.* **591**(11): 2833-2850.

McNally, B. A., A. Somasundaram, M. Yamashita and M. Prakriya (2012). Gated regulation of CRAC channel ion selectivity by STIM1. *Nature* **482**(7384): 241-245.

McNally, B. A., M. Yamashita, A. Engh and M. Prakriya (2009). Structural determinants of ion permeation in CRAC channels. *PNAS* **106**(52): 22516-22521.

Mercer, J. C., W. I. Dehaven, J. T. Smyth, B. Wedel, R. R. Boyles, G. S. Bird and J. W. Putney, Jr. (2006). Large store-operated calcium-selective currents due to co-expression of Orai1 or Orai2 with the intracellular calcium sensor, Stim1. *J. Biol. Chem.* **281**(34): 24979-24990.

Merck. "DNA Cleanup using illustra™ GFX Kits." from https://www.sigmaaldrich.com/technical-documents/protocols/biology/nucleic-acid-preparation/dna-cleanup-using-illustra-gfx-kits.html.

Meyer, T. and L. Stryer (1991). Calcium spiking. *Annu. Rev. Biophys. Biophys. Chem.* **20**: 153-174.

Miao, Y., Q. Shen, S. Zhang, H. Huang, X. Meng, X. Zheng, Z. Yao, Z. He, S. Lu, C. Cai and F. Zou (2019). Calcium-sensing stromal interaction molecule 2 upregulates nuclear factor of activated T cells 1 and transforming growth factor-β signaling to promote breast cancer metastasis. *Breast Cancer Res.* **21**(1): 99.

Miederer, A. M., D. Alansary, G. Schwar, P. H. Lee, M. Jung, V. Helms and B. A. Niemeyer (2015). A STIM2 splice variant negatively regulates store-operated calcium entry. *Nat. Commun.* **6**: 6899.

Mignen, O., J. L. Thompson and T. J. Shuttleworth (2008). Orai1 subunit stoichiometry of the mammalian CRAC channel pore. *J. Physiol.* **586**(2): 419-425.

Mignen, O., J. L. Thompson and T. J. Shuttleworth (2009). The molecular architecture of the arachidonate-regulated Ca^{2+}-selective ARC channel is a pentameric assembly of Orai1 and Orai3 subunits. *J. Physiol.* **587**(Pt 17): 4181-4197.

Milo, R., P. Jorgensen, U. Moran, G. Weber and M. Springer (2010). BioNumbers--the database of key numbers in molecular and cell biology. *Nucleic Acids Res.* **38**(Database issue): D750–D753.

Misceo, D., A. Holmgren, W. E. Louch, P. A. Holme, M. Mizobuchi, R. J. Morales, A. M. De Paula, A. Stray-Pedersen, R. Lyle, B. Dalhus, G. Christensen, H. Stormorken, G. E. Tjonnfjord and E. Frengen (2014). A dominant STIM1 mutation causes Stormorken syndrome. *Hum. Mutat.* **35**(5): 556-564.

Miura, Y., J. C. Henquin and P. Gilon (1997). Emptying of intracellular Ca^{2+} stores stimulates Ca^{2+} entry in mouse pancreatic beta-cells by both direct and indirect mechanisms. *J. Physiol.* **503**(Pt 2): 387-398.

Mojica, F. J., C. Diez-Villasenor, J. Garcia-Martinez and E. Soria (2005). Intervening sequences of regularly spaced prokaryotic repeats derive from foreign genetic elements. *J. Mol. Evol.* **60**(2): 174-182.

Mojica, F. J., C. Ferrer, G. Juez and F. Rodriguez-Valera (1995). Long stretches of short tandem repeats are present in the largest replicons of the Archaea Haloferax mediterranei and Haloferax volcanii and could be involved in replicon partitioning. *Mol. Microbiol.* **17**(1): 85-93.

Monkawa, T., A. Miyawaki, T. Sugiyama, H. Yoneshima, M. Yamamoto-Hino, T. Furuichi, T. Saruta, M. Hasagawa and K. Mikoshiba (1995). Heterotetrameric complex formation of inositol 1,4,5-trisphosphate receptor subunits. *J. Biol. Chem.* **270**(24): 14700-14704.

Montero, M., M. Brini, R. Marsault, J. Alvarez, R. Sitia, T. Pozzan and R. Rizzuto (1995). Monitoring dynamic changes in free Ca^{2+} concentration in the endoplasmic reticulum of intact cells. *EMBO J.* **14**(22): 5467-5475.

Morgan, A. J., F. M. Platt, E. Lloyd-Evans and A. Galione (2011). Molecular mechanisms of endolysosomal Ca^{2+} signalling in health and disease. *Biochem. J.* **439**(3): 349-374.

Mori, Y., M. Wakamori, T. Miyawkawa, M. Hermosura, Y. Hara, M. Nishida, K. Hirose, A. Mizushima, M. Kurosaki, E. Mori, K. Gotoh, T. Okada, A. Fleig, R. Penner, M. Iino and T. Kurosaki (2002). Transient receptor potential 1 regulates capacitative Ca^{2+} entry and Ca^{2+} release from endoplasmic reticulum in B lymphocytes. *J. Exp. Med.* **195**(6): 673-681.

Morin, G., N. O. Bruechle, A. R. Singh, C. Knopp, G. Jedraszak, M. Elbracht, D. Bremond-Gignac, K. Hartmann, H. Sevestre, P. Deutz, D. Herent, P. Nurnberg, B. Romeo, K. Konrad, M. Mathieu-Dramard, J. Oldenburg, E. Bourges-Petit, Y. Shen, K. Zerres, H. Ouadid-Ahidouch and J. Rochette (2014). Gain-of-function mutation in STIM1 (P.R304W) is associated with Stormorken Syndrome. *Hum. Mutat.* **35**(10): 1221-1232.

Moscou, M. J. and A. J. Bogdanove (2009). A simple cipher governs DNA recognition by TAL effectors. *Science* **326**(5959): 1501-1501.

Mostowy, S. and P. Cossart (2012). Septins: the fourth component of the cytoskeleton. *Nat. Rev. Mol. Cell Biol.* **13**(3): 183-194.

Muik, M., M. Fahrner, R. Schindl, P. Stathopulos, I. Frischauf, I. Derler, P. Plenk, B. Lackner, K. Groschner, M. Ikura and C. Romanin (2011). STIM1 couples to ORAI1 via an intramolecular transition into an extended conformation. *EMBO J.* **30**(9): 1678-1689.

Muik, M., I. Frischauf, I. Derler, M. Fahrner, J. Bergsmann, P. Eder, R. Schindl, C. Hesch, B. Polzinger, R. Fritsch, H. Kahr, J. Madl, H. Gruber, K. Groschner and C. Romanin (2008). Dynamic coupling of the putative coiled-coil domain of ORAI1 with STIM1 mediates ORAI1 channel activation. *J. Biol. Chem.* **283**: 8014-8022.

Mullins, F. M. and R. S. Lewis (2016). The inactivation domain of STIM1 is functionally coupled with the Orai1 pore to enable Ca^{2+}-dependent inactivation. *J. Gen. Physiol.* **147**(2): 153-164.

Mullins, F. M., C. Y. Park, R. E. Dolmetsch and R. S. Lewis (2009). STIM1 and calmodulin interact with Orai1 to induce Ca^{2+}-dependent inactivation of CRAC channels. *PNAS* **106**(36): 15495-15500.

Mullins, F. M., M. Yen and R. S. Lewis (2016). Orai1 pore residues control CRAC channel inactivation independently of calmodulin. *J. Gen. Physiol.* **147**(2): 137-152.

Naeem, M., S. Majeed, M. Z. Hoque and I. Ahmad (2020). Latest developed strategies to minimize the off-target effects in CRISPR-Cas-mediated genome editing. *Cells* **9**(7): 1608.

Nakamura, L., K. Sandrock-Lang, C. Speckmann, T. Vraetz, M. Buhrlen, S. Ehl, J. W. Heemskerk and B. Zieger (2013). Platelet secretion defect in a patient with stromal interaction molecule 1 deficiency. *Blood* **122**(22): 3696-3698.

Navarro-Borelly, L., A. Somasundaram, M. Yamashita, D. Ren, R. J. Miller and M. Prakriya (2008). STIM1-Orai1 interactions and Orai1 conformational changes revealed by live-cell FRET microscopy. *J. Physiol.* **586**(22): 5383-5401.

NEB PCR Using Q5® Hot Start High-Fidelity DNA Polymerase (M0493).

NEB (2020). "NEB Tm Calculator." from https://tmcalculator.neb.com/#!/main.

Negulescu, P. A., N. Shastri and M. D. Cahalan (1994). Intracellular calcium dependence of gene expression in single T lymphocytes. *PNAS* **91**(7): 2873-2877.

Nemudryi, A. A., K. R. Valetdinova, S. P. Medvedev and S. M. Zakian (2014). TALEN and CRISPR/Cas genome editing systems: tools of discovery. *Acta naturae* **6**(3): 19-40.

Nick McElhinny, S. A. and D. A. Ramsden (2004). Sibling rivalry: competition between Pol X family members in V(D)J recombination and general double strand break repair. *Immunol. Rev.* **200**: 156-164.

Nishibe, S., M. Wahl, S. Hernandez-Sotomayor, N. Tonks, S. Rhee and G. Carpenter (1990). Increase of the catalytic activity of phospholipase C-gamma 1 by tyrosine phosphorylation. *Science* **250**(4985): 1253-1256.

North, R. A. (2002). Molecular physiology of P2X receptors. *Physiol. Rev.* **82**(4): 1013-1067.

Nystoriak, M. A., M. Nieves-Cintrón and M. F. Navedo (2013). Capturing single L-type Ca^{2+} channel function with optics. *Biochim. Biophys. Acta Mol. Cell. Res.* **1833**(7): 1657-1664.

Oancea, E. and T. Meyer (1998). Protein kinase C as a molecular machine for decoding calcium and diacylglycerol signals. *Cell* **95**(3): 307-318.

Oh-Hora, M., M. Yamashita, P. G. Hogan, S. Sharma, E. Lamperti, W. Chung, M. Prakriya, S. Feske and A. Rao (2008). Dual functions for the endoplasmic reticulum calcium sensors STIM1 and STIM2 in T cell activation and tolerance. *Nat. Immunol.* **9**(4): 432-443.

Ong, H. L., L. B. de Souza, C. Zheng, K. T. Cheng, X. Liu, C. M. Goldsmith, S. Feske and I. S. Ambudkar (2015). STIM2 enhances receptor-stimulated Ca^{2+} signaling by promoting recruitment of STIM1 to the endoplasmic reticulum-plasma membrane junctions. *Sci. Signal.* **8**(359): ra3.

Ong, H. L., X. Liu, K. Tsaneva-Atanasova, B. B. Singh, B. C. Bandyopadhyay, W. D. Swaim, J. T. Russell, R. S. Hegde, A. Sherman and I. S. Ambudkar (2007). Relocalization of STIM1 for activation of store-operated Ca^{2+} entry is determined by the depletion of subplasma membrane endoplasmic reticulum Ca^{2+} store. *J. Biol. Chem.* **282**(16): 12176-12185.

Orci, L., M. Ravazzola, M. Le Coadic, W. W. Shen, N. Demaurex and P. Cosson (2009). STIM1-induced precortical and cortical subdomains of the endoplasmic reticulum. *PNAS* **106**(46): 19358-19362.

Otsu, K., H. F. Willard, V. K. Khanna, F. Zorzato, N. M. Green and D. H. MacLennan (1990). Molecular cloning of cDNA encoding the Ca^{2+} release channel (ryanodine receptor) of rabbit cardiac muscle sarcoplasmic reticulum. *J. Biol. Chem.* **265**(23): 13472-13483.

Pabo, C. O., E. Peisach and R. A. Grant (2001). Design and Selection of Novel Cys2His2 Zinc Finger Proteins. *Annu. Rev. Biochem.* **70**(1): 313-340.

Pacher, P., A. P. Thomas and G. Hajnóczky (2002). Ca^{2+} marks: miniature calcium signals in single mitochondria driven by ryanodine receptors. *PNAS* **99**(4): 2380-2385.

Palty, R., Z. Fu and E. Y. Isacoff (2017). Sequential steps of CRAC channel activation. *Cell Rep.* **19**(9): 1929-1939.

Palty, R. and E. Y. Isacoff (2016). Cooperative binding of Stromal Interaction Molecule 1 (STIM1) to the N and C Termini of Calcium Release-activated Calcium Modulator 1 (Orai1). *J. Biol. Chem.* **291**(1): 334-341.

Palty, R., W. F. Silverman, M. Hershfinkel, T. Caporale, S. L. Sensi, J. Parnis, C. Nolte, D. Fishman, V. Shoshan-Barmatz, S. Herrmann, D. Khananshvili and I. Sekler (2010). NCLX is an essential component of mitochondrial Na^+/Ca^{2+} exchange. *PNAS* **107**(1): 436-441.

Palty, R., C. Stanley and E. Y. Isacoff (2015). Critical role for Orai1 C-terminal domain and TM4 in CRAC channel gating. *Cell Res.* **25**(8): 963-980.

Parekh, A. B. (2010). Decoding cytosolic Ca^{2+} oscillations. *Trends Biochem. Sci.* **36**(2): 78-87.

Park, C. Y., P. J. Hoover, F. M. Mullins, P. Bachhawat, E. D. Covington, S. Raunser, T. Walz, K. C. Garcia, R. E. Dolmetsch and R. S. Lewis (2009). STIM1 clusters and activates CRAC channels via direct binding of a cytosolic domain to Orai1. *Cell* **136**(5): 876-890.

Parker, I., J. Choi and Y. Yao (1996). Elementary events of $InsP_3$-induced Ca^{2+} liberation in *Xenopus* oocytes: hot spots, puffs and blips. *Cell Calcium* **20**(2): 105-121.

Pathak, T. a. T. M. (2018). Mitochondrial Ca2+ signaling. *Pharmacology \& Therapeutics*.

Pavletich, N. P. and C. O. Pabo (1991). Zinc finger-DNA recognition: crystal structure of a Zif268-DNA complex at 2.1 A. *Science* **252**(5007): 809-817.

Peckys, D. B., D. Gaa, D. Alansary, B. A. Niemeyer and N. Jonge (2021). Supra-molecular assemblies of ORAI1 at rest precede local accumulation into puncta after activation. *Int. J. Mol. Sci.* **22**(2): 799.

Peel, S. E., B. Liu and I. P. Hall (2006). A key role for STIM1 in store operated calcium channel activation in airway smooth muscle. *Respir. Res.* **7**(1): 119.

Peinelt, C., M. Vig, D. L. Koomoa, A. Beck, M. J. Nadler, M. Koblan-Huberson, A. Lis, A. Fleig, R. Penner and J. P. Kinet (2006). Amplification of CRAC current by STIM1 and CRACM1 (Orai1). *Nat. Cell Biol.* **8**: 771-773.

Penna, A., A. Demuro, A. V. Yeromin, S. L. Zhang, O. Safrina, I. Parker and M. D. Cahalan (2008). The CRAC channel consists of a tetramer formed by Stim-induced dimerization of Orai dimers. *Nature* **456**(7218): 116-120.

Perni, S., J. L. Dynes, A. V. Yeromin, M. D. Cahalan and C. Franzini-Armstrong (2015). Nanoscale patterning of STIM1 and Orai1 during store-operated Ca^{2+} entry. *PNAS* **112**(40): E5533-E5542.

Pinton, P., T. Pozzan and R. Rizzuto (1998). The Golgi apparatus is an inositol 1,4,5-trisphosphate-sensitive Ca^{2+} store, with functional properties distinct from those of the endoplasmic reticulum. *EMBO J.* **17**(18): 5298-5308.

Pitts, B. J. (1979). Stoichiometry of sodium-calcium exchange in cardiac sarcolemmal vesicles. Coupling to the sodium pump. *J. Biol. Chem.* **254**(14): 6232-6235.

Popugaeva, E. and I. Bezprozvanny (2013). Role of endoplasmic reticulum Ca^{2+} signaling in the pathogenesis of Alzheimer disease. *Front. Mol. Neurosci.* **6**: 29.

Porter, K. R. and G. E. Palade (1957). Studies on the endoplasmic reticulum. III. Its form and distribution in striated muscle cells. *J. Biophys. Biochem. Cytol.* **3**(2): 269-300.

Pozo-Guisado, E., D. G. Campbell, M. Deak, A. Alvarez-Barrientos, N. A. Morrice, I. S. Alvarez, D. R. Alessi and F. J. Martin-Romero (2010). Phosphorylation of STIM1 at ERK1/2 target sites modulates store-operated calcium entry. *J. Cell Sci.* **123**(Pt 18): 3084-3093.

Pozo-Guisado, E., V. Casas-Rua, P. Tomas-Martin, A. M. Lopez-Guerrero, A. Alvarez-Barrientos and F. J. Martin-Romero (2013). Phosphorylation of STIM1 at ERK1/2

target sites regulates interaction with the microtubule plus-end binding protein EB1. *J. Cell Sci.* **126**(Pt 14): 3170-3180.

Prakriya, M., S. Feske, Y. Gwack, S. Srikanth, A. Rao and P. G. Hogan (2006). Orai1 is an essential pore subunit of the CRAC channel. *Nature* **443**(7108): 230-233.

Prakriya, M. and R. S. Lewis (2015). Store-operated calcium channels. *Physiol. Rev.* **95**(4): 1383-1436.

Protasi, F. (2002). Structural interaction between RYRs and DHPRs in calcium release units of cardiac and skeletal muscle cells. *Front Biosci.* **7**(4): 650-658.

Putney, J. W. (1986). A model for receptor-regulated calcium entry. *Cell Calcium* **7**(1): 1-12.

Putney, J. W. (2004). Store-operated calcium channels: how do we measure them, and why do we care? *Sci. STKE* **2004**(243): pe37.

Qiagen. "QIAGEN Plasmid Kits." from https://www.qiagen.com/gb/products/discovery-and-translational-research/dna-rna-purification/dna-purification/plasmid-dna/qiagen-plasmid-kits/?catno=12125.

Qin, X., L. Liu, S. K. Lee, A. Alsina, T. Liu, C. Wu, H. Park, C. Yu, H. Kim, J. Chu, A. Triller, B. Z. Tang, C. Hyeon, C. Y. Park and H. Park (2020). Increased confinement and polydispersity of STIM1 and Orai1 after Ca^{2+} Store Depletion. *Biophys. J.* **118**(1): 70-84.

Rahman, T. U., A. Skupin, M. Falcke and C. W. Taylor (2009). Clustering of IP_3 receptors by IP_3 retunes their regulation by IP_3 and Ca^{2+}. *Nature* **458**(7238): 655-659.

Ramirez, C. L., J. E. Foley, D. A. Wright, F. Müller-Lerch, S. H. Rahman, T. I. Cornu, R. J. Winfrey, J. D. Sander, F. Fu, J. A. Townsend, T. Cathomen, D. F. Voytas and J. K. Joung (2008). Unexpected failure rates for modular assembly of engineered zinc fingers. *Nat. Methods* **5**(5): 374-375.

Rana, A., M. Yen, A. M. Sadaghiani, S. Malmersjo, C. Y. Park, R. E. Dolmetsch and R. S. Lewis (2015). Alternative splicing converts STIM2 from an activator to an inhibitor of store-operated calcium channels. *J. Cell Biol.* **209**(5): 653–670.

Rapizzi, E., P. Pinton, G. r. Szabadkai, M. R. Wieckowski, G. g. Vandecasteele, G. Baird, R. A. Tuft, K. E. Fogarty and R. Rizzuto (2002). Recombinant expression of the voltage-dependent anion channel enhances the transfer of Ca^{2+} microdomains to mitochondria. *J. Cell Biol.* **159**(4): 613-624.

Rash, B. G., J. B. Ackman and P. Rakic (2016). Bidirectional radial Ca^{2+} activity regulates neurogenesis and migration during early cortical column formation. *Sci. Adv.* **2**(2): e1501733.

Rasola, A. and P. Bernardi (2007). The mitochondrial permeability transition pore and its involvement in cell death and in disease pathogenesis. *Apoptosis* **12**(5): 815-833.

Rebhan, M., V. Chalifa-Caspi, J. Prilusky and D. Lancet (1997). GeneCards: integrating information about genes, proteins and diseases. *Trends Genet.* **13**(4): 163.

Rizzuto, R., D. De Stefani, A. Raffaello and C. Mammucari (2012). Mitochondria as sensors and regulators of calcium signalling. *Nat. Rev. Mol. Cell Biol.* **13**(9): 566-578.

Robinson, C. R. and S. G. Sligar (1993). Molecular recognition mediated by bound water: A mechanism for star activity of the restriction endonuclease EcoRI. *J. Mol. Biol.* **234**(2): 302-306.

Roos, J., P. J. DiGregorio, A. V. Yeromin, K. Ohlsen, M. Lioudyno, S. Zhang, O. Safrina, J. A. Kozak, S. L. Wagner, M. D. Cahalan, G. Velicelebi and K. A. Stauderman (2005). STIM1, an essential and conserved component of store-operated Ca^{2+} channel function. *J. Cell Biol.* **169**(3): 435-445.

Ruano, Y., M. Mollejo, T. Ribalta, C. Fiaño, F. I. Camacho, E. Gómez, A. R. de Lope, J.-L. Hernández-Moneo, P. Martínez and B. Meléndez (2006). Identification of novel

candidate target genes in amplicons of Glioblastoma multiforme tumors detected by expression and CGH microarray profiling. *Mol. Cancer* **5**(1): 39.

Rust, M. J., M. Bates and X. Zhuang (2006). Sub-diffraction-limit imaging by stochastic optical reconstruction microscopy (STORM). *Nat. Methods* **3**(10): 793-795.

Saitoh, N., K. Oritani, K. Saito, T. Yokota, M. Ichii, T. Sudo, N. Fujita, K. Nakajima, M. Okada and Y. Kanakura (2011). Identification of functional domains and novel binding partners of STIM proteins. *J. Cell Biochem.* **112**(1): 147-156.

Salazar, C., A. Zaccaria Politi and T. Höfer (2008). Decoding of calcium oscillations by phosphorylation cycles: analytic results. *Biophys. J.* **94**(4): 1203-1215.

Santo-Domingo, J. and N. Demaurex (2010). Calcium uptake mechanisms of mitochondria. *Biochim Biophys Acta.* **1797**(6-7): 907-912.

Sasajima, H., X. Wang and C. van Breemen (1997). Fractional Ca^{2+} release from the endoplasmic reticulum activates Ca^{2+} entry in freshly isolated rabbit aortic endothelial cells. *Biochem. Biophys. Res. Commun.* **241**(2): 471-475.

Schermelleh, L., A. Ferrand, T. Huser, C. Eggeling, M. Sauer, O. Biehlmaier and G. P. C. Drummen (2019). Super-resolution microscopy demystified. *Nat. Cell Biol.* **21**(1): 72-84.

Schindl, R., J. Bergsmann, I. Frischauf, I. Derler, M. Fahrner, M. Muik, R. Fritsch, K. Groschner and C. Romanin (2008). 2-aminoethoxydiphenyl borate alters selectivity of Orai3 channels by increasing their pore size. *J. Biol. Chem.* **283**(29): 20261-20267.

Schmidt, B., D. Alansary, I. Bogeski, B. A. Niemeyer and H. Rieger (2019). Reaction-diffusion model for STIM-ORAI interaction: The role of ROS and mutations. *J. Theor. Biol.* **470**: 64-75.

Schuhmann, M. K., D. Stegner, A. Berna-Erro, S. Bittner, A. Braun, C. Kleinschnitz, G. Stoll, H. Wiendl, S. G. Meuth and B. Nieswandt (2010). Stromal interaction molecules 1

and 2 are key regulators of autoreactive T cell activation in murine autoimmune central nervous system inflammation. *J. Immunol.* **184**(3): 1536-1542.

Scrimgeour, N., T. Litjens, L. Ma, G. J. Barritt and G. Y. Rychkov (2009). Properties of Orai1 mediated store-operated current depend on the expression levels of STIM1 and Orai1 proteins. *J. Physiol.* **587**(Pt 12): 2903-2918.

Seo, M.-D., S. Velamakanni, N. Ishiyama, P. B. Stathopulos, A. M. Rossi, S. A. Khan, P. Dale, C. Li, J. B. Ames, M. Ikura and C. W. Taylor (2012). Structural and functional conservation of key domains in $InsP_3$ and ryanodine receptors. *Nature* **483**(7387): 108-112.

Sham, J. S., L. Cleemann and M. Morad (1995). Functional coupling of Ca^{2+} channels and ryanodine receptors in cardiac myocytes. *PNAS* **92**(1): 121-125.

Sharma, S., A. Quintana, G. M. Findlay, M. Mettlen, B. Baust, M. Jain, R. Nilsson, A. Rao and P. G. Hogan (2013). An siRNA screen for NFAT activation identifies septins as coordinators of store-operated Ca^{2+} entry. *Nature* **499**(7457): 238-242.

Shen, W. W., M. Frieden and N. Demaurex (2011). Local cytosolic Ca^{2+} elevations are required for stromal interaction molecule 1 (STIM1) de-oligomerization and termination of store-operated Ca^{2+} entry. *J. Biol. Chem.* **286**(42): 36448-36459.

Shen, Y., N. B. Thillaiappan and C. W. Taylor (2021). The store-operated Ca^{2+} entry complex comprises a small cluster of STIM1 associated with one Orai1 channel. *PNAS* **118**(10): e2010789118.

Shin, S. W. and J. S. Lee (2020). Optimized CRISPR/Cas9 strategy for homology-directed multiple targeted integration of transgenes in CHO cells. *Biotechnol. Bioeng.* **117**(6): 1895-1903.

Shoshan-Barmatz, V. and D. Gincel (2003). The voltage-dependent anion channel. *Cell Biochem. Biophys.* **39**(3): 279-292.

Shuai, J. and I. Parker (2005). Optical single-channel recording by imaging Ca^{2+} flux through individual ion channels: theoretical considerations and limits to resolution. *Cell Calcium* **37**(4): 283-299.

Skibinska-Kijek, A., M. B. Wisniewska, J. Gruszczynska-Biegala, A. Methner and J. Kuznicki (2009). Immunolocalization of STIM1 in the mouse brain. *Acta Neurobiol. Exp. (Wars)* **69**(4): 413-428.

Smith, I. F., S. M. Wiltgen, J. Shuai and I. Parker (2009). Ca^{2+} puffs originate from pre established stable clusters of inositol trisphosphate receptors. *Sci. Signal.* **2**(98): ra77.

Smith, J., J. M. Berg and S. Chandrasegaran (1999). A detailed study of the substrate specificity of a chimeric restriction enzyme. *Nucleic Acids Res.* **27**(2): 674-681.

Smith, J., M. Bibikova, F. G. Whitby, A. R. Reddy, S. Chandrasegaran and D. Carroll (2000). Requirements for double-strand cleavage by chimeric restriction enzymes with zinc finger DNA-recognition domains. *Nucleic Acids Res.* **28**(17): 3361-3369.

Smith, J. S., T. Imagawa, M. Jianje, M. Fill, K. P. Campbell and R. Coronado (1988). Purified ryanodine receptor from rabbit skeletal muscle is the calcium-release channel of sarcoplasmic reticulum. *Biophys. J.* **92**(1): 1-26.

Smyth, J. T., A. M. Beg, S. Wu, J. W. Putney and N. M. Rusan (2012). Phosphoregulation of STIM1 leads to exclusion of the endoplasmic reticulum from the mitotic spindle. *Curr. Biol.* **22**(16): 1487-1493.

Smyth, J. T., W. I. DeHaven, G. S. Bird and J. W. Putney, Jr. (2007). Role of the microtubule cytoskeleton in the function of the store-operated Ca^{2+} channel activator STIM1. *J. Cell Sci.* **120**(Pt 21): 3762-3771.

Smyth, J. T., W. I. Dehaven, G. S. Bird and J. W. Putney, Jr. (2008). Ca^{2+}-store-dependent and -independent reversal of Stim1 localization and function. *J. Cell Sci.* **121**(Pt 6): 762-772.

Soboloff, J., M. A. Spassova, T. Hewavitharana, L. P. He, W. Xu, L. S. Johnstone, M. A. Dziadek and D. L. Gill (2006). STIM2 is an inhibitor of STIM1-mediated store-operated Ca^{2+} Entry. *Curr. Biol.* **16**(14): 1465-1470.

Soboloff, J., M. A. Spassova, X. D. Tang, T. Hewavitharana, W. Xu and D. L. Gill (2006). Orai1 and STIM reconstitute store-operated calcium channel function. *J. Biol. Chem.* **30**(30): 20661-20665.

Song, M. Y., A. Makino and J. X. Yuan (2011). STIM2 contributes to enhanced xtore-operated Ca^{2+} entry in pulmonary artery smooth muscle cells from patients with idiopathic pulmonary arterial hypertension. *Pulm. Circ.* **1**(1): 84-94.

Spassova, M. A., J. Soboloff, L. P. He, W. Xu, M. A. Dziadek and D. L. Gill (2006). STIM1 has a plasma membrane role in the activation of store-operated Ca^{2+} channels. *PNAS* **103**(11): 4040-4045.

Srikanth, S., M. Jew, K. D. Kim, M. K. Yee, J. Abramson and Y. Gwack (2012). Junctate is a Ca^{2+}-sensing structural component of Orai1 and stromal interaction molecule 1 (STIM1). *PNAS* **109**(22): 8682-8687.

Srikanth, S., H. J. Jung, K. D. Kim, P. Souda, J. Whitelegge and Y. Gwack (2010). A novel EF-hand protein, CRACR2A, is a cytosolic Ca^{2+} sensor that stabilizes CRAC channels in T cells. *Nat. Cell Biol.* **12**(5): 436-446.

Srikanth, S., H. J. Jung, B. Ribalet and Y. Gwack (2010). The intracellular loop of Orai1 plays a central role in fast inactivation of Ca^{2+} release-activated Ca^{2+} channels. *J. Biol. Chem.* **285**(7): 5066-5075.

Srikanth, S., M. K. Yee, Y. Gwack and B. Ribalet (2011). The third transmembrane segment of orai1 protein modulates Ca^{2+} release-activated Ca^{2+} (CRAC) channel gating and permeation properties. *J. Biol. Chem.* **286**(40): 35318-35328.

Srinivasan, P. (2019). Detecting In-Situ oligomerization of engineered STIM1 proteins by diffraction-limited optical imaging. *PLoS One* **14**(3): e0213655.

Stathopulos, P. B. and M. Ikura (2019). Does stromal interaction molecule-1 have five senses? *Cell Calcium* **77**: 79-80.

Stathopulos, P. B., G. Y. Li, M. J. Plevin, J. B. Ames and M. Ikura (2006). Stored Ca^{2+} depletion-induced oligomerization of stromal interaction molecule 1 (STIM1) via the EF-SAM region: An initiation mechanism for capacitive Ca^{2+} entry. *J. Biol. Chem.* **281**(47): 35855-35862.

Stathopulos, P. B., R. Schindl, M. Fahrner, L. Zheng, G. M. Gasmi-Seabrook, M. Muik, C. Romanin and M. Ikura (2013). STIM1/Orai1 coiled-coil interplay in the regulation of store-operated calcium entry. *Nat. Commun.* **4**: 2963.

Stathopulos, P. B., L. Zheng, G. Y. Li, M. J. Plevin and M. Ikura (2008). Structural and mechanistic insights into STIM1-mediated initiation of store-operated calcium entry. *Cell* **135**(1): 110-122.

Steinbach, Joe H. and G. Akk (2011). Use of Concatemers of Ligand-Gated Ion Channel Subunits to Study Mechanisms of Steroid Potentiation. *Anesthesiology* **115**(6): 1328-1337.

Subedi, K. P., H. L. Ong, G. Y. Son, X. Liu and I. S. Ambudkar (2018). STIM2 induces activated conformation of STIM1 to control Orai1 function in ER-PM junctions. *Cell Rep.* **23**(2): 522-534.

Supattapone, S., P. F. Worley, J. M. Baraban and S. H. Snyder (1988). Solubilization, purification, and characterization of an inositol trisphosphate receptor. *J. Biol. Chem.* **263**(3): 1530-1534.

Tadross, M. R., I. E. Dick and D. T. Yue (2008). Mechanism of local and global Ca^{2+} sensing by calmodulin in complex with a Ca^{2+} channel. *Cell* **133**(7): 1228-1240.

Takahashi, Y., M. Murakami, H. Watanabe, H. Hasegawa, T. Ohba, Y. Munehisa, K. Nobori, K. Ono, T. Iijima and H. Ito (2007). Essential role of the N-terminus of murine Orai1 in store-operated Ca^{2+} entry. *Biochem. Biophys. Res. Commun.* **356**(1): 45-52.

Takemura, H., H. Ohshika, N. Yokosawa, K. Oguma and O. Thastrup (1991). The thapsigargin-sensitive intracellular Ca^{2+} pool is more important in plasma membrane Ca^{2+} entry than the IP_3-sensitive intracellular Ca^{2+} pool in neuronal cell lines. *Biochem. Biophys. Res. Commun.* **180**(3): 1518-1526.

Tan, W. and M. Colombini (2007). VDAC closure increases calcium ion flux. *Biochim. Biophys. Acta. Biomembr.* **1768**(10): 2510-2515.

Tateishi, Y., M. Hattori, T. Nakayama, M. Iwai, H. Bannai, T. Nakamura, T. Michikawa, T. Inoue and K. Mikoshiba (2005). Cluster formation of inositol 1,4,5-trisphosphate receptor requires its transition to open state. *J. Biol. Chem.* **280**(8): 6816-6822.

Taylor, C. W., P. C. A. da Fonseca and E. P. Morris (2004). IP_3 receptors: the search for structure. *Trends Biochem. Sci.* **29**(4): 210-219.

Taylor, C. W. and K. Machaca (2019). IP_3 receptors and store-operated Ca^{2+} entry: a license to fill. *Curr. Opin. Cell Biol.* **57**: 1-7.

Thastrup, O., A. P. Dawson, O. Scharff, B. Foder, P. J. Cullen, B. K. DrØbak, P. J. Bjerrum, S. B. Christensen and M. R. Hanley (1989). Thapsigargin, a novel molecular probe for studying intracellular calcium release and storage. *Agents Actions* **27**(1-2): 17-23.

Thillaiappan, N. B., P. Chakraborty, G. Hasan and C. W. Taylor (2019). IP_3 receptors and Ca^{2+} entry. *Biochim. Biophys. Acta Mol. Cell. Res.* **1866**(7): 1092-1100.

Thillaiappan, N. B., A. P. Chavda, S. C. Tovey, D. L. Prole and C. W. Taylor (2017). Ca^{2+} signals initiate at immobile IP_3 receptors adjacent to ER-plasma membrane junctions. *Nat. Commun.* **8**(1): 1505.

Thillaiappan, N. B., H. A. Smith, P. Atakpa-Adaji and C. W. Taylor (2021). KRAP tethers IP_3 receptors to actin and licenses them to evoke cytosolic Ca^{2+} signals. *Nat. Commun.* **12**(1): 4514.

Thomas, D., P. Lipp, S. C. Tovey, M. J. Berridge, W. Li, R. Y. Tsien and M. D. Bootman (2000). Microscopic properties of elementary Ca^{2+} release sites in non-excitable cells. *Curr. Biol.* **10**(1): 8-15.

Thompson, J. L. and T. J. Shuttleworth (2013). How many Orai's does it take to make a CRAC channel? *Sci. Rep.* **3**: 1961.

Tiffner, A., L. Maltan, M. Fahrner, M. Sallinger, S. Weiss, H. Grabmayr, C. Hoglinger and I. Derler (2021). Transmembrane domain 3 (TM3) governs Orai1 and Orai3 pore opening in an isoform-specific manner. *Front. Cell Dev. Biol.* **9**: 635705.

Tiffner, A., L. Maltan, S. Weiss and I. Derler (2021). The Orai pore opening mechanism. *Int. J. Mol. Sci.* **22**(2): 533.

Tinevez, J. Y., N. Perry, J. Schindelin, G. M. Hoopes, G. D. Reynolds, E. Laplantine, S. Y. Bednarek, S. L. Shorte and K. W. Eliceiri (2017). TrackMate: An open and extensible platform for single-particle tracking. *Methods* **115**: 80-90.

Tinker, A. and A. J. Williams (1992). Divalent cation conduction in the ryanodine receptor channel of sheep cardiac muscle sarcoplasmic reticulum. *J. Gen. Physiol.* **100**(3): 479-493.

Tirado-Lee, L., M. Yamashita and M. Prakriya (2015). Conformational changes in the Orai1 C-terminus evoked by STIM1 binding. *PLoS One* **10**(6): e0128622.

Tojyo, Y., T. Morita, A. Nezu and A. Tanimura (2008). The clustering of inositol 1,4,5-trisphosphate (IP_3) receptors is triggered by IP_3 binding and facilitated by depletion of the Ca^{2+} store. *J. Pharmacol. Sci.* **107**(2): 138-150.

Tomida, T., K. Hirose, A. Takizawa, F. Shibasaki and M. Iino (2003). NFAT functions as a working memory of Ca^{2+} signals in decoding Ca^{2+} oscillation. *EMBO J.* **22**(15): 3825-3832.

Treves, S., C. Franzini-Armstrong, L. Moccagatta, C. Arnoult, C. Grasso, A. Schrum, S. Ducreux, M. X. Zhu, K. Mikoshiba, T. Girard, S. Smida-Rezgui, M. Ronjat and F. Zorzato (2004). Junctate is a key element in calcium entry induced by activation of $InsP_3$ receptors and/or calcium store depletion. *J. Cell Biol.* **166**(4): 537-548.

Ulbrich, M. H. and E. Y. Isacoff (2007). Subunit counting in membrane-bound proteins. *Nat. Methods* **4**(4): 319-321.

Vaeth, M., M. Maus, S. Klein-Hessling, E. Freinkman, J. Yang, M. Eckstein, S. Cameron, S. E. Turvey, E. Serfling, F. Berberich-Siebelt, R. Possemato and S. Feske (2017). Store-operated Ca^{2+} entry controls clonal expansion of T cells through metabolic reprogramming. *Immunity* **47**(4): 664-679 e666.

Vaeth, M., J. Yang, M. Yamashita, I. Zee, M. Eckstein, C. Knosp, U. Kaufmann, P. Karoly Jani, R. S. Lacruz, V. Flockerzi, I. Kacskovics, M. Prakriya and S. Feske (2017). ORAI2 modulates store-operated calcium entry and T cell-mediated immunity. *Nat. Commun.* **8**: 14714.

Vais, H., J. K. Foskett and D. O. Mak (2010). Unitary Ca^{2+} current through recombinant type 3 $InsP_3$ receptor channels under physiological ionic conditions. *J. Gen. Physiol.* **136**(6): 687-700.

Van Baelen, K., J. Vanoevelen, G. Callewaert, J. B. Parys, H. De Smedt, L. Raeymaekers, R. Rizzuto, L. Missiaen and F. Wuytack (2003). The contribution of the SPCA1 Ca2+ pump to the Ca2+ accumulation in the Golgi apparatus of HeLa cells assessed via RNA-mediated interference. *Biochem. Biophys. Res. Commun.* **306**(2): 430-436.

van de Linde, S., M. Sauer and M. Heilemann (2008). Subdiffraction-resolution fluorescence imaging of proteins in the mitochondrial inner membrane with photoswitchable fluorophores. *J. Struct. Biol* **164**(3): 250-254.

Vandecaetsbeek, I., P. Vangheluwe, L. Raeymaekers, F. Wuytack and J. Vanoevelen (2012). The Ca^{2+} pumps of the endoplasmic reticulum and Golgi apparatus. *Cold Spring Harb. Perspect. Biol.* **3**(5): a004184.

Varga-Szabo, D., A. Braun, C. Kleinschnitz, M. Bender, I. Pleines, M. Pham, T. Renne, G. Stoll and B. Nieswandt (2008). The calcium sensor STIM1 is an essential mediator of arterial thrombosis and ischemic brain infarction. *J. Exp. Med.* **205**(7): 1583-1591.

Varnai, P., B. Toth, D. J. Toth, L. Hunyady and T. Balla (2007). Visualization and manipulation of plasma membrane-endoplasmic reticulum contact sites indicates the presence of additional molecular components within the STIM1-Orai1 complex. *J. Biol. Chem.* **282**(40): 29678-29690.

Vasington, F. D. and J. V. Murphy (1962). Ca^{2+} ion uptake by rat kidney mitochondria and its dependence on respiration and phosphorylation. *J. Biol. Chem.* **237**(8): 2670-2677.

Venkiteswaran, G. and G. Hasan (2009). Intracellular Ca^{2+} signaling and store-operated Ca^{2+} entry are required in Drosophila neurons for flight. *PNAS* **106**(25): 10326-10331.

Vig, M., A. Beck, J. M. Billingsley, A. Lis, S. Parvez, C. Peinelt, D. L. Koomoa, J. Soboloff, D. L. Gill, A. Fleig, J. P. Kinet and R. Penner (2006). CRACM1 multimers form the ion-selective pore of the CRAC channel. *Curr. Biol.* **16**(20): 2073-2079.

Vig, M., C. Peinelt, A. Beck, D. L. Koomoa, D. Rabah, M. Koblan-Huberson, S. Kraft, H. Turner, A. Fleig, R. Penner and J. P. Kinet (2006). CRACM1 is a plasma membrane protein essential for store-operated Ca^{2+} entry. *Science* **312**(5777): 1220-1223.

Voets, T., J. Prenen, A. Fleig, R. Vennekens, H. Watanabe, J. G. J. Hoenderop, R. J. M. Bindels, G. Droogmans, R. Penner and B. Nilius (2001). CaT1 and the calcium release-activated calcium channel manifest distinct pore properties. *J. Biol. Chem.* **276**(51): 47767-47770.

Wacquier, B., V. Voorsluijs, L. Combettes and G. Dupont (2019). Coding and decoding of oscillatory Ca^{2+} signals. *Semin. Cell Dev. Biol.* **94**: 11-19.

Walsh, C. M., M. Chvanov, L. P. Haynes, O. H. Petersen, A. V. Tepikin and R. D. Burgoyne (2009). Role of phosphoinositides in STIM1 dynamics and store-operated calcium entry. *Biochem. J.* **425**(1): 159-168.

Wang, H., C. Wang, L. Wang, T. Liu, Z. Wang, H. You, Y. Zheng and D. Luo (2018). Orai1 downregulation impairs lymphocyte function in type 2 diabetes mellitus. *Biochem. Biophys. Res. Commun.* **500**(2): 384-390.

Wang, J. Y., J. Sun, M. Y. Huang, Y. S. Wang, M. F. Hou, Y. Sun, H. He, N. Krishna, S. J. Chiu, S. Lin, S. Yang and W. C. Chang (2015). STIM1 overexpression promotes colorectal cancer progression, cell motility and COX-2 expression. *Oncogene* **34**(33): 4358-4367.

Wang, X., Y. Wang, Y. Zhou, E. Hendron, S. Mancarella, M. D. Andrake, B. S. Rothberg, J. Soboloff and D. L. Gill (2014). Distinct Orai-coupling domains in STIM1 and STIM2 define the Orai-activating site. *Nat. Commun.* **5**: 3183.

Wang, Y., H. Wang, T. Pan, L. Li, J. Li and H. Yang (2017). STIM1 silencing inhibits the migration and invasion of A549 cells. *Mol. Med. Rep.* **16**(3): 3283-3289.

Wes, P. D., J. Chevesich, A. Jeromin, C. Rosenberg, G. Stetten and C. Montell (1995). TRPC1, a human homolog of a Drosophila store-operated channel. *PNAS* **92**(21): 9652-9656.

Wilfinger WW, M. K., Chomczynski P. (2006). DNA Sequencing II: Optimizing Preparation and Cleanup, Jones and Bartlett Publishers.

Williams, R. T., S. S. Manji, N. J. Parker, M. S. Hancock, L. Van Stekelenburg, J. P. Eid, P. V. Senior, J. S. Kazenwadel, T. Shandala, R. Saint, P. J. Smith and M. A. Dziadek

(2001). Identification and characterization of the STIM (stromal interaction molecule) gene family: coding for a novel class of transmembrane proteins. *Biochem. J.* **357**(Pt 3): 673-685.

Williams, R. T., P. V. Senior, L. Van Stekelenburg, J. E. Layton, P. J. Smith and M. A. Dziadek (2002). Stromal interaction molecule 1 (STIM1), a transmembrane protein with growth suppressor activity, contains an extracellular SAM domain modified by N-linked glycosylation. *Biochim. Biophys. Acta, Protein Struct. Mol. Enzymol.* **1596**(1): 131-137.

Wilson, B. S., J. R. Pfeiffer, A. J. Smith, J. M. Oliver, J. A. Oberdorf and R. J. H. Wojcikiewicz (1998). Calcium-dependent clustering of inositol 1,4,5-trisphosphate receptors. *Mol. Biol. Cell* **9**(6): 1465-1478.

Wilson, T. E., U. Grawunder and M. R. Lieber (1997). Yeast DNA ligase IV mediates non-homologous DNA end joining. *Nature* **388**(6641): 495-498.

Wiltgen, S. M., I. F. Smith and I. Parker (2010). Superresolution localization of single functional IP_3R channels utilizing Ca^{2+} flux as a readout. *Biophys. J.* **99**: 437-446.

Woodard, G. E., G. M. Salido and J. A. Rosado (2008). Enhanced exocytotic-like insertion of Orai1 into the plasma membrane upon intracellular Ca^{2+} store depletion. *Am. J. Physiol. Cell. Physiol.* **294**(6): C1323-1331.

Wu, M. M., J. Buchanan, R. M. Luik and R. S. Lewis (2006). Ca^{2+} store depletion causes STIM1 to accumulate in ER regions closely associated with the plasma membrane. *J. Cell Biol.* **174**(6): 803-813.

Wu, M. M., E. D. Covington and R. S. Lewis (2014). Single-molecule analysis of diffusion and trapping of STIM1 and Orai1 at endoplasmic reticulum-plasma membrane junctions. *Mol. Biol. Cell* **25**(22): 3672-3685.

Wu, X., G. Babnigg and M. L. Villereal (2000). Functional significance of human trp1 and trp3 in store-operated Ca^{2+} entry in HEK-293 cells. *Am. J. Physiol. Cell. Physiol.* **278**(3): C526-536.

Xu, P., J. Lu, Z. Li, X. Yu, L. Chen and T. Xu (2006). Aggregation of STIM1 underneath the plasma membrane induces clustering of Orai1. *Biochem. Biophys. Res. Commun.* **350**(4): 969-976.

Yamakage, M. and A. Namiki (2002). Calcium channels--basic aspects of their structure, function and gene encoding; anesthetic action on the channels--a review. *Can. J. Anaesth.* **49**(2): 151-164.

Yamashita, M., C. E. Ing, P. S. Yeung, M. M. Maneshi, R. Pomes and M. Prakriya (2020). The basic residues in the Orai1 channel inner pore promote opening of the outer hydrophobic gate. *J. Gen. Physiol.* **152**(1): e201912397.

Yamashita, M., L. Navarro-Borelly, B. A. McNally and M. Prakriya (2007). Orai1 mutations alter ion permeation and Ca^{2+}-dependent fast inactivation of CRAC channels: evidence for coupling of permeation and gating. *J. Gen. Physiol.* **130**(5): 525-540.

Yamashita, M., P. S. Yeung, C. E. Ing, B. A. McNally, R. Pomes and M. Prakriya (2017). STIM1 activates CRAC channels through rotation of the pore helix to open a hydrophobic gate. *Nat. Commun.* **8**: 14512.

Yang, S., J. J. Zhang and X. Y. Huang (2009). Orai1 and STIM1 are critical for breast tumor cell migration and metastasis. *Cancer Cell* **15**(2): 124-134.

Yang, X., H. Jin, X. Cai, S. Li and Y. Shen (2012). Structural and mechanistic insights into the activation of Stromal interaction molecule 1 (STIM1). *PNAS* **109**(15): 5657-5662.

Yen, M. and R. S. Lewis (2018). Physiological CRAC channel activation and pore properties require STIM1 binding to all six Orai1 subunits. *J. Gen. Physiol.* **150**(10): 1373-1385.

Yen, M. and R. S. Lewis (2019). Numbers count: How STIM and Orai stoichiometry affect store-operated calcium entry. *Cell Calcium* **79**: 35-43.

Yen, M., L. A. Lokteva and R. S. Lewis (2016). Functional analysis of Orai1 concatemers supports a hexameric stoichiometry for the CRAC channel. *Biophys. J.* **111**(9): 1897-1907.

Yeromin, A. V., S. L. Zhang, W. Jiang, Y. Yu, O. Safrina and M. D. Cahalan (2006). Molecular identification of the CRAC channel by altered ion selectivity in a mutant of Orai. *Nature* **443**(7108): 226-229.

Yeung, P. S., M. Yamashita, C. E. Ing, R. Pomes, D. M. Freymann and M. Prakriya (2018). Mapping the functional anatomy of Orai1 transmembrane domains for CRAC channel gating. *PNAS* **115**(22): E5193-E5202.

Yu, F., L. Sun, R. Courjaret and K. Machaca (2011). Role of the STIM1 C-terminal domain in STIM1 clustering. *J. Biol. Chem.* **286**(10): 8375-8384.

Yu, F., L. Sun, S. Hubrack, S. Selvaraj and K. Machaca (2013). Intramolecular shielding maintains the ER Ca^{2+} sensor STIM1 in an inactive conformation. *J. Cell Sci.* **126**(Pt 11): 2401-2410.

Yu, J., H. Zhang, M. Zhang, Y. Deng, H. Wang, J. Lu, T. Xu and P. Xu (2013). An aromatic amino acid in the coiled-coil 1 domain plays a crucial role in the auto-inhibitory mechanism of STIM1. *Biochem. J.* **454**(3): 401-409.

Yu, S. P. and D. W. Choi (1997). Na^{+}—Ca^{2+} exchange currents in cortical neurons: concomitant forward and reverse operation and effect of glutamate. *Eur. J. Neurosci.* **9**(6): 1273-1281.

Yu, Y., M. H. Ulbrich, M. H. Li, Z. Buraei, X. Z. Chen, A. C. Ong, L. Tong, E. Y. Isacoff and J. Yang (2009). Structural and molecular basis of the assembly of the TRPP2/PKD1 complex. *PNAS* **106**(28): 11558-11563.

Yuan, J. P., W. Zeng, M. R. Dorwart, Y. J. Choi, P. F. Worley and S. Muallem (2009). SOAR and the polybasic STIM1 domains gate and regulate Orai channels. *Nat. Cell Biol.* **11**(3): 337-343.

Zhan, Z. Y., L. X. Zhong, M. Feng, J. F. Wang, D. B. Liu and J. P. Xiong (2015). Over-expression of Orai1 mediates cell proliferation and associates with poor prognosis in human non-small cell lung carcinoma. *Int. J. Clin. Exp. Pathol.* **8**(5): 5080-5088.

Zhang, J.-P., X.-L. Li, G.-H. Li, W. Chen, C. Arakaki, G. D. Botimer, D. Baylink, L. Zhang, W. Wen, Y.-W. Fu, J. Xu, N. Chun, W. Yuan, T. Cheng and X.-B. Zhang (2017). Efficient precise knockin with a double cut HDR donor after CRISPR/Cas9-mediated double-stranded DNA cleavage. *Genome Biol.* **18**(1): 35.

Zhang, S. L., J. A. Kozak, W. Jiang, A. V. Yeromin, J. Chen, Y. Yu, A. Penna, W. Shen, V. Chi and M. D. Cahalan (2008). Store-dependent and -independent modes regulating Ca^{2+} release-activated Ca^{2+} channel activity of human Orai1 and Orai3. *J. Biol. Chem.* **283**(25): 17662-17671.

Zhang, S. L., A. V. Yeromin, J. Hu, A. Amcheslavsky, H. Zheng and M. D. Cahalan (2011). Mutations in Orai1 transmembrane segment 1 cause STIM1-independent activation of Orai1 channels at glycine 98 and channel closure at arginine 91. *PNAS* **108**(43): 17838-17843.

Zhang, S. L., A. V. Yeromin, X. H. Zhang, Y. Yu, O. Safrina, A. Penna, J. Roos, K. A. Stauderman and M. D. Cahalan (2006). Genome-wide RNAi screen of Ca^{2+} influx identifies genes that regulate Ca^{2+} release-activated Ca^{2+} channel activity. *PNAS* **103**(24): 9357-9362.

Zhang, S. L., Y. Yu, J. Roos, J. A. Kozak, T. J. Deerinck, M. H. Ellisman, K. A. Stauderman and M. D. Cahalan (2005). STIM1 is a Ca^{2+} sensor that activates CRAC channels and migrates from the Ca^{2+} store to the plasma membrane. *Nature* **437**(7060): 902-905.

Zhang, W., Y. Jiang, Q. Wang, X. Ma, Z. Xiao, W. Zuo, X. Fang and Y.-G. Chen (2009). Single-molecule imaging reveals transforming growth factor-β-induced type II receptor dimerization. *PNAS* **106**(37): 15679-15683.

Zheng, H., M. H. Zhou, C. Hu, E. Kuo, X. Peng, J. Hu, L. Kuo and S. L. Zhang (2013). Differential roles of the C and N termini of Orai1 protein in interacting with stromal interaction molecule 1 (STIM1) for Ca^{2+} release-activated Ca^{2+} (CRAC) channel activation. *J. Biol. Chem.* **288**(16): 11263-11272.

Zheng, L., P. B. Stathopulos, G. Y. Li and M. Ikura (2008). Biophysical characterization of the EF-hand and SAM domain containing Ca^{2+} sensory region of STIM1 and STIM2. *Biochem. Biophys. Res. Commun.* **369**(1): 240-246.

Zheng, L., P. B. Stathopulos, R. Schindl, G. Y. Li, C. Romanin and M. Ikura (2011). Auto-inhibitory role of the EF-SAM domain of STIM proteins in store-operated calcium entry. *PNAS* **108**(4): 1337-1342.

Zheng, S., L. Zhou, G. Ma, T. Zhang, J. Liu, J. Li, N. T. Nguyen, X. Zhang, W. Li, R. Nwokonko, Y. Zhou, F. Zhao, Y. Huang, D. L. Gill and Y. Wang (2018). Calcium store refilling and STIM activation in STIM- and Orai-deficient cell lines. *Pflugers Archiv* **470**(10): 1555-1567.

Zhou, Y., X. Cai, N. A. Loktionova, X. Wang, R. M. Nwokonko, Y. Wang, B. S. Rothberg, M. Trebak and D. L. Gill (2016). The STIM1-binding site nexus remotely controls Orai1 channel gating. *Nat. Commun.* **7**: 13725.

Zhou, Y., X. Cai, R. M. Nwokonko, N. A. Loktionova, Y. Wang and D. L. Gill (2017). The STIM-Orai coupling interface and gating of the Orai1 channel. *Cell Calcium* **63**: 8-13.

Zhou, Y., P. Meraner, H. T. Kwon, D. Machnes, M. Oh-hora, J. Zimmer, Y. Huang, A. Stura, A. Rao and P. G. Hogan (2010). STIM1 gates the store-operated calcium channel ORAI1 in vitro. *Nat. Struct. Mol. Biol.* **17**(1): 112-116.

Zhou, Y., R. M. Nwokonko, X. Cai, N. A. Loktionova, R. Abdulqadir, P. Xin, B. A. Niemeyer, Y. Wang, M. Trebak and D. L. Gill (2018). Cross-linking of Orai1 channels by STIM proteins. *PNAS* **115**(15): E3398-E3407.

Zhou, Y., S. Ramachandran, M. Oh-Hora, A. Rao and P. G. Hogan (2010). Pore architecture of the ORAI1 store-operated calcium channel. *PNAS* **107**(11): 4896-4901.

Zhou, Y., P. Srinivasan, S. Razavi, S. Seymour, P. Meraner, A. Gudlur, P. B. Stathopulos, M. Ikura, A. Rao and P. G. Hogan (2013). Initial activation of STIM1, the regulator of store-operated calcium entry. *Nat. Struct. Mol. Biol.* **20**(8): 973-981.

Zhou, Y., X. Wang, N. A. Loktionova, X. Cai, R. M. Nwokonko, E. Vrana, Y. Wang, B. S. Rothberg and D. L. Gill (2015). STIM1 dimers undergo unimolecular coupling to activate Orai1 channels. *Nat. Commun.* **6**: 8395.

Zhou, Z. and I. Neher (1993). Mobile and immobile calcium buffers in bovine adrenal chromaffin cells. *J. Physiol.* **469**(1): 245-273.

Zhu, Z., N. Verma, F. González, Z.-D. Shi and D. Huangfu (2015). A CRISPR/Cas-mediated selection-free knockin strategy in human embryonic stem cells. *Stem Cell Rep.* **4**(6): 1103-1111.

Zweifach, A. and R. S. Lewis (1995). Rapid inactivation of depletion-activated calcium current (I_{CRAC}) due to local calcium feedback. *J. Gen. Physiol.* **105**(2): 209-226.